



**HAL**  
open science

# Structure chimique et électronique des interfaces métal/ferroélectrique en fonction de la polarisation ferroélectrique

Julien Rault

► **To cite this version:**

Julien Rault. Structure chimique et électronique des interfaces métal/ferroélectrique en fonction de la polarisation ferroélectrique. Science des matériaux [cond-mat.mtrl-sci]. Université Pierre et Marie Curie - Paris VI, 2013. Français. NNT : 2013PA066797 . tel-00840865

**HAL Id: tel-00840865**

**<https://theses.hal.science/tel-00840865>**

Submitted on 3 Jul 2013

**HAL** is a multi-disciplinary open access archive for the deposit and dissemination of scientific research documents, whether they are published or not. The documents may come from teaching and research institutions in France or abroad, or from public or private research centers.

L'archive ouverte pluridisciplinaire **HAL**, est destinée au dépôt et à la diffusion de documents scientifiques de niveau recherche, publiés ou non, émanant des établissements d'enseignement et de recherche français ou étrangers, des laboratoires publics ou privés.

**THESE DE DOCTORAT DE  
L'UNIVERSITE PIERRE ET MARIE CURIE**

Spécialité

Physique de la Région Parisienne  
(ED 107)

Présentée par

M. Julien RAULT

Pour obtenir le grade de

**DOCTEUR de l'UNIVERSITÉ PIERRE ET MARIE CURIE**

Sujet de la thèse :

Chemical and Electronic Structure of the Metal/Ferroelectric Interface as a Function of Ferroelectric Polarization

soutenue le 17/06/2013

devant le jury composé de :

M. Nick BARRETT : Directeur de thèse

M. Andreas KLEIN et Mme. Beatriz NOHEDA PINUAGA : Rapporteurs

MM. Thomas MAROUTIAN, Claus M. SCHNEIDER et Massimiliano MARANGOLO : Examineurs



# Chemical and Electronic Structure of the Metal/Ferroelectric Interface as a Function of Ferroelectric Polarization

Julien E. RAULT

2010 – 2013

Commissariat à l'énergie atomique et aux énergies alternatives  
Direction des Sciences de la Matière  
Institut Rayonnement Matière de Saclay  
Service de Physique et Chimie des Surfaces et Interfaces

*Sous la direction de :*

**Dr. Nick BARRETT**

julien.e.rault@gmail.com

Chemical and Electronic Structure of the  
Metal/Ferroelectric Interface as a Function of  
Ferroelectric Polarization

Julien E. RAULT

2010–2013



# Abstract

Screening phenomena at the interface between a ferroelectric (FE) and an electrode are of great interest both from a fundamental point of view and for potential applications using a FE layer (FeRAM, FE tunnel junctions). In particular, when reducing thickness of the ferroelectric layer, the depolarizing field due to surface charges induced by the FE polarization might become sufficiently important to suppress the ferroelectric properties of the system. Understanding how an electrode screens the depolarizing field is therefore of great importance in the quest for nanoscale devices.

The objective of this thesis was to investigate the electronic and chemical properties of a FE layer submitted to a screening process. *Screening process* is a general term which encompasses screening provided via a metallic overlayer, free carriers inside the FE material or FE domain ordering. We used photoemission-based techniques since they provide chemical and electronic information on a surface or a shallow interface.

Firstly, we used PhotoElectron Emission Microscopy (PEEM) and Low-Energy Electron Microscopy (LEEM) to access the work function of a polarized-domain, a quantity directly related to the polarization magnitude. PEEM and LEEM have been used to investigate the behavior of films of  $\text{BiFeO}_3$ . The loss of polarization observed experimentally when reducing thickness is explained by a FE phase transition from a monodomain phase (non-zero out-of-plane polarization) to a polydomain phase with stripes of opposite polarization (zero out-of-plane polarization). Using the same techniques on  $\text{BaTiO}_3$  single crystals, we studied the role of oxygen vacancies as a mechanism of internal screening. It seems that above a critical doping in vacancies, the polarization-induced intensity contrast in PEEM is lost. The screening provided by the electrons released by the vacancies is sufficient to suppress the FE polarization over a thin dead layer leading to the loss of intensity contrast. In addition, we showed that oxygen vacancies better screen domain polarized downward than domain polarized upward.

Secondly, we designed special sample and sample-holder to allow the application of a voltage on the sample while doing X-ray Photoemission Spectroscopy (XPS) measurements. This novel procedure allows *in-situ* switching of the polarization while measuring the XPS spectra. Two different interfaces have been studied with this technique: Platinum/ $\text{BaTiO}_3$  and  $\text{SrRuO}_3$ / $\text{BaTiO}_3$ . The electronic band shifts are a quantitative measurement of the polarization imperfect screening at the metal/ferroelectric interface and we observed similar shifts for the Pt/BTO and the SRO/BTO interfaces. However,

the screening mechanisms are different: in the case of a pure metal as platinum, the screening is due to the free carriers of the electrode. In the case of SRO, the epitaxial growth of the electrode on the ferroelectric allows an additional screening mechanism via the ionic displacements of the SRO ions.

*Keywords:* Photoemission spectroscopy (XPS), Photoemission electron microscopy (PEEM) Ferroelectrics, Multiferroics, Thin films, BaTiO<sub>3</sub>, BiFeO<sub>3</sub>.

# Acknowledgments

I want to thank Serge PALACIN, head of the *Service de Physique Chimie des Surfaces et Interfaces* and Didier NORMAND, head of the *Institut Rayonnement Matière de Saclay* of the CEA-Saclay for giving me the opportunity to work three years as a PhD student in a very motivating environment and a resourceful laboratory.

I am very grateful to Beatriz NOHEDA and Andreas KLEIN for agreeing to be my reading committee and for their useful comments on my work. I also thank the other members of my oral defense committee: Thomas MAROUTIAN, Claus SCHNEIDER and Max MARANGOLO.

I want to thank my PhD Director Nick BARRETT, head of the *Photoemission, Photodiffraction and Spectromicroscopy* group, for giving me the opportunity of doing this PhD thesis, for the huge amount of work and commitment he brought during these three years and all the professional and scientific knowledge he taught me. In these difficult days for public research, I really want to point out the excellent material conditions in which I worked, the numerous conferences and synchrotron beamtimes I went thanks to his dedication.

I am in great debt of the others members of the group too: I warmly thank Jocelyne LEROY and Bruno DELOMEZ for teaching and helping me so much through these years; I thank Claire MATHIEU for all her help since day one, but in particular for the last months when she had to read the same manuscript again and again, always cheerfully. I want to thank Jiale WANG who was the perfect co-PhD student, joyful, independent and challenging at the same time. I want to thank Jelle DIONOT for all the fun he brought to the group and I wish him good luck for the rest of his journey. I do not forget the former members of the group: Giovanni, Maylis, Alexandre and Yanyu and the members of the group working at Cergy: Marie-Christine, Olivier and Karol. Finally, I want to acknowledge Sara, Dana, Vahan, Avishek, Henri and Ruidy, the interneers who enlightened the group each year.

I am grateful to all the people from the Service, in particular Catherine and Christine for their help on many administrative issues; Sylvain L, Ludo, Bruno L, Yannick, Cyrille, Jérôme, Laurent, Jean-Baptiste, Fabien, Luc and Jacques for all the fun and scientific moments we shared; Dominique, Sylvain F, Fred, Christophe, Thierry and François for their great technical/joke support; and my fellow PhD students Marina, Jonathan, Jeremy, José, Moslem, Vincent, Nessima and Parwana.

I want to thank all the co-workers who helped me to conduct my experiments and understand my results. I thank Manuel BIBES, Stéphane FUSIL and Agnès BARTHELEMY from UMR CNRS/THALES; Thomas MAROUTIAN, Guillaume AGNUS, Valérie PILLARD and Philippe LECOEUR from *Institut d'Electronique Fondamentale* of Orsay; Gang NIU and Bertrand VILQUIN from *Ecole Centrale de Lyon*; Brahim DHKIL from *Ecole Centrale Paris* and Olivier RENAULT from *CEA-LETI*. I also had the pleasure to meet and work with the researchers of the *University of Arkansas*, namely Wei REN, Sergey PROSANDEEV and Laurent BELLAICHE and to work with Gregory GENESTE from *CEA-DAM*. I want to acknowledge all the support I got from the synchrotron teams: Mathieu SILLY, Azzedine BENDOUNAN and Fausto SIROTTI (and of course Deborah, Héloïse and Nathan.) from TEMPO, SOLEIL; Denis CEOLIN and Jean-Pascal RUEFF from GALAXIES, SOLEIL; Sebastian THIESS and Wolfgang DRUBE from PETRA III and Onur MENTES, Andrea LOCATELLI, Marten PATT and Vitaliy FEYER from ELETTRA.

On a more personal note, I thank the whole and extended Viro Crew for all the fun I have with them, and Loïc who is already a Doctor. I want to thank my parents and argentino Tom' for their support during this long journey. Finally, I thank Margaux for urging me to do a thesis, to pursue a career in public research and for everything she has done for the last eight years.

# Contents

<b>1 Photoelectron Spectroscopy</b>	<b>13</b>
1.1 The Process of Photoemission	13
1.1.1 Theoretical Overview	13
1.1.2 Three-step Model	15
1.2 Photoemission: Use in Material Science	21
1.2.1 Secondary Electrons	21
1.2.2 Primary Electrons	23
1.2.3 Photoemission on Insulators	30
<b>2 Ferroelectricity</b>	<b>31</b>
2.1 Ferroelectricity Background	32
2.1.1 Illustration with a Typical Ferroelectric: BaTiO <sub>3</sub>	33
2.1.2 Modern Theory of Polarization	37
2.1.3 The Concept of Dynamical Charges	39
2.2 Ferroelectricity in Nanoscale Systems	40
2.3 Experimental Tools to Study Ferroelectricity	42
2.3.1 Polarization - Electric Field Loop Analysis	43
2.3.2 Other Electrical Characterization	45
2.3.3 Piezoresponse Force Microscopy	46
<b>3 Ferroelectric Surfaces</b>	<b>49</b>
3.1 Domain Ordering in BiFeO <sub>3</sub> Thin Films	50
3.1.1 Ferroelectricity in Ultrathin Films	50
3.1.2 Bismuth Ferrite	52
3.1.3 Experimental Investigation of BiFeO <sub>3</sub> Ultrathin Films	53
3.1.4 Theoretical Resolution of the Experimental Paradox	61
3.2 Internal Free Charges in BaTiO <sub>3</sub> Single Crystals	65
3.2.1 Oxygen Vacancies in Oxides	65
3.2.2 Internal Screening as a Function of Oxygen Vacancies	66
3.2.3 Internal Screening by Photo-induced Charges	71
3.2.4 Polarization-dependent Chemistry of Ferroelectric Domains	74
3.2.5 Band Structure of BaTiO <sub>3</sub> Single Crystals	77

<b>4 Metal/Ferroelectric Interfaces</b>	<b>81</b>
4.1 Photoemission Spectroscopy with Bias Application	82
4.1.1 Main Issues	82
4.1.2 Proposed Solution	83
4.2 Investigation of the Platinum/BaTiO <sub>3</sub> interface	85
4.2.1 Growth of the Pt/BTO/NSTO heterostructure	86
4.2.2 Electrical characterization	90
4.2.3 Photoelectron Spectroscopy with Applied Bias	90
4.2.4 Polarization-dependent Band Lineup	94
4.2.5 Electronic band response to applied bias	96
4.2.6 The role of oxygen vacancies	98
4.2.7 Time-resolved Response to Applied Pulses	99
4.3 Investigation of the SRO/BTO Interface	104
4.3.1 Growth of the SRO/BTO/SRO Heterostructure	104
4.3.2 Electrical Characterization	106
4.3.3 Photoelectron Spectroscopy with Applied Bias	107
4.3.4 Discussion	111
<b>A Electron Emission Microscopy</b>	<b>117</b>
A.1 PhotoElectron Emission Microscopy	118
A.2 Low Energy Electron Microscopy	121
<b>B PEEM investigation of Few-layers Graphene</b>	<b>125</b>
<b>C Automatized Data Analysis</b>	<b>139</b>
C.1 Pixel-by-pixel Data Analysis	139
C.2 Energy Dispersion Correction	141
<b>D Landau Theory Applied to BiFeO<sub>3</sub> Ultrathin Films</b>	<b>143</b>
<b>E Publications</b>	<b>147</b>

## List of Acronyms

BiFeO <sub>3</sub>	BFO
BaTiO <sub>3</sub>	BTO
(La, Sr)MnO <sub>3</sub>	LSMO
PbTiO <sub>3</sub>	PTO
SrRuO <sub>3</sub>	SRO
SrTiO <sub>3</sub>	STO
Nb-doped SrTiO <sub>3</sub>	NSTO

---

Low Energy Electron Diffraction	LEED
Low Energy Electron Microscopy	LEEM
Molecular Beam Epitaxy	MBE
PhotoElectron Emission Microscopy	PEEM
PhotoEmission Spectroscopy	PES
Pulsed Laser Deposition	PLD
Reflection High Energy Electron Diffraction	RHEED
Ultraviolet Photoemission Spectroscopy	UPS
Ultra-High Vacuum	UHV
X-ray Diffraction	XRD
X-ray Photoemission Spectroscopy	XPS
X-Ray Reflectivity	XRR

---

Low Binding Energy	LBE
High Binding Energy	HBE
Conduction Band Offset	CBO
Valence Band Offset	VBO

## Symbols

Boltzmann's constant	$k$	$1.380 \times 10^{-23} \text{ J.K}^{-1}$
Electronic charge	$q$	$1.602 \times 10^{-19} \text{ C}$
Planck's constant	$h$	$6.626 \times 10^{-34} \text{ m}^2.\text{kg}.\text{s}^{-1}$
Vacuum permittivity	$\epsilon_0$	$8.854 \times 10^{-12} \text{ F.m}^{-1}$

# Introduction

This thesis reports on the investigation of ferroelectric perovskites with the support of photoemission-based techniques. The main goal is to elucidate the influence of the ferroelectric polarization on the electronic and chemical properties of the ferroelectric interface with an electrode. The understanding of the electrode/ferroelectric interface is of great importance in the perspective of nanometer-sized devices based on ferroelectric materials. In this thesis, the term *electrode* is taken in a general sense as any process which screens the surface charges due to the ferroelectric polarization. It can be a metallic overlayer as well as intrinsic free carriers inside the ferroelectric layer, adsorbates at the surface or domain ordering.

To do so, electron microscopy - namely PhotoElectron Emission Microscopy (PEEM) and Low Energy Electron Microscopy (LEEM) - was used to probe the polarization-dependent chemical and electronic properties of ferroelectric surfaces. In addition, an original solution to conduct photoemission spectroscopy with *in-situ* applied bias on electrode/ferroelectric interfaces has been developed. When needed, information coming of theoretical simulations have been used to better understand the experimental results.

This thesis was done at the French Atomic Energy Authority (CEA) in the *Service de Physique Chimie des Surfaces et Interfaces* (SPCSI), part of the IRAMIS institute. However, it involved many collaborations. Photoemission spectroscopy with *in-situ* bias experiments have been conducted at Synchrotron SOLEIL (Saint-Aubin, France) on the TEMPO and GALAXIES beamlines and PETRA III (Hambourg, Germany) on the P09 beamline. Photoemission Microscopy experiments have been conducted at Sincrotrone ELETTRA (Triest, Italy) on the two branches of the nanoSpectroscopy beamline. The development of the micro-fabrication processes and growth of pulsed laser deposition samples have been done jointly with the *Institut d'Electronique Fondamentale* (Orsay, France). The BFO thin films study have been done with the help of the *UMR CNRS/Thales* (Palaiseau, France) for sample preparation and the *University of Arkansas* (Fayetteville, U.S.A.) for theoretical calculations.. Finally, molecular beam epitaxy samples have been grown by the *Institut des Nanosciences de Lyon* (Lyon, France).

The thesis is divided in four chapters:

- In Chapter 1, the basics of photoemission spectroscopy are presented. The fea-

tures of photoemission spectroscopy on solid-state materials are described. A more thorough technical description of photoelectron emission microscopy and low energy electron microscopy is given in appendix A.

- In Chapter 2, the main concepts of ferroelectricity are introduced. The principal ideas are illustrated with a typical ferroelectric, BaTiO<sub>3</sub>, and afterwards the modern theory of polarization is outlined. Next, we underline that the quest for the nanometer scale brings new issues and explore the key concept of *polarization screening*. Finally, a selection of classic experimental techniques designed for measuring ferroelectric materials properties are described.
- In Chapter 3, we used electron microscopy on free surface of ferroelectric samples. Firstly, we investigate the thickness dependence of the polarization magnitude on BiFeO<sub>3</sub> very thin films. The sudden loss of polarization magnitude as measured by the electron microscopy techniques is explained by stripe domain formation for low thickness. This study emphasizes the role of domain organization as an efficient screening process. The film growth, the piezoresponse force microscopy and the x-ray diffraction measurements have been done in collaboration with *UMR CNRS/Thales* (Palaiseau, France). The theoretical calculations have been conducted by L. Bellaïche's group in *University of Arkansas* (Fayetteville, U.S.A.). Secondly, the domain-induced PEEM contrast of BaTiO<sub>3</sub> single crystals as a function of oxygen vacancy concentration has been monitored. We observe that free carriers released by oxygen vacancies can efficiently screen opposite polarization and that oxygen vacancies favor one polarization (downward) over another (upward). The calculations have been conducted with G. Geneste from *CEA-DAM*. The photoemission experiments have been conducted at Synchrotrone ELETTRA on nanoSpectroscopy and NanoESCA beamlines.
- In Chapter 4, the challenge of photoemission spectroscopy while applying a bias on the sample is introduced and our experimental solution is reported. This technique is then applied on two thin film heterostructures: Platinum/BaTiO<sub>3</sub> and SrRuO<sub>3</sub>/BaTiO<sub>3</sub>. We measure how the interface chemical and electronic properties are affected by polarization switching, and how the two different type of interfaces (non-epitaxial vs epitaxial) have different screening properties. The growth of the thin films and the micro-processing was a collaboration with the *Institut d'Electronique Fondamentale* (Orsay, France) and *Institut des Nanosciences de Lyon* (Lyon, France). Photoemission experiments have been conducted at synchrotron SOLEIL on TEMPO and GALAXIES beamlines and at synchrotron PETRA III on P09 beamline.

# Chapter 1

## Photoelectron Spectroscopy

PhotoElectron Spectroscopy (PES) is a very efficient technique for determining the electronic and chemical properties of a material surface. In crude terms, incident photons lift up electrons from core and valence energy levels to energies high enough for them to escape the sample. Then, different experimental apparatus can resolve the kinetic energy (X-Ray PhotoEmission Spectroscopy, XPS), take-off angle (Angle-Resolved X-ray PhotoEmission Spectroscopy, ARPES and X-ray Photoemission Diffraction, XPD), position and wave-vector (PhotoElectron Emission Microscopy, PEEM) or even moment of emission (Time-resolved XPS, tr-XPS) of the photo-electron. In that way, PES provides numerous information on the sample electronic properties and is widely used in material science, primarily in solid-state surface science and gas phase.

Historically, the technique is based on the photoelectric effect discovered by Frank and Hertz in 1887 [86] and given a theoretical basis by Einstein in 1905 in one of his three seminal papers this year [58]. In the 1950s, K. Siegbahn *et al.* developed significant improvements in the technique [158]. Siegbahn received a Nobel Prize in 1981 for “his contribution to the development of high-resolution electron spectroscopy”<sup>1</sup>. Since then, many contributors helped the development of this technique [48, 53, 63, 62, 87, 104, 167].

### 1.1 The Process of Photoemission

#### 1.1.1 Theoretical Overview

Under illumination, the absorption of a photon of sufficient energy by an atom leads with a given probability to the (photo)emission of an electron. This phenomenon has been described by A. Einstein in 1905 [58]. In photoemission spectroscopy experiments, one collects and analyzes the kinetic energy of the emitted electron to describe various properties of the emitting atom.

Energy conservation states that the initial system (a photon of energy  $h\nu$  + an atom

---

<sup>1</sup>[http://www.nobelprize.org/nobel\\_prizes/physics/laureates/1981/siegbahn-lecture.html](http://www.nobelprize.org/nobel_prizes/physics/laureates/1981/siegbahn-lecture.html)

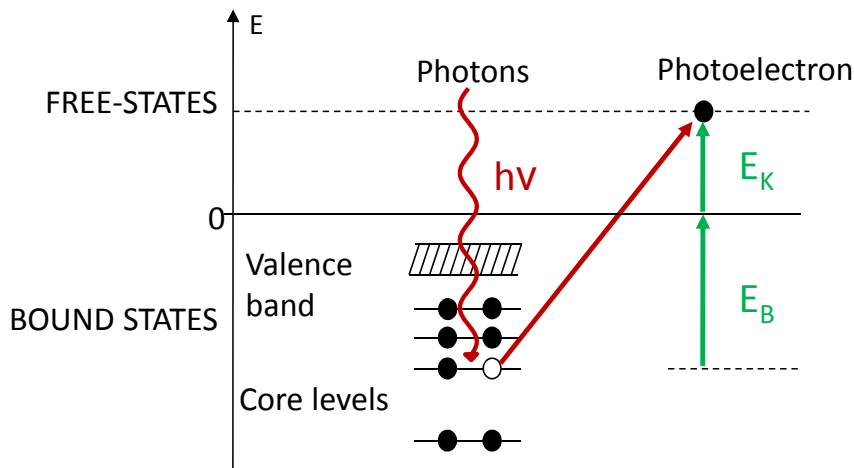


Figure 1.1: Schematic of the photoemission process. After the absorption of a photon of energy  $h\nu$ , an electron is emitted from a core-level with a binding energy  $E_B$  to vacuum with a kinetic energy  $E_K$

with  $N$  electrons of total energy  $E(N)$ ) has the same energy than the final system (an atom with  $(N-1)$  electrons of total energy  $E(N-1)$  and one electron in vacuum with a kinetic energy  $E_K$ ).

$$h\nu + E(N) = E(N - 1) + E_K \quad (1.1)$$

In this context, the binding energy of the photoemitted electron is defined by:

$$E_B = E(N) - E(N - 1) \quad (1.2)$$

so that we get the well-known relationship between the kinetic energy and binding energy of a photoelectron:

$$h\nu = E_K - E_B \quad (1.3)$$

The binding energy is specific to the electronic level of the emitter atom, therefore to the chemical environment of this emitter atom. That is why K. Siegbahn named this technique Electron Spectroscopy for Chemical Analysis (ESCA).

The interpretation of a photoemission spectrum can be illustrated using a simple element. For instance, the initial electronic configuration of Neon is  ${}^1S_0|1s^22s^22p^6\rangle$ . Emission of a photoelectron leads to four possible ionized state  ${}^2S_{1/2}|1s^12s^22p^6\rangle$ ,  ${}^2S_{1/2}|1s^22s^12p^6\rangle$ ,  ${}^2P_{1/2}|1s^22s^22p^5\rangle$  and  ${}^2P_{3/2}|1s^22s^22p^5\rangle$ . This gives rise to four photoemission peaks of a given binding energy. We must keep in mind that photoemission spectroscopy measures a quantum system in its final state (one electron in vacuum +  $(N-1)$  electrons in the emitting atom). This final-state system has an excited electron cloud prone to relaxation to minimize its energy. The relaxed final-state can be significantly different from the

unrelaxed state, especially in systems with many electrons (strongly-correlated solids for instance). The measured binding energy can only be linked to the energy of the electron in the initial state through theoretical development and approximations. The most used approximation comes from T. Koopmans's theorem [111] (frozen orbitals approximation) which neglects the effect of orbital relaxation and electron correlations. In that case, the binding energy defined above is equal to the Hartree-Fock orbital energy of the electron in its initial state. The width of the photoemission peak is due to the convolution of an experimental broadening (Gaussian shape) and the intrinsic energy width of the photoionized state (Lorentzian shape). The intrinsic energy width is directly related to the lifetime of the state, as expected from the uncertainty principle.

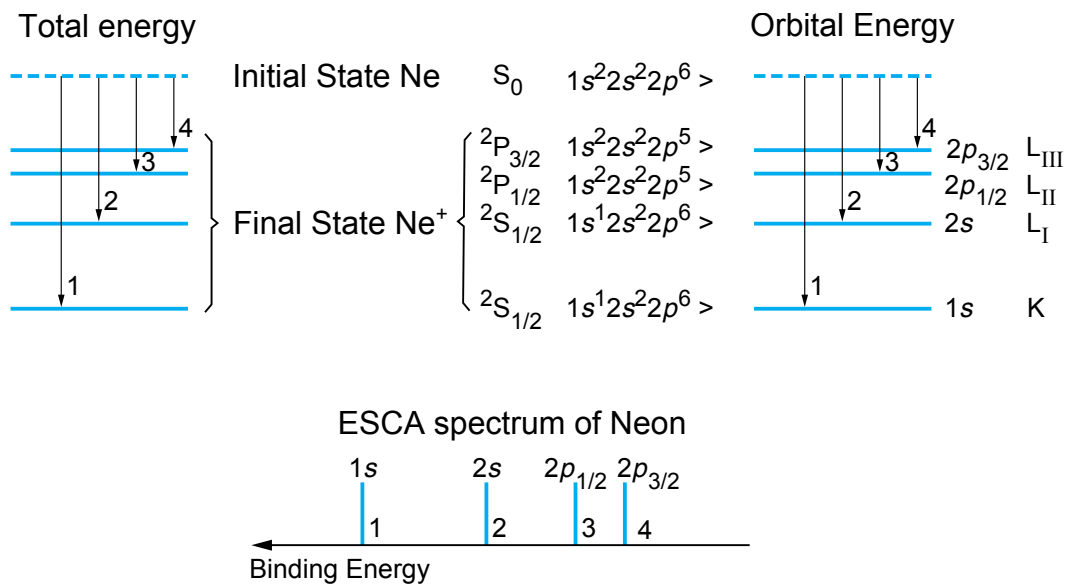


Figure 1.2: Energy levels involved in a typical photoemission spectroscopy experiment on a noble gas (Ne).

### 1.1.2 Three-step Model

The most accurate description of the photoemission process, the so-called one-step model, has been developed in Ref. [3, 167]. This model is based on a full quantum description of the photoemission phenomena, taking into account the coupling of an initial state (Bloch wave in the crystal) of an electron with an available final state (Free electron wave in vacuum damped in the solid, named time-reversed LEED state). Though less accurate than the one-step model, the three steps model is more didactic to understand the process of photoemission in solids. Within certain limits, it offers a clear illustration of the phenomena involved in a photoemission spectrum.

### Step 1: Optical excitation of the electron in the solid

An incident photon extracts an electron from the initial state  $|i, \mathbf{k}_i\rangle$  to the final state  $|f, \mathbf{k}_f\rangle$  inside the solid with a given probability. The photoelectron intensity spectra can be theoretically calculated with the equation (1.4)<sup>2</sup>:

$$I(E, h\nu) \propto \sum_{f,i} \left( |M_{(f,i)}(k_i, k_f)|^2 \delta(E_f(k_f) - E_i(k_i) - h\nu) \delta(\mathbf{k}_f - \mathbf{k}_i) \right) \quad (1.4)$$

$$\times \delta(E - (E_f(k_f) - \Phi_S))$$

Where  $\Phi_S$  is the work function of the surface (see Section 1.1.2 which describes the third step),  $h\nu$  is the incident photon energy,  $E_{i,f}(k_{i,f})$  are the energy of the initial and final state of momentum  $k_{i,f}$ . Finally,  $|M_{(f,i)}(k_i, k_f)|^2$  is the square of the matrix element of the transition. This formulation contains the energy and momentum conservation (though we neglect the momentum of the incident photon here, an approximation valid for photon energy below the several keV range) and the matrix element term. The matrix element contains all information about the transition probability between the initial and the final state. Its formulation depends on the degree of approximation one needs. Classically, the framework of small perturbations, *i.e.* the Fermi's golden rule<sup>3</sup>, and the dipole approximation (the potential vector of the incident photon is constant over the interaction volume, namely the interatomic distance) are exploited and the matrix element reads<sup>2</sup>:

$$M_{(f,i)}(k_i, k_f) = \langle \phi_{f,E_{kin}} | r | \phi_i \rangle \langle \psi_f(N-1) | \psi_i(N-1) \rangle \quad (1.5)$$

In that case, the matrix element is the product of a one-electron matrix element (left bracket) and a (N-1) electrons overlap integral (right bracket). After the ejection of the electron, the system will readjust its remaining charges to minimize its energy. This leads to different excited states (indexed by  $s$  in the following) of different wave function  $\langle \psi_{f,s}(N-1) \rangle$  and energy  $E_s$ . The transition matrix becomes:

$$M_{(f,i)}(k_i, k_f) = \langle \phi_{f,E_{kin}} | r | \phi_i \rangle \sum_s c_s \quad (1.6)$$

where  $c_s = \langle \psi_{f,s}(N-1) | \psi_i(N-1) \rangle$ .

In the frozen orbitals approximation, the remaining orbitals are identical in the initial and final state (whence frozen) : there is only one available final state, therefore only one  $c_s$  is non-zero and the photoemission spectrum only shows the *main line*. In that case, the binding energy of the main line is the Hartree-Fock orbital energy, or the Koopman's binding energy. However, in realistic cases, many excited states are available, *i.e.* many

<sup>2</sup>For more details, see Ref. [87], Chapter 1.4.

<sup>3</sup>Fermi's golden rule is a way to calculate the transition rate (probability of transition per unit of time) from one energy eigenstate of a quantum system into a continuum of energy eigenstates due to a perturbation.

$c_s$  are non-zero, and the spectrum shows additional lines corresponding to these states, often called satellites.

Experimentally, the transition probability is often estimated using the photoionization cross section of the electron. For instance, cross sections for elements with  $Z = 1$  to  $Z = 103$  have been calculated using the Hartree-Fock one-electron central potential and the dipole approximation in Ref. [243]. They are available in a user-friendly interface on this [website](#)<sup>4</sup>. The matrix element, and therefore the cross section, depends on the emitting element, the electronic level of the emitted electron, the photon energy and photon polarization. Thus, a careful choice of photon energy/polarization can enhance or extinct the contribution from a given core-level.

The formulation of equation (1.4) is quite general. In the formalism of the one-step model, one can use this equation and change the final state from the final state in the solid (three-step model) to the so-called reverse LEED state (one-step model) [3, 167].

Thus, after photoionization, the ejected electron has a kinetic energy which depends on the photon energy, its initial state in the emitting atom and its environment.

## Step 2: the photoelectron travels towards the surface

While traveling towards the surface of the sample, a photo-excited electron might interact strongly with its surroundings:

- the electron does not encounter inelastic scattering: it will contribute to the main photoemission peak of the emitting element (see Figure 1.3, case (i))
- the electron encounters at least one inelastic scattering: it will loose kinetic energy and contribute to the secondary electrons background (see Figure 1.3, case (ii))
- the electron undergoes so many inelastic scattering events: it will not leave the surface (see Figure 1.3, case (iii))

This leads to a fundamental feature of PES: surface sensitivity. The (inelastic) mean free path of photoelectron describes the average length an electron travels between two successive (inelastic) scattering events. This quantity ( $\lambda$ ) depends on the material, the element and the electron kinetic energy. However, the so-called universal curve shown in Figure 1.4 is a good estimation of mean free path for many materials. Then, one can use the well-known attenuation law (or Beer-Lambert law) to estimate the probing length of photoemission experiments:

$$I(z) = I_0 \exp\left(-\frac{z}{\lambda \sin\theta}\right) \quad (1.7)$$

where:

---

<sup>4</sup><http://ulisse.elettra.trieste.it/services/elements/WebElements.html>

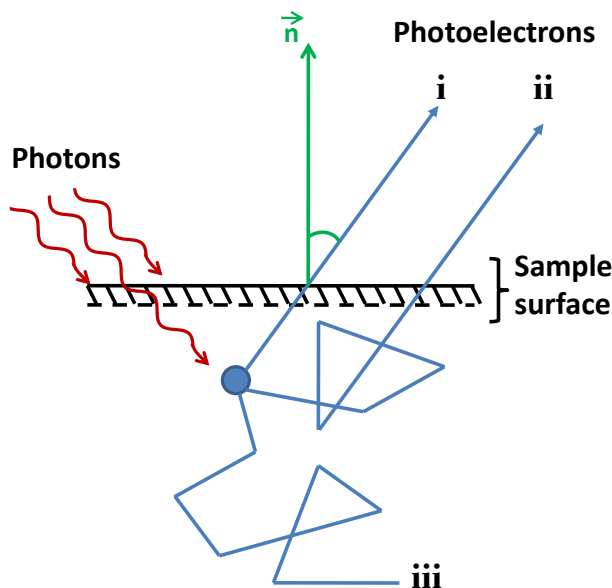


Figure 1.3: Scattering processes involved in photoemission: (i) primary electron, (ii) secondary electrons and (iii) reabsorbed electrons.

- $z$  is the probing depth
- $I(z)$  is the measured intensity coming from the layer at depth  $z$
- $I_0$  is the theoretical intensity without attenuation
- $\lambda$  is the inelastic mean free path
- $\theta$  is the take-off angle of the photoelectron

Thus, 95% of the signal comes from the first  $3\lambda$  of the surface. Using soft x-ray (1486.70 eV for the widespread Al  $K\alpha$  source), photoemission experiments probe the first 3-4 nm of the sample. However, using synchrotron radiation and hard x-ray (above 5 keV), one can probe deeper in the material (up to 10-20 nm) and therefore access buried interfaces [164]. Alternatively, to have higher surface sensitivity, one can select the take-off angle of the photoelectron (often by rotating the analyzer with respect to the sample). Grazing versus normal emission experiments are a good way to determine the relative contribution to the signal of surface and bulk atoms.

As a consequence of the utilization of electrons, a practical limitation is that experiments must be conducted in ultra-high vacuum (below  $10^{-9}$  mbar in typical PES experiments) so that emitted photoelectron will not scatter while traveling from the sample to the analyzer.

### Step 3: The photoelectron leaves the surface

The potential felt by electrons is lower in the solid than in vacuum. Energy has to be consumed so that the photo-electron leaves the surface. The definition of the work

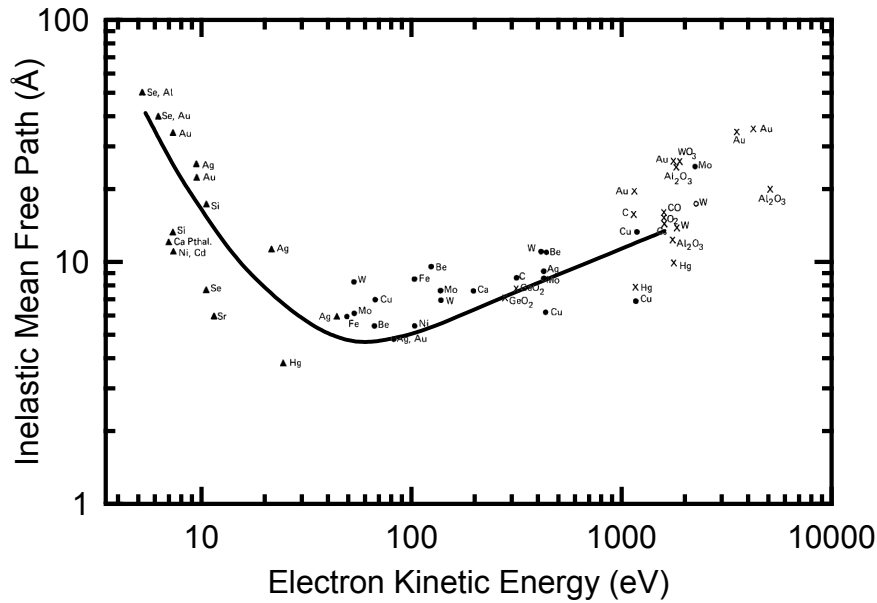


Figure 1.4: The solid line is the “universal” inelastic mean free path curve of electrons in solids. Experimental points are taken from Ref. [35].

function of a surface is the smallest energy needed to extract an electron from the solid at 0 K to a point immediately outside the solid surface. “Immediately” means that the final electron position is far from the surface on the atomic scale, but still too close to the solid to be influenced by ambient electrostatic potentials in the vacuum.

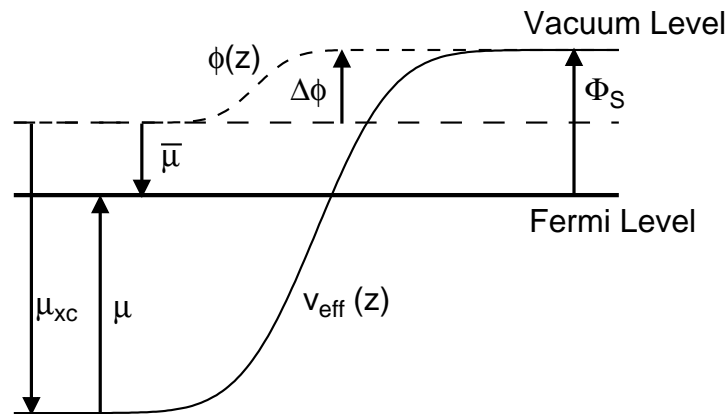


Figure 1.5: Energies involved at the surface of a solid.  $\phi(z)$  is the electrostatic potential,  $v_{\text{eff}}(z)$  is the full one-electron potential,  $\bar{\mu}$  and  $\mu$  are the chemical potentials relative to  $\phi$  and  $v_{\text{eff}}$  respectively; and  $\Phi_S$  is the work function.

Energies involved at a solid surface are shown in Figure 1.5: two phenomena lower the energy of electrons inside the solid in comparison to vacuum. The first is the electrostatic potential  $\phi(z)$  which decreases a little when going into the crystal. The change is due to the surface dipole layer which is caused by the spill-out of the conduction electrons. The potential difference between inside and outside the crystal is noted  $\Delta\phi$ . Any change in the surface in terms of morphology, adsorption or surface charges will change  $\Delta\phi$ . The

second contribution is the full one-electron potential  $v_{\text{eff}}(z)$ . This quantity is obtained from the electrostatic potential by adding the exchange-correlation potential  $\mu_{\text{xc}}$  which further lowers the potential of the electrons inside the solid. The work function of the sample is the difference between the vacuum level  $\phi(+\infty)$  and the Fermi level and is noted  $\Phi_S$ . One can also define the chemical potential relative to  $\phi$  (named  $\bar{\mu}$ ) and relative to  $v_{\text{eff}}$  (named  $\mu$ ). Another quantity useful for the analysis of angle-resolved photoemission spectroscopy (see Section 1.2.2) is the so-called *inner potential*  $V_0 = \mu + \Phi_S$  which is simply the occupied band width plus the work function.

Finally, equation (1.8) gives the kinetic energy  $E_K$  of a photo-electron emitted after absorption of a photon of energy  $h\nu$  from a level of binding energy  $E_B$ , taking into account the work function  $\Phi_S$ :

$$E_K = h\nu - \Phi_S - E_B \quad (1.8)$$

This relation is illustrated in Figure 1.6.

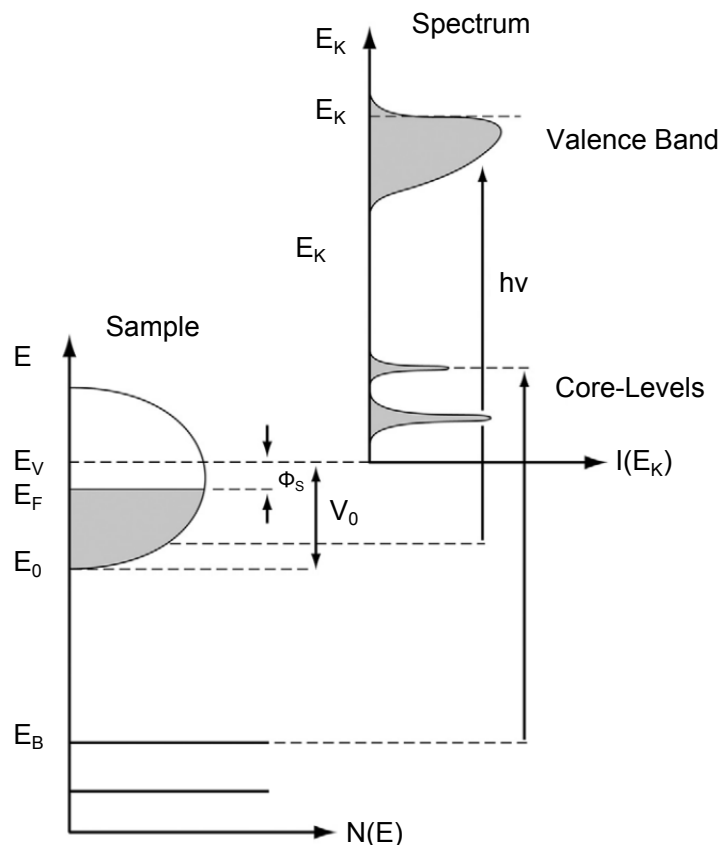


Figure 1.6: Energetics of the photoemission process (from Ref. [87]). Photo-electrons of kinetic energy  $E_K$  are emitted after absorption of a photon of energy  $h\nu$  from a electronic level of binding energy  $E_B$ .

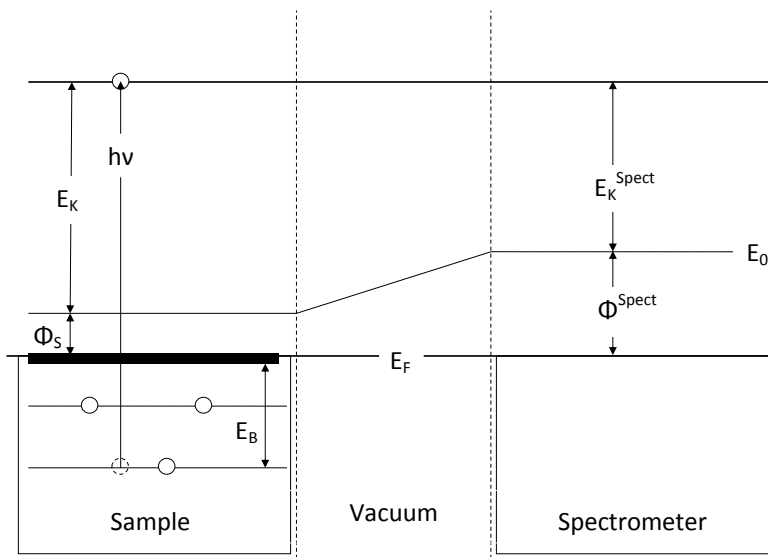


Figure 1.7: Energy alignment of a metallic sample connected to the spectrometer in thermodynamic equilibrium (both have the same Fermi energy  $E_F$ ) The energy scale in the spectrometer (of work function  $\Phi^{\text{Spect}}$ ) has to be calibrated in order to obtain the correct binding energies  $E_B$  of electron photo-emitted from the sample (of work function  $\Phi_S$ ) with a kinetic energy  $E_K$ .  $E_0$  is the vacuum energy level.

## 1.2 Photoemission: Use in Material Science

In a typical photoemission apparatus the energy levels of the sample and of the energy analyzer line up, as sketched in Figure 1.7: after thermodynamic equilibrium, the Fermi levels of both the spectrometer and the sample are aligned. The first step in any photoemission experiment is to use reference samples to calibrate the energy scale of the spectrometer, this will be described in Section 1.2.1. A typical spectrum<sup>5</sup> is shown in Figure 1.8.

A full photoemission spectrum contains many information from several type of photoemitted electrons. In the simplest case of a angle-averaged, position-averaged spectrum, we can already distinguish at least three types of photoelectrons described in the following sections. The roles of take-off angle will also be discussed.

### 1.2.1 Secondary Electrons

Inelastically-scattered electrons (or secondary electrons (SE)) form the so-called photoemission background as captioned in Figure 1.8. Most of the time, SE have lost all coherence with their initial state and this background is discarded using a adequate subtracting procedure. In the simplest cases, background is removed by subtracting a linear (in energy) contribution to the spectrum. A more sophisticated shape, the Shirley background, is often a better choice to model the background [199]. In this model, the background

<sup>5</sup>This spectrum was taken on a Polyoxometalate molecules using an Al-K $\alpha$  x-ray source and a Sphera analyser from Omicron nanotechnology.

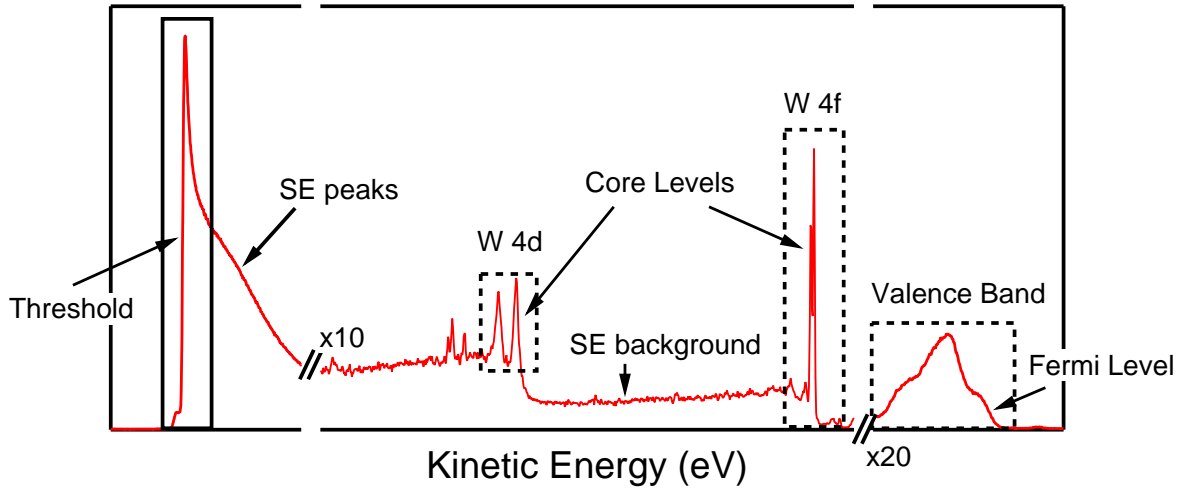


Figure 1.8: Typical photoemission spectrum. There are three important regions: the photoemission threshold, the core-level peaks (here tungsten  $4d$  and  $4f$ ) and the valence band spectrum. SE stands for Secondary Electrons.

intensity at the kinetic energy  $E_{K_0}$  is the sum of all photoemission signal at kinetic energy higher than  $E_{K_0}$ . Equation (1.9) gives the background  $B = f(E_K)$  from a photoemission spectrum  $I = f(E)$ :

$$B(E_K) = \frac{\int_{E_K}^{E_{K_{\max}}} I(E) \cdot dE}{\int_{E_{K_{\min}}}^{E_{K_{\max}}} I(E) \cdot dE} \quad (1.9)$$

where the range of kinetic energy is  $[E_{K_{\min}}, E_{K_{\max}}]$ . Contrary to the linear shape, this model explicitly takes into account the fact that the more electrons are excited by the photoemission process, the more electrons are likely to be scattered. Therefore, each main line induces a step in the background intensity and the Shirley background accurately correct this phenomenon. An example of background subtraction for the W  $4f$  core-level of a Polyoxometalate molecule is shown in Figure 1.9.

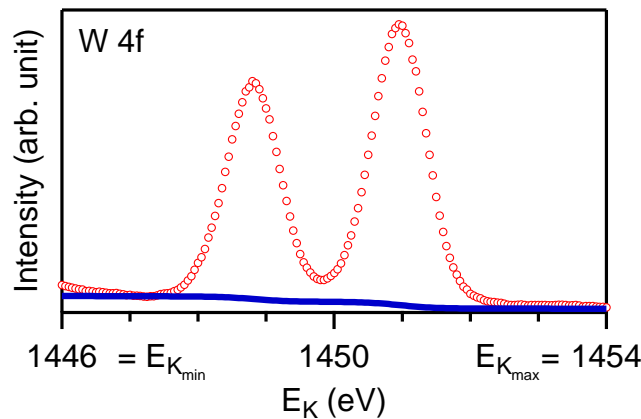


Figure 1.9: Example of background calculations based on equation (1.9) using the Shirley model [199]. The tungsten  $4f$  core-level presented here has been measured on a Polyoxometalate molecule.

This model is a very efficient, self-consistent method to subtract the background of a core-level spectrum. This shape will be used in this thesis. Other shapes have been proposed in the literature and are more suited to some materials or experiments [166].

Secondary electrons may keep some altered information on their initial state. Using the proper approximation, these secondaries bring information on the probed element. The most striking use is the study of plasmons and shake-up satellites<sup>6</sup>. More importantly in this thesis, secondary electrons of low kinetic energy form an intense peak just above the threshold (see the part of the spectrum enclosed in the plain square in Figure 1.8). The lowest kinetic energy experimentally reachable  $E_{K_{min}}$  (often called the cut-off energy) is directly related to the work function  $\Phi_S$  of the sample by the equation (1.10):

$$E_{K_{min}} = \Phi_S - \Phi^{Spect} \quad (1.10)$$

Using the photoemission spectrum from a reference sample with a known work function  $\Phi_S$  and equation (1.10), one can deduce the spectrometer work function  $\Phi^{Spect}$ . This method gives an important value which will be considered constant: the spectrometer work function ( $\Phi^{Spect}$  in Figure 1.7). A didactic tutorial on energy calibration in photoemission experiments can be found [here](#)<sup>7</sup>. After calibration, the spectrometer work function is considered a constant and the unknown is the work function of the studied sample. Equation (1.10) can now be used to get  $\Phi_S$ .

Thus, the threshold spectrum contains important information since it provides an accurate measurement of the work function [40, 42]. Using photoemission microscopy which gives access to the position of the emitted electron on the surface, one can obtain spatially-resolved photoemission threshold spectra and thus a mapping of the surface work function [135, 182]. In the case of ferroelectric materials, the work function can be related to the ferroelectric polarization at the surface, a direct application of work function mapping is the quantitative measurement of polarization magnitude from ferroelectric domains, as we will see in Chapter 3.

### 1.2.2 Primary Electrons

The main feature of photoemission spectroscopy are the elastic peaks, they are enclosed in the dotted squares in Figure 1.8. These peaks are due to electrons which did not scatter inelastically. In solid-state science, two regions are often distinguished: electrons coming from the localized, non-dispersive core-levels which gives sharp peaks and those coming from the delocalized, dispersive valence band.

In solids, and especially in highly-correlated systems in which many  $c_s$  (as defined in Section 1.1.2) are nonzero, a formalism slightly different from the one presented in Section 1.1.2 is more powerful to describe the elastic peaks. The approach is based on the

<sup>6</sup>For more details on satellites, see Ref. [87], Chapter 3 and 4.

<sup>7</sup><http://rsl.eng.usf.edu/Documents/Tutorials/PEScalibration.pdf>

Green's function formalism where the propagation of an electron in a many-body system is described by a one-electron removal<sup>8</sup> Green's functions [54].

Following the work of L. Hedin, equation (1.4) can be rewritten as follows [15, 85]:

$$I(E) \propto \sum_{f,i,k} |\langle \phi_{f,E_{kin}} | r | \phi_{i,\mathbf{k}} \rangle|^2 A(\mathbf{k}, E) \quad (1.11)$$

where  $A(\mathbf{k}, E)$  is the *spectral function* for the wave vector  $\mathbf{k}$  and energy  $E$  and is related to the one-electron Green's function by:

$$A(\mathbf{k}, E) = \frac{1}{\pi} \Im(G(\mathbf{k}, E)) \quad (1.12)$$

The spectral function describes the probability of removing an electron with energy  $E$  and wave vector  $\mathbf{k}$  from the (N) electron system. For a non-interacting system and the one-electron energy  $E_{\mathbf{k}}^0$ , the Green's functions reduces to:

$$G_0(\mathbf{k}, E) = \frac{1}{E - E_{\mathbf{k}}^0 - i\epsilon} \quad (1.13)$$

where  $\epsilon$  is very small. Therefore, the spectral function becomes:

$$A_0(\mathbf{k}, E) = \delta(E - E_{\mathbf{k}}^0) \quad (1.14)$$

and reduces to a  $\delta$ -function peaked at  $E_{\mathbf{k}}^0$ , which is in that case the Koopman's binding energy described in Section 1.1.2.

In an interacting system, the correction to the Green's function due to electron-electron correlations can be expressed by the so-called *self-energy* of the electron  $\Sigma(\mathbf{k}, E) = \Sigma'(\mathbf{k}, E) + i\Sigma''(\mathbf{k}, E)$ . The real and imaginary parts contain all the information on the energy renormalization and lifetime, respectively, of an electron propagating in a many-body system. The Green's and spectral functions become:

$$G(\mathbf{k}, E) = \frac{1}{E - E_{\mathbf{k}}^0 - \Sigma(\mathbf{k}, E)} \quad (1.15)$$

$$A(\mathbf{k}, E) = \frac{1}{\pi} \frac{\Im(\Sigma(\mathbf{k}, E))}{[E - E_{\mathbf{k}}^0 - \Re(\Sigma(\mathbf{k}, E))]^2 + [\Im(\Sigma(\mathbf{k}, E))]^2} \quad (1.16)$$

Though every peak in a photoemission spectrum reflects the spectral function of the ejected electron, the methodology based on Green's functions is mostly used for understanding the valence band where electron-electron correlations have the most impact on the spectral function. It is also very useful to better understand the behavior of satellites, plasmons or any final-state phenomena since it explicitly takes into account the removal of the photo-electron (contrary to density-functional-theory-based calculations for instance). Though such calculations are difficult in terms of computation time and

---

<sup>8</sup>In the case of Inverse PhotoEmission Spectroscopy, the addition Green's function is used.

complexity, the [European Theoretical Spectroscopy Facility](http://www.etsf.eu/)<sup>9</sup> has been created to provide theoretical support to better understand experimental results, including photoemission spectroscopy.

### Core-levels

The accurate calculation of binding energy is often very difficult in terms of computation time, particularly in the Green's function formalism described just before. Less time-consuming models based on the Born-Haber cycle [28, 79] have been developed to calculate the binding energy of core-levels but cannot be as accurate nor general. But for core-levels, the measurement of *shifts* in binding energy, which are characteristic of a change in the chemical environment of the emitting element, is often more interesting than an absolute determination of the binding energy. The cause of such shift is related to the change in orbital energies when valence electrons surrounding change. A classic, simple example is the behavior of lithium oxide compared to metallic lithium. Lithium electrons do not have the same environment in pure metal lithium and in oxidized lithium. This is seen in photoemission spectroscopy by a binding energy shift of the 1s core-level. In the metal, the binding energy of this core-level is lower because of the good screening of the coulomb attraction of the nucleus by the conduction 2s electrons. In the oxide, the 2s electrons have been lost to oxygen 2p core-level. The 1s electrons feel a higher attractive field from the nucleus hence a higher binding energy.

However, this model is for illustration purpose only, over-simplified and even sometimes not qualitatively correct: the binding energy shifts of oxidized Barium is a well-known example in the field of oxides and goes in the opposite direction as the one predicted by this simple model [95]. Many numerical methods exist to estimate the shift in energy from Hartree-Fock Self Consistent Field numerical simulations to electrostatic models using the Madelung potential of the solid to predict or explain the magnitude and the direction of the shifts [228]. A thermodynamic methodology to determine binding energy shifts can be found in Chapter 2 of Ref. [87].

Other phenomena might cause binding energy shifts in solids which are not related to a chemical change of the emitting element. While traveling to vacuum, electrons are affected by the electrostatic boundary conditions of the sample. This is particularly important when studying the buried interface of any multilayer structure. At the interface between a semiconductor and a metal for instance, band bending induces an internal electric field in the semiconductor [212]. Electronic orbitals from each layer are shifted in energy by the electric field. This lead to a distribution of core-level peaks coming from each atomic layer with a slightly different binding energy. Due to instrumental resolution and the finite depth sensibility, this often leads to a broad core-level peak [45]. If the band bending occurs on a distance significantly smaller than the probing depth (i.e. one atomic

---

<sup>9</sup><http://www.etsf.eu/>

layer), it can be modeled as an interface dipole and it induces a rigid energy shift to the whole electronic structure. Both have been studied in Refs. [93, 94, 112, 250]. Figure 1.10 shows the consequence of band bending (or of an interfacial dipole) on the photoemission spectrum of any surface or interface. This phenomenon goes beyond semiconductors. For instance, the screening processes involved at the interface between a ferroelectric layer and an electrode is often modeled as an interfacial dipole which induces a rigid shift of both electronic levels energy and the work function. However, this model has to be carefully considered since we observed non-rigid core-levels shifts at a metal/FE interface as discussed in Chapter 4–Section 4.2 and 4.3.

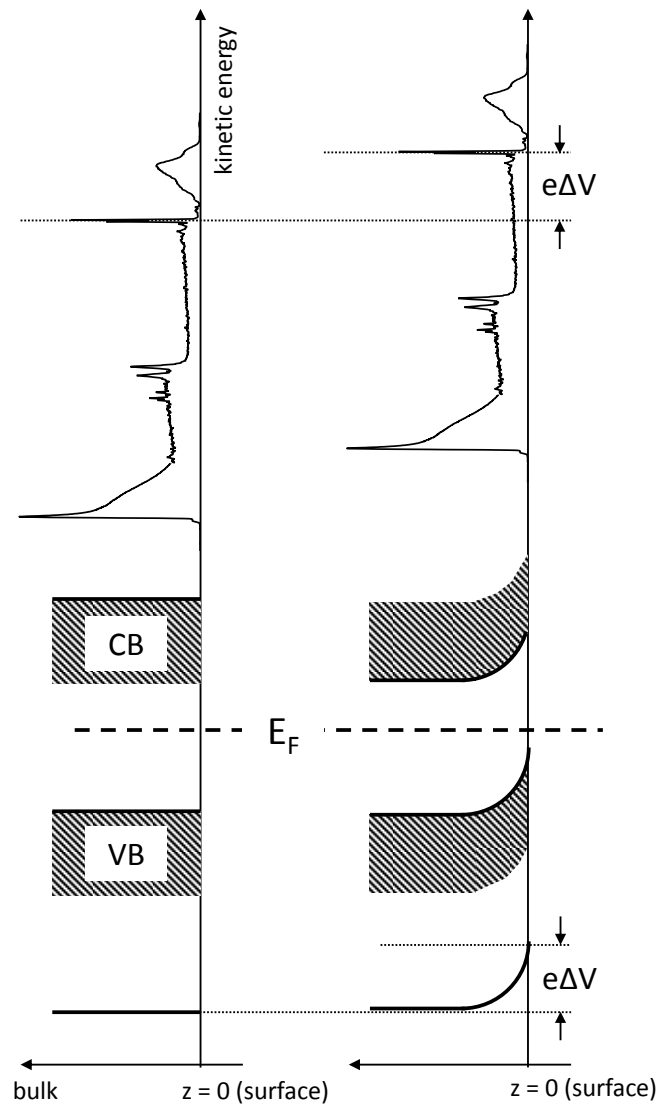


Figure 1.10: Simplified diagram modeling the consequence of band bending on the photoemission spectrum of a surface: the whole spectrum (core-levels and threshold) are displaced by a quantity related to the interface dipole resulting from the band bending, here  $e\Delta V$ . This is correct in the framework of a rigid shift of the bands which is not always true for strongly correlated solids such as  $\text{BaTiO}_3$ .

## Valence Band

When approaching the Fermi level of a solid, the dispersive behavior of the electrons has to be considered. Valence levels can even be defined by the fact that their dispersion relation is no longer trivial, or equivalently that electrons are no longer localized.

Taking advantage of the finite angular acceptance of a photoemission analyzer one can collect photo-electrons of a given take-off angle. The analyzer also gives the kinetic energy then the momentum  $\mathbf{K}$  of the photo-electron in vacuum is completely determined. The modulus is  $|\mathbf{K}| = \frac{1}{\hbar}\sqrt{2m \cdot E_K}$ , and is often expressed in units more suited to photoemission spectroscopy by  $|\mathbf{K}|[\text{\AA}^{-1}] = 0.512 \cdot \sqrt{E_K[\text{eV}]}$ . The parallel  $\mathbf{K}_{\parallel}$  (plane  $x - y$ ) and perpendicular  $\mathbf{K}_{\perp}$  (direction  $z$ ) components are obtained in terms of the polar  $\theta$  and azimuthal  $\phi$  angles:

$$K_x = |\mathbf{K}| \sin \theta \cos \phi \quad (1.17)$$

$$K_y = |\mathbf{K}| \sin \theta \sin \phi \quad (1.18)$$

$$K_z = |\mathbf{K}| \cos \theta \quad (1.19)$$

The following arguments will be discussed in the framework of the *Ultraviolet Photoemission Spectroscopy (UPS) regime*, *i.e.* when the photon energy is below 100 eV, for two reasons:

- A high-photon energy means a high kinetic energy for the photo-electron emitted from the valence levels. The derivative of equation (1.19) for the parallel component of the momentum gives  $\Delta K_{\parallel}[\text{\AA}^{-1}] = 0.512 \cdot \cos \theta \sqrt{E_K[\text{eV}]} \Delta \theta$ . For a typical XPS experiment, namely a photon energy of 1486.70 eV, an angular acceptance of  $\Delta \theta \approx 1^\circ$  and electrons detected at the Fermi level ( $E_K \approx 1486$  eV), we obtain  $\Delta K_{\parallel} \approx 0.34 \text{\AA}^{-1}$ . The dimensions of the Brillouin Zone (BZ) of BaTiO<sub>3</sub> are  $2\pi/a \approx 1.6 \text{\AA}^{-1}$  meaning the photo-electron momentum is smeared out over one fourth of the BZ preventing any good resolution in the reciprocal space.
- A high-photon energy means the photon wave vector is relatively large ( $\mathbf{k}_{\text{photon}} \approx 0.75 \text{\AA}^{-1}$  for 1486.70 eV). In that regime, the photon momentum cannot be neglected as we will do in the following [165].

Now, the problem is to relate  $E_B$  and  $\mathbf{k}$ , the energy and momentum of the electron propagating inside the solid to  $E_K$  and  $\mathbf{K}$ , the energy and momentum of the electron propagating in vacuum. The relation  $E_K = h\nu - \Phi_S - E_B$  has already been discussed in Section 1.1.2. The relation between the momenta is more involved. In the UPS regime, the optical transition<sup>10</sup> between the initial and the final states is a vertical transition in

<sup>10</sup>*i.e.* the first step of the three-step model, again the focus is on the three-step models in this section for the sake of simplicity and consistency.

the reduced-zone scheme. However, the reduced-zone scheme might be deceiving in the analysis of the photoemission process, as explicated by Mahan: “the absorption of the photon provides the electron with the additional energy it needs to get to the excited state. The crystal potential imparts to the electron the *additional momentum it needs to reach the excited state*. This momentum comes in multiples of the reciprocal-lattice vectors  $G$ : So in a reduced zone picture, the transitions are vertical in wave-vector space. But in photoemission, it is more useful to think in an extended-zone scheme.” [130]. Indeed, the transmission (third step) through the sample surface is obtained via the matching of the final state Bloch wave inside the sample and a free-electron wave in vacuum, and is only possible via the addition of momentum from the reciprocal-lattice vectors. Figure 1.11 illustrates the kinematics of the photoemission process.

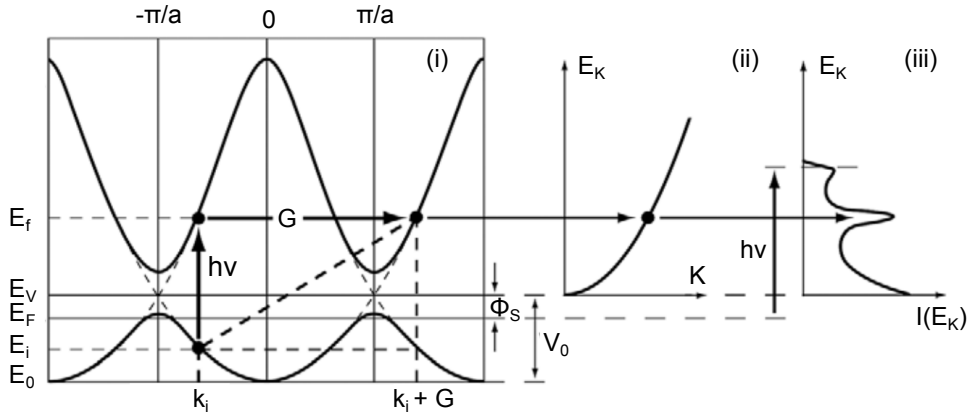


Figure 1.11: Kinematics of the photoemission process within the three-step model and nearly-free-electron final state model (from Ref. [54]): (i) Optical transition in the solid in an extended zone scheme; (ii) Free-electron final state in vacuum and (iii) the measured photoemission spectrum.

The translation symmetry in the parallel plane imposes the conservation of the parallel component of the photo-electron momentum, we obtain:

$$\mathbf{k}_{\parallel} = \mathbf{K}_{\parallel} = \frac{1}{\hbar} \sqrt{2m \cdot E_K} \cdot \sin \theta \quad (1.20)$$

On the contrary, due to the abrupt potential change at the surface along the perpendicular direction, the perpendicular component of the photo-electron momentum is distorted when crossing the surface. It can only be recovered by modeling the dispersion of the final state  $E_f(\mathbf{k})$ . The most common model adopts a nearly-free-electron description for the final Bloch state (this is the model adopted in Figure 1.11):

$$E_f(\mathbf{k}) = \frac{\hbar^2}{2m} (\mathbf{k}_{\parallel}^2 + \mathbf{k}_{\perp}^2) - (V_0 - \Phi_S) \quad (1.21)$$

where  $V_0$  and  $\Phi_S$  are the sample inner potential and work function, respectively, and have been defined in Figures 1.6 and 1.11. Using equation (1.20), one obtains:

$$\mathbf{k}_\perp = \frac{1}{\hbar} \sqrt{2m (E_K \cos^2 \theta - V_0)} \quad (1.22)$$

In this model, the issue is to determine the inner potential. The most used method is to vary  $V_0$  so that experimental results fits theoretical calculations.  $V_0$  can also be obtained from the zero muffin-tin potential used in band structure calculations [201]. Besides, band structure calculations can be used to model the dispersion of the final state with a better degree of approximation than the simple nearly-free-electron model. In any case, the mapping of the perpendicular dispersion is further complicated by the finite probing depth of photoemission which leads to the confinement of the final state along the the perpendicular direction, and by the uncertainty principle, to an intrinsic broadening of  $\mathbf{k}_\perp$  [209].

Instrumentally, angle-resolved experiments are usually conducted by rotating the analyzer (or the sample) to select photoemitted electrons with a given take-off angle and map  $\mathbf{k} \parallel$ . More recently, the electrostatic lenses of a photoemission microscope can be tuned to display an image of the reciprocal space (Fourier plan) instead of the real space on the microscope screen (see Refs. [135, 137, 191] for more details on this technique known as Angle-Resolved PhotoEmission Microscopy or k-PEEM). In both cases, the result is a stack of data giving the intensity of photoelectron as a function of binding energy and parallel momentum. At normal emission ( $\cos \theta = 1$ ) and by changing the photon energy while analyzing the same initial state, *i.e.*  $E_B$  stays the same, but  $E_K$  is varying, one can probe the perpendicular dispersion (the parallel momentum is zero at normal emission). Such experiments are only possible at Synchrotron where adjustable photon energy is available. The latter constraint, the intrinsic broadening of  $\mathbf{k} \perp$  and the difficulty of modeling the final states make the mapping of the perpendicular dispersion a difficult experiment.

All these measurements are an image of the excited final state; still it is often considered as a good approximation of the initial band structure of the sample. This is why such results are often compared to Density Functional Theory simulations of the band structure at the ground state [127, 216]. However, calculations based on Green's functions are much more reliable since they explicitly take into account the removal of the electron on the electron cloud. Such calculations are scarce due to great computation time and complexity, however recent work showed how promising this framework is for modeling spectroscopic data beyond the quasiparticle approximation [78, 162].

Electron emitted from core-levels also displays an angle-dependent behavior. In some very particular cases, this phenomenon is attributed to core-level dispersion [128] though this conclusion is rather controversial. In most cases, the angle-dependent behavior is due to multiple elastic scattering event due to the periodicity of the sample. This technique is called X-Ray Photoemission Diffraction (XPD). It gives access to a very accurate estimation of the emitting atom cristallographic environment. It adds to classical X-Ray

Diffraction (XRD) experiments the chemical sensitivity of photoemission, but it is limited to the study of surfaces [24, 233].

### 1.2.3 Photoemission on Insulators

The photoemission process removes an electron from the near surface of the studied sample: the surface charges positively. In metals, the charges reorganize themselves quickly enough so that the charging effect has no effect on the measurements. This is not the case for insulators where the progressive charging lead to severe distortion of the spectrum (in the case of photoemission spectroscopy) or the image (photoemission microscopy). Therefore, using photoemission experiments to probe ferroelectrics, which are insulating by essence, is not straightforward. However, the potency of this technique to access spatial, electronic and chemical information on ferroelectric materials has forced researchers to find solutions for the charge evacuation, with metallic grids for instance. Ferroelectric thin films are often sufficiently conducting to allow photoemission-based experiments. Finally, annealing an oxide at sufficiently high-temperature in vacuum generates oxygen vacancies. The electrons released by the vacancies induce a nonzero conduction which is often sufficient to limit the charging of the surface. Nonetheless, the charging of the sample has to be kept in mind in every experiment involving insulators since it can induces irrelevant broadening and energy shifts.

# Chapter 2

## Ferroelectricity

The discovery of  $\text{BaTiO}_3$ , a robust and structurally simple ferroelectric, during the second world war years really started the development of ferroelectric-based electronics. Investigation on  $\text{BaTiO}_3$  and similar ferroelectric perovskites have pushed forward the theoretical and experimental knowledge on ferroelectrics. On an industrial point of view, billions of  $\text{BaTiO}_3$  condensers are still in production nowadays. The first historical step was the understanding of phase transitions and the discovering of new ferroelectric materials. This went with the development of bulk ceramics as actuators, piezoelectric transducers and pyroelectric detectors. The second step came with the development of ferroelectric thin-film grown on silicon wafers. Over the years, this led to the development of ferroelectric field-effect transistor, ferroelectric memories [194] and ferroelectric tunnel junctions [26] thanks to a lot of fundamental work on the effects of strain, film/substrate and electrode/film interfaces and finite size on the properties of the ferroelectric film. More recently, the research on ferroelectrics has passed a third step with the renewed interest<sup>1</sup> on materials showing simultaneous ferromagnetic and ferroelectric ordering. The production of high-quality single-crystal samples on the one hand, and the improvements in first-principles-based calculations on the other hand, significantly helped in the understanding of the phenomena involved, and in the design of new multiferroics [177]. The goal of devices based on such materials is obviously the control of the magnetization of the sample by using an electric field, via the coupling of the two ferroic orders. This would have outstanding applications in high-density data storage with the development of devices which combine the high-density and long-retention of magnetic storage with the easiness and low-consumption of electric manipulation.

---

<sup>1</sup>Materials showing magnetoelectric properties have been studied since the 1960s [8], but the term multiferroic was used for the first time in 1994 [190].

## 2.1 Ferroelectricity Background

In 1920, J. Valasek described for the first time the electric hysteresis behavior of polarization in Rochelle Salt [227]. Henceforth, a new class of material was called *ferroelectric* by analogy with the theory of ferromagnetism. Indeed, ferroelectric materials exhibit a typical Polarization - Electric Field loop showing an hysteresis behavior similar (in shape) to the Magnetization - Magnetic Field loop of ferromagnetic materials (see Section 2.3.1–Figure 2.8 for a typical P-E loop of a ferroelectric material).

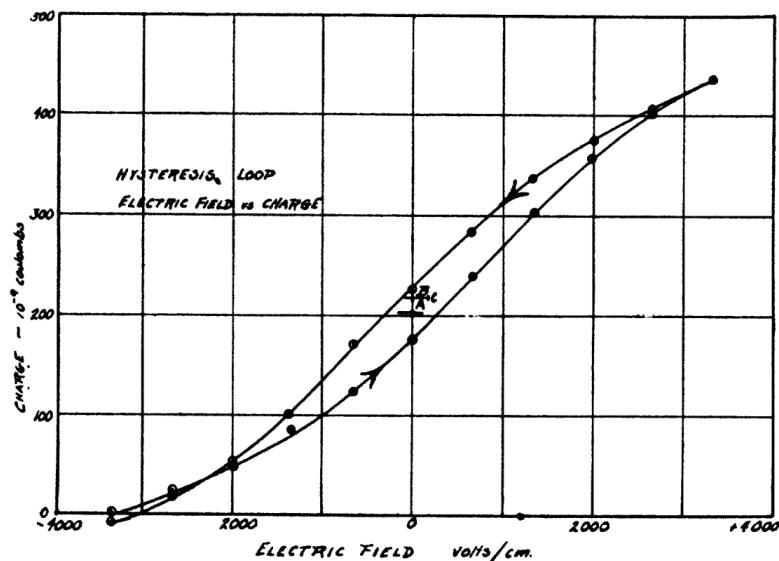


Figure 2.1: The first Polarization - Electric Field loop measured by J. Valasek on Rochelle Salt in 1920 [227].

A ferroelectric is an insulating system with two or more discrete stable or metastable states of different nonzero electric polarization in zero applied electric field, referred to as spontaneous polarization. The other necessary, defining property is the possibility to switch between these states with the application of an external electric field<sup>2</sup>. This definition is schematized in Figure 2.2: the free energy of at least one set of ions of the ferroelectric material consists of a double-well (blue curve). An electric field, named the coercive field  $E_c$  – of magnitude smaller than, and not to be confused with, the breakdown field - can switch the polarization from one ground state to the other (red curve). There are two models to describe the ferroelectric-paraelectric phase transition. In the order-disorder model, with increasing temperature, ions progressively acquire enough kinetic energy to hop back and forth between the two sides of the potential double well so their average position is midway between the two polar states<sup>3</sup>. In the displacive model, with increasing temperature, the free energy becomes a single well with a minimum for zero polarization (see Figure 2.2b). The material is then in a paraelectric state. It follows

<sup>2</sup>This definition is taken from *Physics of Ferroelectrics: A modern perspective* [176] which is an excellent, modern reference for understanding ferroelectricity and ferroelectric materials.

<sup>3</sup>See *Ferroelectric Memories*, by J.F. Scott, edited by Springer.

that a ferroelectric phase must therefore have a non-centrosymmetric structure. In a centrosymmetric structure, restoring forces cancel the relative ionic displacements.

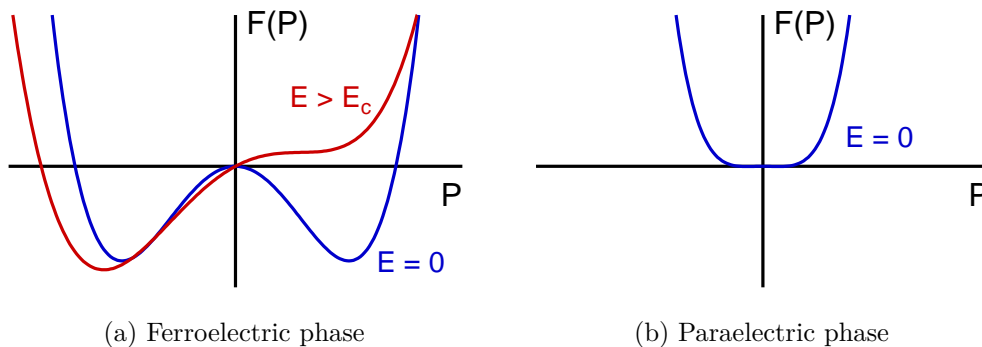


Figure 2.2: (a) Free energy double-well of a ferroelectric system as a function of polarization. The blue curve is for zero external electric field: both polarization states have the same energy. The red curve is when an electric field stronger than the coercive field  $E_c$  is applied on the material, promoting one state over the other. (b) Free energy of a paraelectric system. Both images schematize second-order transition materials. First-order transitions have a slightly different energy landscape.

Electric polarization is the key concept to understand ferroelectricity. Its definition is rather simple in the case of finite systems where polarization is defined as the electric dipole moment (charge density divided by the volume) of the system. The definition is more tricky when dealing with infinite crystals. The widely-accepted solution proposed by Resta, King-Smith and Vanderbilt will be introduced in Section 2.1.2. However, for the sake of simplicity, the basic concepts of ferroelectricity can be described using a didactic yet widely-studied ferroelectric system:  $\text{BaTiO}_3$ .

### 2.1.1 Illustration with a Typical Ferroelectric: $\text{BaTiO}_3$

$\text{BaTiO}_3$  has a perovskite structure, *i.e.* it has the same crystal structure as calcium titanium oxide ( $\text{CaTiO}_3$ ). The conventional cell is a face-centered pseudo-cubic (fcc) cell where barium atoms lie on the apices of the cube and oxygen atoms are in the face centers. The titanium atom is at the center of the cube of barium, or equivalently at the center of the oxygen octahedron, as depicted on Figure 2.3a. The perovskite structure is adopted by many oxides having the chemical formula  $\text{ABO}_3$ . These oxides exhibit many interesting properties such as ferroelectricity ( $\text{BaTiO}_3$ ,  $\text{PbTiO}_3$ ), colossal magnetoresistance (doped  $\text{LaMnO}_3$ ), or multiferroicity ( $\text{BiFeO}_3$ ,  $\text{EuTiO}_3$ ).

With increasing temperature, a free-standing single crystal of  $\text{BaTiO}_3$  exhibits three non-centrosymmetric phases: rhomboedral (up to 183 K), orthorhombic (183 K to 278 K) and tetragonal (278 K to 393 K) [120]. In these low-symmetry phases, the titanium atom is displaced from the center of the cube towards a preferential direction, usually called *polar axis*. The resulting asymmetric charge distribution induces a local dipole moment. Due to long-range coulombic interactions between the dipole moments,  $\text{BaTiO}_3$  exhibits a

macroscopic polarization along the polar axis. Dipoles rearrange themselves to minimize the sample energy as a function of several internal and external parameters (temperature, strain, crystallographic defects, adsorbates, history of the sample. . .) to form ferroelectric domains wherein polarization is in the same direction. Experimentally, these domains can be imaged by optical microscopy (see Figure. 2.4), electronic microscopy (see Chapter 3) or Piezoresponse Force Microscopy (PFM, see Section 2.3.3). The tetragonal phase of  $\text{BaTiO}_3$  is of greater interest since it is stable at room temperature. In that case, polar axis lies along one of the  $\langle 001 \rangle$  directions, see Figure. 2.3b. Above the Curie temperature ( $T_c = 393 \text{ K}$ ),  $\text{BaTiO}_3$  becomes cubic and therefore paraelectric.

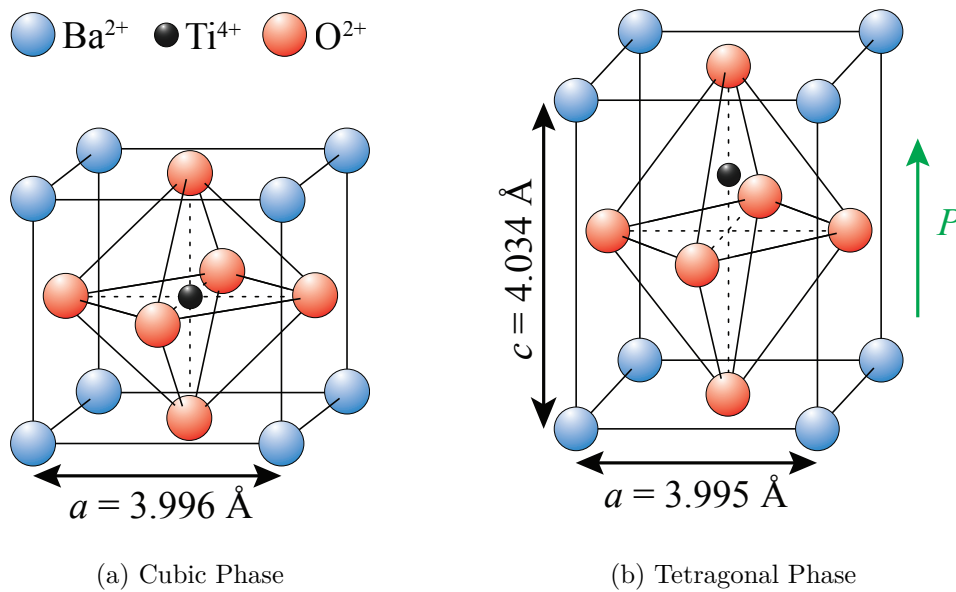


Figure 2.3:  $\text{BaTiO}_3$  perovskite structure.

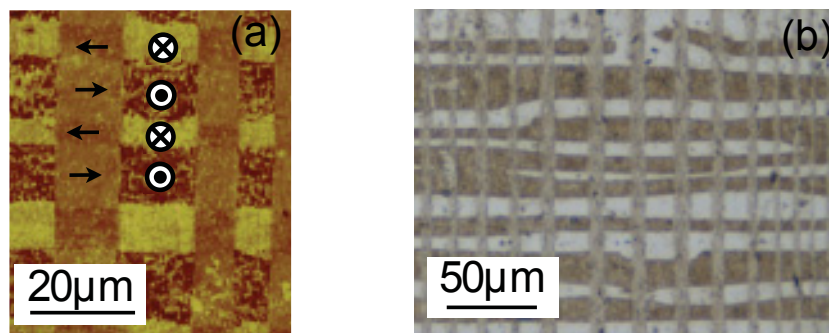


Figure 2.4: (a) PFM and (b) optical images of ferroelectric domains in a  $\text{BaTiO}_3$  single crystal, from Tsou *et al.* [222].

W. Cochran developed in Ref. [49] a description of ferroelectricity in terms of the mode of vibrations of a crystal lattice. For the sake of simplicity, we consider a linear chain of O - Ti - O atoms along the polar axis in  $\text{BaTiO}_3$ , the dynamics of a small displacement  $x$  of the titanium atom from its equilibrium position can be described in the framework of classical Newtonian physics:

$$\mu \frac{\partial^2 x}{\partial t^2} = -R \cdot x + A \cdot x \quad (2.1)$$

Where  $R$  describes the restoring, stabilizing force due to the short-range potential interaction between the ions and  $A$  describes the destabilizing force due to the long range Coulombic forces (dipole-dipole coupling).  $\mu$  is the reduced mass of the Ti - O unit. The existence of ferroelectricity depends on the competition between the pro-ferroelectric forces (long range coulombic forces  $A$ ) and the anti-ferroelectric forces (short-range repulsion  $R$ ).

Now, it seems natural to work in the framework of phonon physics. Acoustic modes cannot contribute to ferroelectricity since they are a coherent movement of every atom of the lattice out of their equilibrium position: positive titanium and negative oxygen ions move in the same direction and there is no change in the local electric dipoles. On the contrary, optical modes consist in an out-of-phase movements of atoms and should have a role in ferroelectricity. Indeed, Cochran showed that the transverse optical (TO) mode have the frequency given in equation (2.2):

$$\mu\omega^2(TO) = R - \frac{4\pi(\epsilon + 2)(Zq^2)}{3V(T)} \quad (2.2)$$

while the longitudinal optical (LO) mode have the frequency given in equation (2.3):

$$\mu\omega^2(LO) = R + \frac{8\pi(\epsilon + 2)(Zq^2)}{9V(T)} \quad (2.3)$$

where  $\epsilon$  is the optical dielectric constant,  $Z$  the effective charge of the mode and  $V(T)$  is the temperature-dependent cell volume.  $V(T)$  increases with  $T$ , and small changes in  $V(T)$  can cause the cancellation of  $\omega$  in equation (2.2). In the high-symmetry, high-temperature phase, the short-range forces  $R$  are dominant over the long-range forces: the system is paraelectric. With decreasing temperature (hence decreasing  $V(T)$ , increasing  $A$ ), the long-range forces progressively takes over the short-range ones. The transverse optical phonon softens (i.e. progressively goes to zero) and is finally canceled at the transition temperature. Below this temperature, long-range forces become dominant and the system becomes ferroelectric. Since both terms in equation (2.3) are positive, the longitudinal optic phonon has no role in the ferroelectric transition in this model.

At the transition temperature, the competing force acting on the ions are balanced. Therefore, any optical excitation should induce a great displacement of the ions, hence the name "soft" mode. This can be experimentally seen by monitoring the behavior of the dielectric constant of BaTiO<sub>3</sub> during phase transitions. The dielectric constant links the electric displacement field with an external electric field via equation (2.4).

$$\mathbf{D} = \epsilon \mathbf{E} \quad (2.4)$$

It can be related to phonon modes via the Lyddane-Sachs-Teller (LST) relation for a

crystal with  $N$  infrared-active optical modes ( $N = 3$  for  $\text{BaTiO}_3$ ) which reads:

$$\frac{\epsilon(\omega)}{\epsilon(\infty)} = \prod_j^N \frac{\omega_j^2(LO)}{\omega_j^2(TO)} \quad (2.5)$$

Thus, during phase transition a dramatic increase of the dielectric constant due to the softening of the TO phonon mode is expected. Figure 2.1.1 displays the evolution of the dielectric constant of  $\text{BaTiO}_3$  with temperature clearly showing the asymptotic behavior at the phase transitions.

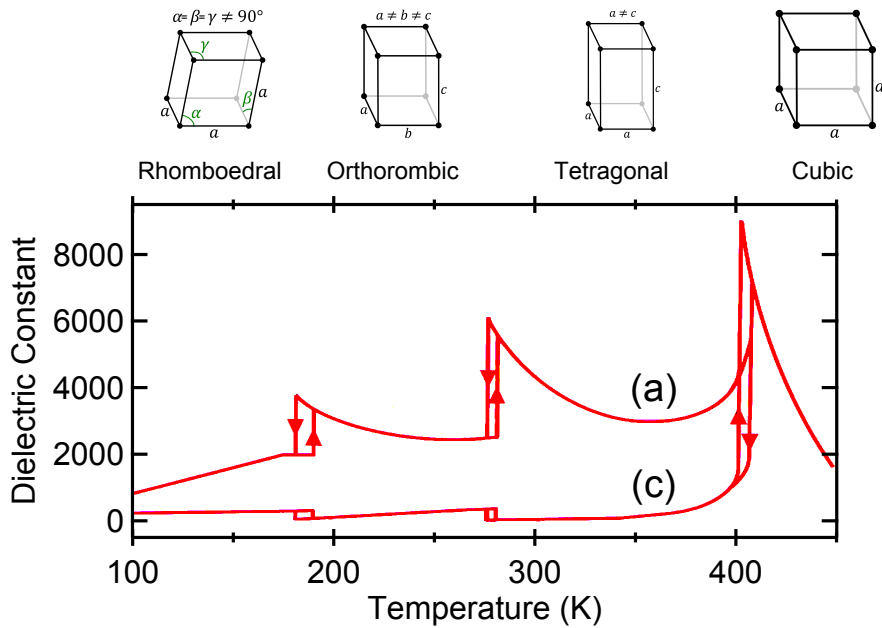


Figure 2.5: Dielectric constant evolution along axis  $[100]$  (a) and  $[001]$  (c) as a function of temperature in the case of  $\text{BaTiO}_3$ . Corresponding ferroelectric phases are shown on top of the graph.

The model proposed by Cochran [49] is a displacive theory: titanium ions progressively displace from a centered position to the off-center polar positions when crossing the transition temperature. In the order-disorder theory supported for instance by R. Comès [52] and B. Ravel [181], titanium is always displaced in one of the eight possible off-center positions along  $\langle 111 \rangle$  directions. Thermal agitations over the eight possible sites lead to the different phases. When the temperature is higher than the Curie temperature, every site is equivalent, the mean polarization is zero and  $\text{BaTiO}_3$  is paraelectric. With decreasing temperature, less and less sites are equivalent leading to lower symmetry phases. In the particular case of  $\text{BaTiO}_3$ , it seems that both phenomena have a role, and both theories have been reconciled in Ref. [206] by E. Stern.

### 2.1.2 Modern Theory of Polarization

Defining polarization in a ferroelectric system is a long-standing theoretical issue. The traditional picture considers polarization as an intensive quantity that quantifies the integrated contribution of individual local dipoles. However, for the case of crystalline solids, this definition fails to unambiguously describe a *bulk* polarization  $\mathbf{P}_{\text{bulk}}$ . One may apply the finite system model, i.e.  $\mathbf{P}_{\text{bulk}}$  equals the dipole of the macroscopic sample divided by its volume. However, any change at the surface, due for instance to surface preparation, would give a different value of  $\mathbf{P}_{\text{sample}}$  whereas bulk polarization would not have changed. To overcome these boundary issues, one can define  $\mathbf{P}_{\text{bulk}}$  as the local dipole of a bulk unit cell divided by its volume. In that case, the problem lies in the choice of the unit cell. In solid crystalline materials, the electronic charge has a periodic, continuous distribution which cannot be unambiguously separated into localized unit cells. This is particularly true for the ferroelectric oxides where chemical bonds present a mixed covalent/ionic character<sup>4</sup>. Thus, the knowledge of the periodic electronic charge distribution in a polarized crystalline solid cannot be used to construct a definition of bulk polarization, since any definition would be ambiguous. This establishes a fundamental difference between finite systems (clusters, molecules) where a finite volume can be unambiguously defined and infinite crystals.

In the early 1990s, R. Resta [183] on the one hand, and King-Smith, Vanderbilt [109] on the other hand, developed an original solution to tackle this fundamental issue, known as the *modern theory of polarization*. In this approach, one focuses on the *difference* in polarization between two states of the crystal that can be connected by an adiabatic process. The polarization difference is equal to the integrated transient macroscopic current that flows through the sample during this process. Formally, one can introduce a parameter  $\lambda$  which has the meaning of a dimensionless adiabatic time.  $\lambda$  varies continuously from zero (initial state) to 1 (final state). Polarization change is given by the following equation:

$$\Delta\mathbf{P} = \int_0^1 d\lambda \frac{d\mathbf{P}}{d\lambda} \quad (2.6)$$

The transition from the initial to final state is achieved by slow sublattice displacements, strain or electric fields for instance. In this equation, the quantity  $\frac{d\mathbf{P}}{d\lambda}$  is a well-defined bulk property: the transient current carried by electrons and nuclei. This theory has to take into account the quantum nature of electrons whereas the nuclei can be safely dealt as classical point charges. In a quantum-mechanical description, current is closely related to the phase of the wavefunctions. The necessity of the wavefunction phase to define bulk polarization is another proof, if needed, of the fundamental impossibility of defining polarization using only the charge distribution. Indeed, charge distribution is obtained by using the modulus of the wavefunction, any phase information being discarded.

---

<sup>4</sup>This issue is also very important in the promising field of oxide-oxide interfaces, where the definition of local dipoles is very problematic, see Ref. [97]

Here, the resulting phase (from which one extracts the current, hence the polarization difference) of the Bloch wavefunctions when going from  $\lambda = 0$  to  $\lambda = 1$  is expressed in the more general framework of Berry phases [246]. Thus, the *modern theory of polarization* is often referred as the *Berry-phase theory of polarization*. This elegant approach is very potent for numerical calculations of bulk polarization but is also an accurate description of what is experimentally measured in Polarization - Electric Field experiments described later in Section 2.3. This framework provided an accurate method to calculate *ab-initio* experimentally-accessible quantities such as piezoelectric coefficients, spontaneous polarization and dynamical charges (see Section 2.1.3). Nonetheless, this method has serious limitations common to every *ab-initio* technique: firstly, the limited-size of the numerical cluster makes the study of realistic (in terms of size) ferroelectric domains impossible; secondly, non-equilibrium phenomena cannot be monitored, which prevents any insight on phase transition for instance.

To overcome these limitations, the Landau theory applied to ferroelectric systems is still widely-used. Actually, it has been used on ferroelectrics long before the recent rise of *ab-initio* simulations. This theory is a symmetry-based, phenomenological approach which relates measurable quantities one to another using a minimum set of input parameters. These parameters can be determined by comparison to experimental results, or more recently from first-principles-based approach. By essence, Landau theory assumes spatial averaging of all local fluctuations and thus is well suited for long-range interactions systems such as ferroelectrics. Landau-based theory is often referred as the "continuum approach" of the ferroelectric materials.

Landau theory is used to analyze the behavior of a system near a phase transition<sup>5</sup>. It describes the transition from one phase to another of different symmetry. The phases are characterized by an order parameter (polarization in the case of ferroelectrics) which is zero in the high-symmetry phase (cubic phase in the case of BaTiO<sub>3</sub>) and continuously change to a finite value in the low-symmetry phase (tetragonal phase for BaTiO<sub>3</sub>). Devonshire applied this theory to ferroelectrics in Refs [55, 56, 57]. He used as relevant variables the temperature, the polarization, the electric field, the strain and the stress. The development of free energy as a function of these variables using phenomenological parameters gave the transition energy, Curie temperature and other properties of many ferroelectrics [49, 82, 139]. The effect of free surfaces was investigated by Kretschmer and Binder [117] and was extended later to take into account the effect of imperfect screening [121]. However, this methodology fails to describe systems of reduced size when the averaging of the order parameter is no longer possible. In addition, the difficulty to obtain precise, unambiguous phenomenological microscopic data hindered further development of this method in favor of the following.

First-principles based effective Hamiltonian techniques have been widely-used on ferro-

---

<sup>5</sup>See *Collected Papers of L. D. Landau* by D. Ter-haar, edited by Pergamon (Oxford, 1965) for an English translation of Landau articles

electrics to investigate domain behavior and temperature dependence of the ferroelectric properties [248]. Using Landau theory as a conceptual base, the first step consists in finding the relevant degrees of freedom of the system, then, describe the system energy (via an effective Hamiltonian) as a function of these degrees of freedom in a polynomial expansion. But in this case, microscopic coefficients are calculated using first-principle calculations. The final step is to minimize the total energy of the system as a function of the degrees of freedom using the Monte-Carlo methodology [249]. This framework produced excellent results on domain patterns [46] or phase transition [98] in ferroelectric systems, even when the system size is reduced. It combines the precision of first-principle calculations (access to chemical, strain properties of the materials) and the temperature dependent properties provided by Monte-Carlo techniques. Besides, it can simulate much larger systems than purely *ab-initio* techniques.

### 2.1.3 The Concept of Dynamical Charges

One of the most useful quantity which can be calculated using the Berry-phase theory of polarization is the so-called dynamical charge of a given atom. The partition of charge in a crystalline solid is an issue that goes beyond the impossibility of defining a meaningful bulk polarization, as pointed out in the previous section. The static charge picture where each atom possesses a well-separated, static electronic charge, is rather arbitrary since the covalent character of bonding orbitals prevents the unambiguous attribution of electronic charge to an atom. Again, the best solution is to consider a *varying* quantity instead of a static one. The concept of dynamical charge models the changes in the atom polarization induced by an infinitesimal atomic displacement.

In periodic systems, a dynamical charge tensor  $Z^*$  is conventionally defined as the coefficient of proportionality (linear approximation) between the macroscopic polarization per unit cell created in direction  $\beta$  and a rigid displacement  $\tau$  of the sublattice of atoms  $\kappa$  in direction  $\alpha$ , times the unit cell volume  $\Omega_0$ <sup>6</sup>:

$$Z_{\kappa,\alpha\beta}^* = \Omega_0 \frac{\partial P_\beta}{\partial \tau_{\kappa,\alpha}} \quad (2.7)$$

This quantity is not uniquely defined, as the change of polarization  $\partial P$  depends on the boundary conditions fixing the macroscopic electric field through the sample. Depending on the boundary conditions, different dynamical charges have to be considered (in theory, any boundary condition leads to a new kind of dynamical charge). The Born effective charge [29], or transverse charge  $Z^{*,(T)}$ , refers to a system under the condition of zero macroscopic electric field (i.e. short-circuit conditions). On the contrary, the Callen charge [37], or longitudinal charge  $Z^{*,(L)}$ , corresponds to a system under zero macroscopic displacement field (open-circuit conditions).

---

<sup>6</sup>This definition is taken from a thorough review of the concept of dynamical charges on perovskites compounds, by P. Ghosez, J.-P. Michenaud and X. Gonze [76].

Applying this concept on  $ABO_3$  compounds leads to outstanding results. In  $BaTiO_3$ , dynamical charges are much higher than the static charge calculated from a ionic picture:  $Ti^{4+}$  has +7.25,  $Ba^{2+}$  has +2.77 and  $O^{2-}$  -2.15 and -5.71 dyn. charge depending on its chemical environment (see Ref. [76] for further details). This so-called *anomalous* contribution to atomic charge is closely related to the *rate of change* of hybridization (rather than its magnitude) under atomic displacement. Dynamical charges are thus an excellent tool to identify and quantify even the smallest band hybridization. In addition to exciting theoretical perspective, this element-dependent, enhanced response to excitation might be probed by actual experiment. This will be discussed in Chapter 4–Section 4.2.5.

## 2.2 Ferroelectricity in Nanoscale Systems

The nanometer scale has become the new standard in solid-state physics. Exciting properties only appear when reducing dimensions of thin films, dots, wires or clusters to nanometers. The physics at this scale is of great interest since quantum-related phenomena can be still dominant. The potential industrial applications in the long-standing quest for nanotechnology, high-storage density or low-consuming devices are very promising. However, reducing size often comes with new issues. A major one for prospective nanoscale, strain-engineered ferroelectric applications is the decrease of the polarization when reducing dimensions.

In the previous section, one key feature of any ferroelectric real system was eluded: the boundary conditions. Since this thesis will focus on 2D systems (thin films, single crystals), the following arguments will be based on layered heterostructures. However, these arguments can also be applied to any 1D (wires) or 3D (cluster, dots) nanometric structures.

If a ferroelectric polarization ( $\mathbf{P}$ ) arises in the out-of-plane direction (vector  $\mathbf{n}$ ) of the slab, it will induces a surface charge density ( $\sigma_{\text{pol}}$ ) at the FE/vacuum interface (see Figure 2.6):

$$\sigma_{\text{pol}} = \mathbf{P} \cdot \mathbf{n} \quad (2.8)$$

These charges generate an electric field  $\mathbf{E}_{\text{depol}}$  which acts against the ferroelectric polarization (Figure 2.6):

$$\mathbf{E}_{\text{depol}} = -\frac{\mathbf{P}}{\epsilon \cdot \epsilon_0} \quad (2.9)$$

where  $\epsilon$  is the dielectric constant of the slab. The electrical boundary condition, i.e. the screening of the surface polarization charges, appears as a fundamental property of such system. Slight changes in boundary conditions can for example induce a ferroelectric to paraelectric transition. Two hypothetical boundary conditions are often used for modeling or calculations:

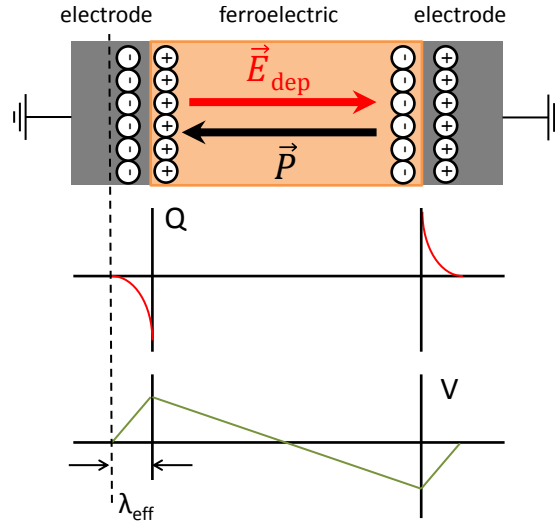


Figure 2.6: (top panel) Schematic of an electrode/ferroelectric/electrode structure. The fixed charges, induced by the ferroelectric polarization  $\mathbf{P}$ , are imperfectly screened by free charge carriers (charge  $Q$ , middle panel) from the metallic electrode over the effective screening length  $\lambda_{\text{eff}}$ . The resulting electrostatic potential ( $V$ , bottom panel), or equivalently the depolarizing field  $\mathbf{E}_{\text{depol}}$ , acts against  $\mathbf{P}$ .

- In the short-circuit boundary conditions, the ferroelectric charges are perfectly screened. The depolarizing field is zero.
- In the open-circuit boundary conditions, the ferroelectric charges are not screened at all. The depolarizing field is maximal.

In realistic system, the screening mechanism is imperfect, with screening charges slightly displaced away from the surface of the ferroelectric, thus leading to finite dipoles. Considering two identical metallic electrodes at both surfaces of the ferroelectric slab of thickness  $d$ , a simple electrostatic model gives the following voltage drop:

$$\Delta V = \frac{\lambda_{\text{eff}}}{\epsilon_0} \cdot |\mathbf{P}| \quad (2.10)$$

Where  $\lambda_{\text{eff}}$  is the effective screening length.  $\lambda_{\text{eff}}$  is a measurement of the main displacement of the screening charge from the ferroelectric surface. It models the distance over which the polarization charges are screened. In the case of a short-circuited circuit (i.e. both metallic electrodes are at equipotential), the depolarizing field reduces to:

$$\mathbf{E}_{\text{depol}} = -2 \frac{\lambda_{\text{eff}}}{d \epsilon_0} \cdot \mathbf{P} \quad (2.11)$$

The electrode/ferroelectric/electrode system is a straightforward model to illustrate the concepts of screening length and depolarizing field. However, in realistic systems, other screening mechanisms have to be considered:

- The screening by mobile charges inside the ferroelectric slab is possible, as shown in Figure 2.7a. For instance in  $\text{BaTiO}_3$ , oxygen vacancies created by vacuum annealing

generates free electrons via the reaction equation  $O_O \rightarrow V_O^{\bullet\bullet} + \frac{1}{2}O_2 + 2e^-$  [146]. These carriers screen the polarization-induced charges, and may favor one ferroelectric polarization over the other. This will be further developed in Chapter 3–Section 3.2.

- Domain organization is a very important screening mechanism (see Figure 2.7b). The field induced by adjacent domains can screen the depolarizing field of a ferroelectric domain. Such domain organization can explain the ferroelectric stability of very thin films. It will be further developed in Chapter 3–Section 3.1.
- Adsorbates provide screening dipoles as figured in Figure 2.7c. Not only can adsorbates stabilize ferroelectricity, but also they can even switch the domains [90, 91, 179].

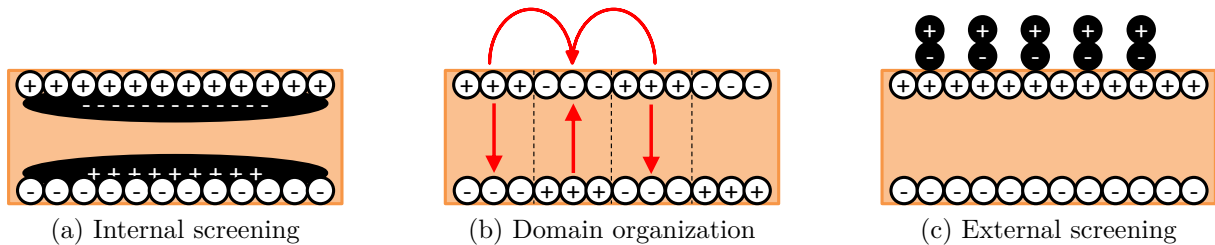


Figure 2.7: Different mechanisms for screening the polarization-induced charges.

The key parameter is the so-called effective screening length  $\lambda_{\text{eff}}$  (Figure 2.6) A small screening length means good screening by the electrodes, therefore a weak depolarizing field, and a better ferroelectric stability. This screening length can be estimated from experimental results [241] or obtained from *ab-initio* calculations using electrode/ferroelectric supercells [101, 205]. Recently, a very interesting framework emerged from effective Hamiltonian methods. Ponomareva *et al.* used a screening factor (named  $\beta$ ) which models the efficiency of screening [174]. It is explicitly considered in the energy expansion and has been successfully used in many ferroelectric systems [113, 122] with the advantages of effective Hamiltonian framework (large clusters, temperature dependence). In Chapter 3–Section 3.1.4, an application of this theoretical framework for the study of thin films of  $\text{BiFeO}_3$  will be presented.

## 2.3 Experimental Tools to Study Ferroelectricity

A wide range of experimental techniques are used to investigate the properties of ferroelectric materials. Raman spectroscopy measure the effect of polarization on phonon modes [10, 81]. A polarized-light microscope images the FE domains exploiting the birefringence of differently-polarized domains [138, 140]. As developed later, Photoemission experiments can probe the consequences of FE polarization on band-alignment (see Chapter 4) and surface potential or work function (see Chapter 3). In this section will be

presented the most typical methodologies for probing polarization and ferroelectricity in solid materials. On a technical point of view, every measurement presented in this section needs electrodes to apply voltage and probe the desired quantity (current, capacitance). We can use deposited electrodes, micro-tips or an Atomic Force Microscope tip to probe the sample. Even if it will not be described in this section, one should not forget that electrodes alter the sample properties and they have to be taken into account in real experiments. Indeed, electrode/ferroelectric interactions are the main interest of this thesis.

### 2.3.1 Polarization - Electric Field Loop Analysis

The defining feature of the electrical properties of a ferroelectric material is how its polarization  $\mathbf{P}$  behaves in presence of an electric field  $\mathbf{E}$ . Obtaining  $\mathbf{P}$  as a function of  $\mathbf{E}$  gives key information such as remnant and saturation polarization ( $P_r$ ,  $P_s$ ) or coercive fields ( $E_c$ ), as shown in Figure 2.8. However, there is no electrical measurement of the polarization vector itself. One has to quantify the consequences of a variation of polarization when applying a strain (piezoelectricity) or a temperature (pyroelectricity) or, in the case of P-E loops, an electric field. In Polarization - Field (P-E) loops, one measures the current flowing through the ferroelectric material while applying a voltage. The current is directly related to the change in polarization when it is switched by the electric field.

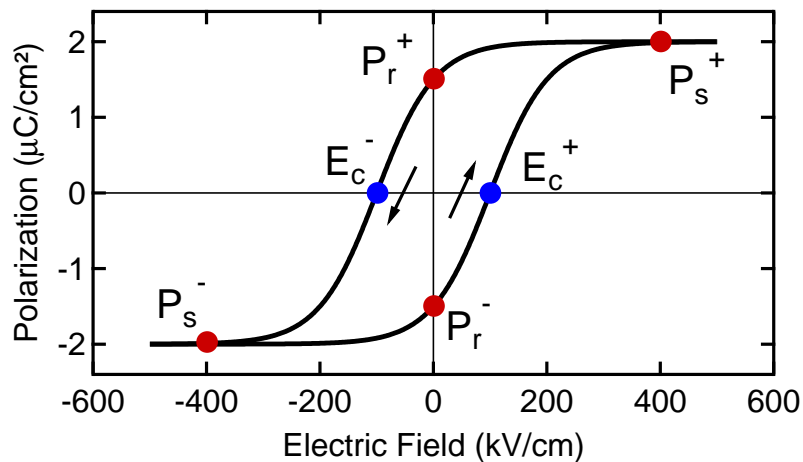


Figure 2.8: Theoretical Polarization - Field loop for an ideal ferroelectric material. The index + (-) means upward (downward) direction.  $P_r$  and  $P_s$  are the remnant and saturation polarization respectively.  $E_c$  is the coercive field.

#### Sawyer - Tower measurement

This method was introduced by Sawyer and Tower in 1930 on Rochelle Salt [186]. The principle is to measure the variation of charge (or equivalently time-integrated current) induced by a voltage sweep. A standard Sawyer - Tower circuit is shown in Figure 2.9

The source applies a sweeping voltage  $X$  across the capacitors, forcing charge onto the top plate of the ferroelectric material. The same amount of charge will leave the opposite

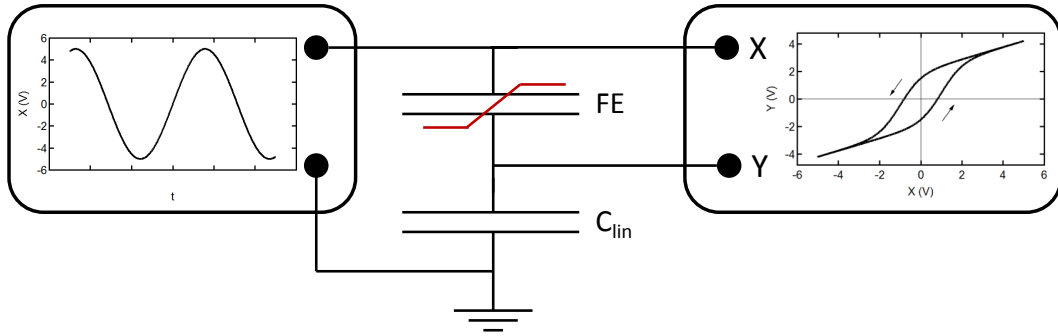


Figure 2.9: Schematic circuit for a Sawyer-Tower measurement.  $C_{lin}$  is the known capacitor, FE is the unknown.

plate of the ferroelectric capacitor and accumulates at the top plate of the linear sense capacitor ( $C_{lin}$ ). According to the equation  $Q = C_{lin} \cdot Y(X)$ , the voltage  $Y = f(X)$  across the linear sense capacitor will thus represent the charge  $Q$  that move in or out of the ferroelectric capacitor as a result of the applied voltage  $X$ . The oscilloscope in the  $X : Y$  graphing mode gives the expected loop. Equation (2.12) gives the P-E loop, provided one knows the thickness  $d$  and surface area  $A$  of the ferroelectric capacitor:

$$P = Q/A = C_{lin} \cdot Y/A \quad (2.12)$$

$$E = V/d = X/d$$

However, experimental loops obtained from this circuit must be carefully interpreted since non-ferroelectric phenomena can significantly alter the signal or make the measurement impossible. The main parasitic signal is the linear (non-switching) dielectric response of the ferroelectric which overlaps the ferroelectric (switching) response [30]. In some cases, a linear dielectric can at first glance look like a ferroelectric material because of the contribution from the probing circuit [193]. Moreover, in partially conducting samples (which is often the case for very thin films since leakage current increases exponentially when reducing thickness [12]), the probing voltage might lead to high current which will severely distort the signal and even damage the material under study or the probing devices. This is why this technique is less and less used for the investigation of thin film ferroelectric capacitors.

### Pulsed Measurement on Ferroelectrics

To overcome the limitation of the Sawyer - Tower system, Traynor et al. [220] developed a methodology using a pulsed voltage source. In that case, one measures the current flowing through the FE capacitor as a function of time: the time-integrated quantity is the change in polarization charge induced by the voltage pulse. To get rid of the non-switching contribution, this methodology often uses the P.U.N.D. (Positive - Up - Negative - Down) train of pulses as depicted in Figure 2.10a. After a preset pulse, which produces the initial

polarization state (P- for instance), the source applies a switching pulse (Positive: P- to P+), a non-switching pulse (Up), a inverse switching pulse (Negative: P+ to P-) and a non-switching pulse (Down). The charge displacement (or time-integrated current, see Figure 2.10b for typical current from a P.U.N.D. test  $Q_U$ ,  $Q_D$  after non-switching pulses are subtracted from the switching charges  $Q_P$ ,  $Q_N$  to give a measurement of the remnant polarization  $P_r$ :

$$2.P_r = \frac{Q_P - Q_U}{Q_N - Q_D}$$

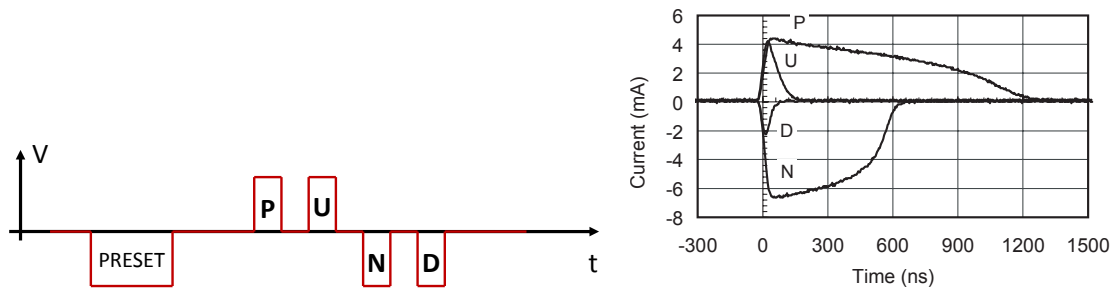


Figure 2.10: (a) Schematic train of voltage pulses for a P.U.N.D. test, (b) Typical results (Current through the ferroelectric as a function of time) for the test after offsetting the data so that current curves start at  $t = 0$ . Data from Abe *et al.* [2]

This method is widely-used in research since it is the prime feature of main ferroelectric testers (from Radiant Technology or Aixacct). Such measurements depend on the width, magnitude, rise time and time separation of each voltage pulse and give access to a lot of information such as coercive fields, switching time, internal fields [2, 100, 251].

### 2.3.2 Other Electrical Characterization

In addition to P-E hysteresis loop analysis, electrical techniques often used in semiconductor physics are now widely-employed to characterize ferroelectric materials.

#### Capacitance - Voltage curve

Capacitance - Voltage (C-V) curves are very specific for a FE material and contain precious information not only on the dielectric properties but also on the ferroelectric properties of the sample. Brennan developed a thorough analysis of the phenomena involved in the C-V curves of ferroelectrics [33]. In such an experiment, one investigates the dielectric properties of the sample by superimposing an a.c. probe signal to a d.c. bias. A LCR (Inductance - Capacitance - Resistance) meter measures for each d.c. voltage step the capacitance for a fixed a.c. amplitude and frequency. When approaching the coercive voltage, hence the polarization switching, the ferroelectric material exhibits a very high permittivity (any small change in applied field induces a large change in material polarization) and consequently a very high capacitance. This happens twice in a FE material:

firstly when switching from P- to P+, then from P+ to P-. Therefore, one does a d.c. bias loop to obtain the main feature of C-V in the case of FE materials: the so-called butterfly shape which indicates the existence of two remnant states of opposite polarization. Figure 2.11 displays a typical C-V loop for an ideal ferroelectric material. The main information are the coercive voltages/fields. By analyzing the quantitative information, C-V loops give access to information on charge carriers, built-in field and permittivity of the ferroelectric layer [33, 169, 170].

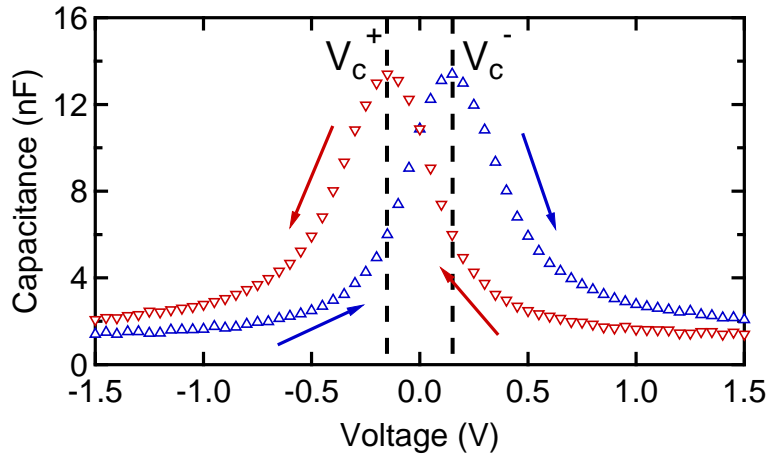


Figure 2.11: Theoretical Capacitance - Voltage loop for an hypothetical ideal ferroelectric material.

### Current - Voltage curve

In addition to C-V experiments, it seems logical to investigate the conductive properties of the sample. Therefore, C-V curves often go with Current - Voltage (I-V) curves. Many concepts from semi-conductors field are used to discuss these measurements on ferroelectrics. For instance, thin ferroelectric films may exhibit thermionic emission<sup>7</sup> or ohmic conduction [105, 171]. The main feature proper to ferroelectrics is the polarization-dependent tunneling current, which is a promising property of ferroelectric tunnel junctions and can be investigated with state-of-the-art I-V experiments [27, 230].

### 2.3.3 Piezoresponse Force Microscopy

Up to now, one of the main tool to investigate and manipulate ferroelectric materials is the Piezoresponse Force Microscope (PFM). PFM is part of the larger group of Scanning Probe Microscope (SPM). The operation principle of a SPM is based on the detection of the position of a soft cantilever-type spring with a sharp tip mounted at its end. The forces acting on the tip after it has approached the sample surface cause a deflection of

<sup>7</sup>Thermionic emission is defined by the heat-induced flow of charge carriers over a potential-energy barrier, in this case the electrode/ferroelectric barrier [212]

the cantilever according, in a first approximation, to the Hooke's law. The deflection is measured by the refraction of a laser beam on the cantilever. Bending of the cantilever will induce a displacement of the laser spot on a four-sectional photodiode and consequently a change of voltage in one of the quadrant of the photodiode. The feedback provided by the diode allows the regulation of the vertical position of the tip with respect to the sample surface. By keeping the deflection constant while scanning the sample, a three-dimensional map of the surface topography can be obtained. Figure 2.12 shows a schematic of a scanning probe microscope.

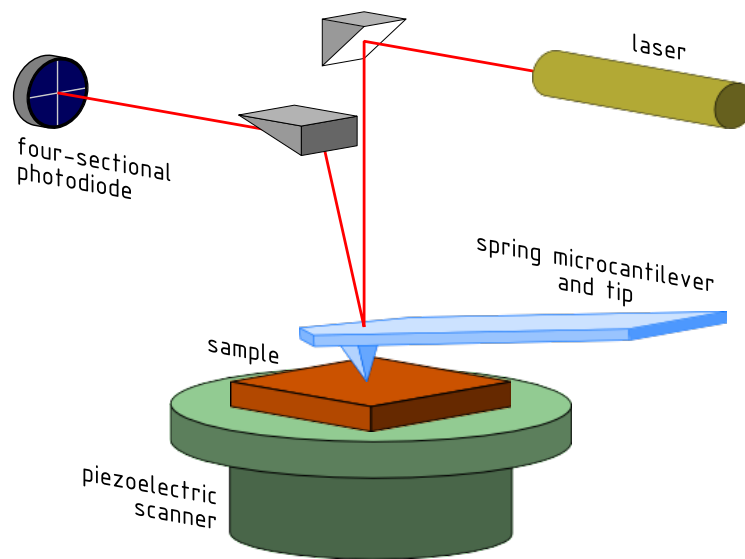


Figure 2.12: Schematic of a scanning probe microscope. The piezoelectric scanner allows movement in the plane. The tip is mounted on a cantilever which reflects a laser beam onto a four-sectional photodiode. The repelling-attractive forces between the surface and the tip induces vertical movements of the microcantilever which deflects the beam and changes the photo-diode signal.

The force involved in the PFM technique is due to the converse piezoelectric effect. The linear coupling between the electrical and mechanical properties of the sample is probed by the PFM tip. Since all ferroelectrics exhibit piezoelectricity, an electric field applied to a ferroelectric sample results in changes of its dimensions. To detect or switch the polarization orientation the PFM tip acts as a top electrode which can be moved over the sample surface. In reading mode, for each position step, an a.c. signal is used to detect the alteration of the excitation phase due to out-of-plane polarization orientation. The PFM gives an image of the phase shift of the a.c. signal which can be related to the out-of-plane direction of polarization (up or down). Using more complex scanning procedures, PFM can even access polarization directions in the plane [38, 106, 136]. In writing mode, for each position step, a d.c. bias is applied between the tip and a grounded bottom electrode in order to switch the ferroelectric polarization in the desired direction. Figure 2.13 displays a typical PFM image (acquired using the PFM reading mode) of a  $\text{BiFeO}_3$  thin film after poling (done using the PFM writing mode).

PFM has the advantages of any scanning microscopy: a very good lateral resolution (nano-sized domains can be written or detected on ferroelectric surfaces [38]), simultaneous ferroelectric and topographic information, the possibility of time-resolved PFM to investigate the kinetics of domain switching [77]. However, this technique cannot provide any quantitative information on the polarization. A P-E hysteresis loop experiment as described in section 2.3.1 is the only solution. However, a key difference is that the probe is local. In addition the tip has a very small surface (a few nanometers) compared to the electrodes (a few micrometers) used in classic P-E hysteresis loops. This limits the effect of exponential leakage currents. Combined to P.U.N.D. pulses, PFM sometimes gives access to P-E loops in thin films (see Figure 3.7a in Chapter 3–Section 3.1.3 for a P-E loop on a 70 nm thin film of  $\text{BiFeO}_3$ ). However, in most cases, the leakage current hides the useful signal and hinders the measurement of P-E loops [12]. In addition, tip-surface contact might modify the boundary conditions of the system altering the ferroelectric properties. Therefore, PFM is widely-used in the ferroelectric community though alternative non-contact, full-field microscopic techniques are gaining momentum as will be described in Chapter 3.

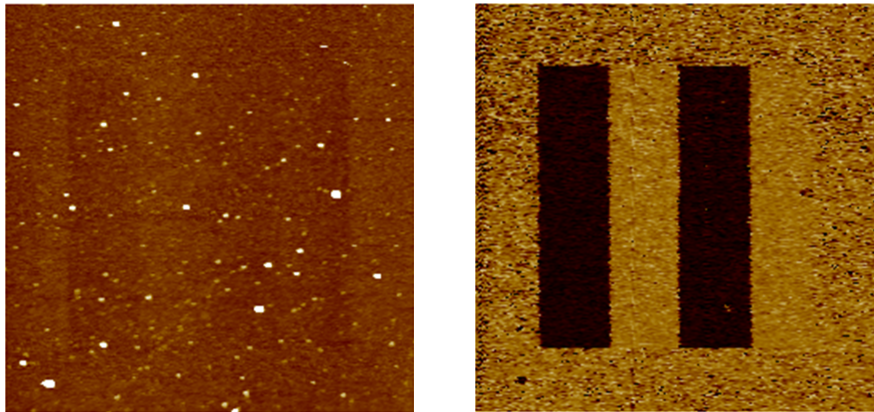


Figure 2.13: (left) Topography of a  $\text{BiFeO}_3$  thin film surface and (right) ferroelectric domains poled and read by PFM.

# Chapter 3

## Ferroelectric Surfaces

### Introduction

As previously described in Chapter 2–Section 2.2, the competition between ferroelectric polarization and the depolarizing field is a crucial issue in the understanding of ferroelectric materials. It is particularly important for ultrathin films for which polarization is reduced or even suppressed below the so-called *critical thickness* [101]. This phenomenon hinders the development of ferroelectric devices which need a tunneling ferroelectric film to work, such as ferroelectric tunnel junctions, or very high density ferroelectric memories [194, 202].

The critical thickness depends on the ferroelectric material but also on the electrical boundary conditions of the sample. To this end (*i.e.* surface screening studies), in this chapter, we focus on two samples with at least one free surface. The available screening processes of a free surface are domain ordering, internal screening and adsorbate screening. In the first part of this chapter, the study of BiFeO<sub>3</sub> strained thin-films reveals the crucial role of domain ordering in the screening of the depolarizing field. In the second part, we investigate BaTiO<sub>3</sub> monocrystals to understand the role of internal, free charges screening in the stabilization of ferroelectric polarization. Adsorbate screening is not treated in this thesis. The reader can explore the subject with the following references: Krug *et al* investigated the effect of external screening (namely contaminant molecules in that case) on the ferroelectric properties of Pb(Zr,Ti)O<sub>3</sub> [119]. Rappe *et al.* showed that polarization can even be switched by using molecules with a controlled concentration [179]. Wang *et al.* studied experimentally the influence of water adsorption on BaTiO<sub>3</sub> surfaces [233] following the theoretical work of Geneste *et al.* [73] for instance. More generally, Kalinin and Bonnell investigated the relative contribution of adsorbates and internal screening in the stabilization of the ferroelectric polarization [102].

## 3.1 Domain Ordering in BiFeO<sub>3</sub> Thin Films

### 3.1.1 Ferroelectricity in Ultrathin Films

With the recent developments and significant improvement in the growth of strained, nanometer-thick, oxide films [177, 188], a lot of research in material science has focused on oxide multilayers. As pointed out by D. Schlom: “Oxides exhibit the full spectrum of electronic, optical, and magnetic behavior: insulating, semiconducting, metallic, superconducting, ferroelectric, pyroelectric, piezoelectric, ferromagnetic, multiferroic, and nonlinear optical effects are all possessed by structurally compatible oxides” [188]. Thus, oxides heterostructures can potentially allow engineering of an extremely wide range of physical properties. Strain-engineering of such systems further expands the horizon of possible [7, 163, 189]. In the particular case of ferroelectrics, expected applications in nanoscale electronics have driven research in the last years [26, 192]. For instance, the development of ferroelectric tunnel junctions (FTJs), which need both a high ferroelectric polarization magnitude and a very thin ferroelectric layer, goes with the fundamental understanding of ferroelectricity in ultrathin (or tunneling, *i.e.* with thickness below 5 nm) films [72]. The question is how does the polarization magnitude changes with decreasing thickness, or equivalently how the energy of the thin film accommodates for the increasing depolarizing field.

A lot of theoretical work has been done in the past few years on the expected behavior of ferroelectric thin films when reducing thickness. On the one hand, *ab-initio* methods based on the modern theory of polarization of Resta, King-smith and Vanderbilt (see Chapter 2–Section 2.1.2) have led to significant progress in the field. The pioneer work of Junquera and Ghosez [101] on the evaluation of the critical thickness of BaTiO<sub>3</sub> thin films opened the way for numerous simulations on ferroelectrics thin films sandwiched between two realistic electrodes [184, 205, 226], free-standing layers under an applied electrical field [141] or domain walls [142]. On the other hand, effective-Hamiltonian, Monte-Carlo methods gave complementary information by simulating system with realistic size and submitted to adjustable boundary conditions. They predict different domain ordering in thin films submitted to increasing depolarizing field [175] or the evolution of the Curie temperature with thickness [5]. These predictions have been confirmed by experiments [152].

From an experimental point of view, Piezoresponse Force Microscopy (see Chapter 2–Section 2.3.3) can qualitatively prove the existence of a switchable polarization in very thin films and gave a lower limit for critical thicknesses in several systems [12, 38, 47, 71]. However, quantitative measurement of the polarization magnitude is made impossible in the tunneling regime, due to the high leakage current which hides the switching current (see Chapter 2–Section 2.3 and Ref. [107]). Further progress requires experimentally measurable properties which are quantitatively modified by the ferroelectric polarization.

Lichtensteiger *et al.* measure the out-of-plane ( $c$ ) and in-plane ( $a$ ) cell parameters of PbTiO<sub>3</sub> thin films on Nb-doped SrTiO<sub>3</sub> [126]. The ratio  $c/a$  is known as the tetragonality ratio of the thin film. This quantity is determined by the polarization magnitude as shown by the *ab-initio* calculations [126]. Thus, the authors give a critical thickness for this system of 2 nm and describe quantitatively the decrease of polarization with decreasing thickness (Figure 3.1).

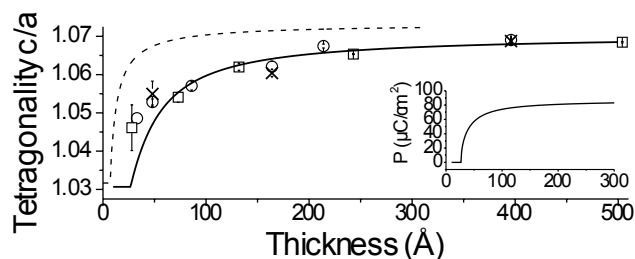


Figure 3.1: Evolution of the  $c/a$  ratio with thickness for PbTiO<sub>3</sub> thin films on Nb:SrTiO<sub>3</sub>. Symbols are the experimental points measured by x-ray diffraction. The dashed line is numerically calculated from a Landau-based model and the plain line from a first-principles-based model. Inset: calculated polarization dependence with thickness. This figure is taken from Ref. [126].

Maksymovych *et al.* studied the out-of-plane piezoresponse of BiFeO<sub>3</sub> thin films grown on (La,Sr)MnO<sub>3</sub>/SrTiO<sub>3</sub> using PFM [131]. They developed a Landau-based model (see Chapter 2–Section 2.1.2) and expressed this piezoresponse as a function of the polarization magnitude in the thin film. They obtain a critical thickness of approximately 2 nm, in agreement with the qualitative experiments of Béa *et al.* [12]. In their work, the added value is a quantitative law for the decrease of polarization magnitude with thickness, which nicely fits the theoretical predictions (Figure 3.2) [131]. However, the tip contact with the ferroelectric surface is critical in PFM-based experiments: imperfect contact can significantly change the boundary conditions [106] and alter the polarization while measuring.

When the depolarizing field is too important, the system can reduce its energy by a transition from a monodomain state to a polydomains state formed by stripes with opposite polarization. This is the case for instance for PbTiO<sub>3</sub> grown on SrTiO<sub>3</sub>. Insulating SrTiO<sub>3</sub> cannot efficiently screen the depolarizing field and the PbTiO<sub>3</sub> thin film undergoes a monodomain to polydomain transition [125] contrary to PbTiO<sub>3</sub> films on conducting Nb:SrTiO<sub>3</sub> substrates [126]. In addition, Pertsev and Kohlstedt showed the importance of misfit strain for the critical thickness of the monodomain-polydomain stability for PbTiO<sub>3</sub> and BaTiO<sub>3</sub> [168].

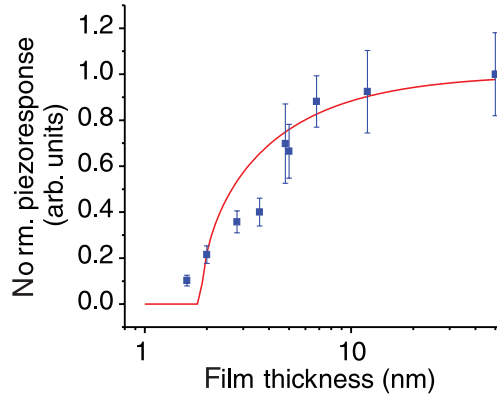


Figure 3.2: Evolution of the normalized piezoresponse with thickness for  $\text{BiFeO}_3$  thin films on  $(\text{La,Sr})\text{MnO}_3/\text{SrTiO}_3$ . Symbols are the experimental points measured by piezoresponse force microscopy. The plain line is numerically calculated from a Landau-based model. This figure is taken from Ref. [131].

### 3.1.2 Bismuth Ferrite

$\text{BiFeO}_3$  is a perovskite oxide showing ferroelectric and anti-ferromagnetic properties at room temperature. Two unit cells are shown in Figure 3.3.  $\text{BiFeO}_3$  is a multiferroic material since it has two ferroic order parameters [177]. More specifically in  $\text{BiFeO}_3$ , the ferroelectric and magnetic orders are coupled, a property named magnetoelectric coupling (see Figure 3.4 for definitions of order parameters coupling). The magnetoelectric coupling allows control of the ferroelectric order with a magnetic field and the magnetic order with an electric field. The latter is of great interest for the development in spintronics controlled by an electric field (easy control, low energy consumption). However, in the case of  $\text{BiFeO}_3$ , this coupling is too weak to be usable in realistic devices (CITE REF). Now, research on magnetoelectric coupling rather focuses on heterostructure combining ferroelectric and ferromagnetic layers [92, 143].

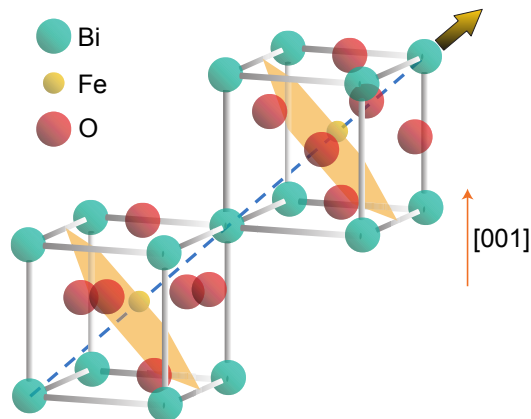


Figure 3.3:  $\text{BiFeO}_3$  perovskite structure. In this figure, the ferroelectric polarization lies along the  $[111]$  direction.

However,  $\text{BiFeO}_3$  is still intensively studied because of its intriguing properties: a band-gap in the visible range with potential applications in photovoltaics [242] and a

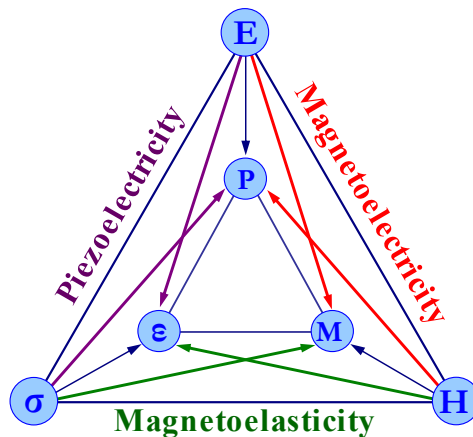


Figure 3.4: A definition of coupling between order parameters (Polarization  $P$  is controlled by the electric field  $E$ , magnetization  $M$  by the magnetic field  $H$  and strain  $\epsilon$  by the stress field  $\sigma$ ) related to ferroic orders (respectively (anti-)ferroelectricity, (anti-)ferromagnetism and (anti-)ferroelasticity).

complex interplay between its ferroic orders and the various degrees of freedom available. Indeed, below the Curie Temperature  $T_C = 1100$  K, bulk BiFeO<sub>3</sub> is described by the rhombohedral R3c space group [99]. It allows antiphase octahedral tilting (anti-ferrodistorsive order) and ionic displacements from the centrosymmetric positions. Both phenomena follow the same  $\langle 111 \rangle$  pseudocubic directions. In addition, below the Néel Temperature  $T_N = 640$  K, BiFeO<sub>3</sub> shows antiferromagnetic spin ordering with a cycloid-type spatial spin modulation [39]. BiFeO<sub>3</sub> can accommodate in-plane compressive strain via out-of-plane extension but also through oxygen octahedron rotation about  $\langle 111 \rangle$ , a degree of freedom not available in P4mm films such as BaTiO<sub>3</sub> or PbTiO<sub>3</sub>. This interplay between strain, tetragonality, and octahedra rotations leads to an unexpected decrease of  $T_C$  with strain, at odds with the variation of  $c/a$  ratio [99]. Several studies have shown that BiFeO<sub>3</sub> remains ferroelectric down to a few unit cells [12, 131] but the relationship between structural parameters and the remnant out-of-plane polarization in very thin films remains an open question.

### 3.1.3 Experimental Investigation of BiFeO<sub>3</sub> Ultrathin Films

To further understand the thickness dependence of ferroelectricity, we have studied the polarization of BiFeO<sub>3</sub> (BFO) films from 70 to 3.6 nm thick using a combination of x-ray diffraction (XRD), mirror electron microscopy (MEM) and photoelectron emission microscopy (PEEM). Using Piezoresponse Force Microscopy, we wrote upwards ( $P^+$ ) and downwards ( $P^-$ ) micron-sized domains in the BFO layer. The electron microscopy techniques provide full-field imaging of the surface electrostatic potential work function *difference* between oppositely-polarized domains. The tetragonality is measured by XRD. The results are interpreted in the light of a three-dimensional (3D) generalization of previously developed dead layer model for thin films within the framework of continuous medium

theory that predicts a fast decrease of the polarization when decreasing the thickness.

Bilayers of  $\text{BiFeO}_3/(\text{La,Sr})\text{Mn}_3$  (BFO/LSMO) were epitaxially grown on (001)-oriented  $\text{SrTiO}_3$  substrates by pulsed laser deposition using a frequency tripled ( $h\nu = 355$  nm) Nd-doped Yttrium Aluminium Garnet (Nd:YAG) laser with a 2.5 Hz repetition rate. We used the growth conditions and parameters developed by Béa *et al.* [9] to prevent the growth of parasitic phase (*i.e.*  $\text{Bi}_x\text{O}_y$  and  $\text{Fe}_x\text{O}_y$ ) in the BFO thin films. Therefore,  $\text{BiFeO}_3$  was grown at  $T_{\text{dep}} = 850$  K and  $P_{\text{dep}} = 10^{-2}$  mbar. The 20 nm thick LSMO layer serves as a metallic bottom electrode for PFM characterization and charge evacuation in photoemission experiments.

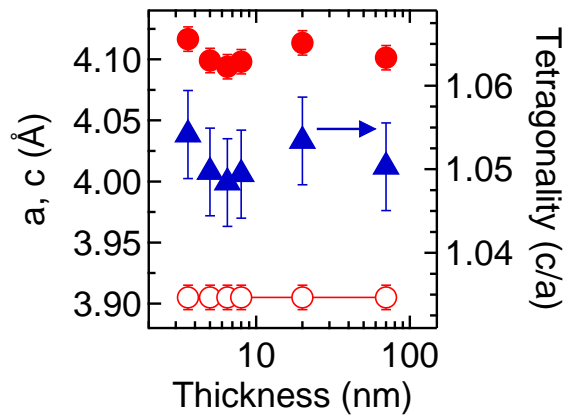


Figure 3.5: Evolution of pseudocubic lattice parameters  $a$  (blank red circles) and  $c$  (full red circles) and of the  $c/a$  ratio (blue triangles) with thickness.

XRD measurements on 70 nm to 3.6 nm-thick thin films were performed to track the out-of-plane parameter ( $c$ ), the in-plane parameter ( $a$ ) and the  $c/a$  ratio or tetragonality<sup>1</sup>. The results are shown in Figure. 3.5. The in-plane parameter is obtained assuming that the growth of the BFO and LSMO films is fully epitaxial, *i.e.*  $a_{\text{BFO}} = a_{\text{LSMO}} = a_{\text{STO}} = 3.905$  Å. This assumption is based on previous results which show that 70-nm and thinner thin films are fully strained on STO [10, 11]. The  $c/a$  ratio increases slightly from 1.050 for the 70 nm film to 1.053 for 7 nm, then remains constant down to 3.6 nm. This contrasts dramatically with the behavior of  $\text{PbTiO}_3$  reported in [126] where  $c/a$  decreases with thickness (Fig 3.1).

The chemistry of the films was studied by X-ray Photoelectron Spectroscopy (XPS)<sup>2</sup>. The XPS spectra show that the chemical environment was identical in the limit of photoemission spectroscopy detection. Indeed, Figures 3.6a and 3.6b shows core-level spectra

<sup>1</sup>XRD was carried out with a high-resolution X-ray diffraction (Panalytical X'pert Pro) using  $\text{Cu K}\alpha_1$  radiation with a resolution of  $0.01\text{Å}$

<sup>2</sup>X-ray PhotoEmission Spectroscopy (XPS) was carried out using a Kratos Ultra DLD with monochromatic  $\text{Al K}\alpha$  ( $h\nu = 1486.7$  eV). The analyzer pass energy of 20 eV gave an overall energy resolution (photons and spectrometer) of 0.35 eV. The sample is at floating potential and a charge compensation system was used. The binding energy scale was calibrated using a clean gold surface and the  $\text{Au } 4f_{7/2}$  line at 84.0 eV as a reference. A take-off angle of  $90^\circ$ , *i.e.* normal emission, was used for all spectra presented.

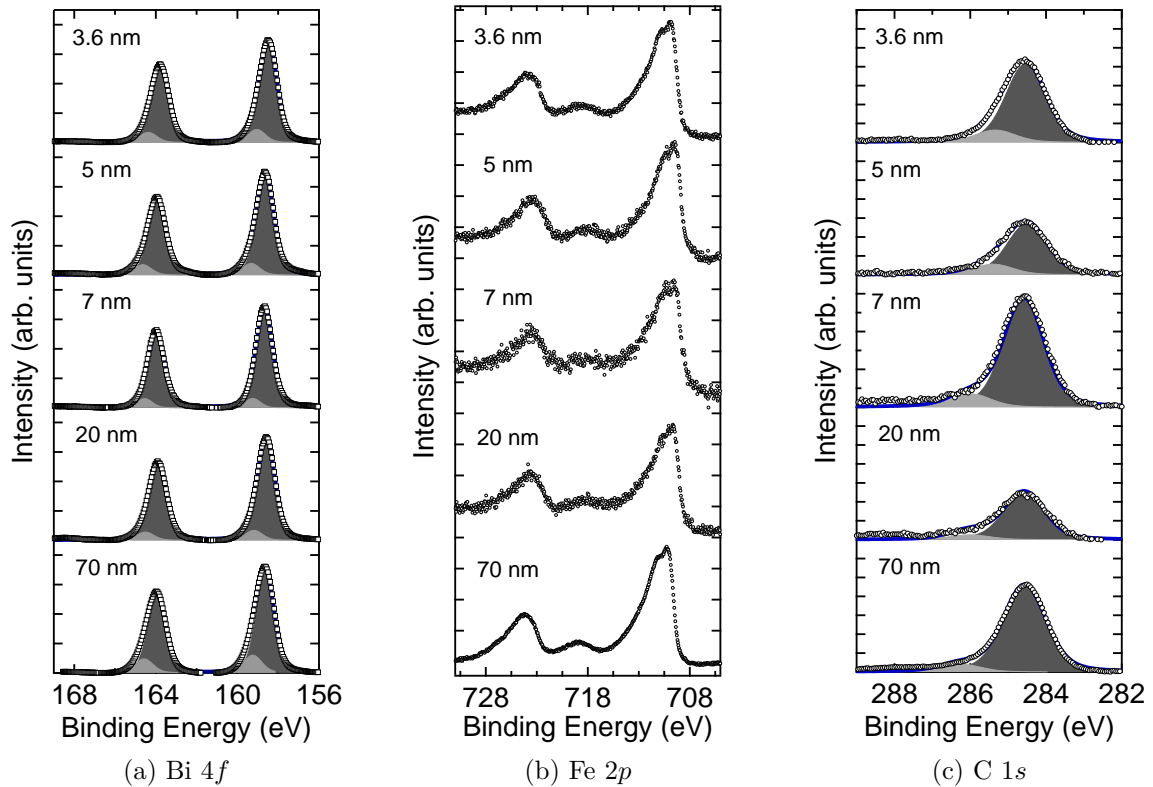


Figure 3.6: XPS spectra of BiFeO<sub>3</sub> thin films for every thickness taken at  $h\nu = 1486.7$  eV.

virtually identical for every thickness. Each spin-orbit core-level of Bi 4*f* has two components. The main component is attributed to bismuth in bulk environment. The second component is shifted by 0.6 eV to higher binding energy (HBE). A similar component has been observed on BFO single crystals and has been attributed to a several nanometer thick skin layer with altered ferroelectric properties [133]. In this experiment however, with decreasing thickness, we should observe an enhancement of the signal from the skin layer in comparison to the signal from the main component. In our case, the intensity ratio for the two components is identical for every thickness. Therefore, this component is not due to a skin layer, but rather to a different chemical or electrical environment for the topmost Bi-O layer, also observed for barium in BaTiO<sub>3</sub> [96, 233].

Thickness (nm)	$\frac{I_{C1s}}{\sigma_{C1s}} / \frac{I_{Bi4f}}{\sigma_{Bi4f}}$
3.6	2.22
5.0	1.49
7.0	3.30
20	1.40
70	2.20

Table 3.1: C 1*s* to Bi 4*f* area ratio calculated from XPS spectra of Figure 3.6.

Krug *et al.* pointed out the importance of adsorbates on LEEM and PEEM mea-

surements [119]. For a contaminated surface, they observed the disappearance of LEEM contrast due to a better screening of the surface charge provided by the carbonates. Table 3.1 shows the relative ratio of C 1s intensity and Bi 4f intensity taking into account the respective cross section. It shows that surface contamination is similar in 3.6 (no contrast) and 70 nm (high contrast) thin films. This clearly indicates that the systematic disappearance of ferroelectric contrast in LEEM/PEEM is not due to differential contamination. In addition, the 5 nm film has the lowest carbonates concentration but still shows a weak contrast in LEEM/PEEM experiments.

For the 70 nm BFO film, the film is thick enough so that the ferroelectric properties can be investigated using standard polarization versus electric field  $P(E)$  loops as shown in Figure 3.7a. The piezo-response hysteresis loops are shown in Figure 3.7b. They are position independent and exhibit similar coercive values as non local  $P-E$  loops, attesting to sample homogeneity. For thinner film however the measure was made impossible by the large leakage currents.

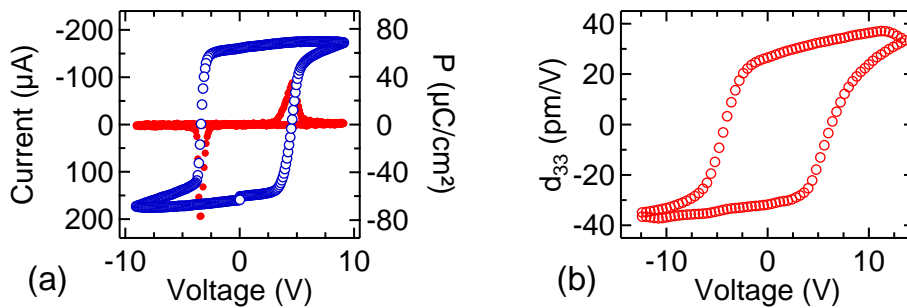


Figure 3.7: (a) Polarization-voltage and current-voltage hysteresis loop of BFO(70 nm)/LSMO(20 nm)//STO(001), (b) Piezoresponse hysteresis loop (local measurement under the PFM tip).

In a (001) BFO film,  $P^+$  and  $P^-$  states are the projections of  $\langle 111 \rangle$  polarization along [001] and [00-1], respectively. Poling of micron sized domains ( $20 \times 5 \mu\text{m}^2$ ) was performed by applying a d.c. voltage higher than the coercive voltage (inferred from the piezoresponse loops) on the tip while the bottom electrode was grounded. We applied an electric field at least twice as high as the coercive field. PFM imaging was carried out at an excitation frequency of 4-7 kHz and an a.c. voltage of 1 V. Figure 3.8 displays the Piezoresponse Force Microscopy (PFM) images for every thickness showing that the films have been successfully poled.

PFM writing can significantly modify the surface, namely inject charges during the poling process and/or alter surface topography. The former issue is a well-know artifact in PFM-based experiment which can lead to spatial variation of surface potential which is not due to the remnant polarization [223]. In this experiment, we want to measure the remnant state of the BFO films after a given poling process, which is the key quantity for a better understanding of ferroelectricity in thin films. Therefore, all electronic microscopy experiments were done at least two days after domain writing to ensure that any injected

charge has vanished. Thus, we expect to avoid any tip-related screening by injected charges stuck in the first layers. Possible morphology changes have been checked by atomic force microscopy.

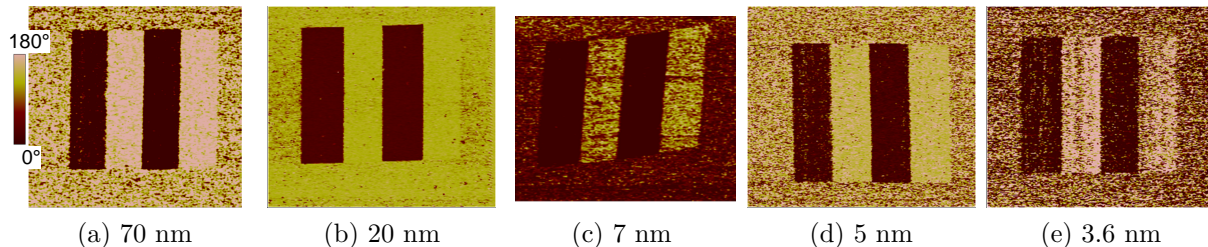


Figure 3.8: PFM phase images for every thickness after the writing process.

The electron kinetic energy of the MEM (reflected electrons)–LEEM (backscattered electrons) was measured with a low-energy electron microscope (LEEM, Elmitec GmbH) with a spatial resolution of 30 nm. The transition energy from the MEM to LEEM regime is a measure of electrostatic potential just above the sample surface [44] and depends on polarization and the screening of polarization-induced surface-charge [119]. The relationship between surface charge (or equivalently polarization) and MEM–LEEM transition energy will be developed later in this section. It allows a non-contact estimation of the out-of-plane polarization for tunneling films, otherwise inaccessible to standard electrical methods. A more detailed description of LEEM apparatus can be found in Appendix A.

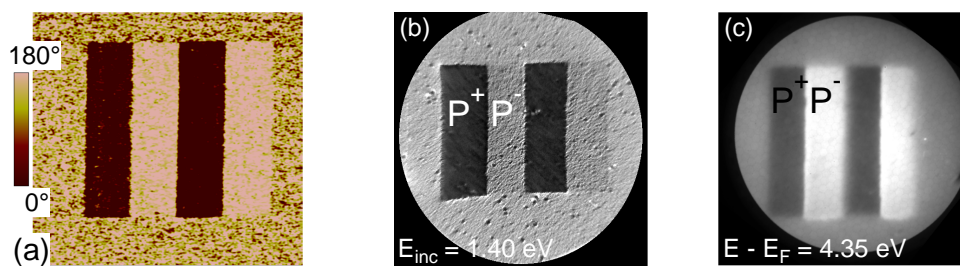


Figure 3.9: (a) PFM phase image of written P<sup>+</sup>/P<sup>-</sup> domains. Each domain is 20 × 5 μm<sup>2</sup>, (b) LEEM raw image for E<sub>inc</sub> = 1.40 eV, (c) PEEM raw image at E - E<sub>F</sub> = 4.35 eV (the three images have been acquired on the 70 nm BFO film).

Figure 3.9b shows a typical LEEM image with a field of view (FoV) of 33 μm for incident electron energy (E<sub>inc</sub>) of 1.40 eV. The observed contrast reproduces well the PFM image of Figure 3.9a. A full image series<sup>3</sup> across the MEM–LEEM transition (E) was acquired by varying E<sub>inc</sub> from -2.0 to 3.0 eV. Figure 3.10a displays the electron reflectivity curves showing the MEM (high reflectivity) to LEEM (low reflectivity) transition for the P<sup>+</sup> (brown upwards triangles, E = 0.75 eV) and P<sup>-</sup> (green downwards triangles, E

<sup>3</sup>The full serie is available as a video here: [https://dl.dropboxusercontent.com/u/20744866/shared\\_data\\_thesis/chapter\\_3\\_BFO\\_70nm\\_LEEM.avi](https://dl.dropboxusercontent.com/u/20744866/shared_data_thesis/chapter_3_BFO_70nm_LEEM.avi)

= 1.20 eV) domains. Using complementary error function fits we obtain MEM-LEEM transition maps showing clear contrast in the electrostatic potential above the surface between the  $P^+$ ,  $P^-$  and unwritten regions (Figure 3.10b). The full set of MEM-LEEM transition maps is shown in Figure 3.13.

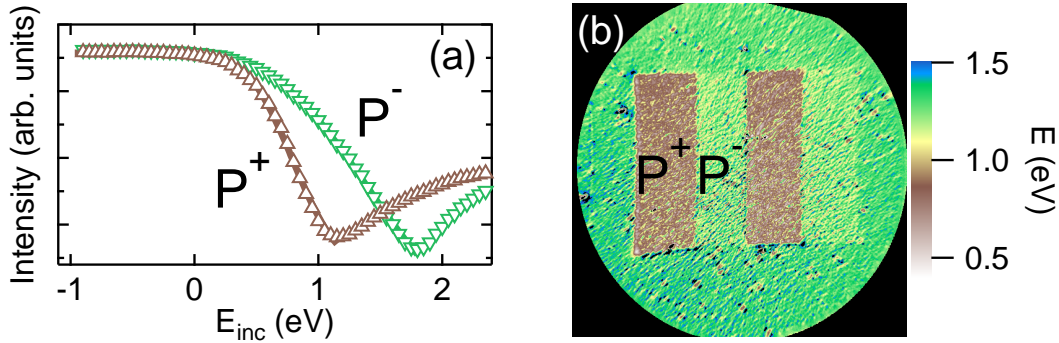


Figure 3.10: (a) Reflectivity spectra extracted from the  $P^+$  and  $P^-$  domains, (b) MEM-LEEM transition map obtained from the image series (70 nm thin film).

The energy filtered PEEM experiments used a NanoESCA X-PEEM (Omicron Nanotechnology GmbH). PEEM of the photoemission threshold gives a direct, accurate ( $\pm 20$  meV) and nondestructive map of the work function [135] that may depend, for example, on domain polarization, see Ref. [17]. Image series<sup>4</sup> were acquired over the photoemission threshold region with a mercury lamp excitation ( $h\nu = 4.9$  eV). The lateral resolution was estimated to be 200 nm and energy resolution 200 meV. A more detailed description of the PEEM apparatus and the analysis of PEEM data can be found in Appendix A. Figure 3.9c shows a typical PEEM image of the prepoled  $P^+$  and  $P^-$  regions for the 70 nm BFO film. The energy contrast between oppositely polarized domains fits the PFM image except at the domain boundary where the lateral electric field induced by a  $P^+/P^-$  domain wall deflects electrons [155]. We extract the threshold from the pixel-by-pixel spectra using an error function to model the rising edge of the photoemission (Figure 3.11a). A map of the work function in the  $P^+$ ,  $P^-$  and as-grown regions is shown in Figure 3.11b and the full set of workfunction maps is shown in Figure 3.12.

The difference in the MEM-LEEM transition of the  $P^+$  and  $P^-$  regions,  $\Delta E$ , varies from 450 meV for the 70 nm film to 25 meV for the 3.6 nm film and is plotted in Figure 3.14a (black circles, right axis). The mean work function difference measured in PEEM between  $P^+$  and  $P^-$  domains,  $\Delta\Phi_F = \Phi_F(P^+) - \Phi_F(P^-)$ , is plotted as a function of thickness in Figure 3.14a (left axis). While  $\Delta\Phi_F$  is 300 meV between 70 nm and 7 nm, between 7 and 5 nm it drops to 20 meV.

We used the following model to relate quantitatively the contrast in surface potential, work-function and the polarization magnitude in the thin films. The polarization charges

<sup>4</sup>The full serie is available as a video here: [https://dl.dropboxusercontent.com/u/20744866/shared\\_data\\_thesis/chapter\\_3\\_BFO\\_70nm\\_HgPEEM.avi](https://dl.dropboxusercontent.com/u/20744866/shared_data_thesis/chapter_3_BFO_70nm_HgPEEM.avi)

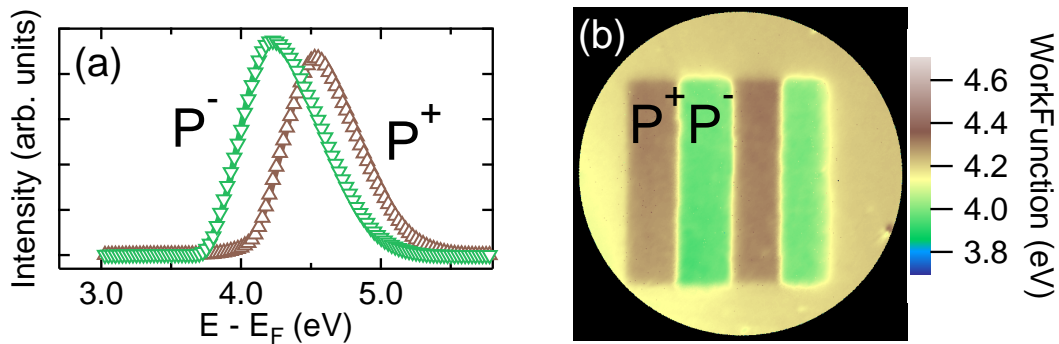


Figure 3.11: (a) Threshold spectra extracted from  $P^+$  and  $P^-$  domains (b) Work function map obtained from the threshold image series (70 nm thin film).

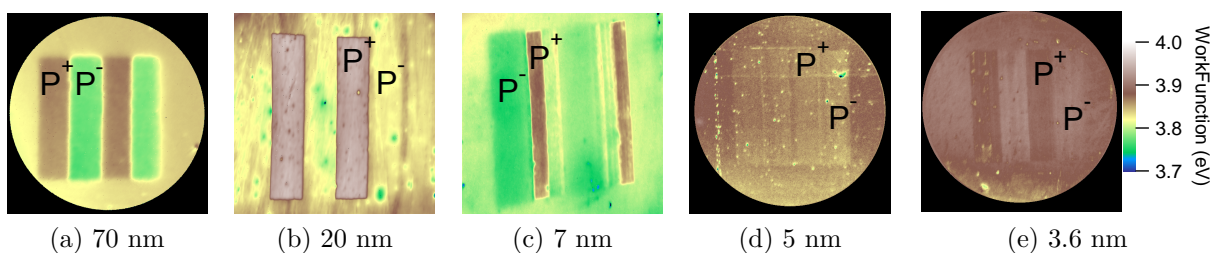


Figure 3.12: Work function maps for every thickness. A drop in workfunction contrast occurs between 7 and 5 nm.

at the BFO surface are screened over a given screening length (or equivalently dead layer thickness) leading to an inward ( $P^+$ ) or outward ( $P^-$ ) surface dipole. As shown by Figure 3.15, in LEEM, the incident electron see a positive potential step of  $\Delta V^+$  for the  $P^+$  state in comparison to  $P^-$ . It is then easier to penetrate the  $P^+$  surface than the  $P^-$ : the MEM-LEEM transition is lower for  $P^+$ . By measuring the work function (or surface potential) *difference* between two opposite domains, our method allows a direct measurement of the polarization-induced dipoles since any averaged non ferroelectric contribution is canceled. The surface dipole difference is proportional to the difference in polarization charges when going from the  $P^+$  to the  $P^-$  domains:

$$\Delta\Phi_F, \Delta E \propto \frac{e}{\epsilon_0} (P^+ \cdot d^+ - P^- \cdot d^-) \approx 2 \frac{e}{\epsilon_0} P_r \cdot d \quad (3.1)$$

where  $P^+$  ( $P^-$ ) and  $d^+$  ( $d^-$ ) are the polarization and the dead layer thickness, respectively, for the upward (downward domains);  $P_r$  is the average magnitude of the polarization in the two poled domains and  $d$  is the average dead layer thickness. A consequence of this model is that electron microscopy experiments can only probe the projection of the polarization vector along the  $\langle 001 \rangle$  directions (normal to the surface). The notations are shown on Figure 3.15. For the sake of generality, one can take into account electronic screening via a high-frequency dielectric permittivity, but it would still leave a linear relation between polarization and  $\Delta\Phi_F$ ,  $\Delta E$ .

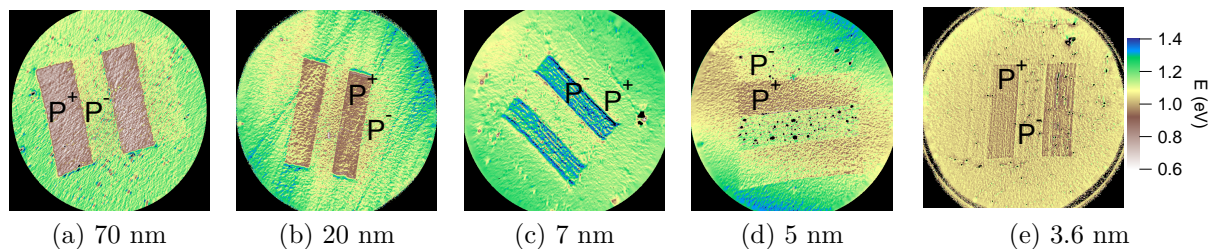


Figure 3.13: MEM-LEEM transition (E) maps for every thickness. A drop in MEM-LEEM transition contrast occurs between 7 and 5 nm.

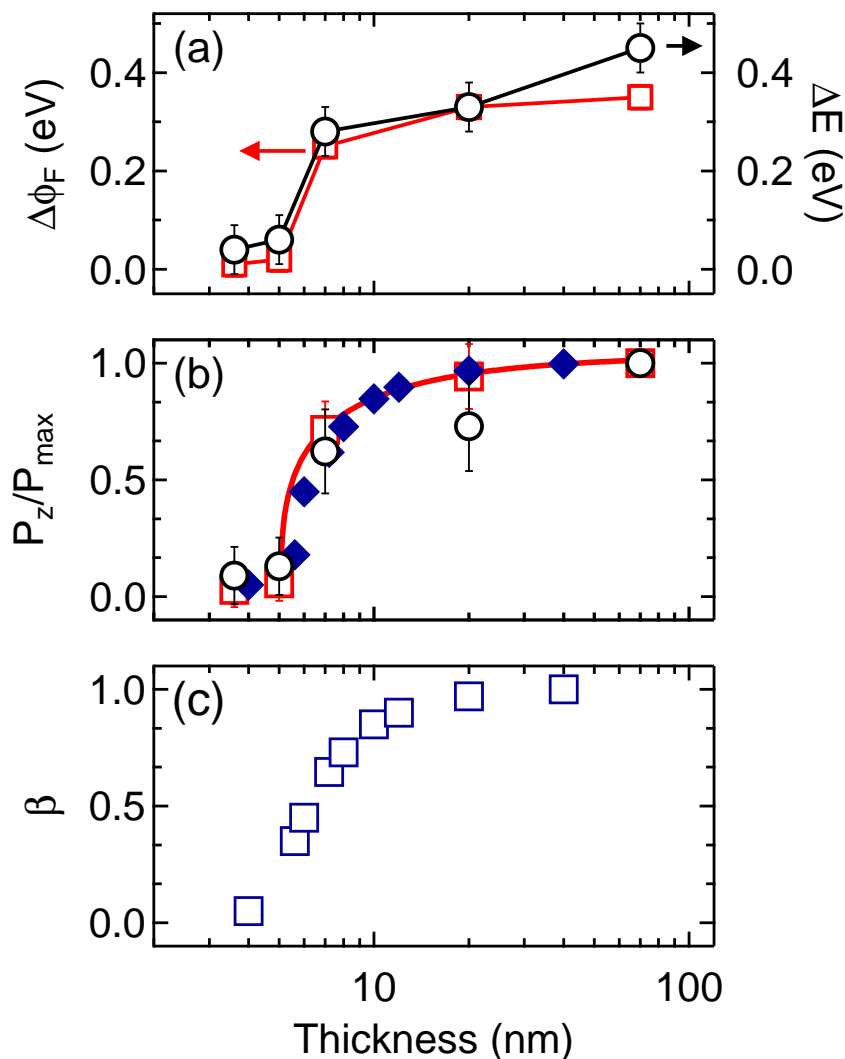


Figure 3.14: Thickness dependence of (a)  $\Delta\Phi_F$  (red squares) and  $\Delta E$  (black circles), (b)  $P_z/P_{\max}$  calculated from PEEM (red squares) and MEM-LEEM (black circles). Red curve is fit to PEEM/LEEM data with  $h_{\text{eff}} = 5.6$  nm. Blue diamonds are  $P_z/P_{\max}$  values used for numerical simulations, (c) screening coefficient  $\beta$  calculated from experimental  $P_z/P_{\max}$  values.

$P_z/P_{\max}$ , where  $P_z$  is the measured out-of-plane polarization and  $P_{\max}$  the value for the 70 nm film, is plotted as a function of film thickness in Figure 3.14b. By comparison with Figure 3.5, the drop of average polarization between 7 and 5 nm does not result from

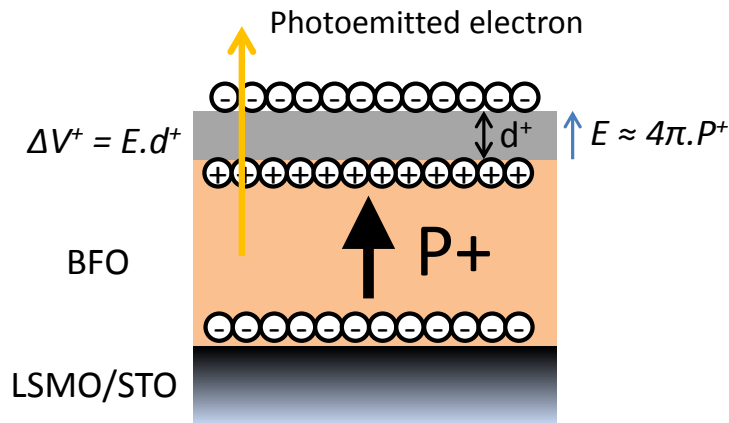


Figure 3.15: Schematic modeling of the consequence of polarization on electrons for the particular case of  $P^+$  polarization. The imperfect screening over a distance  $d^+$  induces an electric field which slows down the photoemitted electron and leads to a higher work function. The screening layer can also be modeled as an inward dipole. In LEEM, the incident electron sees a positive potential step of  $\Delta V^+$  for the  $P^+$  state in comparison to  $P^-$ . It is then easier to penetrate the  $P^+$  surface than the  $P^-$ : the MEM-LEEM transition is lower for  $P^+$ .

a decrease in the  $c/a$  ratio, contrary to PTO thin films [126]. Here the  $c/a$  ratio increases for thinner films and is constant at 1.054 below 5 nm. If there were no polarization then it should be about 1.03 as demonstrated by first-principles-based calculations presented further in this section. However, PTO is almost fully relaxed whereas BFO is compressively strained. Secondly, in BFO, the polarization deviates appreciably from the [001] direction and is the macroscopic average of four  $\langle 111 \rangle$  type distortions. To understand better this apparent contradiction, a theoretical input taking into account electric and stress boundary conditions is necessary.

### 3.1.4 Theoretical Resolution of the Experimental Paradox

Firstly, we have generalized the 1D dead layer Landau-based model of Bratkovsky and Levanyuk [31] to the 3D polarization case. The full development is given in Appendix D. It gives the following relation for thickness dependence of polarization:

$$\frac{P_z}{P_{max}} = A \sqrt{B + \sqrt{1 - \frac{h_{eff}}{h}}} \quad (3.2)$$

where  $h_{eff}$  is the effective thickness below which the macroscopic  $P_z$  goes to zero, and  $A$ ,  $B$  are fitting parameters. Equation (3.2) has the same analytical form than the formula provided by Maksymovych *et al* [131]. However, the physical meaning of the parameters entering Equation (3.2) is different from those given in Ref. [131], because in our case the polarization has three non-zero Cartesian components (rather than a single one). A good fit to the experimental data is obtained with  $h_{eff} = 5.6$  nm (see Figure 3.14b, red curve). This has to be compared with the critical thickness of 2.4 nm obtained for PTO.

Likewise, results from Ref. [131] strongly indicate the persistence of ferroelectricity in BFO films below 5.6 nm. Furthermore, this model cannot explain the apparent contradiction between our data obtained using electronic microscopy and the constant tetragonal ratio.

To understand why the measured polarization suddenly drops in these BFO films, while the axial ratio is still very large, we have conducted first-principles-based, effective Hamiltonian calculations (see Chapter 2–Section 2.1.2 and Ref. [4, 114, 175]) that take into account free surfaces [175]. We used the lattice parameter of the STO substrate for the pseudo-cubic in-plane lattice constant of BFO, leading to a misfit strain of -1.8%, in agreement with the experimental value. The calculation take into account the local electric dipoles, the strain tensor and the tilting of the oxygen octahedra. The electrical boundary conditions are governed by a coefficient denoted as  $\beta$  described in Ref. [174]. Practically,  $\beta$  can vary between 0 (ideal open-circuit, maximal depolarizing field) and  $\beta = 1$  (ideal short-circuit, fully screened depolarizing field). To determine  $\beta$  for each of our films we first extract the  $P_z/P_{\max}$  values from a B-spline interpolation of the experimental data (Figure 3.14b, blue diamonds). Then, we vary  $\beta$  in the calculations until the predicted  $P_z/P_{\max}$  perfectly agrees with the experimentally extracted one. Figure 3.14c shows the resulting  $\beta$  values.  $\beta$  decreases with thickness, indicating that the observed decrease of polarization is related to imperfect screening of the depolarizing field. The vanishing of the overall z-component of the polarization (which occurs experimentally for thicknesses lower than 5.6 nm, see Figure 3.14b) is associated with values of  $\beta$  lower than 0.4 (see Figure 3.14c).

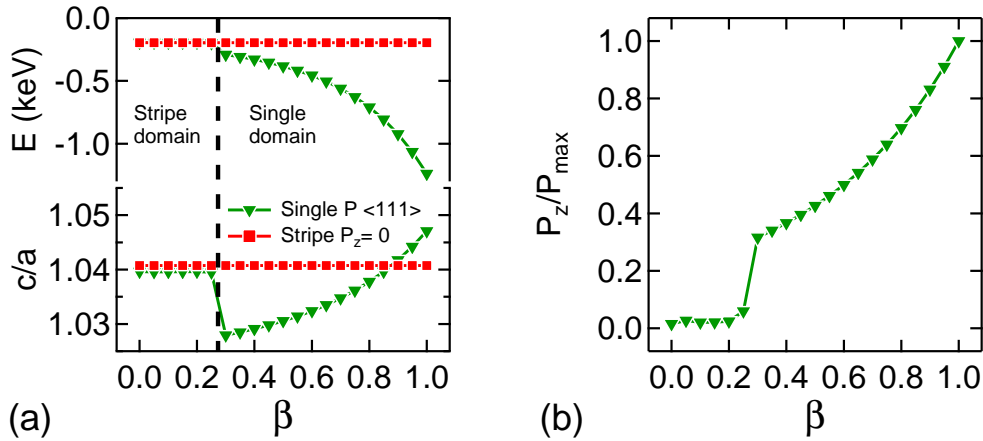


Figure 3.16: (a) (top panel) Slab energy with  $\beta$  showing a transition from single domain (out-of-plane polarization, green triangles) to stripe domains (no total out-of-plane polarization, red squares) below  $\beta_{crit} = 0.30$ , (bottom panel) theoretical  $c/a$  ratio with  $\beta$  for the two phases, (b) Evolution of  $P_z/P_{\max}$  with  $\beta$ . All data are for a  $20 \times 20 \times 20$  slab, *i.e.* a film with a thickness of 8 nm.

To understand what happens for these  $\beta$  values, we performed additional first-principles-based effective Hamiltonian calculations on a single  $20 \times 20 \times 20$  supercell (*i.e.* with a thickness of 8 nm) allowing  $\beta$  to vary. This supercell was chosen because around

8 nm the polarization is very sensitive to the thickness (Figure 3.14b). The results are shown in Figure 3.16. At a critical value of  $\beta$  of  $0.275 \pm 0.025$  the BFO supercell goes from a phase with a uniform out-of-plane polarization to a stripe domain phase with a vanishing overall out-of-plane polarization. Figure 3.16a displays the energy of these two phases as a function of  $\beta$ . The monodomain phase is energetically more favorable than the stripe nanodomains for  $\beta$  above 0.30 and less for smaller  $\beta$  values. The predicted evolution of the  $c/a$  ratio, and of the overall  $P_z/P_{\max}$ , with  $\beta$  for single and stripe domain phases are shown in Figures 3.16a and 3.16b, respectively. Interestingly, a continuous ferroelectric to paraelectric transition would lead to a large monotonic decrease of tetragonality (green triangles in Figure 3.16a), which we do not measure below  $h_{\text{eff}}$ . Rather, the transformation from ferroelectric monodomains to nanostripe domains leads to a (large)  $c/a$  similar to the one associated with short-circuit-like conditions (*i.e.* for which  $\beta$  is close to 1). Such results are consistent with our experimental findings that  $c/a$  does not vary between 70 nm and 3.6 nm, and explains that such insensitivity to strain is likely due to the formation of nanostripe domains. The single to stripe domain transition explains the loss of contrast in electronic microscopy observed in LEEM and PEEM contrast between 7 and 5 nm, because these regions do not possess any overall z-component of the polarization. The stripes have a typical dimension of a few nanometers, which is below the lateral resolution of our experiments. However, the spatial resolution of LEEM can be as low as 2 nm when using state-of-the-art aberration-correcting lenses [221]. Therefore, we expect that experiments on similar thin films with such setups will reveal the nanostripes. Figure 3.17 illustrates the morphology of these domains and their lateral dimensions. However, stripe domains in BFO thin films close to the  $h_{\text{eff}}$  value have been observed by PFM [38]. For such thin films, one might also ask to what extent the screening at the LSMO/BFO interface affects the measured polarization. Transmission electron microscopy of the interface between LSMO and a 3.2 nm BFO film suggests that the first three BFO unit cells are screened by the interface charge [41]. This also fits nicely with our experimental observation of an abrupt decrease in polarization starting at 7 nm, 1.4 nm above the calculated  $h_{\text{eff}}$ .

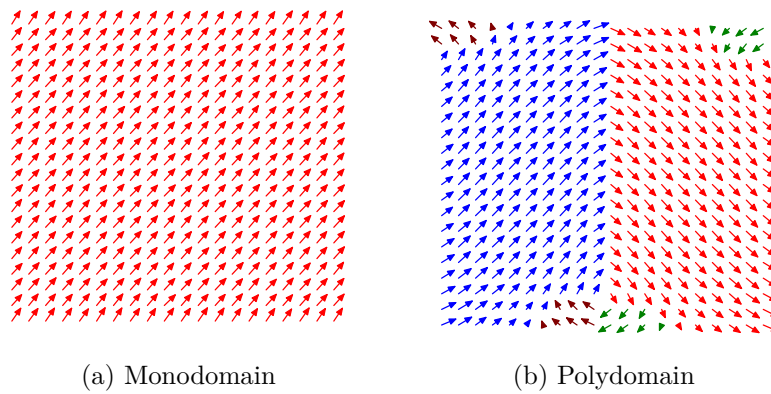


Figure 3.17: Morphology of the two types of domain in BiFeO<sub>3</sub> thin films. (a) Monodomain configuration has a experimentally-measurable out-of-plane polarization, (b) stripe domain configuration has an overall zero out-of-plane polarization.

## 3.2 Internal Free Charges in $\text{BaTiO}_3$ Single Crystals

At the surface of a ferroelectric, domain ordering appears to minimize the free energy of the system. Polarization is in and out of plane and can combine  $\pm a$ ,  $\pm b$  or  $\pm c$ . The definition of the direction of polarization used in this section is given by Figure 3.18.

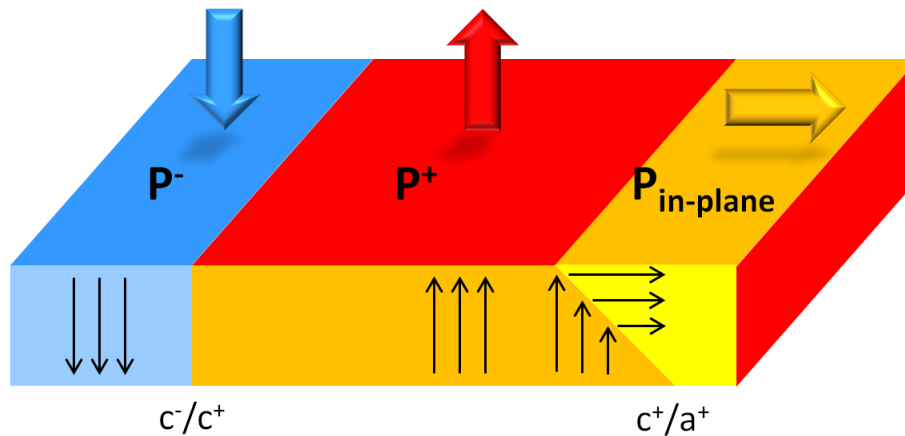


Figure 3.18: Definition of the direction of polarization used in this chapter. The observer (namely electron emission microscopes or other experimental apparatus) looks at the top free surface.

### 3.2.1 Oxygen Vacancies in Oxides

The role of oxygen vacancies, a common point defect in oxides, has been the subject of much research in material science. The lack of one oxygen ( $\text{O}^{2-}$ ) ion in the perovskite unit cell leads to the release of two electrons. As a function of vacancy concentration, the electronic and chemical properties of the sample can dramatically change. The resistive switching properties of  $\text{Ti}/\text{HfO}_2/\text{TiN}$  heterostructures have been explained by the migration of oxygen vacancies under an applied field [25]. Similarly, the 2-dimension electron gas (2DEG) at the interface of  $\text{LaAlO}_3/\text{SrTiO}_3$  (LAO/STO) or at the surface of  $\text{SrTiO}_3$  might be due to the formation of oxygen vacancies over few layers leading to a thin (hence quasi 2-dimensional) layer of free electrons released by the vacancies [161, 185]. Besides, the switching properties of conductivity at the LAO/STO interface over the application of an electric field is also explained by the migration of oxygen vacancies [16].

In the case of ferroelectric oxides, it has been shown that oxygen vacancies can promote one polarization direction over another in  $\text{PbTiO}_3$  ultra thin films [69]. The complex interplay between domains and vacancies leads to domain wall pinning [83], or domain wall conductivity [64, 132]. We will see in this section how oxygen vacancies can modify the ferroelectric properties of  $\text{BaTiO}_3$  monocrystals, by altering the internal screening mechanisms (Section 3.2.2) favoring a polarization direction over another (Section 3.2.4).

Experimentally, oxygen vacancies in oxides appear when a sample is annealed in a atmosphere with a very low concentration in oxygen. For instance, a careful control of

oxygen partial pressure, and even of the oxygen molecular state, is necessary for the proper growth of oxide thin films to limit the appearance of oxygen vacancies [157]. In single crystals, the control of oxygen vacancy concentration is done by annealing the sample in vacuum (reduction of titanium, increase of oxygen vacancies) or in an O<sub>2</sub>-rich environment (oxidation of titanium, decrease of oxygen vacancies).

Photoemission spectroscopy is an ideal tool for measuring the concentration of oxygen vacancies in ABO<sub>3</sub> surfaces where B is a transition metal. Indeed, the electrons released by the oxygen vacancies will occupy the empty *d*-states of the transition metal [36]. The reduction of the metal leads to a binding energy shift of the core-levels, and already can be qualitatively and quantitatively probed in photoemission spectroscopy. It has been done on buried interfaces [25, 151, 200] or on surfaces [147, 233]. It will be our method in the following.

### 3.2.2 Internal Screening as a Function of Oxygen Vacancies

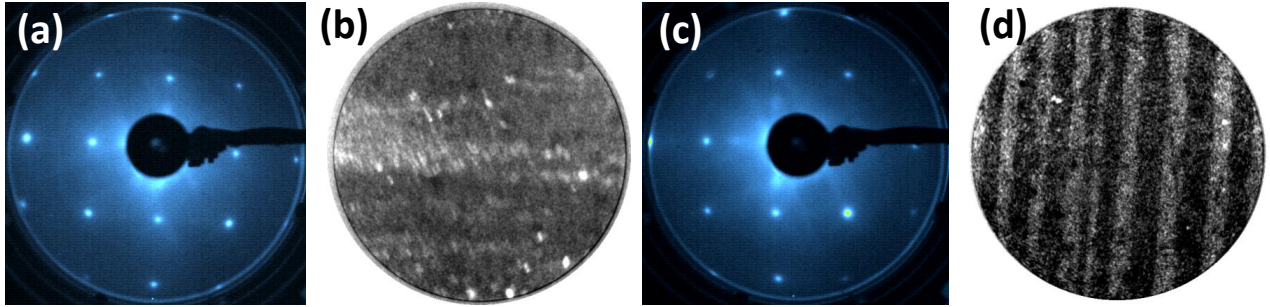
To investigate the role of oxygen vacancies on the ferroelectric polarization, a BaTiO<sub>3</sub> single crystal has been analyzed for three different oxygen vacancy concentrations. We used a single crystal of (001) BaTiO<sub>3</sub> from SurfaceNet GmbH. Experiments have been conducted on the NanoESCA beamline<sup>5</sup> at synchrotron ELETTRA in Italy. The beamline owns a NanoESCA PhotoElectron Emission Microscope from Omicron Nanotechnology, described in Appendix A.

The single crystal has been prepared by *ex-situ* ozone-cleaning to get rid of the surface carbonates contamination [68]. Afterwards, the sample has been exposed to a mild argon ion sputtering. From this starting point, the control of oxygen vacancies in the sample consist of three steps : a long annealing in vacuum (700 °C at 10<sup>-9</sup> mbar for three hours) henceforth noted step (1) to get to a relatively high vacancy concentration. Then two steps (noted steps (2) and (3)) of annealing under a O<sub>2</sub>-rich vacuum (700 °C at P<sub>O<sub>2</sub></sub> = 6.10<sup>-6</sup> mbar for one hour) are conducted to regain progressively the nominal stoichiometry of BaTiO<sub>3</sub>. After each step, the sample surface structure has been checked by Low-Energy Electron Diffraction (LEED). PhotoElectron Emission Microscopy (PEEM) images at threshold of photoemission has been taken with a Mercury lamp ( $h\nu = 4.9$  eV) to measure the intensity contrast due to ferroelectric domains. The sample chemical properties have been monitored by x-ray photoemission spectroscopy using the nanoESCA in the spectroscopic mode.

The LEED patterns (beam energy of 95 eV) and PEEM images (kinetic energy relative to Fermi level  $(E - E_F) = 4.30$  eV) obtained after step (1) and step (3) are shown in Figure 3.19. LEED patterns shown in Figure 3.19a and c demonstrate the excellent crystalline properties of the surface and show a 1 × 1 surface construction. PEEM images

<sup>5</sup><http://www.elettra.trieste.it/it/lightsources/elettra/elettra-beamlines/nanoesca/nanoesca.html>

	Temperature (K)	Pressure (mbar)	Duration (minutes)
step (1)	975	$P_{vac} = 1.10^{-9}$	180
step (2)	965	$P_{O_2} = 6.10^{-6}$	60
step (3)	965	$P_{O_2} = 6.10^{-6}$	60

Table 3.2: Summary of the annealing steps done on the  $\text{BaTiO}_3$  single crystal.Figure 3.19: LEED images (at 95 eV) (a) and PEEM image (at  $E - E_F = 4.30$  eV) (b) after step (1) and step (3) (c, d).

at a kinetic energy of 4.30 eV, *i.e.* at the threshold of photoemission, are sensitive to domain polarization as demonstrated in the previous section on  $\text{BiFeO}_3$ . Thus, contrast in intensity are due to different work functions from areas of different polarization. After step (1), there is no domain pattern, the intensity contrast is only due to defects on the surface as shown by Figure 3.19b. It is still the case after step (2) (not shown here). However, after step (3), a polarization-induced pattern is clearly visible on Figure 3.19d. To understand this evolution, we have to look at the chemical properties of the sample as a function of the annealing step.

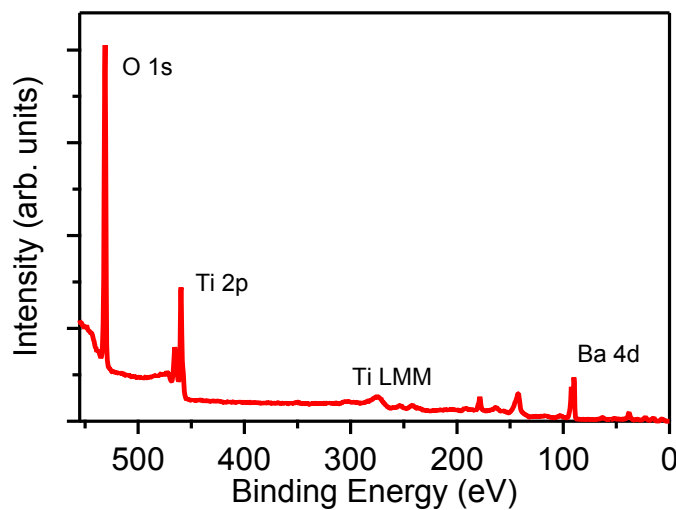


Figure 3.20: XPS survey spectrum at 650 eV photon energy after the first annealing step. There is no signal at the binding energy of C 1s core-level.

The XPS survey scan of Figure 3.20 does not show any signal at the expected location

of the C 1s core-level. This spectrum was taken after step (1). We can conclude that there is only a very weak contribution from extrinsic adsorbate screening in this experiment which cannot account for the contrast differences in the PEEM images after steps (1) and (3).

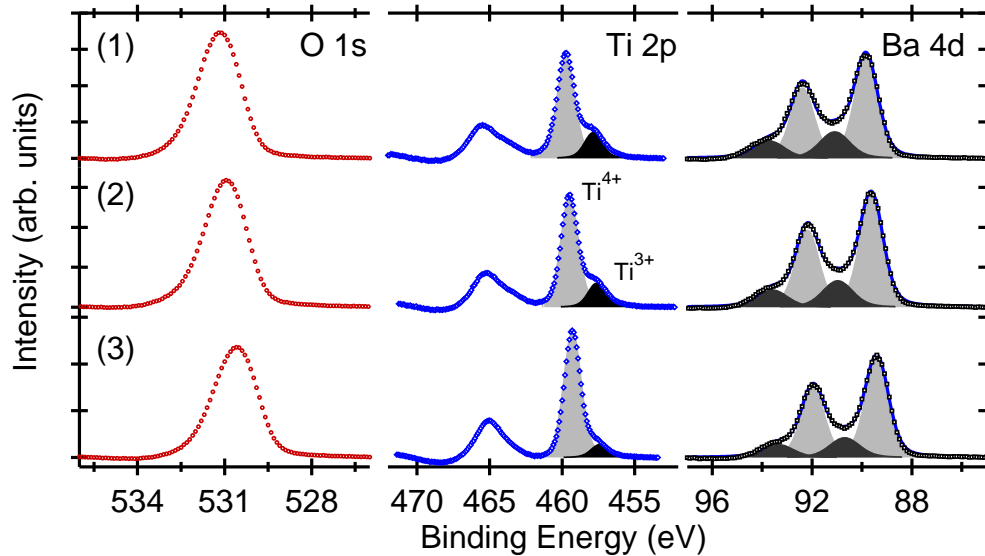


Figure 3.21: XPS spectra at 650 eV photon energy after each annealing step. Steps are described in Table 3.2

Figure 3.21 displays the photoemission spectra for each annealing step taken with a photon energy of 650 eV. The secondary electron background has been removed using a Shirley background [199]. Ba 4d and Ti 2p spectra are fitted with Voigt functions. The FWHM of Ba 4d components are 1.40 eV (Ba 4d high-binding energy) and 1.10 eV (Ba 4d low-binding energy). That of Ti 2p<sub>3/2</sub> components are 1.40 eV. The energy and spatial resolution of the PEEM were 200 meV and 200 nm respectively.

First of all, there is no high-binding energy (HBE) shoulder located at a BE of  $\approx 533$  eV in the O 1s spectra which is typical of signal from carbonates species [207]).

The barium 4d core-level shows two components for each spin-orbit peak. The low-binding energy (LBE, light grey in Figure 3.21) component is from the bulk-coordinated Ba. The HBE (dark grey in Figure 3.21) component can be attributed to undercoordinated Barium at the surface for BaO termination [96, 124]. For a TiO<sub>2</sub> terminated surface the topmost Ba atoms are in the first layer below the surface and are fully oxygen coordinated therefore we do not expect a surface peak due to undercoordinated Ba. The discontinuity creates a surface dipole giving rise to an effective core level shift for the first BaO layer (see Chapter 4). In the case of single crystal, we do not have a precise control of BaTiO<sub>3</sub> termination so we cannot conclude on the origin of this additional peak. It is unlikely that the HBE component is due to contamination. Contaminated phases of BaTiO<sub>3</sub> (BaCO<sub>3</sub>) should produce a strong shoulder in the O 1s spectra at higher-binding energy which is not the case as previously mentioned [14].

The titanium  $2p$  core-level shows two components for each spin-orbit peak. Here, the attribution of each component is much less controversial. The low-binding energy component is commonly attributed to titanium in a reduced state (noted here as  $\text{Ti}^{3+}$ ). This reduced state is due to the electron released by oxygen vacancies. The high-binding energy component is attributed to  $\text{Ti}^{4+}$  from stoichiometric  $\text{BaTiO}_3$ . Table 3.3 shows the ratio of the signal coming from  $\text{Ti}^{3+}$  (reduced titanium due to oxygen vacancies) over signal from  $\text{Ti}^{4+}$  (bulk titanium in the  $\text{BaTiO}_3$  cell). As expected, the ratio progressively decreases with each oxidizing step. In addition to the measurement at 650 eV, additional spectra at 900 eV photon energy have been acquired. Then, the kinetic energy of the titanium  $2p$  core-levels increases from 190 eV to 490 eV. To estimate the relative probing depth for the two photon energy, the Inelastic Mean Free Path (IMFP) of photo-emitted electrons have to be evaluated. This can be done by the NIST IMFP software<sup>6</sup> which uses the formula of Tanuma *et al.* [217]. The IMFP of Ti  $2p$  electrons is of 0.83 nm (1.50 nm) for 650 eV (900 eV) photon energy. Therefore, the surface signal is greatly enhanced relatively to bulk signal for 650 eV in comparison to 900 eV. The  $\text{Ti}^{3+}/\text{Ti}^{4+}$  ratio for this photon energy is also reported in Table 3.3. Firstly, the ratio is higher for 650 eV than for 900 eV after step (1) showing that annealing in vacuum mostly generates oxygen vacancies near the surface. Secondly, the ratio is the same for the two photon energies after step (3): at this point, the very first layers and the deeper layers probably have the same concentration in oxygen vacancies. We reached some equilibrium and it is likely that further annealing in  $\text{O}_2$  in the same pressure and temperature conditions will not have much influence on vacancy concentration. To regain a pristine  $\text{BaTiO}_3$ , a long annealing in one bar of oxygen and at much higher temperature ( $\approx 1200$  K) might be necessary, as for the preparation of  $\text{SrTiO}_3$  surfaces [103].

Now, we define  $n$  the free electron concentration per unit cell (e/u.c.). Since a Ti atom of valence state 3+ hosts one free electron, we can estimate  $n$  using the ratio of  $\text{Ti}^{3+}$  over the signal coming from all titanium atoms  $I(\text{Ti}_{\text{total}}) = I(\text{Ti}^{3+}) + I(\text{Ti}^{4+})$ :

$$n = \frac{I(\text{Ti}^{3+})}{I(\text{Ti}_{\text{total}})} \quad (3.3)$$

Assuming that an oxygen vacancy releases two electrons [148], the concentration in oxygen vacancy  $x$  in  $\text{BaTiO}_{3(1-x)}$  is obtained with the following equation:

$$x = \frac{1}{3} \cdot \frac{1}{2} n \quad (3.4)$$

The free electron concentration  $n$  after each step are reported on Table 3.3.

Valence band spectra have been taken at a photon energy of 50 eV. This photon energy is chosen to enhance the signal from the valence band thanks to a higher cross section. In addition, at such photon energy, the IMFP is of 0.50 nm, therefore this measurement

---

<sup>6</sup><http://www.nist.gov/srd/nist71.cfm>

	step (1)	step (2)	step (3)
I(Ti <sup>3+</sup> ) / I(Ti <sup>4+</sup> ) ( $h\nu = 650$ eV)	0.25	0.22	0.10
$n$ (e/u.c.)	0.20	0.18	0.093
I(Ti <sup>3+</sup> ) / I(Ti <sup>4+</sup> ) ( $h\nu = 900$ eV)	0.18	0.17	0.10
$n$ (e/u.c.)	0.15	0.15	0.090
I(Gap states) / I(Background)	1.17	0.74	0.71
Intensity contrast (PEEM)	no contrast	no contrast	domain contrast

Table 3.3: Ti<sup>3+</sup>/Ti<sup>4+</sup> ratio for two photon energies and signal intensity from the gap states over the background signal in the valence band spectra, after each annealing step. The free electron concentration in electron per unit cell is also obtained by taking the ratio Ti<sup>3+</sup>/Ti<sub>total</sub>. The bottom line indicates whether we observe polarization-induced intensity contrast in threshold image using the PEEM.

is very surface sensitive. Figure 3.22 shows valence band spectrum for each annealing step. The signal near the Fermi level has been magnified ten times. The intensity of this signal is normalized by the value of the intensity at 9 eV binding energy, *i.e.* in the background of the valence band spectrum, and reported in Table 3.3. The signal in the gap decreases as the Ti<sup>3+</sup>/Ti<sup>4+</sup> ratio with oxidizing annealing. We can conclude that the in-gap electrons come from the oxygen vacancies and more specifically from 3*d* states of titanium in the valence band near the Fermi edge (n-type doping in the terminology of semiconductors) [148, 244]. However, the behavior is slightly different here: the ratio significantly decreases after the first oxidation, and stay rather constant after the second step. The signal from reduced titanium significantly decreases only after the second oxidation. It is likely that gap states are also due to another mechanism in addition to the filling of 3*d* orbitals of Ti. The identification of an additional mechanism is beyond the scope of our study. Interstitial Ti sites is a possible cause [239], but the topic is still strongly debated, for instance in the study of TiO<sub>2</sub> [238, 244]

To summarize, the loss of polarization-induced contrast in PEEM images at the threshold of photoemission occurs when the electron doping is higher than 0.093 e/u.c. (and below 0.18 e/u.c.) which corresponds to a vacancy concentration of 1.6% (3.2%). It seems that the vacancy concentration at the topmost layers has to be sufficiently high to make the contrast disappears. This is the case for the first two steps in this experiment. On the contrary, when the vacancy concentration decreases, we observe the reappearance of intensity contrasts.

Theoretical results showed that conductivity suppress the ferroelectric displacements in BaTiO<sub>3</sub> for an electron concentration above 0.11 electron per unit cell [235]. This is explained in terms of a very efficient screening of the polarization-induced charges by the electrons released by the oxygen vacancies. The very efficient screening of the

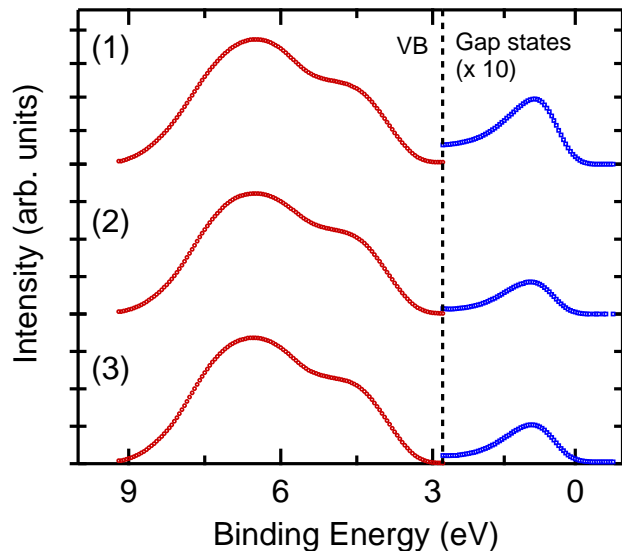


Figure 3.22: XPS spectra of the valence band at 50 eV photon energy after each annealing step. The signal from the gap of  $\text{BaTiO}_3$  has been magnified ten times.

surface charges translates in the loss of contrast in PEEM images. Indeed, as we saw in Section 3.1, the work function contrast between two oppositely-polarized domains is related to the polarization magnitude and to the dead-layer thickness via equation (3.5):

$$\Delta\Phi_F \propto \frac{e}{\epsilon_0} (P^+ \cdot d^+ - P^- \cdot d^-) \approx 2 \frac{e}{\epsilon_0} P_r \cdot d \quad (3.5)$$

Where  $P^{+,-}$  and  $d^{+,-}$  are the polarization and dead layer thickness for the upward, downward domains;  $P_r$  is the average magnitude of the polarization in the two poled domains and  $d$  is the average dead layer thickness as discussed in Section 3.1.

In Section 3.1, the loss of contrast was due to a loss in the averaged polarization magnitude due to a monodomain to polydomain transition in the BFO thin film. In this case, higher vacancy concentration induces more free carriers at the surface and diminish the screening length. In this PEEM experiment, this results in a loss of work function contrast as observed. The critical doping concentration inducing the transition from the absence of intensity contrast to the apparition of domain-induced contrast is above 0.093 electron per unit cell in our experiment. This value is compatible to previous theoretical results [235] which found a critical value of 0.11 electron per unit cell.

### 3.2.3 Internal Screening by Photo-induced Charges

In addition to evolution of the domain contrast as a function of oxygen vacancies described in the previous section, we observe a time-dependent loss of contrast when the sample is kept under ultraviolet (UV) illumination provided by the mercury lamp of the PEEM setup. Figure 3.23 shows a selection of PEEM images at constant energy ( $E - E_F$ ) = 3.90 eV as a function of time. The actual experiment was done by acquiring a movie

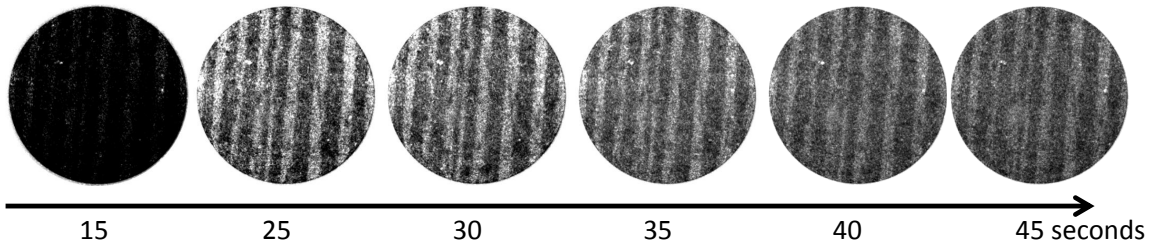


Figure 3.23: PEEM images at  $(E - E_F) = 3.90$  eV under mercury lamp illumination. The grayscale range is the same for every image to show the loss of contrast with time.

at one frame per second for ten minutes (600 images). The intensity contrast on the PEEM image is attributed to domains of opposite polarization. The time scale is set to zero when the mercury lamp is turned on. Firstly, we observe a rise in intensity due to the warm-up period of the lamp. After  $t = t_0 = 25$  seconds, we observe a progressive diminution of the intensity contrast. This phenomenon is reversible after turning off the mercury lamp for five minutes. Turning the lamp back on, we acquired another sequence and the intensity contrast follows the same time-dependence. Figure 3.24 shows the time-dependent intensity from the bright (red empty squares) and dark (black plain squares) domains. The blue circles shows the contrast intensity  $\Delta I = I_{\text{bright}} - I_{\text{dark}}$ . After  $t_0$ , we can fit the contrast evolution using a simple rate equation  $\Delta I = A + B \cdot \exp(-t/\tau)$ . The time constant  $\tau$  is 9.0 seconds in that case: after that the contrast stays weak and stable.

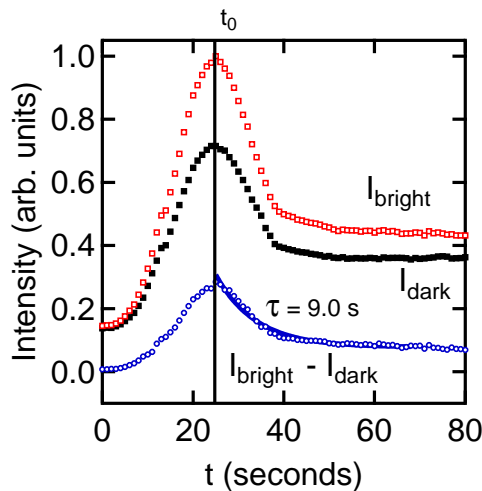


Figure 3.24: Evolution of the intensity of bright areas (red squares), dark areas (black plain squares) and the intensity difference (blue circles) as a function of time.

As in the previous section, the loss of contrast can only be due to the efficiency of the screening of the surface charges, since the polarization magnitude in  $\text{BaTiO}_3$  has no reason to change under UV illumination. This means UV illumination provides additional screening of the surface charges. This phenomenon has been previously observed and explained - by Shao *et al.* in Ref. [196] for instance<sup>7</sup> - by taking into account the photo generation

<sup>7</sup>The main reference in the field of photoferroelectrics is the book of V. M. Fridkin [70].

of electron–holes pairs. Under UV illumination, part of the photo-excited electrons are emitted in vacuum: this is what we measure in any photoemission experiment. However, a non-negligible quantity of photo-excited electrons never reach vacuum. Under the effect of the internal depolarizing field (see Chapter 2), photo-generated electrons and holes drift apart to screen the surface charges. For instance, for a  $P^+$  domain (polarization vector out of the plane, directed from the  $\text{BaTiO}_3$  to the vacuum) the internal field drives holes to the bulk and keep electrons near the surface. The electrons screen the fixed, positive surface charge due to polarization. Some photo-generated carriers are trapped in vacant states generating a space-charge field opposing the internal field due to polarization. After some illumination time, the two phenomena are balanced, but when the lamp is switched off, the trapped carriers recombine after thermal diffusion: the additional screening is lost. Shao finds a time-constant when turning on the lamp of 6.43 seconds, which is very close to our result. The dynamical evolution we observe can also be compared to the experiment of Wang *et al.* [234]. With LEEM and a  $\text{BaTiO}_3$  single crystal illuminated by a UV lamp, they followed the intensity contrast due to opposite domains as a function of time. They also observed the decrease energy with time and found a time-constant of 41.3 seconds for the time-dependent decrease of the intensity contrast. The discrepancies can be explained by the two main differences in the experiment:

- In our experiment, the photon source serves both for the measurement and for inducing photo-generated electron-hole pairs. Thus, we cannot get rid of the warm-up period of the mercury lamp and the steep rise in intensity due to warming of the lamp probably overlaps the decrease due to the additional screening process. This phenomenon can hide part of the time-dependent law for the contrast loss. In addition, we obviously cannot follow the evolution of intensity contrast when turning off the lamp. We can only observe that the surface comes back to its initial state after some minutes in the dark.
- In our experiment and in Shao’s experiment, the  $\text{BaTiO}_3$  has a very low concentration in oxygen vacancies contrary to Wang’s experiment. We estimate our concentration after step (3) at 1.6% while Wang measured a concentration of 3%. Oxygen vacancies can act as traps for charges and slow down the charge drift: this might explain the significant longer time constant in Wang’s experiment.

The time constant extracted confirms the competition between oxygen vacancies and photo-generated charges in the screening of polarization-induced surface charges. Shao used a pristine  $\text{BaTiO}_3$  ( $\tau_{\text{Shao}} = 6.43$  seconds), we used a re-oxidized  $\text{BaTiO}_3$  ( $\tau_{\text{Rault}} \approx 9.0$  seconds) and Wang used a vacuum annealed  $\text{BaTiO}_3$  ( $\tau_{\text{Wang}} = 41.3$  seconds) highlighting that the more vacancies a surface has, the longer the photo-induced screening process will take.

### 3.2.4 Polarization-dependent Chemistry of Ferroelectric Domains

In this section, a BaTiO<sub>3</sub> single crystal has been annealed in vacuum in reducing conditions. We quantify the relative proportions of  $P^+$ ,  $P^-$  and  $P_{\text{in-plane}}$  domains using MEM-LEEM transition maps of the surface before and after a ferroelectric to paraelectric to ferroelectric heating cycle. After the cycle, the relative area of  $P^-$  domains is higher than the others. DFT calculations explain this phenomenon in terms of a preferential screening provided by oxygen vacancies favoring  $P^-$  domains over  $P^+$  and  $P_{\text{in-plane}}$ .

We used a single crystal of (001) BaTiO<sub>3</sub> from SurfaceNet GmbH. Experiments have been conducted on the Low-Energy Electron Microscope of CEA-Saclay/IRAMIS/SPCSI<sup>8</sup>. This instrument is described in Appendix A.

The single crystal has been prepared by *ex-situ* annealing in O<sub>2</sub> at 4.5 mbar at 1150 K to obtain a clean surface reconstruction followed by ozone-cleaning, just before introduction in the ultra-high vacuum chamber, to get rid of the surface carbonate contamination [68]. *In-situ* annealing to create oxygen vacancies has been conducted at 975 K at a pressure of  $5.10^{-10}$  mbar.

We checked the absence of carbon contamination by Auger electron spectroscopy (AES) and surface crystallographic properties by LEED using the LEEM steup. The LEED patterns of Figures 3.25a-3.25b show a  $c(2\times 2)$  surface reconstruction associated with a TiO<sub>2</sub> termination as expected after the *ex-situ* annealing in oxygen [110] and contrary to the single crystal of the previous section which was  $(1\times 1)$ . Figure 3.25c shows the differential AES spectrum with no signal at the kinetic energy of the Auger peak of carbon (275 eV) attesting the cleanness of the surface.

Following the same procedure as in Section 3.1.3 on BiFeO<sub>3</sub> thin films, a full image series across the MEM-LEEM transition (E) was acquired by varying  $E_{\text{inc}}$  from -1.0 to 1.0 eV. Figure 3.26a shows a typical MEM image at  $E_{\text{inc}} = 0.05$  V for a field of view (FoV) of 71  $\mu\text{m}$ . The intensity contrast we observe is due to ferroelectric domains of different polarization direction. Figure 3.26b displays the electron reflectivity curves showing the MEM (high reflectivity) to LEEM (low reflectivity) transition for the three domains.

Then, we slowly heated the sample up to 520 K, well above the Curie temperature of BaTiO<sub>3</sub> ( $\approx 400$  K) so that the sample is paraelectric - and then cooled back to room temperature. Another image series across MEM-LEEM transition was acquired after the ferroelectric - paraelectric - ferroelectric (FE-PE-FE) cycle. Using complementary error function fits we obtain MEM-LEEM transition maps before and after the heating cycle. They both show clear contrast in the electrostatic potential above the surface between the  $P^+$ ,  $P^-$  and  $P_{\text{in-plane}}$  (Figures 3.27a-3.27c). However, the distribution of domains have

<sup>8</sup><http://iramis.cea.fr/spcsi/>

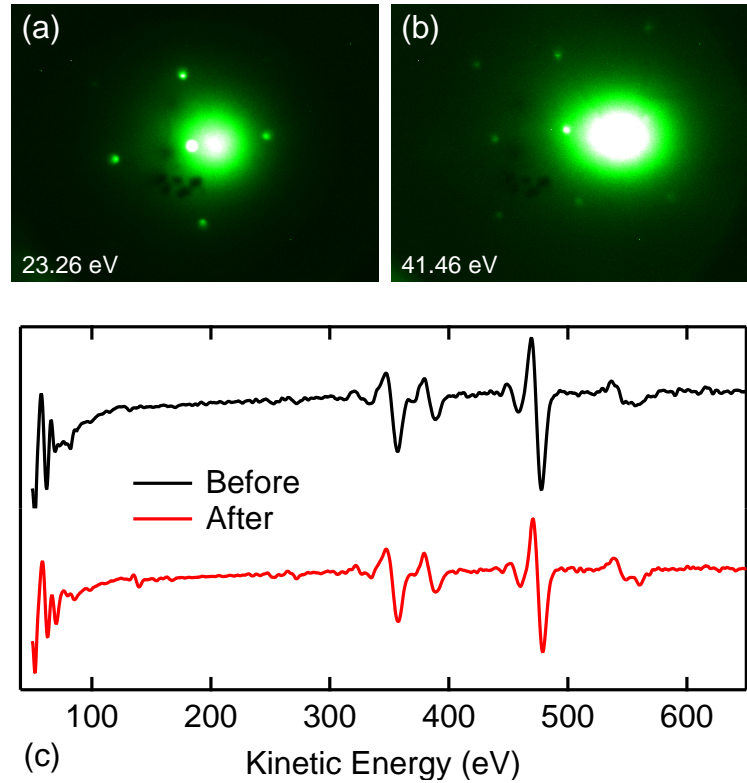


Figure 3.25: LEED patterns at 21.36 eV (a) and 41.46 eV (b) showing a  $c(2 \times 2)$  for the surface of the  $\text{BaTiO}_3$  single crystal. (c) Auger electron spectra before and after the FE-PE-FE cycle showing no carbon contamination at 275 eV.

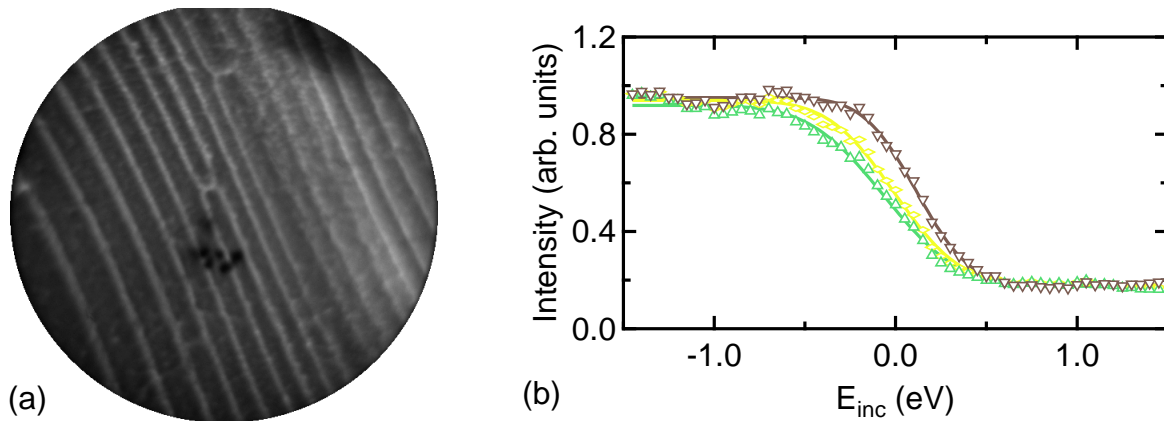


Figure 3.26: (a) Typical MEM images at  $E_{\text{inc}} = 0.05$  V showing three polarization-induced contrasts. (b) Reflectivity spectra extracted from the  $P^+$  (green upward triangles),  $P^-$  (brown downward triangles) and  $P_{\text{in-plane}}$  domains (yellow diamonds).

changed. This is confirmed by analyzing the statistical distribution of  $(E)$  on the maps. The histograms of  $(E)$  are shown in Figures 3.27b–3.27d before and after the heating cycle. They can be fitted using three Gaussian components of fixed width for each histogram. Each component matches a different domain orientation. Using the same arguments as for  $\text{BiFeO}_3$  thin films we can infer that the lowest MEM–LEEM transition  $(E)$  is due to

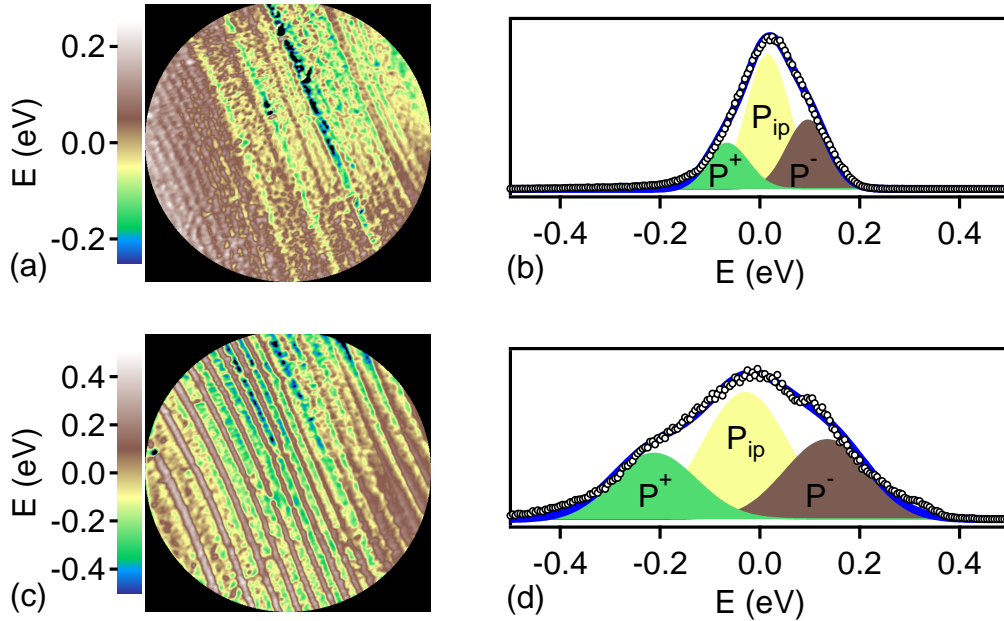


Figure 3.27: MEM-LEEM transition map obtained from the image series before (a) and after (c) the FE-PE-FE heating cycle. Histogram of the distribution in MEM-LEEM transitions ( $E$ ) before (b) and after (d).  $P_{ip}$  stands for  $P_{in-plane}$

$P^+$ , the highest to  $P^-$  and the half-way value is due to  $P^{in-plane}$  domains. We observe three features:

- After the FE-PE-FE cycle, the potential difference between  $P_{out-of-plane}$  domains and  $P_{in-plane}$  increases. This is likely due to the increase in domain width which can be seen in Figure 3.27c. This leads to a poorer domain - domain screening of the surface charges and therefore a higher difference in ( $E$ ).
- The proportion of  $P_{out-of-plane}$  domains over  $P_{in-plane}$  domains increases after the cycle. The minimization of elastic energy by favoring  $180^\circ$  domain walls might cause such change in proportion. Indeed,  $90^\circ$  domain walls induces a lattice mismatch which is energetically costly [173]. Another transition from PE to FE phase should lead to more  $180^\circ$  walls but has not been conducted on this experiment.
- Finally, both before and after heating, the  $P_-$  domains are more widespread than the  $P_+$ .

This last observation is the main point of this section. First, we checked that AES spectra and LEED patterns before and after the heating cycle are identical, excluding any extrinsic contribution to these observations. Second, the heating temperature (500 K) during the FE-PE-FE cycle is well below the temperature required for a significant creation of oxygen vacancies, even in ultra-high vacuum. Thus, the alteration of domain ordering is not due to a different concentration of oxygen vacancies, contrary to Section 3.2.2. To further understand these results, we conducted Density-Functional Theory calculations on

a  $\text{BaTiO}_3$  slab with one oxygen vacancy at one free surface [144]. I will not go into details of the calculations, since they have been mostly conducted and analyzed by G. Geneste. However, the main message is that the numerically-computed total energy of the system is always lower for  $P_-$  than for  $P_+$ . This theoretical result supports the experimental observation: during the cycle, the system can overcome initial constraints and minimize further its total energy: energy is reduced (1) by adopting more  $180^\circ$  domain walls and (2) by favoring  $P_-$  over  $P_+$ .

### 3.2.5 Band Structure of $\text{BaTiO}_3$ Single Crystals

Section 3.2.2, 3.2.3 and 3.2.4 studied the influence of chemistry (namely oxygen vacancies) on the screening properties of a  $\text{BaTiO}_3$  single crystal. A natural step forward would be to investigate the electronic properties of such samples. Indeed, many theoretical studies emphasize the critical importance of the band structure in many key properties of ferroelectric-based devices such as electron transport in ferroelectric tunnel junctions [229], magnetization and magneto-electric coupling in extrinsic multiferroics [92] or spin-polarization [230]. Cohen showed in Ref. [50] the importance of the Ti  $3d$  - O  $2p$  hybridization in the stabilization of the ferroelectric polarization of  $\text{BaTiO}_3$  opening the way for many theoretical calculations of the band structure of BTO. However, to the best of our knowledge, experimental investigation of the BTO band-structure has not been done yet.

Angle-resolved PhotoEmission Spectroscopy (ARPES) is the main technique to investigate band structure. The principles have been described in Chapter 1–Section 1.2.2. An alternative to “classic” ARPES measurements, where the sample has to be rotated to access the full momentum distribution, is to use a PhotoEmission Electron Microscope (PEEM) with a specific lens configuration. The focal (or diffraction) plane of the PEEM can be imaged to give parallel momentum resolved dispersion curves  $E(k_x, k_y)$ . This technique is known as k-resolved photoemission electron microscopy (k-PEEM). Imaging the focal plane in PEEM produces a map for all azimuths simultaneously. Conservation of the component of the electron wave vector parallel to the sample surface automatically transforms this map into one of photoelectron intensity as a function of  $(k_x, k_y)$ , which is a horizontal cut in reciprocal space. Combined with energy analysis, this produces an image in reciprocal space of the local intensity as a function of the wave vector parallel to the surface. Adding a field limited aperture, such apparatus enable k-PEEM measurements from areas of a few  $\mu\text{m}^2$  [118, 137]. In this section, the results presented have been acquired on the SPELEEM of the nanoSpectroscopy beamline<sup>9</sup> at ELETTRA. The single crystal has been prepared using the same protocol as the one described in Section 3.2.4 and shows a sharp  $1 \times 1$  LEED pattern (Figure 3.28a). The Brillouin zone of  $\text{BaTiO}_3$  is

<sup>9</sup><http://www.elettra.trieste.it/it/lightsources/elettra/elettra-beamlines/nanospectroscopy/nanospectroscopy.html>

shown in Figure 3.28b and the high-symmetry points are represented.

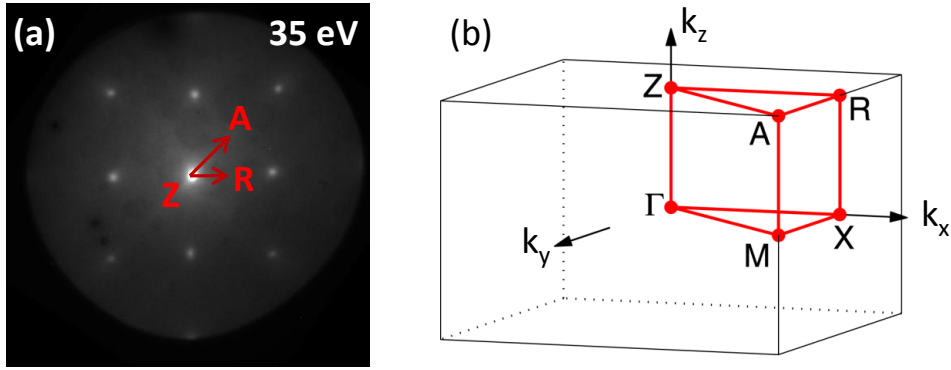


Figure 3.28: (a)  $1 \times 1$  LEED pattern of the  $\text{BaTiO}_3$  single crystal and (b) Brillouin zone of a cubic structure with the high-symmetry points [195]

The determination of photon energy is of prime importance in such experiments since it determines both the probing depth and the momentum perpendicular to the surface ( $K_z$ ) of the outgoing electrons (see Chapter 1). Assuming nearly-free-electron final states, we have the following relationship between  $K_z$  and photon energy  $h\nu$ :

$$K_z = \sqrt{\frac{2m}{\hbar^2} \sqrt{h\nu - \Phi_{\text{BTO}} - E_B + V_0}} \quad (3.6)$$

where  $E_B$  is the binding energy of the photo-electron,  $\Phi_{\text{BTO}} \approx 4.5$  eV is the work function of BTO [17] and we chose  $V_0 = 17$  eV based on the (scarce) literature on ARPES on perovskites [216]. By using a photon energy of 52 eV and taking  $E_B \approx 6$  eV (middle of the valence band), we obtain  $K_z \approx 3.88 \text{ \AA}^{-1}$ . Taking the lattice constant  $c = 4.03 \text{ \AA}$  (value taken from Ref. [120]) for  $\text{BaTiO}_3$ , we obtain  $K_z = 2.5 \cdot \frac{2\pi}{c}$ . The perpendicular momentum is then the  $Z(k_x, k_y, 1)$  point (see Figure 3.28b).

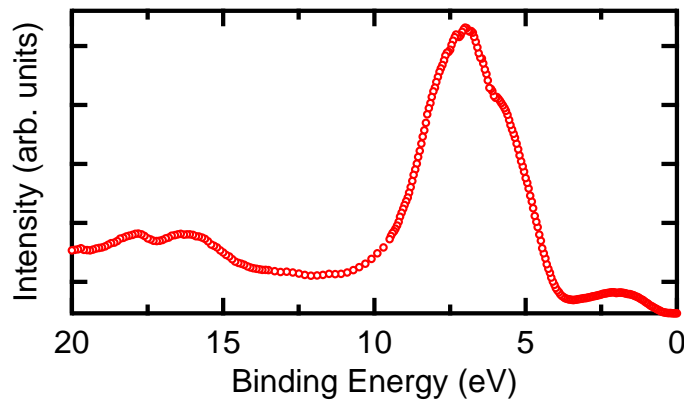


Figure 3.29: Angle-averaged valence band spectrum of the  $\text{BaTiO}_3$  single crystal.

The angle-averaged valence band spectrum is shown in Figure 3.29. As in Section 3.2.2, intensity is visible in the band gap due to the oxygen vacancies created during the sample preparation (vacuum annealing). Figure 3.30 shows selected constant angle-resolved

energy cuts<sup>10</sup> and is the first experimental measurement of the complex band structure of a  $\text{BaTiO}_3$  single crystal.

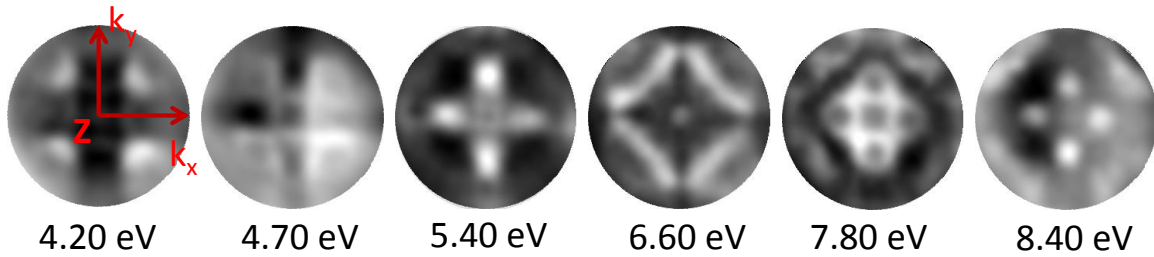


Figure 3.30: Second derivative of the intensity (greyscale) of  $k$ -resolved constant energy cuts.

From a stack of  $I(k_x, k_y, E)$  data<sup>11</sup>, we can easily obtain momentum cuts along the high-symmetry directions as shown in Figure 3.31.

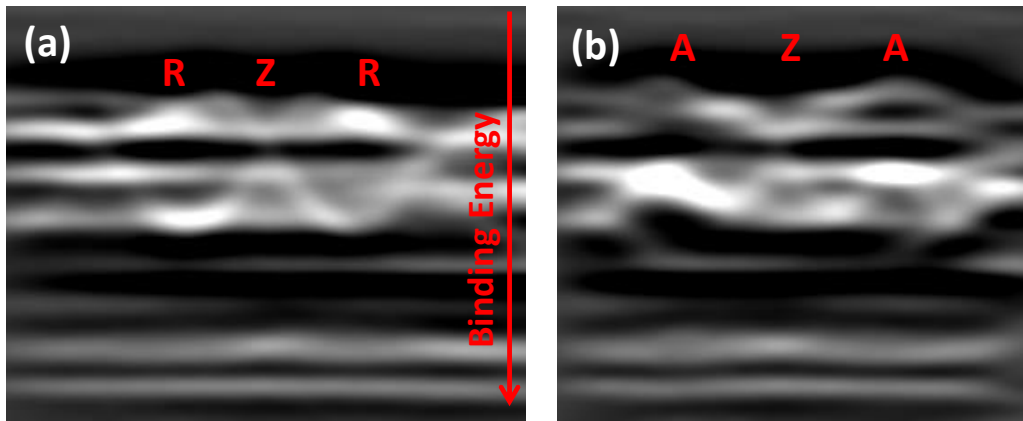


Figure 3.31: Second derivative of the intensity (greyscale) of energy curve distributions along (a)  $ZR$  and (b)  $ZA$  (see Figure 3.28b).

The cubic symmetry (Figure 3.30) and the dispersion relations near the valence band maximum (Figure 3.31) are clearly visible. However, it is not obvious to further interpret these experiment. Indeed, these are the first ARPES results on  $\text{BaTiO}_3$  and this experiment shows the feasibility of  $k$ -PEEM experiments on ferroelectrics. However, further work is necessary to gather physical information from the experimental results. For instance, it would be very interesting to:

- Compare the experimental data with DFT band structure calculations to allocate  $k$ -PEEM bands to simulated bands. This work is underway in our group as a collaboration with G. Geneste from CEA-DAM.
- Investigate the changes in the band structure when increasing/decreasing the oxygen vacancy concentration.

<sup>10</sup>The raw data have been differentiated twice to enhance the signal/noise ratio.

<sup>11</sup>The full stack is available here as a video: [https://dl.dropboxusercontent.com/u/20744866/shared\\_data\\_thesis/chapter\\_3\\_BT0\\_SC\\_kPEEM.avi](https://dl.dropboxusercontent.com/u/20744866/shared_data_thesis/chapter_3_BT0_SC_kPEEM.avi)

- Study the influence of the polarization direction (in-plane or out-of-plane) on the band structure. Indeed, preliminary theoretical calculations (also done by G. Geneste) suggests that in-plane polarization induces an asymmetric band structure that has yet to be observed experimentally. For such experiment, a field aperture with lateral dimensions below the size of a ferroelectric domain (few  $\mu\text{m}^2$  in a single crystal for instance) is necessary so that all signal come from a unique domain. This will be done in the new PEEM setup which just arrived in our group named [MesoXcope](#)<sup>12</sup>.

## Conclusion

In this chapter, several screening mechanisms taking place at ferroelectric surfaces have been investigated. First, the formation of nano-stripes of opposite polarization are responsible for the loss of macroscopic polarization in  $\text{BiFeO}_3$  thin films of decreasing thickness. Then, the surface oxygen vacancy concentration has a direct influence on the dead layer thickness, or screening length, in  $\text{BaTiO}_3$  single crystals. Finally, oxygen vacancies at the surface promotes the downward over upward polarization in  $\text{BaTiO}_3$  single crystals. This chapter also shows the potency of photoemission microscopy to probe ferroelectric surfaces. This method allows a quantitative, spatially-resolved measurement of the work function which can be directly related to relevant properties of ferroelectric materials (namely polarization magnitude or dead-layer thickness).

In future work, the LENSIS group will carry on the work on the relation between domain organization and oxygen vacancies by a combined theoretical (Monte Carlo and DFT) and experimental (X-ray PEEM for the chemistry and the work function, LEEM for the surface potential and k-PEEM for the band structure). Besides, it would be very interesting to conduct similar experiment to the one of polarization magnitude in  $\text{BiFeO}_3$  thin films on other ferroelectrics with different polar structure (namely  $\text{PbTiO}_3$  and  $\text{BaTiO}_3$ ). Obviously, it will be a considerable breakthrough to observe experimentally the nano-domains predicted by effective Hamiltonian theory, but significant progress in spatial resolution of PEEM and LEEM has first to be achieved. Recently, Tromp *et al.* showed a spatial resolution of 2 nm in a aberration-corrected LEEM [221]. This resolution might be sufficient to observe the nanostripes predicted in Section 3.1.

---

<sup>12</sup>[http://iramis.cea.fr/Phoce/Vie\\_des\\_labos/Ast/ast\\_visu.php?id\\_ast=2061](http://iramis.cea.fr/Phoce/Vie_des_labos/Ast/ast_visu.php?id_ast=2061)

# Chapter 4

## Metal/Ferroelectric Interfaces

### Introduction

The previous chapter focused on screening mechanisms of free surfaces of ferroelectrics, purposely leaving aside the most studied mechanism: the screening provided by a metallic electrode connected to the ferroelectric (FE) surface. Indeed, switching the polarization in realistic devices requires a metallic contact at both ends of the ferroelectric, raising fundamental issues on the behavior of the interface between the ferroelectric layer and the electrode. In a FE, the polarization leads to fixed surface charges of opposite sign at the two metal/ferroelectric interfaces. Free charge carriers in the metal electrodes act to screen these surface charges. The distance between the surface charges and the screening charges is often referred as the screening length. The distribution of charge spaced by the screening length generates dipoles of the same sign at the two metal/ferroelectric interfaces. If the screening is perfect, the positive and negative charge are at the same position, the screening length is zero and the dipole canceled. However, the screening is usually imperfect leading to a finite screening length and non-zero interfacial dipoles [101, 184, 204]. In those materials, the partially covalent nature of the bonds in the FE changes the band structure with respect to that of a perfectly ionic compound [203]. Intense theoretical activity has been deployed to understand the electronic structure and band alignment at the interface of a ferroelectric and a metallic electrode [27, 156, 160, 184, 204]. The effective barrier height between an electrode and a FE is therefore difficult to predict, depending on both macroscopic electrical properties and microscopic chemical and electronic structure.

Pintilie *et al.* have extended semiconductor theory of the metal/insulator interface to the case of ferroelectric capacitors, including the effect of the polarization on the band lineup and the consequence on the transport properties [171]. The change in electron (or hole) barrier height with polarization has been thoroughly studied in view of the potential applications of such ferroelectric capacitors as tunnel junctions [27, 229]. Umeno *et al.* predict that the polarization state of ferroelectric capacitor can change the barrier height by up to 1 eV [225] for instance. Stengel *et al.* predict that a particular combination of

electrode and ferroelectric layer (Platinum/BaTiO<sub>3</sub>) can even lead to an enhancement of polarization stability at the interface.

Despite these important theoretical advances, there is little direct experimental data, due to the intrinsic difficulty of measuring the electronic structure of a buried interface. Such measurements under applied bias are even more challenging. Several groups have conducted electrical measurement on these systems [105, 171, 224] but they do not directly probe the microscopic interfacial electronic structure. X-ray photoelectron spectroscopy (XPS) can reveal the electronic structure. It has been used to measure an electron barrier height of 0.5 eV at the Pt/(Ba, Sr)TiO<sub>3</sub> (BSTO) interface and the role of oxygen vacancies was discussed [187]. The polar dependence interface dipole of PbTiO<sub>3</sub>/(La, Sr)MnO<sub>3</sub> (PTO/LSMO) was studied with XPS [241]. Chen and Klein used XPS with in-situ bias to probe the interface between single crystal BaTiO<sub>3</sub> and Pt or RuO<sub>2</sub> electrodes [43]. This technique is the best way to investigate the electronic and chemical properties of interfaces in realistic working conditions.

In this chapter, the experimental challenge of probing the interface of a electrically active sample by photoemission spectroscopy is carefully described to encourage future work on such systems. Then, the methodology is used for the study of two heterostructures with two techniques: on the one hand a highly asymmetric Platinum/BaTiO<sub>3</sub>/Nb-doped SrTiO<sub>3</sub> (Pt/BTO/NSTO) capacitor investigated with XPS and on the other hand a symmetric SrRuO<sub>3</sub>/BaTiO<sub>3</sub>/SrRuO<sub>3</sub> (SRO/BTO/SRO) capacitor investigated with Hard X-ray Photoemission Spectroscopy (HAXPES). Platinum is chosen for its excellent free carriers screening capabilities whereas SrRuO<sub>3</sub> is chosen since it can epitaxially grow on BaTiO<sub>3</sub> and provides screening via free carriers as well as via ionic displacements.

## 4.1 Photoemission Spectroscopy with Bias Application

### 4.1.1 Main Issues

In the vast majority of x-ray photoemission spectroscopy experiments, samples are at the same potential as the spectrometer, *i.e.* ground potential to facilitate the calibration of the energy scale. Threshold spectrum measurements are a noteworthy exception: in that case, the sample is negatively biased relatively to the spectrometer in order to part the contribution from the spectrometer and from the sample.

Recently, the increasing need of knowledge on electronic and chemical properties of functional interfaces drives the development of photoemission spectroscopy with *in-situ* bias application. Suzer *et al.* used photoemission spectroscopy to do chemically-resolved impedance-like measurements on the Rb/SiO<sub>2</sub> interface [211]. Nagata *et al.* conducted several experiments using hard x-ray photoemission on resistive switching devices to probe

the interfacial chemical properties as a function of the bias-induced resistive state [150, 151].

In the ferroelectrics community, very recently, Chen and Klein did photoemission spectroscopy on a BaTiO<sub>3</sub> single crystal covered with either Platinum or RuO<sub>2</sub> as a function of the ferroelectric polarization. The ferroelectric polarization is switched *in-situ* in this experiment [43]. In the next sections, I describe similar experiments on different heterostructures.

To conduct such experiments on metal/ferroelectric interfaces, several issues have to be tackled:

- The interface has to be as free of contamination and as sharp as possible. The best solution is the growth of the full structure in the same ultra-high vacuum chamber.
- The interface must not be too deeply buried so that the photoemission signal from the interface buried under the thin electrode is still significant. Using soft x-ray ( $\approx 1$  keV), the probing depth is of 3-4 nm whereas hard x-ray (above 4 keV) can probe 10-20 nm.
- The capacitor area must not be too large so that leakage currents due to defects are minimized.
- The capacitor area must not be too small so that the photoemission signal comes only from the interface of interest.
- The electrical connections must be compatible with an ultra-high vacuum (UHV) chamber both in terms of vacuum contamination and easiness of *in-situ* manipulation.

The two first issues have been resolved differently for the two heterostructures presented in this chapter. For the Pt/BTO/NSTO capacitor (Section 4.2), after the epitaxial growth of the BTO layer on the NSTO substrate, the BTO surface has been cleaned by an ozone treatment before deposition of the platinum layer. The top electrode thickness is 2.8 nm in that case allowing soft x-ray photoemission spectroscopy on the buried interface. For the SRO/BTO/SRO capacitor (Section 4.3), the full heterostructure was grown in a unique deposition chamber. The top electrode thickness is 5 nm allowing hard x-ray photoemission spectroscopy.

### 4.1.2 Proposed Solution

To address the issues of biased photoemission, the metal/ferroelectric/metal structure, designated henceforth as a ferroelectric capacitor, has to be carefully designed. The starting point is a  $(5 \times 5)$ mm<sup>2</sup> multilayer, plane sample. In photoemission spectroscopy,

signal from small areas can be measured by using a small beam spot focused on the region of interest. In a synchrotron light facility such as [SOLEIL](http://www.synchrotron-soleil.fr/)<sup>1</sup> in France, several beamlines offer photoemission end-stations with beam spots of full width at half maximum (FWHM) of ( $\approx 100 \times 100$ )  $\mu\text{m}^2$ . This is the case for the TEMPO (Section 4.2) and the GALAXIES beamlines (Section 4.3). Therefore, by adding a margin of error which takes account of the tails of the beam, we chose ( $300 \times 300$ )  $\mu\text{m}^2$  as the area of a capacitor. With such large electrodes, it is likely that defects inducing high leakage current, namely high conduction channels through grain boundaries, occur randomly for some capacitors. That is why we chose to fabricate twenty independent capacitors per sample to ensure hopefully that at least some of them have a low enough defect concentration for FE stability.

The dimension problem settled, the next issue is to design a system which can be both electrically connected to many ultra-high vacuum manipulator and suitable for photoemission spectroscopy. The thin top electrode cannot hold any wire and an intermediate stage has to be designed to allow an easy connection. This is done by the deposition of a thicker layer of metal, overlapping a small part of the electrode of interest, which will serve as a connecting pad. It can be wired by micro-wiring to the sample holder. However, it has to be electrically separated from the ferroelectric layer not to disturb the electrical properties of the capacitor of interest. This is the last feature of the design: an intermediate, highly insulating, dielectric layer is inserted between the pad and the ferroelectric to limit at best parasitic behaviors. The pad (in green in Figure 4.1) is 300 nm thick and made of Palladium because of its good conduction properties and excellent compatibility with micro-wiring. The intermediate dielectric (red) is 100 nm thick and made of  $\text{Al}_2\text{O}_3$  because of its highly insulating properties, (b) top view of the mask used during the lithography steps of the micro-fabrication. The final design is presented in Figure 4.1, with a side schematic view of the device ready for introduction in any photoemission end-station and a top view of the micro-fabrication mask. In addition to the twenty square top electrodes (in blue), the scheme shows the lithography alignment marks - the crosses near the edge of the sample - and four additional rectangular patterns in the corner which are necessary for connecting the bottom electrode.

The micro-fabrication processes have been done at the [Centrale de Technologie Universitaire](http://www.ief.u-psud.fr/ief/ief.nsf/CTU/CTU_presentation.html)<sup>2</sup> in Orsay (France). They consist of the following steps:

1. Ion beam etching of the plain top layer to obtain twenty  $300 \times 300 \mu\text{m}^2$  electrodes (blue squares in Figure 4.1).
2. Evaporation of the  $\text{Al}_2\text{O}_3$  insulating layer (red squares in Figure 4.1).
3. Ion beam etching of the  $\text{BaTiO}_3$  layer to reach the bottom electrode layer (pink rectangles in Figure 4.1).

<sup>1</sup><http://www.synchrotron-soleil.fr/>

<sup>2</sup>[http://www.ief.u-psud.fr/ief/ief.nsf/CTU/CTU\\_presentation.html](http://www.ief.u-psud.fr/ief/ief.nsf/CTU/CTU_presentation.html)

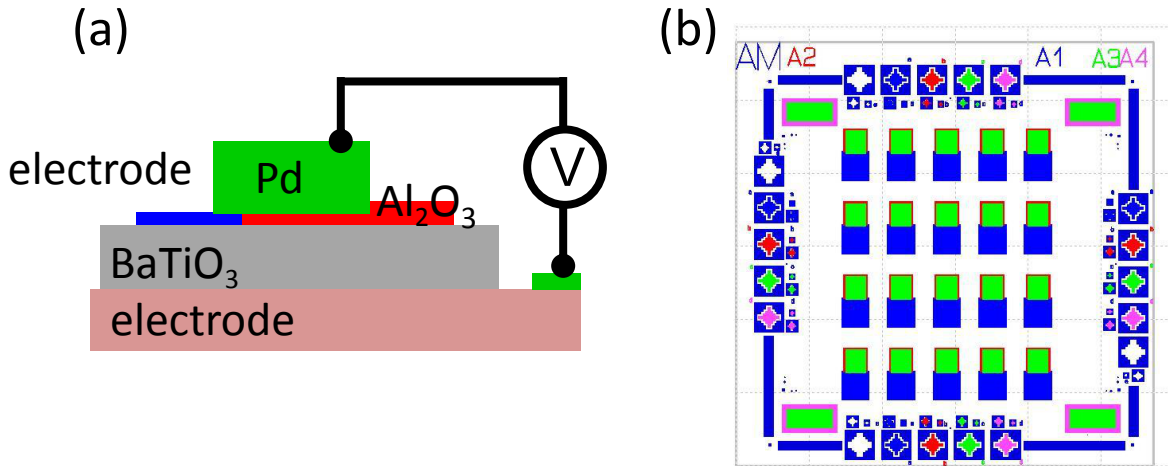


Figure 4.1: (a) Schematic of the electrode/BaTiO<sub>3</sub>/electrode capacitor. The pad (in green) is 300 nm thick and made of Palladium because of its good conduction properties and excellent compatibility with micro-wiring. The intermediate dielectric (red) is 100 nm thick and made of Al<sub>2</sub>O<sub>3</sub> because of its highly insulating properties, (b) top view of the mask used during the lithography steps of the micro-fabrication.

4. Deposition by pulverization of the Palladium pads for contacting both the twenty top electrodes and the four bottom electrodes contacts (green in Figure 4.1).
5. Micro-wiring of the pads to the suitable sample-holder.

The last step is the electrical characterization of the capacitors using the experimental methods described in Chapter 2–Section 2.3. Leakage is checked with Current - Voltage curves and the ferroelectric properties are monitored with Capacitance - Voltage loops. The best capacitor is chosen for the photoemission experiment with *in-situ* bias application. Figure 4.2 shows a patterned sample mounted on the sample holder of P09 beamline<sup>3</sup> at PETRA III synchrotron where some HAXPES experiments have been carried out.

## 4.2 Investigation of the Platinum/BaTiO<sub>3</sub> interface

In this section, the polarization dependent band alignment and electronic structure of a Platinum/BaTiO<sub>3</sub> (Pt/BTO) interface is investigated using photoemission spectroscopy with *in-situ* biasing. This interface is chosen because platinum is theoretically an electrode with excellent screening capabilities due to a very good mobility of its charge carriers. Stengel *et al.* even predict an enhanced ferroelectric polarization stability in BTO with such an electrode combined with a BaO-terminated BTO layer [204]. However, interfaces of Pt and oxides are not epitaxial: platinum tends to form small islands when deposited on BTO even at room temperature. In the experiment presented in this section the band alignment is determined by a combination of imperfect screening by the electrode and the

<sup>3</sup>[https://photon-science.desy.de/facilities/petra\\_iii/beamlines/p09\\_resonant\\_scattering\\_and\\_diffraction/index\\_eng.html](https://photon-science.desy.de/facilities/petra_iii/beamlines/p09_resonant_scattering_and_diffraction/index_eng.html)

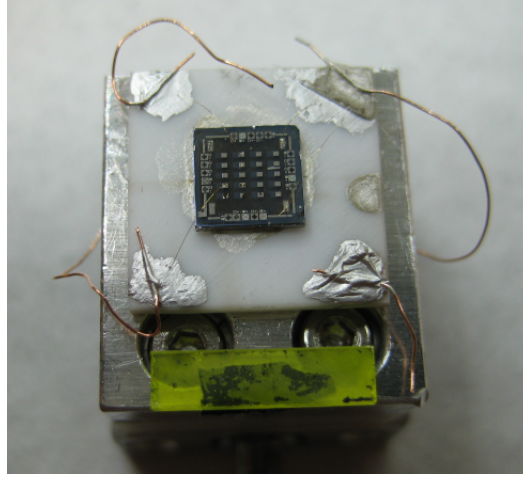


Figure 4.2: Picture of a SRO/BTO/SRO sample mounted on a sample holder. The palladium pads are clearly visible (grey squares) and even the SRO top electrodes can be discerned (dark blue). Micro wires connect the pads to copper wires which serve as connectors to the manipulator.

chemistry of the interface. We demonstrate that a complete Pt/BTO/NSTO heterostructure has a rectifying Schottky behavior. For a  $P^+$  polarization state, i.e. polarization pointing from the bottom electrode to the top electrode, the leakage current is limited by Schottky emission at the Pt/BTO interface whereas in the  $P^-$  state the structure works as a single Schottky diode with a quasi-ohmic BTO/NSTO interface. The band alignment agrees well with the observed transport properties. Finally, we suggest that Callen dynamical charge offers a plausible explanation of the polarization dependent electronic structure near the electrode.

#### 4.2.1 Growth of the Pt/BTO/NSTO heterostructure

The BTO thin film of thickness 64 nm was grown on a Nb-doped (0.5 wt.%) SrTiO<sub>3</sub> (001) (NSTO) conducting substrate using molecular beam epitaxy (MBE). Prior to film growth, the NSTO substrate was cleaned using buffered HF solution and rinsed in deionized H<sub>2</sub>O, followed by annealing under oxygen atmosphere in the MBE chamber to obtain a clean, atomically flat NSTO surface. Oxygen was introduced into the reactor via a pressure-regulated plasma chamber which enables precise control of oxygen partial pressure and the utilization of atomic (O) oxygen which gives better ferroelectric properties [157]. Ba and Ti were co-evaporated using Knudsen cells at 900 K under a oxygen pressure of  $2.67 \cdot 10^{-6}$  mbar and the sample was cooled down under  $P_O = 1.33 \cdot 10^{-6}$  mbar. We used Reflection High Energy Electron Diffraction (RHEED) to monitor the film crystallinity during the growth and guarantee the layer by layer growth and the TiO<sub>2</sub> termination. A X-ray diffractometer with a 1.6 kW fixed anode (Cu K $\alpha$  radiation,  $\lambda = 1.5406$  Å) is used to measure the BTO in and out-of-plane parameters as shown in Figure 4.4. After

10 minutes exposure to ozone to remove the surface carbon contamination, a continuous 2.8-nm Platinum (Pt) top electrode was deposited at room temperature to ensure full coverage of the surface [187]. X-ray Photoemission Spectroscopy (XPS) was performed before and after platinum deposition using monochromatized X-ray Source XM 1000 MkII (Al K $\alpha$ :  $h\nu = 1486.7$  eV) and a SPHERA II analyzer, both from Omicron Nanotechnology GmbH.

The full device architecture is shown in Figure 4.3a and as been described in the Section 4.1.2. The device was introduced in ultrahigh vacuum ( $10^{-10}$  mbar) in the photoemission set-up of the TEMPO Beamline<sup>4</sup> at the SOLEIL synchrotron radiation source [172]. The  $100 \times 100 \mu\text{m}^2$  beam could be directed onto a single top electrode located by a map of the whole sample. This map is obtained by scanning the surface with the photon beam while measuring Pt 4f photoemission spectrum. The intensity at the binding energy of the Pt 4f<sub>7/2</sub> core-level (71.20 eV) is reported in Figure 4.3b.

A photon energy of 1100 eV was used to optimize the signal from the BTO close to the interface (estimated maximum probing depth of  $\approx 5$  nm). This energy is close to those used in typical laboratory based experiments using thin top electrodes [43] but, thanks to synchrotron radiation, the flux has a much higher brilliance and better energy resolution. On the other hand, the higher photon flux can also modify the switching behavior of the capacitor, as will be discussed below. The overall energy resolution was 220 meV. The sample-holder allows *in-situ* bias application and electrical measurements via high quality coax wires to limit parasitic behavior due to the electrical environment. The overall energy resolution was 220 meV. The sample-holder allows *in-situ* bias application and electrical measurements via high quality coax wires to limit parasitic behavior due to the electrical environment.

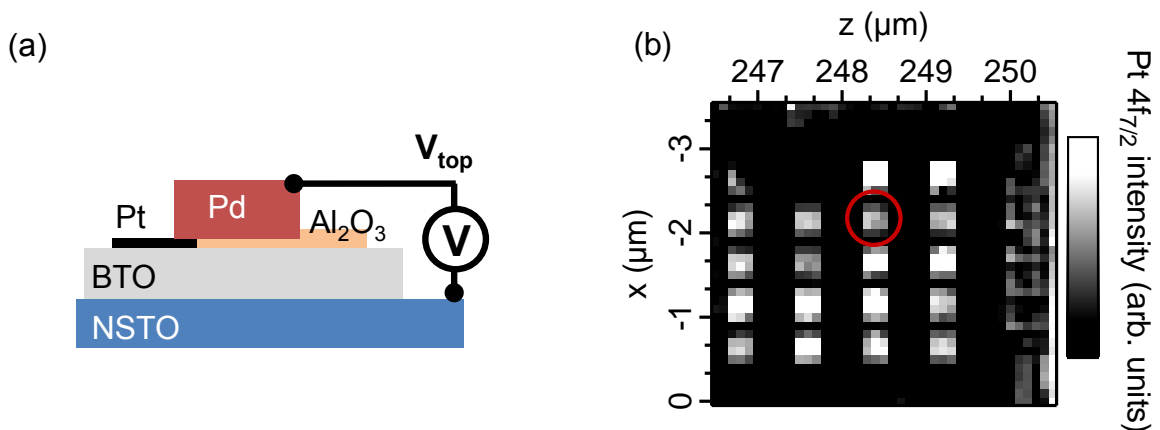


Figure 4.3: (a) Schematic of the capacitor, (b) Pt 4f intensity map for the Pt/BTO/NSTO sample showing 20 identical Pt/BTO/NSTO capacitors ( $300 \times 300 \mu\text{m}^2$ ) on the  $5 \times 5 \text{mm}^2$  surface, allowing location of the wired capacitor (red circle).

<sup>4</sup><http://www.synchrotron-soleil.fr/Recherche/LignesLumiere/TEMPO>

The BTO thin film is fully relaxed on the NSTO substrate with an in-plane parameter  $a = 3.956 \text{ \AA}$ , an out-of-plane parameter  $c = 4.040 \text{ \AA}$  and a tetragonality ratio  $c/a$  of 1.040 (see Figures 4.4a–4.4b). The film thickness determined by X-Ray Reflectivity (XRR) was 64 nm with a 0.37 nm rms roughness, *i.e.* one unit cell (see Figure 4.4c). Low Energy Electron Diffraction (LEED) patterns showed a  $c(2 \times 2)$  surface reconstruction (see Figure 4.4d) expected for  $\text{TiO}_2$  termination [110].

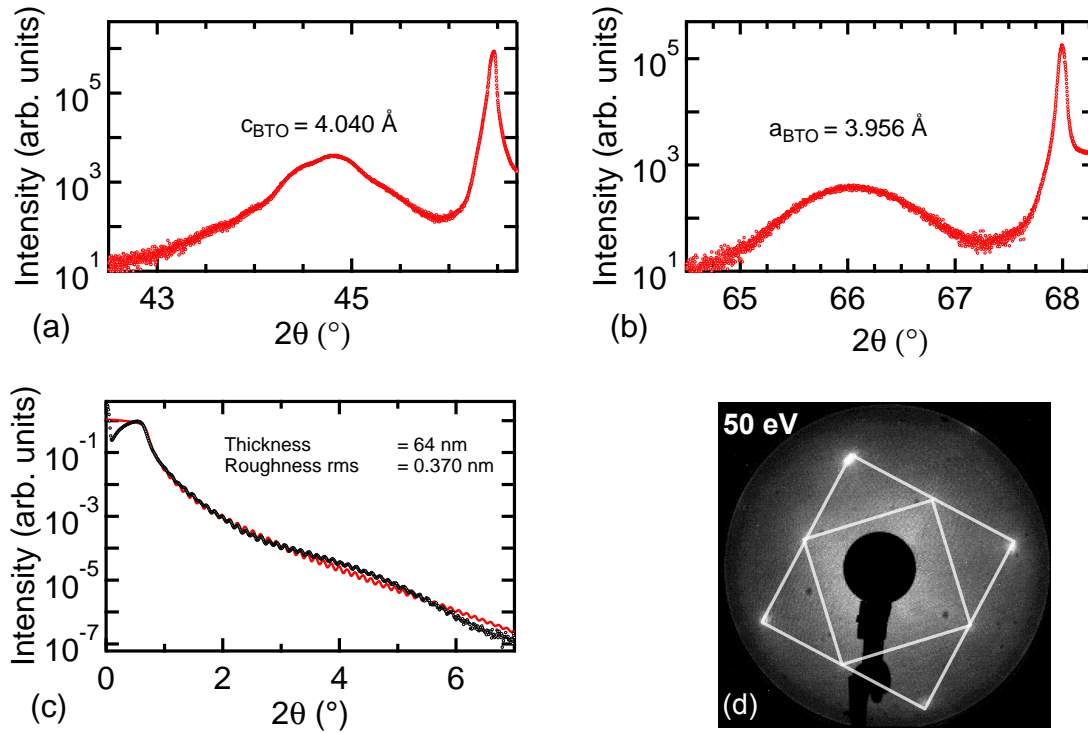


Figure 4.4: (002) (a) and (202) (b) peaks for BTO and STO. BTO is relaxed onto STO with a tetragonality ratio  $c/a$  of 1.040; (c) reflectivity curve indicating the BTO thickness; (d) LEED image of the BTO surface before Pt deposition showing  $c(2 \times 2)$  surface reconstruction

Figure 4.5 shows XPS core-level spectra from the BTO thin film before and after Pt deposition. The secondary electron background has been removed using a Shirley background [199]. Ba  $3d$  and Ti  $2p$  spectra are fitted with Voigt functions. The low-binding-energy (LBE) component is from the bulk-coordinated Ba. The Ba  $3d_{5/2}$  spectrum has a high-binding-energy (HBE) component. It is unlikely that the HBE component is due to contamination. Firstly such peaks (Ba- $\text{CO}_3$  for example) have a much bigger shift [14] and secondly the Ba is protected from surface contamination by the  $\text{TiO}_2$  termination layer. Here, it is more likely caused by the discontinuity in the polarization at the surface for this  $\text{TiO}_2$  termination [65, 233]). This will be discussed further in section 4.2.5. The FWHM of each component of the Ba  $3d_{5/2}$  and Ti  $2p_{3/2}$  are 1.40 eV (Ba  $3d_{5/2}$  HBE), 1.20 eV (Ba  $3d_{5/2}$  LBE) and 1.00 eV (Ti  $2p_{3/2}$ ). The Ba  $3d$  HBE is often attributed to under-coordinated Barium at the surface for BaO termination [96, 124]. However, for a  $\text{TiO}_2$  terminated surface, this is clearly not the case. The topmost Ba atoms are in the

first layer below the surface and are fully oxygen coordinated therefore we do not expected a surface peak due to undercoordinated Ba. O 1s and C 1s spectra before deposition show that there is a very low concentration of carbonate species at the interface confirming the efficiency of ozone cleaning on these surfaces. Ti 2p spectra do not present a shoulder at lower binding energy, classically attributed to Ti<sup>3+</sup> species due to oxygen vacancies [187], neither before nor after Pt deposition. Additionally, measurements of the valence band of BTO at a take-off angle of 30° (see Figure 4.5), therefore more sensitive to the signal from the surface, before deposition showed no signal in the BTO gap which would have corroborated the presence of oxygen vacancies at the BTO surface below our detection limit (1%). The Pt/BTO interface presented here therefore has very low carbonate and oxygen vacancy concentrations. We observe core-level shifts towards lower-binding energy after Pt deposition as previously observed for the (Ba,Sr)TiO<sub>2</sub>/Pt interface [187]. These shifts are classically attributed to a band-bending phenomenon at the metal/ferroelectric interface. In that interpretation, BTO is seen as a n-type, large-gap semiconductor because of the electrons released by oxygen vacancies. However this model does not fit well with our case: the core-levels are not rigidly displaced: Ti 2p<sub>3/2</sub> shifts by 500 meV, the HBE (LBE) component of Ba 3d<sub>5/2</sub> by 350 meV (700 meV) and the concentration in oxygen vacancies is very low. A surface photo voltage due to the photoemission process might alter the band-bending but in that case all bands should be rigidly displaced [84]. Rather, we think that this behavior is due to the different chemical environment for the BTO after deposition of platinum and also due to the change in electrical boundary conditions related to a different screening of the ferroelectric polarization for a BTO free surface and a Pt/BTO interface. This will be further investigated using photoemission spectroscopy with *in-situ* applied bias in section 4.2.3.

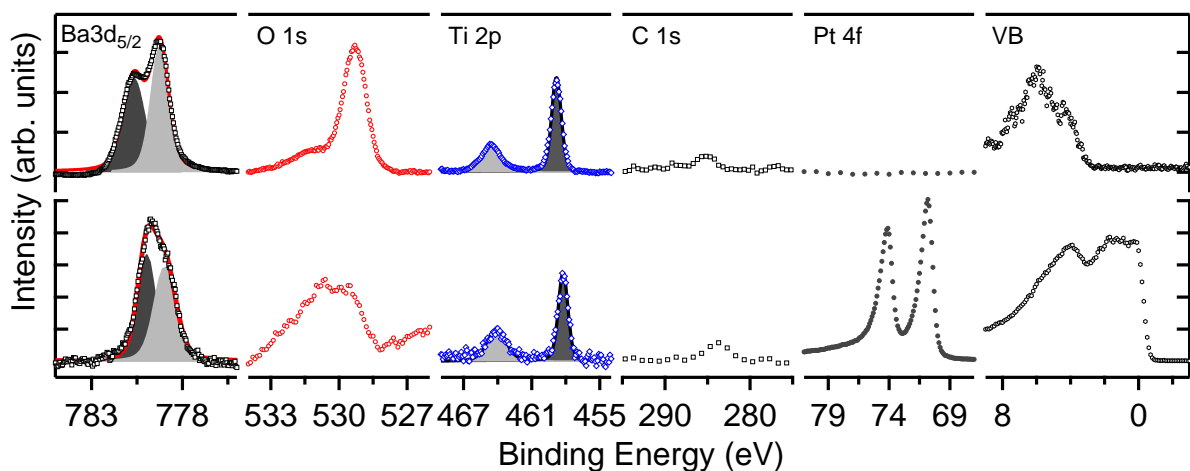


Figure 4.5: XPS spectra before (top) and after (bottom) Pt deposition.

### 4.2.2 Electrical characterization

After the ex-situ microfabrication processes described in section 4.1.1, the Capacitance - Voltage (C-V) characteristic (Figure 4.6a) has a typical butterfly loop shape as previously observed on Pt/BTO/NSTO [1] and Pt/BFO/NSTO [105]. The butterfly loop shows a 0.6 V offset demonstrating ferroelectric<sup>5</sup> behavior with a strong built-in P<sup>+</sup> (pointing from the bottom to the top interface) polarization. The coercive voltage  $V_{c-}$  needed to switch from P<sup>+</sup> to P<sup>-</sup> is 0.80 V.  $V_{c+}$ , switching from P<sup>-</sup> to P<sup>+</sup>, is 0.40 V. The accurate measurement of these values is extremely important for application of correct bias voltages in-situ during the XPS measurements. The current density-voltage (J-V) characteristic is diode-like with high conduction when switching from P<sup>+</sup> to P<sup>-</sup>. The characteristics was acquired from P<sup>+</sup> to P<sup>-</sup> and P<sup>-</sup> to P<sup>+</sup> (see Fig. 4.6b) to confirm that the high conducting state occurs for downward (P<sup>-</sup>) polarization only. The J-V characteristic was also measured on the Pd pad to check we have an ohmic contact between Pd pads and Pt electrodes and that the Pd/Al<sub>2</sub>O<sub>3</sub>/BTO/NSTO path is highly insulating ( $> 1$  Mohm, blue squares in Fig. 4.6b). The C-V curve of Pd/Al<sub>2</sub>O<sub>3</sub>/BTO/NSTO also confirms that parasitic signal from this capacitance is negligible ( $< 1$  pF, blue squares in Fig. 4.6a) in comparison to that from the Pt/BTO/NSTO ( $\approx 1$  nF, black circles in Fig. 4.6a).

Fig. 4.6c displays a plot of  $\ln |J|$  against  $|V_{top}|^{1/2}$  obtained by sweeping the applied voltage ( $V_{top}$ ) from -2 to +2 V. Starting in the direction of the lower arrow, this corresponds to a switch from P<sup>+</sup> to P<sup>-</sup> polarization while measuring the current through the capacitor. For  $V_{top} < 0$  (squares in Fig. 4.6c), we obtain a good linear fit of  $\ln |J|$  typical of Schottky thermionic emission [171]. Similarly, for  $V_{top} > 0$  (upper branch in Fig. 4.6c), we obtain a linear fit but for a smaller voltage range:  $0.2 < |V_{top}|^{1/2} < 0.8$  volt<sup>1/2</sup>. In Fig. 4.6d, for  $V_{top} > V_c = 0.8$  volt, the linear fit to the experimental curve shows an ohmic response.  $V_c$  matches the coercive voltage deduced from the C-V measurements. Therefore, when switching from P<sup>+</sup> to P<sup>-</sup>, we observe a transition from Schottky-like to ohmic conduction. Since high-flux high-energy incident photons might affect the ferroelectric and conduction properties of the heterostructure [241], we also did C-V measurements under X-ray illumination described in Section 4.2.3.

### 4.2.3 Photoelectron Spectroscopy with Applied Bias

To understand the microscopic electronic structure responsible for the electrical properties, photoelectron spectroscopy was carried out on the heterostructure at different values of applied bias on the top (Pt) or bottom (NSTO) electrodes.

Fig. 4.7a displays the C-V measurements with and without synchrotron radiation on the Pt top electrode. It shows that the coercive voltages change slightly when the sample is illuminated:  $V_{c+}$  is shifted up from 0.40 to 0.50 volt,  $V_{c-}$  shifts up from 0.80 to

---

<sup>5</sup>This structure is strictly speaking not a ferroelectric capacitor since at zero field, the BTO is always in the P<sup>+</sup> state. However, we will use the term ferroelectric in the following for the sake of simplicity.

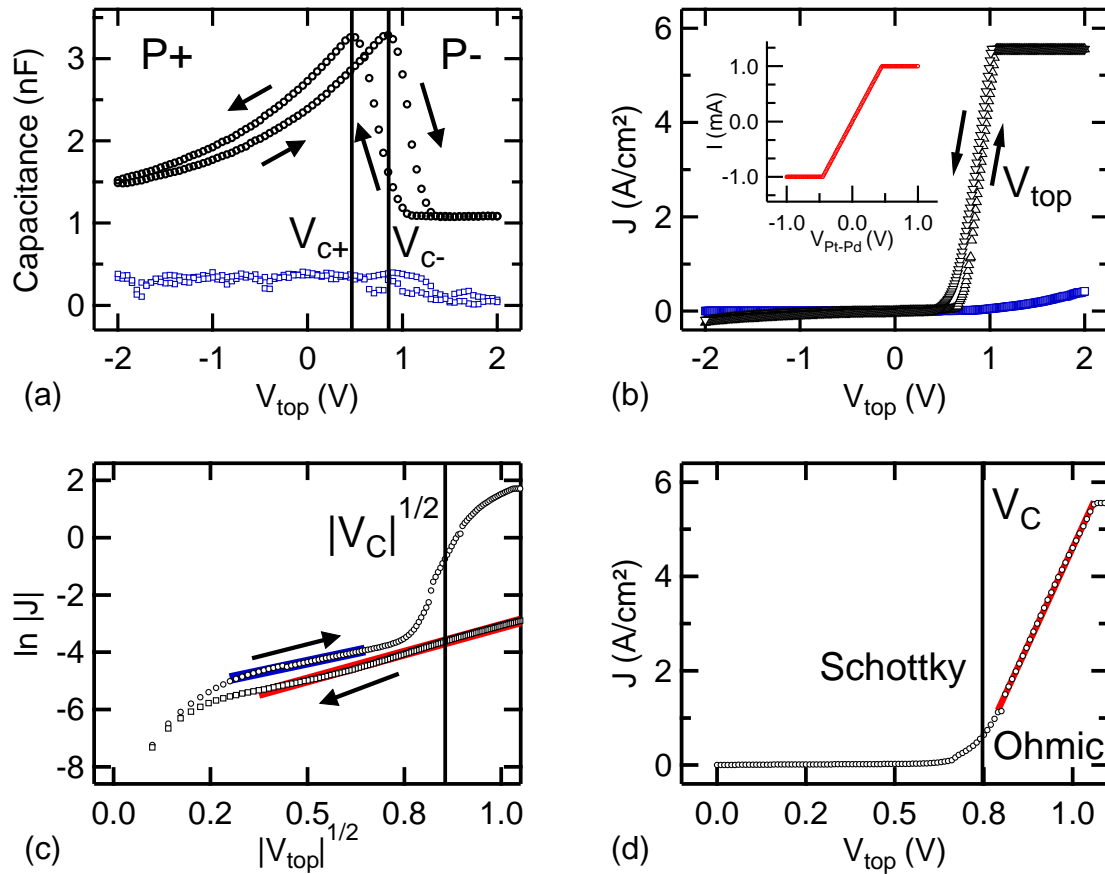


Figure 4.6: (a) C–V measurements for Pt/BTO/NSTO (black circles) and Pd/Al<sub>2</sub>O<sub>3</sub>/BTO/NSTO (blue squares); (b) J–V measurements for Pt/BTO/NSTO (black triangles, upward (downward) triangles for increasing (decreasing) voltage sweep), Pd/Al<sub>2</sub>O<sub>3</sub>/BTO/NSTO (blue squares) and Pd/Pt (inset). (c)  $\ln |J| - |V_{top}|^{1/2}$  showing conduction limited by Schottky emission (arrows indicates sweep direction); (d) J – V showing ohmic behavior for  $V_{top} > V_c$ .

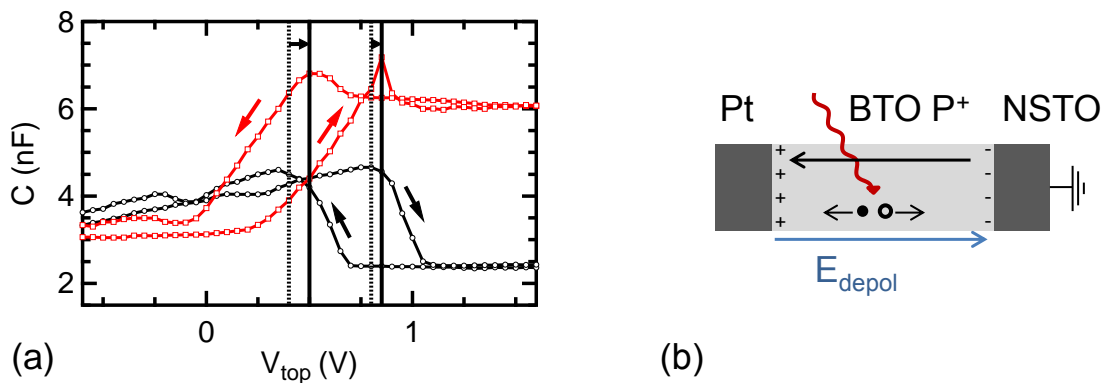


Figure 4.7: (a) Capacitance without  $C_{dark}$  (black circles) and with  $C_{photon}$  (red squares) synchrotron irradiation, (b) capacitor under illumination, short-circuit. Photogenerated electrons (holes) are filled (empty) circles.

0.85 volt. The alteration of the C-V curve only occurs when the photon beam is focused on the platinum top electrode: no change is observed when focusing on the Pd pad. In

Core-Level	$V_{\text{top}}$		$\Delta_{BE}$ wrt Pt 4f
	0.00 (P <sup>+</sup> )	0.75 (P <sup>-</sup> )	
Pt 4f <sub>7/2</sub>	71.20	71.90	0.00
Ba 3d <sub>5/2</sub> LBE	779.45	779.80	-0.35
Ba 3d <sub>5/2</sub> HBE	780.65	781.15	-0.20
Ti 2p <sub>3/2</sub>	458.70	458.95	-0.45

Table 4.1: Binding energy (eV) for the Pt/BTO interface core-levels when applying different biases  $V_{\text{top}}$  (V) (column 1,2) and shift with respect to Pt 4f<sub>7/2</sub> BE shift (column 3). Bottom electrode is grounded.

the BTO layer, photo-generated carriers drift under the effect of the depolarizing field and the applied bias. For the P<sup>+</sup> state for instance, electrons (holes) migrates towards top (bottom) interface and contribute to a better screening of the depolarizing field induced by the P<sup>+</sup> polarization. This might lead to a higher stability of the P<sup>+</sup> state, and an overall shift of the C-V loop towards higher voltages. Though weak, this effect was monitored for every photoemission measurements: before each set of acquisition, CV loops were acquired to check the coercive voltages.

The bias-induced displacements of Ba 3d and Ti 2p core levels binding energies (BE) were measured relative to the Pt 4f core-levels of the top electrode (see Figure 4.8). The Ba 3d<sub>5/2</sub> spectra again have two components: at low and high binding energy (LBE and HBE respectively). The spectra were fitted using Voigt functions with FWHM of 1.60 eV (Ba 3d<sub>5/2</sub>) and 1.40 eV (Ti 2p). For the P<sup>+</sup> (P<sup>-</sup>) polarization state, we kept  $V_{\text{top}}$  at -0.5 V (+1.30 V) *i.e.* well above the coercive voltages, for two minutes to ensure full switching of the polarization before recording the photoemission spectra at  $V_{\text{top}} = 0$  V (+0.75 V). The lower voltage magnitudes with respect to those chosen for switching are chosen to reduce the current flowing through the capacitor while maintaining the correct polarization state. The Pt 4f core-level shifts towards higher BE is 0.70 eV when we apply +0.75 V on the Pd pad. The 0.05 V potential drop is due to the small contact resistance between the two metals ( $\approx 10\Omega$ ). When switching from P<sup>+</sup> to P<sup>-</sup> state, the Ba 3d<sub>5/2</sub> HBE (LBE) shifts downward by 200 meV (300 meV) and the Ti 2p<sub>3/2</sub> by 450 meV relative to the Pt 4f<sub>7/2</sub> reference. Table 4.1 summarizes the BE shifts. The last column shows the BE shifts for BTO core-levels after subtraction of the applied bias. These values are therefore the direct consequence of switching the FE polarization.

We did the same experiment applying bias on the bottom electrode with top electrode grounded. The measured BE shifts are equal (within 50 meV) to those with voltage on top electrode (see Table 4.2).

The valence band offset (VBO) at the Pt/BTO interface may be determined as fol-

Core-Level	V <sub>bottom</sub>		$\Delta_{BE}$ wrt Pt 4f
	0.00 (P <sup>+</sup> )	-0.95 (P <sup>-</sup> )	
Pt 4f <sub>7/2</sub>	71.20	71.20	0.00
Ba 3d <sub>5/2</sub> LBE	779.60	779.30	-0.30
Ba 3d <sub>5/2</sub> HBE	780.70	780.55	-0.15
Ti 2p <sub>3/2</sub>	458.75	458.30	-0.45

Table 4.2: Binding energy (eV) for the Pt/BTO interface core-levels when applying different biases V<sub>bottom</sub> (V) (column 1,2) and BE offsets with respect to Pt 4f<sub>7/2</sub> BE shift (column 3). Top electrode is grounded.

lows [116]:

$$VBO = (E_{Ti2p_{3/2}} - E_{Pt4f_{7/2}})_{Pt/BTO} + (E_{Pt4f_{7/2}} - E_F)_{Pt} - (E_{Ti2p_{3/2}} - VB_{Max})_{BTO} \quad (4.1)$$

$(E_{Ti2p_{3/2}} - E_{Pt4f_{7/2}})_{Pt/BTO}$  is extracted from the *in-situ* photoemission measurements (see Table 4.1).  $(E_{Pt4f_{7/2}} - E_F)_{Pt} = 71.25$  eV was measured on a Pt(111) monocrystal and  $(E_{Ti2p_{3/2}} - VB_{Max})_{BTO} = 455.95$  eV on the clean BTO thin film before Pt deposition, giving a valence band offset of 2.8 eV. Assuming that the BTO thin film has the same gap as in the bulk (3.2 eV [237]) and that it does not change with polarization, we deduce a 0.4 eV (0.85 eV) conduction band offset (CBO) for the P<sup>+</sup> (P<sup>-</sup>) case.

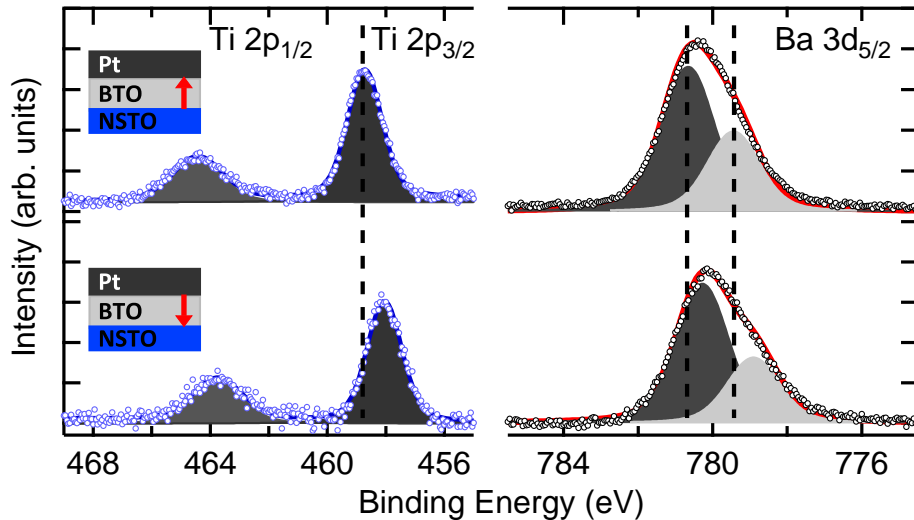


Figure 4.8: Photoemission spectra for the P<sup>+</sup> (top) and P<sup>-</sup> (bottom) FE states for the Ti 2p<sub>3/2</sub> - 2p<sub>1/2</sub> (left) and Ba 3d<sub>5/2</sub> (right). The bottom spectra have been shifted by 0.70 eV towards lower BE using Pt 4f spectra.

#### 4.2.4 Polarization-dependent Band Lineup

The inelastic mean free path of photoemitted electrons by soft x-ray photons is  $\lambda \approx 1.5$  nm [35] limiting the probing depth ( $3\lambda \approx 4.5$  nm) of this experiment to the first layers of BTO beneath the platinum overlayer. The BTO in the center of the film or at the bottom interface is not probed. Even hard x-ray photoemission spectroscopy experiments using photon energy of 6-10 keV cannot probe more than 20-30 nm [164]. Therefore, the signal from the deeply buried bottom interface of our film cannot be directly probed with photoemission experiment. We can deduce the barrier height at the bottom interface from electrical measurements. For both  $P^+$  and  $P^-$  polarization states, the barrier heights at the top interface (0.40 and 0.85 eV) are large enough to suggest Schottky conduction. For negative  $V_{\text{top}}$  a Schottky-like behavior is observed for the whole capacitor. Therefore the bottom interface barrier height must be at least similar to that of Pt/BTO. For positive  $V_{\text{top}}$ , the Pt/BTO barrier height increases, therefore in order to have the observed ohmic behavior, the BTO/NSTO barrier height must be very small. More specifically, the ohmic conduction for  $V_{\text{top}} > V_c = 0.8$  volt suggests a conduction band offset of 0 eV at the bottom interface for this voltage range ( $P^-$  state). When  $V_{\text{top}} < V_c$  (Fig. 4.9, right), the BTO layer switches from  $P^-$  to  $P^+$ . Using photoemission spectroscopy data we obtain a downward shift of 0.45 eV in the conduction band offset at the top interface. The offset is now 0.85 eV at the Pt/BTO interface. Assuming a upward shift of similar magnitude at the bottom interface, we get a conduction band offset value of 0.45 eV for the bottom interface in the  $P^+$  state. However, this analysis must be treated with caution since a higher upward shift might occur at the bottom interface [225].

The full band alignment deduced from the photoemission experiment with *in-situ* bias applications is shown in Fig. 4.9. In the  $P^+$  state, the structure can be modeled as back-to-back Schottky diodes. The conduction band offset is 0.40 eV at the Pt/BTO interface, similar to the value obtained for (Ba,Sr)TiO<sub>3</sub>/Pt (0.5 eV) [187] and 0.45 eV at the BTO/NSTO interface. For  $V_{\text{top}} < 0$ , the Pt/BTO diode is reverse-biased while the BTO/NSTO junction is forward biased. For  $0 < V_{\text{top}} < V_c$ , the reverse-biased BTO/NSTO diode limits the electron current.

In the  $P^-$  state, the BTO/NSTO interface is ohmic and the structure can be modeled as a unique Schottky-diode. This diode is forward-biased when  $V_{\text{top}} > 0$ , leading to relatively high current through the capacitor. The whole structure therefore functions as a resistance switch with a bistable state at a non-zero voltage. An electroresistance can even be defined, in an analogous way to the tunneling electrical resistance, as  $(G_- - G_+)/ (G_- + G_+)$ . We extracted the current for a voltage of 0.65 V on both sides of the I-V characteristic, i.e. coming from  $P^+$  and from  $P^-$  and obtained an electroresistance of 0.79.

The observed band offsets can be compared to the predictions based on the theory of metal-semiconductor junctions extended to ferroelectric materials by Pintilie *et al.* [171].

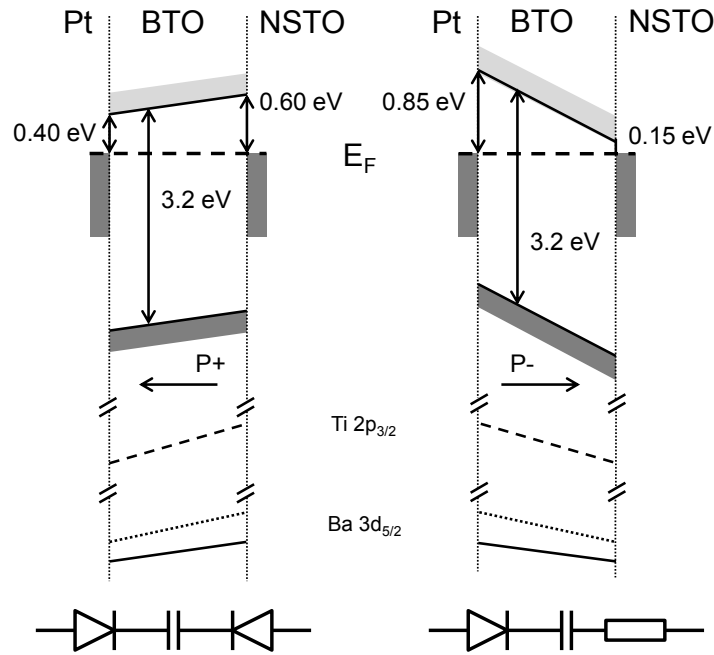


Figure 4.9: Band lineup for the P<sup>+</sup> (left) and P<sup>-</sup> (right) polarization states.

Using Equation (11) from this reference, the theoretical magnitude of barrier height change due to the FE polarization in comparison to a virtual paraelectric (PE) state is:

$$\text{CBO}_{\text{FE}} - \text{CBO}_{\text{PE}} = \sqrt{\frac{eP}{4\pi\epsilon_0^2\epsilon_{\text{op}}\epsilon_r}} \quad (4.2)$$

$P = 0.27 \text{ C/m}^2$  [240] and the optical permittivity is  $\epsilon_{\text{op}} = 5.40$  extrapolated from refractive index measurements [75]. At voltage far from the coercive voltages, capacitance tends to  $\epsilon_r\epsilon_0\frac{A}{d}$ , where  $A = 300 \times 300 \text{ } \mu\text{m}^2$  is the area of the electrode and  $d = 64 \text{ nm}$  is the BTO layer thickness. From Fig. 4.6a, we estimate the dielectric permittivity  $\epsilon_r \approx 90$ . Using these values in equation (4.2), the FE polarization induces a decrease (increase) of 0.30 eV of the top interface conduction band offset in the P<sup>+</sup> (P<sup>-</sup>) state compared to the PE state. The overall upward 0.60 eV shift when switching from P<sup>+</sup> to P<sup>-</sup> is compatible with our spectroscopic measurements.

Fig. 4.9 shows that the P<sup>-</sup> state leads to a highly asymmetric band alignment with a 0.85 eV (0 eV) top (bottom) conduction band offset. The combination of asymmetric electrodes and P<sup>-</sup> (P<sup>+</sup>) FE polarization lead to an increased (decreased) slope of the BTO conduction band. Consequently, BTO in the P<sup>-</sup> (P<sup>+</sup>) state experiences an enhanced (reduced) depolarizing field  $E_{\text{depol}}$  in comparison to a symmetric capacitor. The internal field can be estimated from the slope of the CB over the whole BTO film. We obtain  $E_{\text{depol}} = 130 \text{ kV/cm}$  for the P<sup>-</sup> state. Using the mean coercive voltage  $(V_{c-} - V_{c+})/2$ , we estimate the coercive field to be about 30 kV/cm: a hypothetical P<sup>-</sup> state will always tend to switch back to P<sup>+</sup> in short-circuit boundary conditions (zero voltage). FE instability

due to asymmetric interfaces, produced with the same electrodes but different top and bottom surface termination in the FE, has recently been reported for SRO/BTO/SRO capacitors where the bottom SrO/TiO<sub>2</sub> and top BaO/RuO<sub>2</sub> make the P<sup>+</sup> state unstable [129].

In Ref. [43], Chen and Klein measure a conduction band offset of 0.30 eV (0.95 eV) at the interface between a thin layer of platinum and a single crystal of BTO in the P<sup>+</sup> (P<sup>-</sup>) state. Polarization switching induces a 0.65 eV barrier height shift, to be compared to 0.45 eV in our case. The difference cannot only be due to different energy resolution. Our band offset calculations are the same as Chen and Klein, and  $(E_{Ti2p_{3/2}} - V_{B_{Max}})_{BTO}$  was almost identical in both experiments. For a given material with similar polarization magnitude, a lower barrier shift can be due to a better screening of the ferroelectric polarization, *i.e.* to a smaller screening length. The flux delivered by an undulator in a synchrotron facility is significantly higher than from a laboratory x-ray source and might be responsible for a part of the enhanced screening. However, the data of section 4.2.3 show a rather weak effect of the photon-induced screening. More likely, the interface configuration is responsible for the different screening. As pointed out by Rao *et al.*, the Pt/BTO interface shows multiple configurations with different screening capabilities [178]. The two heterostructure are different and this can explain the different barrier heights. The ferroelectric layer is also not the same. The BTO single crystal studied by Chen and Klein is significantly thicker (0.4 mm) than our BTO thin film (64 nm) leading to a lower depolarizing field hence different interface screening. Their single crystal surface termination and reconstruction are not known and might be different from ours. Finally, the full electrode/ferroelectric/electrode structure is different. They used a symmetric Pt/BTO/Pt capacitor compared to the asymmetric Pt/BTO/NSTO structure presented in this article. The asymmetry has a direct influence on the internal field inside the ferroelectric layer as shown in Fig 4.9. All of these differences can account for the barrier height discrepancies between the two studies. Those studies are clearly only beginning and more systematic studies are required in order to identify the respective contributions.

#### 4.2.5 Electronic band response to applied bias

Although the barrier heights agree with Ref [171], interestingly, switching the polarization does not affect all the core levels in the same way. This may be extremely important because much analysis of band alignment at a FE/electrode interface assumes rigid band shifts for all levels, as in classical semiconductor physics as done by Kraut *et al.* [116] and the rigid-band-shift assumption also underpins equation (4.1). Ti 2*p* core level is shifted by 450 meV compared with 350 meV (200 meV) for the LBE (HBE) Ba 3*d*<sub>5/2</sub>. A rigid shift in the BTO band structure due to the polarization-induced interface dipole cannot explain the different shifts of the Ti and Ba core-levels [241]. This is unexpected and has not been previously reported in the literature. Our group has also observed such

behavior on BTO single crystals using spatially-resolved photoemission spectroscopy on oppositely-polarized domains (unpublished results currently being written up).

First principles calculations [203] showed that near the top electrode of an SRO/BTO/SRO heterostructure in a  $P^+$  polarization state, the Ti 3d conduction band cross the Fermi level, allowing charge spillage into the BTO [203]. A  $P^+/P^-$  shift of 1.4 eV in the band structure is predicted, with the conduction band next to the top electrode in the  $P^+$  state 0.3 eV below the Fermi level. This so-called pathological case of band bending is due to the LDA band gap in these calculations of 1.8 eV. However, if we take the experimental band gap of 3.2 eV and assume that both the VBM and the conduction band offset are increased by about the same amount (0.7 eV) with respect to the LDA values, then the experimental conduction band offset should be 0.4 eV above the Fermi level, which is precisely what we measure. Such a good agreement is most probably fortuitous, for example, the higher screening by Pt with respect to SRO used by Stengel *et al.* might modify this value. The  $P^+/P^-$  shift in the band positions will certainly change as a function of the screening efficiency of the electrode material, which explains why we measure a shift of 0.45 eV compared to the theoretical prediction of 1.4 eV. Nevertheless, the trend is consistent with the interpretation that the origin of the band alignment lies in the imperfect screening by the electrode creating a voltage drop and the residual depolarizing field inside the FE, altering the electrostatic potential. Yet, this still does not account for the differences in the experimentally measured  $P^+/P^-$  Ba and Ti core level shifts.

To do so, we tentatively propose an explanation based on dynamical charge in the vicinity of the interface, i.e. the change in polarization created by an atomic displacement, which is a more measurable quantity. By describing the changes in orbital population as a function of atomic displacements, dynamical charge gives a direct picture of changes in covalency/ionicity [76]. The relevant quantity is the Callen (or longitudinal) charge since we apply a non-zero external field to the BTO layer. It is related to the transverse or Born effective charge by the optical dielectric tensor [134]. DFT simulations on the Pt/BTO interface calculated the lattice mediated contribution to the static inverse capacitance in terms of the Callen dynamical charge and the longitudinal force constant [204]. The latter has a short range interaction and creates an enhanced response at the interface. The Callen charge of Ti is twice as high as that of Ba. We suggest that higher dynamical charge may result in a larger core level shift in the FE state with respect to the PE state. Changes in the local atomic distortions due to the proximity of the electrode interface could magnify or reduce this effect. For TiO<sub>2</sub>-terminated PbTiO<sub>3</sub> surfaces, Fechner *et al.* showed that the layer polarization near the surface (the two first TiO<sub>2</sub> layers and the first PbO layer) is reduced in comparison to bulk layers although in their calculations bulk position were fixed, which created an additional depolarizing field [65]. In our experiment, the Ba 3d HBE shift (200 meV), representative of the BaO layer near the interface is indeed smaller than the LBE shift (350 meV), more sensitive to BaO layers deeper in the film.

Velev *et al.* investigated Pt/TiO<sub>2</sub>-terminated BaTiO<sub>3</sub>/Pt tunnel junctions using first-principles calculations [229]. The Ti displacement at the interface layer in the P<sup>-</sup> state is close to the centrosymmetric PE position, whereas in the P<sup>+</sup> state, the Ti displacement is enhanced relative to bulk FE value. This asymmetry in the atomic displacements should translate in an additional binding energy shift between the corresponding photoemission spectra when switching from P<sup>-</sup> to P<sup>+</sup>. The effect is greater for Ti because it is at the interface where the asymmetry in atomic positions is a maximum. Ti also has a larger dynamical charge than Ba, thus the effect of asymmetric atomic displacements on the BE should be amplified. Evidence of similar phenomena can be seen in High-Resolution Transmission Electron Microscopy (HRTEM) measurements on the BiFeO<sub>3</sub>/(La, Sr)MnO<sub>3</sub> (BFO/LSMO) interface by Chang *et al.* [41]. For BFO the polarization is dominated by the relative displacement of Fe with respect to Bi. Their results show that on approaching the interface, the layer polarization in BFO is progressively reduced to zero over 4-5 atomic layers for polarization pointing away from the LSMO into the BFO (P<sup>-</sup>). For polarization pointing towards the LSMO (P<sup>+</sup>) it remains constant until the interface. Although the ferroelectric induced atomic distortions are more complex in BFO than in BTO (rotation and tilting of oxygen octahedra) and the electrode material is not the same, it appears that in the vicinity of the interface the atomic displacements are strongly modified with respect to those in the bulk FE state, and that these modifications depend on the polarization.

We may therefore have a model which goes beyond the often used non-interacting electron semiconductor vision and which at least qualitatively might account for differential shifts of electron bands under applied bias near the interface. However, this remains hypothetical and further work is necessary, particularly to measure experimentally the layer dependence of the response of the electronic bands to applied voltages. First principles calculations of the Callen charge variations near the interface *under bias* would also be extremely useful. Far from the interface, the dynamical charge for the two polarization states should of course be the same. In addition, we hope that this experimental work will encourage further theoretical work to accurately relate the concept of dynamical charge and core-level binding energies measured by photoemission spectroscopy. Photoemission spectroscopy with bias would be a powerful tool for measuring these quantities.

#### 4.2.6 The role of oxygen vacancies

In transition-metal oxides, oxygen vacancies can migrate under the effect of an electric field and drastically changes the barrier properties of the interfaces. This phenomenon can be the cause of resistive switching behavior [236] similar to the one we measure. Using electrical measurements, Zhang *et al.* explained the diode-like behavior of a Pt/BTO/NSTO heterostructure by oxygen vacancy migration when applying a bias [247]. Here, just as before application of bias, there is no LBE shoulder in the Ti 2*p* spectra typical of Ti<sup>3+</sup> due to oxygen vacancies. This can be seen from Fig. 4.10 which shows P<sup>+</sup> and P<sup>-</sup> Ti 2*p*

spectra, after correction for the polarization-induced BE shifts ( $\Delta_{BE}$ ) extracted from Table 4.1. The spectra are identical showing that migration of bulk oxygen vacancies towards one interface due to the applied electric field is unlikely and cannot explain the conduction changes, contrary to the conclusions of Ref. [247]. However, the latter used thinner films, thus higher applied fields under bias. Their films also had an rms roughness of 5 nm for a 20 nm film, whereas ours show single unit cell steps and flat terrace and therefore are expected to have a much lower defect concentration.

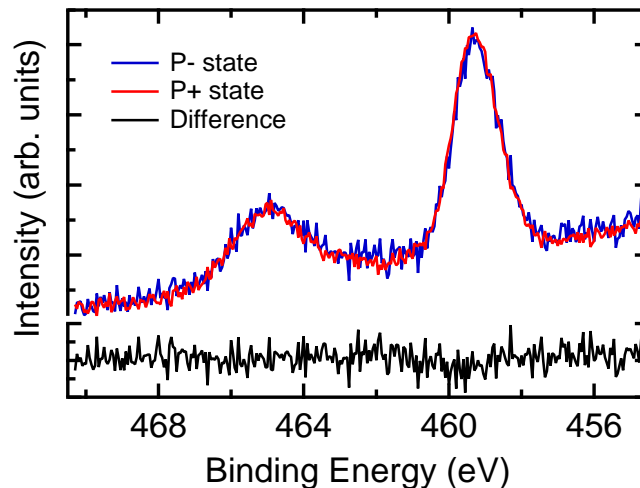


Figure 4.10: Ti  $2p$  spectra for  $P^+/P^-$  and their intensity difference.  $P^-$  spectra has been shifted in binding energy using ( $\Delta_{BE}$ ) from Table 4.1. The two spectra have identical shape.

#### 4.2.7 Time-resolved Response to Applied Pulses

The previous sections demonstrate the use of photoemission experiments with bias application. A possible route for a further understanding of such devices is the investigation of their time-dependent properties. Delay-line detectors allow detection of photoemitted electrons with a time-resolution down to 5 to 10 ns [21]. It gives access to time-resolved analysis of device in the  $10^{6-8}$  Hz frequency range. In this section, we apply bias pulses on the Pt/BTO/NSTO capacitor to probe the time-resolved chemical and electronic structure of the Pt/BTO interface. An equivalent circuit model is used and has a behavior which compares well with the photoemission results on the real system. This shows the potential of time-resolved photoemission spectroscopy to follow the chemical/electronic changes in working model microelectronic devices, here a ferroelectric capacitor.

To investigate the time-resolved properties of the structure described in Figure 4.3a, we use a train of voltages pulses following the methodology of the P.U.N.D. pulse train described in Chapter 2–Section 2.3.1. One is a non-switching pulse ( $P^-$  to  $P^-$ ), the other is a switching pulse ( $P^-$  to  $P^+$ ). This design aims to discriminate the phenomena due to ferroelectric polarization and those due to the whole device. At  $t = 0$ , we set

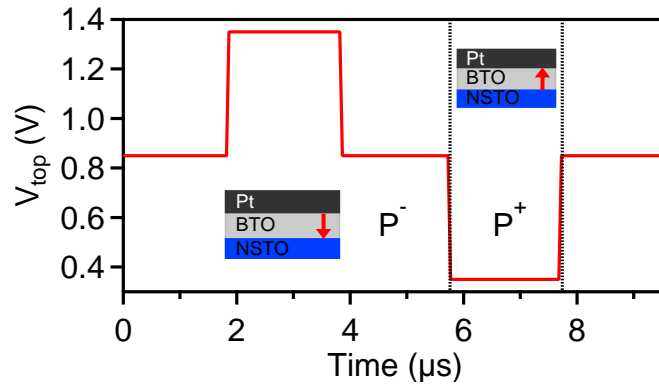


Figure 4.11: Train of pulses applied on  $V_{\text{top}}$  as a function of time. The first pulse is non-switching  $P^-$  to  $P^-$ , the second is switching  $P^-$  to  $P^+$ .

$V_{\text{top}} = 0.85$  V which corresponds to the  $P^-$  state. At  $t = 1.9$   $\mu\text{s}$ , an upward pulse  $V_{\text{top}} = 1.35$  V is applied with a rise (fall) time of 2.5 ns and a width of 2  $\mu\text{s}$ , then  $V_{\text{top}}$  goes back to 0.85 V (idle state). At  $t = 5.8$   $\mu\text{s}$ , a downward pulse  $V_{\text{top}} = 0.35$  V is applied with a rise (fall) time of 2.5 ns and a time width of 2  $\mu\text{s}$  (see Figure 4.11). Photoemitted electrons are acquired with a time step of 45 ns (22 MHz). The pulse train is repeated a thousand times in order to acquire a sufficient photoemission signal/noise ratio.

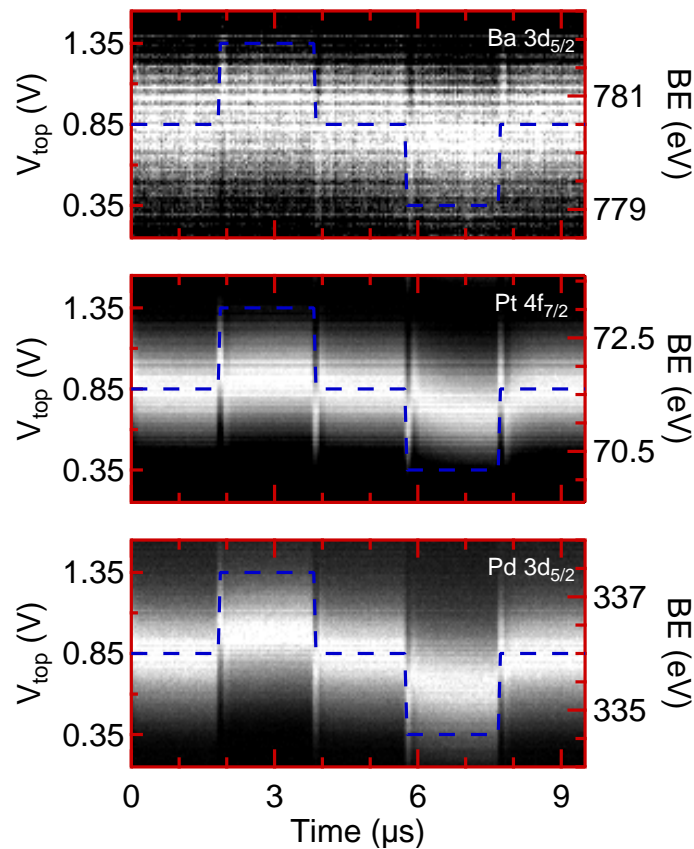


Figure 4.12: Photoemitted electron intensity as a function of time and binding energy (BE) for the three core-levels Pd  $3d_{5/2}$ , Pt  $4f_{7/2}$  and Ba  $3d_{5/2}$ . The blue dotted curve shows the pulse train.

Figure 4.12 shows photo-emitted electron intensity as a function of time and binding energy for the three core-levels Pd  $3d_{5/2}$ , Pt  $4f_{7/2}$  and Ba  $3d_{5/2}$ . It shows the effect of the voltage pulses on the core-level spectrum, but this representation is not well-suited for further analysis. Rather, we developed a fitting procedure which subtracts the secondary electron background and fits the spectrum to a Gaussian shape for each time step. It returns the binding energy position of the peak as a function of time and allows a proper comparison of core-level response to the electrical excitation. The width of each peak is kept constant after a preliminary fit procedure using a reference spectrum taken with both electrodes grounded. We checked that the spectra shape for every core-level did not change with time. This is the case except for the spectra close to the rise and fall of the bias pulses. At this moment, the peaks are highly distorted leading to spikes in the time-dependent binding-energy curves.

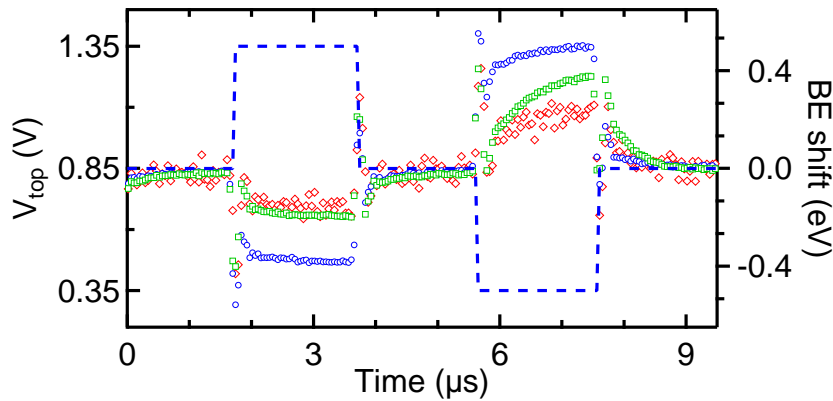


Figure 4.13: Time-dependent evolution of the binding energy (BE) shifts for the Pd  $3d_{5/2}$  (blue circles), Pt  $4f_{7/2}$  (green squares) and Ba  $3d_{5/2}$  (red diamonds). The blue dotted curve shows the pulse train.

Figure 4.13 shows the time evolution of the binding energy obtained from the fitting procedure. All spectra are referenced relatively to their binding energy in the idle state at  $V_{\text{top}} = 0.85$  V. As expected, for the upward (downward) pulse, every core-level shows a decrease (increase) in binding energy due to the more positive (negative) voltage applied on the top electrode in comparison to the idle state. At every pulse rise and fall, spikes are measured in the binding energy. This is likely due to a parasitic capacitance with a very small time-constant in the circuit. Indeed, a capacitance with a time-constant below the rise time of the generator will act as a *differentiator*, *i.e.* will differentiate the signal with respect to time. The time derivative of a step pulse is the delta function we observe as binding energy spikes here. For the non-switching pulse, the core-levels reach a steady value with a time-constant below  $1 \mu\text{s}$ . Then, while Pd roughly follows the source pulse ( $\Delta\text{BE} = 0.4$  eV compared to a pulse of 0.5 V), Pt and Ba only shift by 0.20 eV. For the  $\text{P}^-$  to  $\text{P}^+$  pulse, the core-level shifts occur with a higher time constant (above  $2 \mu\text{s}$ ) and every core-level shift is quantitatively different.

To better understand the time-dependent behavior of the capacitor, we conducted numerical simulations using PSpice software (part of the Orcad package from Cadence Design Systems<sup>6</sup>). This software can simulate the electrical response of a circuit under a pulse excitation. An upward (downward) pulse identical to the experimental one was used to simulate the circuit response. The software cannot take into account the non-linear ferroelectric properties of the BTO layer of this capacitor, nor the consequences on the barrier height of ferroelectric polarization. Therefore, two circuits were developed to emulate the capacitor in the  $P^+$  and  $P^-$  states. We assume the resistances between the pulsed source and the palladium pad (mostly due to silver paste contacts) and between the palladium pad and the platinum electrode (due to an imperfect contact) are ohmic. Besides, the resistance values should not change with ferroelectric switching and are therefore kept constant. The Pt/BTO/NSTO stack is modeled by a RC circuit. Simulating the binding-energy displacement of the barium core-level is a complex issue since it cannot easily be related to a particular probing point in an electrical circuit, contrary to platinum core-level which simply is the top electrode of the RC circuit.

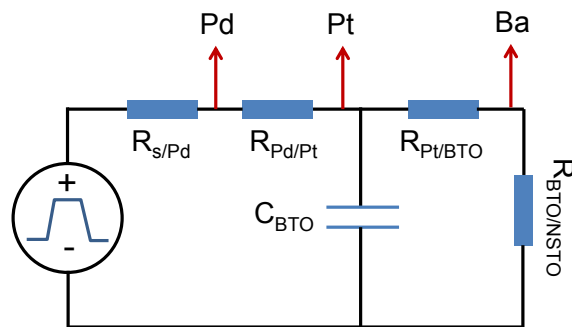


Figure 4.14: Equivalent circuit used in the PSpice simulation software. The components values are summarized in Table 4.3.

With soft x-ray ( $h\nu = 1100$  eV), photoemission experiment probing depth is about 3-4 nm: only the first layers of BTO are probed. We tentatively suggest that the barium core-level we measure by photoemission spectroscopy can be seen as a voltage probe between a resistor modeling the Pt/TiO<sub>2</sub>/[...] interface, and a resistor modeling the bottom part of the stack [...] /BaO/TiO<sub>2</sub>/NSTO. These two resistances and the whole device capacitance can be altered by ferroelectric polarization. Figure 4.14 displays the equivalent circuit used in the simulations. The values which give the best fit to experimental data are given in Table 4.3 for each polarization state. The result of the simulation are shown in Figure 4.15.

For the non-switching pulse, the model circuit fits well the experimental values. The low resistance values for the Pt/BTO/NSTO stack are consistent with the high-current measured by static electrical experiment, as shown in Figure 4.6b. For the  $P^-$  to  $P^+$  pulse, the Pt/BTO/NSTO stack resistances are much higher, consistent with the lower

<sup>6</sup><http://www.electronics-lab.com/downloads/schematic/013/>

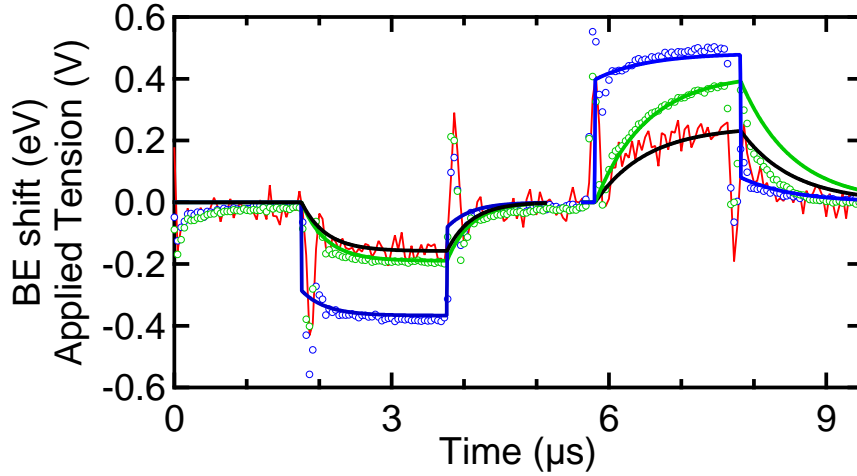


Figure 4.15: Results of the electrical simulations (plain lines) of the experimental Pd  $3d_{5/2}$  (blue circles), Pt  $4f_{7/2}$  (green squares) and Ba  $3d_{5/2}$  (red line) evolution. The simulated curves are generated from the parameters of  $P^-$  (Table 4.3, right column) from  $t = 0$  to  $t = 5.8 \mu\text{s}$  and from the parameters of  $P^+$  (Table 4.3, left column) from  $t = 5.8$  to  $t = 9.2 \mu\text{s}$ .

		$V_{\text{top}} = 0.35 \text{ V } (P^+)$	$V_{\text{top}} = 0.85 \text{ V } (P^-)$
$R_{\text{s/Pd}}$	( $\Omega$ )	210	210
$R_{\text{Pd/Pt}}$	( $\Omega$ )	280	280
$R_{\text{Pt/BTO}}$	( $\Omega$ )	17000	50
$R_{\text{BTO/NSTO}}$	( $\Omega$ )	20000	250
$C_{\text{BTO}}$	(nF)	1.8	1.5

Table 4.3: Best fit values for the components of the equivalent circuit of Figure 4.15.

current. However, any further interpretation of the physical meaning of these resistances is probably dubious since the chemical and electronic reorganization occurring at a metal/ferroelectric interface cannot be simply modeled by a resistance/capacitance model. Indeed, this is the main argument of the previous section. For the non-switching pulse, both rise (“charge”) and fall (“discharge”) sequence fits well the experimental binding energy shifts. On the contrary for the  $P^-$  to  $P^+$  pulse, the model circuit fits well the rise sequence but is far off for the fall sequence. Indeed, at the end of the downward pulse when the voltage goes back to  $V_{\text{top}} = 0.85 \text{ V}$ , the system switches back to the  $P^-$  state. The dynamic of polarization switching in thin films is expected to be in the picosecond to nanosecond range depending on the pulse characteristics [214], the ferroelectric layer properties [149] and the electrodes [108]. This phenomenon is faster than our time resolution. Therefore, the stack instantaneously switches to the  $P^-$  state when  $V_{\text{top}}$  goes from 0.35 V to 0.85 V: the simulation for the  $P^-$  state circuit is a much better fit for the fall sequence.

This experiment is more of a proof of concept for the investigation of realistic devices in operating conditions with time-resolved photoemission spectroscopy. With the spatial and time resolution available, valuable information on the physics of the interface is not accessible. However, using x-ray pulses photoemission, time-resolved experiments can reach the picosecond resolution [21] and thus access valuable information on the chemical/electronic influence of polarization switching as a function of time. Moreover, in our case the spatial resolution is limited by the beam spot size, approximately  $100 \times 100 \mu\text{m}^2$  and prevent from studying realistic microchips. However, the development of Photoelectron emission microscopy with *in-situ* bias application and time-resolved detectors might lead the way for *in-operando* chemical/electronic analysis of realistic device.

### 4.3 Investigation of the SRO/BTO Interface

The screening mechanism provided by SrRuO<sub>3</sub> is very different from the one provided by platinum. Indeed, Gerra *et al.* expect oxide electrodes might be beneficial for the properties of ferroelectric capacitors: in spite of lower carrier mobility than pure metal electrodes such as platinum or gold, ionic relaxations at the interface between the oxides provide an additional, efficient screening mechanism for the depolarizing field [213]. In this section, we study the polarization dependent band alignment and electronic structure at a SRO/BTO interface using XPS with *in-situ* biasing. The structure chosen is a symmetric SrRuO<sub>3</sub>/BaTiO<sub>3</sub>/SrRuO<sub>3</sub> (SRO/BTO/SRO) capacitor. We observe a polarization-induced shift in barrier heights of 0.40 eV when polarization switches. This shift is smaller than those measured in previous experiments and is related to the good screening provided by the epitaxial SRO electrodes, mainly due to ionic displacement of SRO atoms. This is opposite to the screening mechanism provided by Platinum electrodes mainly due to free carriers from the metal.

#### 4.3.1 Growth of the SRO/BTO/SRO Heterostructure

The bottom SRO thin film was grown on a SrTiO<sub>3</sub> (001) (STO) substrate using pulsed laser deposition (PLD) using a KrF excimer laser ( $\lambda = 248 \text{ nm}$ ) [61]. Prior to film growth, the STO substrate was cleaned using buffered HF solution and rinsed in deionized H<sub>2</sub>O, followed by annealing under oxygen atmosphere to obtain a clean, atomically flat STO surface [103]. The bottom SRO thickness is 20 nm, then a BTO layer of 50 nm is deposited and finally a 5 nm top SRO layer covers the structure. The full structure is deposited in the same UHV unit in a single procedure ensuring clean interfaces.

The interface configuration is a crucial parameter in metal/ferroelectric/metal structure since change in termination at the interface lead to significantly different proper-

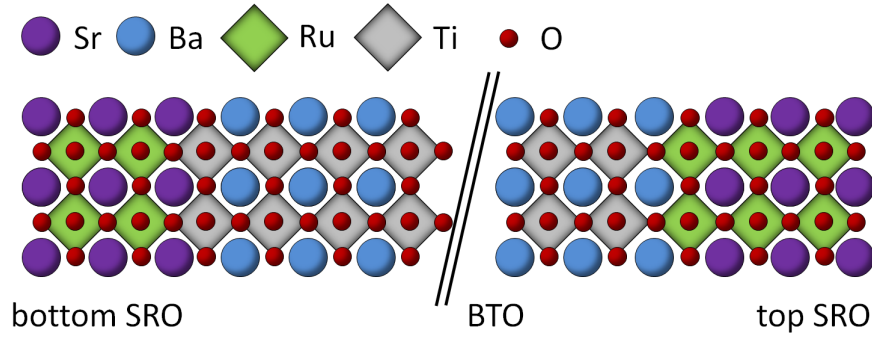


Figure 4.16: Schematic of the heterostructure, only the BTO layers closest to the interfaces are represented. The top interface is  $\text{TiO}_2\text{-BaO-RuO}_2\text{-SrO}$ . The bottom interface is  $\text{RuO}_2\text{-SrO-TiO}_2\text{-BaO}$ .

ties [74, 129]. In our case, it has been shown that the bottom STO is SrO terminated [61, 197], leading to  $\text{RuO}_2\text{-SrO-TiO}_2\text{-BaO}$  for the bottom interface. On the contrary, the BTO surface is BaO terminated leading to a  $\text{TiO}_2\text{-BaO-RuO}_2\text{-SrO}$  top interface [198]. The structure is shown in Figure 4.16.

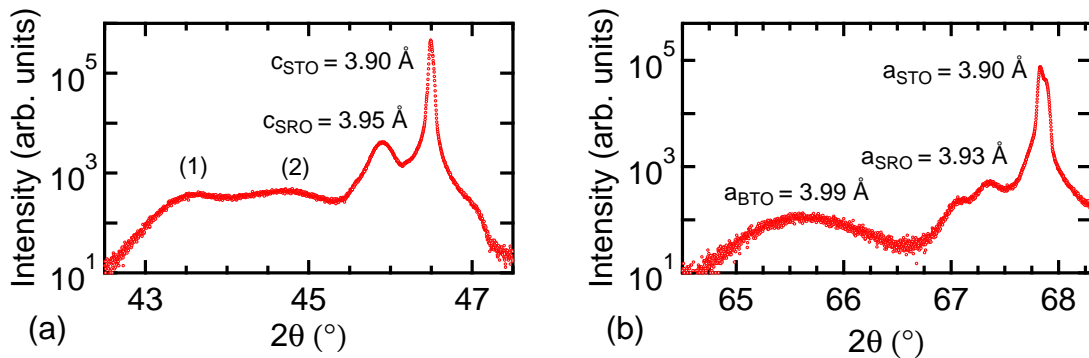


Figure 4.17: (a) (002) peaks for fully-strained BTO (1) and relaxed BTO (2), SRO and STO, (b) (202) peaks for relaxed BTO, relaxed SRO, strained SRO on STO and STO.

A X-ray diffractometer with a 1.6 kW fixed anode (Cu  $K\alpha$  radiation,  $\lambda = 1.5406 \text{ \AA}$ ) is used to measure the bottom SRO, BTO and top SRO in and out-of-plane parameters as shown in Figure 4.17. The signal coming from the (002) crystallographic direction gives access to the lattice constant  $c$  (out-of-plane) of each layer. Obviously, the signal from the STO substrate is the strongest ( $c_{\text{STO}} = 3.90 \text{ \AA}$ ), followed by the SRO ( $c_{\text{SRO}} = 3.95 \text{ \AA}$ ). Finally, BTO shows two contributions: one from the first layers of fully-strained BTO ( $c_{\text{BTO}(1)} = 4.15 \text{ \AA}$ ), the other from relaxed BTO ( $c_{\text{BTO}(2)} = 4.05 \text{ \AA}$ ). The scan along the (202) direction gives access to the lattice constant  $a$  (in-plane). Figure 4.18 shows the reciprocal space probed by the XRD measurements: this scan is centered on the STO lattice constant, then the sample is tilted to access the in-plane parameters of the relaxed layers. Again, the signal from STO ( $a_{\text{STO}} = 3.90 \text{ \AA}$ ) is the strongest and consists of a double peak which might be due to crystallographic defects in the substrate. Then, the double structure is attributed to the SRO layers, but it is not obvious to allocate

one peak to a particular layer of SRO. Finally, the large peak is due to relaxed BTO ( $a_{\text{BTO}} = 3.99\text{\AA}$ ).

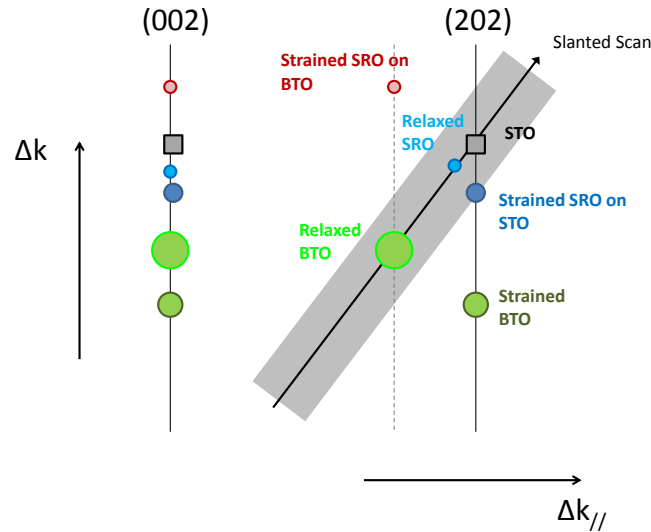


Figure 4.18: Reciprocal space scanned by the XRD experiments on SRO/BTO/SRO//STO for a scan along (002) and a slanted scan along (202).

The full device architecture is shown in Figure 4.19a and as been described in the Section 4.1.2. The device was introduced in ultrahigh vacuum ( $10^{-10}$  mbar) in the photoemission set-up of the GALAXIES Beamline<sup>7</sup> at the SOLEIL synchrotron radiation source [51]. The  $(100 \times 100) \mu\text{m}^2$  beam could be directed onto a single top electrode located by a map of the whole sample. This map is obtained by scanning the surface with the photon beam while measuring Pd 3d photoemission spectrum. The intensity of the intensity at the binding energy of the Pd  $3d_{5/2}$  core-level is reported in Figure 4.19b. A photon energy of 6894.10 eV was used to optimize the signal from the BTO close to the interface (estimated probing depth of  $\approx 15$  nm). The overall energy resolution was better than 200 meV. The sample-holder allows *in-situ* bias application and electrical measurements via high quality coax wires to limit parasitic behavior due to the electrical environment.

### 4.3.2 Electrical Characterization

After the micro-fabrication processes, the C–V characteristic (Figure 4.20a) shows a butterfly loop with coercive voltages of  $V_{c-}$  of 0.35 V ( $V_{c+}$  of -0.05 V) corresponding to a  $P^+$  to  $P^-$  ( $P^+$  to  $P^-$ ) switching. The asymmetry observed in the C–V loop is likely due to the asymmetric configuration of both interfaces. According to Gerra *et al.* the BaO –  $\text{RuO}_2$  termination is detrimental to ferroelectricity, and the  $P^-$  polarization is much more stable than the  $P^+$  polarization due to a downward dipole in the first  $\text{RuO}_2$  layer opposing the  $P^+$  polarization [74].

<sup>7</sup><http://www.synchrotron-soleil.fr/Recherche/LignesLumiere/GALAXIES>

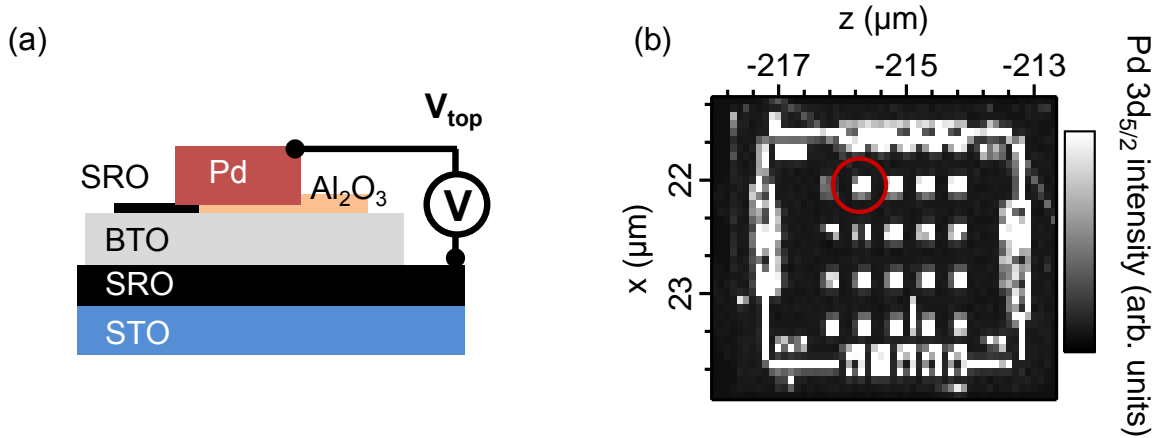


Figure 4.19: (a) Schematic of the capacitor, (b) Pd 3d intensity map for the SRO/BTO/SRO/STO sample showing 20 identical SRO/BTO/SRO capacitors ( $(300 \times 300) \mu\text{m}^2$ ) on the  $(5 \times 5) \text{mm}^2$  surface, allowing location of the wired capacitor (red circle). The wire is even visible in this case.

J–V measurement (Figure 4.20b) shows a Schottky-like conduction for both negative and positive voltages applied on top electrode, and no significant change in current occurs when switching polarization contrary to Pt/BTO/NSTO heterostructure [180]. This back-to-back diodes structure is not surprising considering the 0.7 eV difference in work function between BTO (4.5 eV) and SRO (5.2 eV).

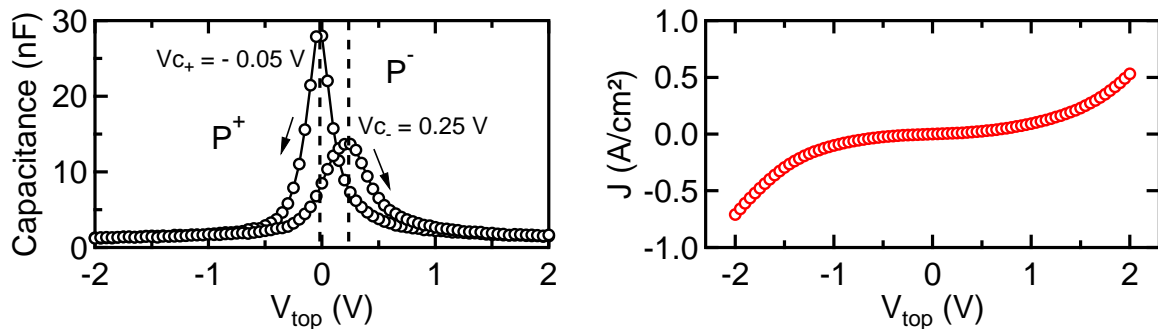


Figure 4.20: (a) C–V measurements and (b) J–V measurements for SRO/BTO/SRO.

### 4.3.3 Photoelectron Spectroscopy with Applied Bias

We conducted hard x-ray photoemission spectroscopy for two saturated polarization state, i.e. P<sup>−</sup> with a positive voltage on the top electrode  $V_{\text{top}} = +1 \text{ V}$  and P<sup>+</sup> with  $V_{\text{top}} = -1 \text{ V}$ . An additional set of measurement has been conducted at ground potential ( $V_{\text{top}} = 0 \text{ V}$ ). Figure 4.21 shows the spectra for  $V_{\text{top}} = 0 \text{ V}$  and Figure 4.23 shows the sets of spectra for the two saturated polarization states.

## Bias-independent Features

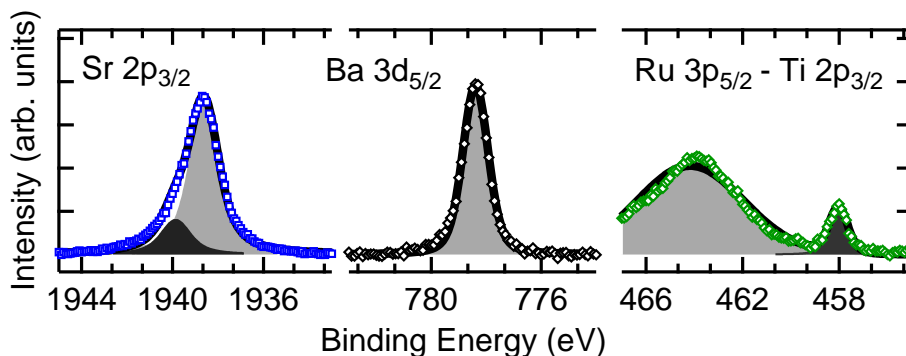


Figure 4.21: Photoemission spectra taken at  $V_{\text{top}} = 0$  V for the Sr  $2p_{3/2}$  (left), Ba  $3d_{5/2}$  (middle) and Ru  $3p_{3/2}$  - Ti  $2p_{3/2}$  (right).

The secondary electron background has been removed using a Shirley background [199]. Sr  $3p$ , Ba  $3d$  and Ti  $2p$  spectra are fitted with Voigt functions. The FWHM of the Sr  $3p_{3/2}$ , Ba  $3d_{5/2}$  and Ti  $2p_{3/2}$  are 1.55 eV, 1.10 eV (Ba  $3d_{5/2}$ ) and 0.90 eV (Ti  $2p_{3/2}$ ). The Ru  $3p_{3/2}$  core-level is fitted using a broad, non-physical Gaussian peak uniquely to be able to fit the much more important Ti  $2p_{3/2}$  core-level spectrum.

We used the Sr  $2p_{3/2}$  core-level from the top electrode as a reference for binding energy shifts. This spectrum has two components. As often in perovskite thin films, the high-binding energy (HBE) component is attributed to the surface of SRO due to Ru loss or segregation [115, 145] and the low-binding energy (LBE) component is due to bulk SRO. The surface related component is probably due to reducing conditions during the micro-fabrication processes. Using the ground potential experiment, we obtain binding energy of 1940 eV (1938.50 eV) for the HBE (LBE) component.

At the interface between SRO and BTO, the very broad Ru  $3p_{3/2}$  core-level hides part of the Ti  $2p$  core-level from BTO [145]. Fortunately, Ti  $2p_{3/2}$  is still clearly separated from Ru  $3p_{3/2}$ . The spectrum does not show any low-binding energy shoulder due to reduced Ti caused by oxygen vacancies. Therefore, we expect that there is a very low concentration of oxygen vacancies (i.e. below our detection limit of 1%) in the BTO.

In the case of SRO/BTO interface, Ba  $3d_{5/2}$  core-level spectrum do not show a high binding energy component, contrary to previous photoemission results on Pt/BTO [180, 187] and BTO free surfaces [96, 233]. The higher probing depth alone cannot explain the complete suppression of the surface-related component. To confirm this behavior, we did HAXPES on a non-patterned SRO (5 nm)/BTO (20 nm)/SRO/STO heterostructure also grown by PLD<sup>8</sup>. The measurements were conducted at the P09 beamline<sup>9</sup> of the PETRA III synchrotron. In this HAXPES setup, we used a photon energy of 5946 eV

<sup>8</sup>This thin film was grown by Cristian Teodorescu's group (<http://lab30.infim.ro/> at the National Institute of Materials Physics in Romania.

<sup>9</sup>[https://photon-science.desy.de/facilities/petra\\_iii/beamlines/p09\\_resonant\\_scattering\\_and\\_diffraction/index\\_eng.html](https://photon-science.desy.de/facilities/petra_iii/beamlines/p09_resonant_scattering_and_diffraction/index_eng.html)

and the overall energy resolution was better than 150 meV. The Ba  $3d$  core-level has been acquired at normal emission (take off angle  $\theta = 0^\circ$ ) and grazing emission ( $\theta = 60^\circ$ ). By doing this, we expect any component due to the SRO/BTO interface configuration to be greatly enhanced at grazing emission (smaller probing depth) compared to normal emission (higher probing depth). Then, this experiment can be compared to normal versus grazing emission measurements done on the free surface of a BTO thin film and on the normal emission spectrum of a Pt/BTO interface (both are described in Section 4.2). Figure 4.22 shows the  $Ba3d_{5/2}$  spectra for the three configurations. For every set of spectra, the fitting function was a Voigt function with a FWHM of 1.20 eV.

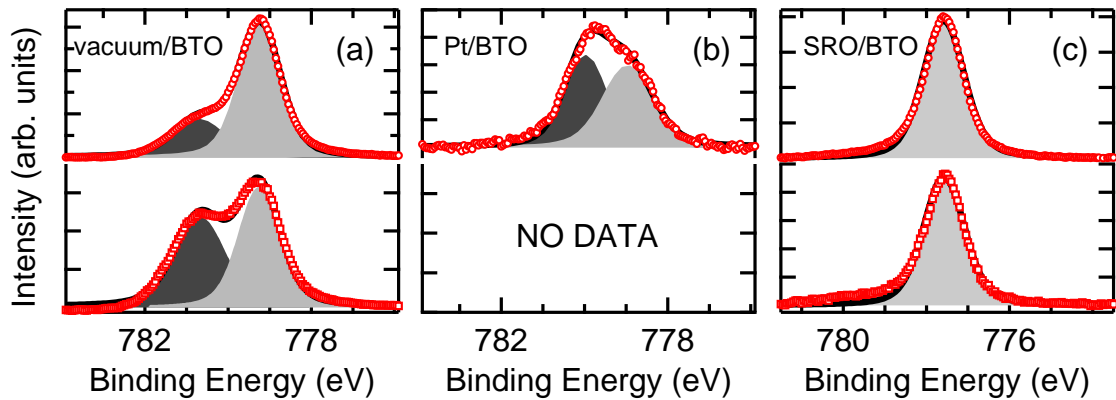


Figure 4.22:  $Ba3d_{5/2}$  core-level spectra of a BTO layer for different interface configurations and take off angles. Top panels show the normal emission (red circles) and bottom panels show the grazing emission (red squares) data for the (a) vacuum/BTO, (b) Pt/BTO and (c) SRO/BTO interface.

The Ba  $3d_{5/2}$  spectrum of the SRO/BTO structure does not show a HBE shoulder (Figure 4.22c). It was impossible to fit the spectrum with two non-trivial components. The phenomenon observed in the patterned sample is therefore confirmed on this heterostructure. On the contrary, the Pt/BTO interface and the free surface of BTO both show a high-binding energy shoulder which clearly depends on the take-off angle. The environment of the topmost layer barium is therefore different in the SRO/BTO case in comparison to the Pt/BTO interface and the free surface of BTO. In the SRO/BTO case, we expect the BTO film to be BaO terminated which is different from the case of the previous section on Pt/BTO. In that situation, the cause of a HBE component in Ba core-levels is the under coordinated barium at the surface layer [96]. In the case of the SRO/BTO interface, it seems that the  $RuO_2$  interface layer provides similar chemical environment to barium as  $TiO_2$  does in bulk BTO suppressing any interface-related component. This is only possible because of the perfect epitaxy of SRO on BTO. To further uphold this interpretation, high-resolution transmission electron microscopy (HR-TEM) experiments on the structure would provide an additional proof of the perfect epitaxy and interface configuration in our particular experiment.

Core-Level	$V_{\text{top}}$		$\Delta_{BE}$ wrt Sr $2p_{3/2}$
	-1.00 (P <sup>+</sup> )	+1.00 (P <sup>-</sup> )	
Sr $2p_{3/2}$	1937.60	1939.60	0.00
Ba $3d_{5/2}$	777.50	779.10	-0.40
Ti $2p_{3/2}$	457.20	458.80	-0.40

Table 4.4: Binding energy (eV) for the SRO/BTO interface core-levels when applying different biases  $V_{\text{top}}$  (V) (column 1,2) and shift with respect to Sr  $2p_{3/2}$  BE shift (column 3). Bottom electrode is grounded.

### Bias-dependent Features

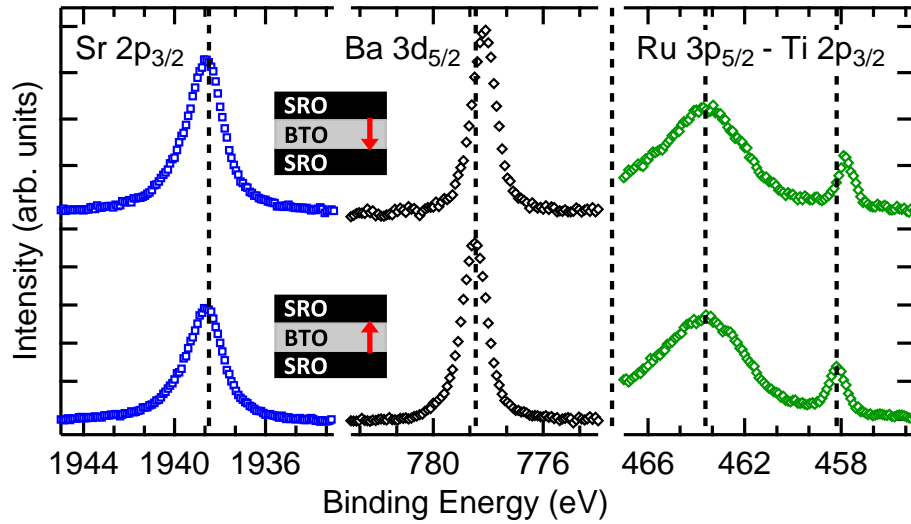


Figure 4.23: Photoemission spectra for the P<sup>-</sup> (top) and P<sup>+</sup> (bottom) FE states for the Sr  $2p_{3/2}$  (left), Ba  $3d_{5/2}$  (middle) and Ru  $3p_{3/2}$  - Ti  $2p_{3/2}$  (right). The top (bottom) spectra have been shifted by 1.00 eV towards higher (lower) BE using Sr  $2p_{3/2}$  spectra.

The application of  $V_{\text{top}} = +1$  V (-1 V) leads to an upward (downward) binding energy shift of 1 eV as expected for a metallic electrode. The core-levels spectra do not show any change in shape with bias application. We report binding energy shifts for the Ba  $3d_{5/2}$  and Ti  $2p_{3/2}$  core-levels in Table 4.4 with respect to the shift of Sr  $2p_{3/2}$ : an upward binding energy shift of 400 meV is observed for both Ti  $2p_{3/2}$  and Ba  $3d_{5/2}$  when switching from P<sup>-</sup> to P<sup>+</sup>. The same result was obtained using  $V_{\text{top}} \pm 0.8$  V.

Using data from several BTO thin films, we know the quantity  $(E_{\text{Ti}2p_{3/2}} - V_{\text{BMax}})_{\text{BTO}} = 455.95$  eV (see Section 4.2 and Ref. [180]) and that BTO has a band gap of 3.2 eV [237]. Following again Kraut [116], we can translate Table 4.4 in valence band offsets of 1.85 eV (2.25 eV) for P<sup>-</sup> (P<sup>+</sup>) polarization, or a conduction band offset of 1.35 eV (0.95 eV) for P<sup>-</sup> (P<sup>+</sup>) polarization. These band offsets are consistent with the back-to-back diode-like behavior of the capacitor. Figure 4.24 shows the band lineup measured by the photoemission experiment as a function of polarization. Since,

photoemission does not give access to the bottom interface, the barrier heights at the bottom interface on Figure 4.24 are purely hypothetical: similar shifts and band offsets at both interfaces have been assumed. This is only schematic since C–V curve shows that the different terminations lead to a different ferroelectric behavior. Therefore, there is no experimental reason for equal shifts at both interfaces.

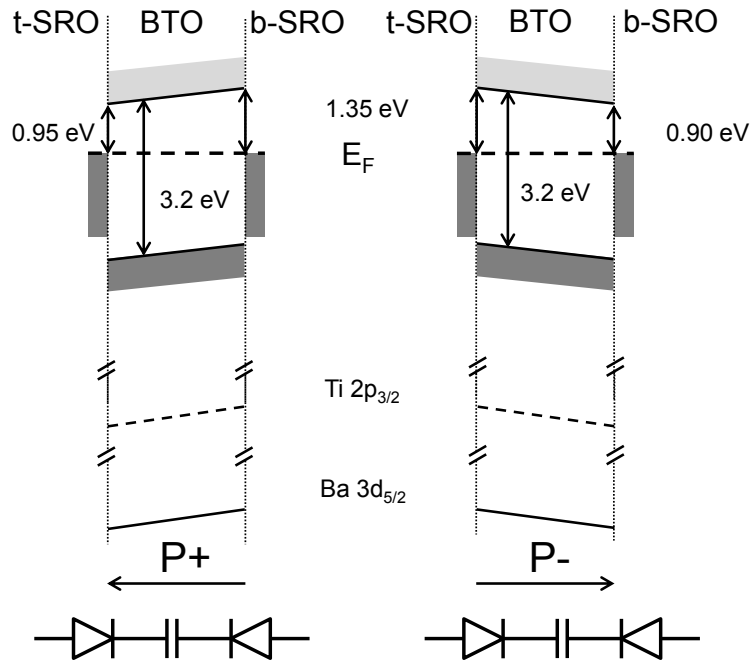


Figure 4.24: Band lineup for the P<sup>+</sup> (left) and P<sup>-</sup> (right) polarization states. t-SRO (b-SRO) stands for top (bottom) SRO electrode. Since, photoemission does not give access to the bottom interface, the barrier heights at the bottom interface are purely hypothetical.

#### 4.3.4 Discussion

Shifts in binding energy are due to the electrostatic difference in the interfacial dead layer due to the imperfect screening of the ferroelectric polarization over a given screening length, as previously seen in Chapter 3 and Section 4.2. According to several first-principles calculations, the screening length of such a SRO/BTO interface is of 0.2 Å [101, 213], and therefore can be approximated in our photoemission experiment as an interfacial dipole which changes signs with polarization switching. The spectra from the buried core-levels do not show any change in shapes, confirming that the dead-layer thickness, or equivalently the screening length does not extend over several atomic layers. Otherwise, we should see a significant broadening of the photoemission peaks from buried BTO due to the inhomogeneous field over several angstroms [45]. Our band offset shift is well below the shifts reported by Chen and Klein on BTO single crystals and RuO<sub>2</sub> electrode [43]. However, it is likely that in our case the epitaxial interface provides an additional, efficient screening mechanism. Contrary to pure metals electrodes, the

penetration of the bound polarization charges inside the SRO film is made possible by the ionic structure of the oxide. When taking into account this additional mechanism, the effective screening length of an epitaxial SRO/BTO interface is halved in comparison to a model taking only into account free-carriers screening [213]. This might be why we observe such small shifts in comparison to previous results on similar, but non epitaxial, interface [43]. This interpretation is further supported by the absence of any high-binding energy shoulder in Ba  $3d_{5/2}$  spectra (see above). Again, HR-TEM images of the structure would be a great addition to this study to investigate the penetration of the polarization inside the SRO electrode, as observed for instance at the LSMO/BFO interface [41].

## Conclusion

In this chapter, the influence of the ferroelectric polarization on the chemical and electronic structure of a metal/ferroelectric interface has been investigated. Photoemission spectroscopy with *in-situ* bias application has been used on two different interfaces, namely Pt/BTO and SRO/BTO. Though the growth of platinum on BTO is not epitaxial, the high-mobility carriers in the metal provide an efficient screening of the ferroelectric polarization. The band offset shifts by 450 meV when switching polarization and this goes with a Schottky to Ohmic conduction for the full Pt/BTO/NSTO capacitor. Moreover, we observe differential shifts for the Ti and Ba core-levels, which might be due to their different dynamical charges. On the contrary, the SRO/BTO interface is epitaxial and the band offset shifts by 400 meV when switching polarization. The even better screening at the interface is due to the ionic displacements in the SRO, an efficient mechanism not available in the poorly bounded Pt/BTO interface and which makes up for the low mobility of carriers in SRO.

In future work, one should focus on tunneling films, *i.e.* with a ferroelectric layer thickness below 5 nm. In that case, very small electrodes (1  $\mu\text{m}$ ) are necessary to prevent damaging current density. The ideal photoemission-based end-station for probing such systems would be a PhotoElectron Emission Microscope with *in-situ* bias application. This raises new challenges, mostly because of the high electric fields involved in PEEM experiments which might interfere with the connectors but it could lead to significant breakthrough. The influence of layer termination is another topic of great value, and photoemission spectroscopy with bias application can surely bring valuable information on differently-terminated interfaces, or engineered interfaces such as the SRO/STO (1 u.c.)/BTO investigated by Lu *et al.* [129]. On an experimental point of view, hard x-ray photons are necessary to have a wide range of probing depth (typically from 5 to 20 nm). By changing photon energy or take-off angle, depth profiling of the electronic and chemical properties are possible with HAXPES experiments [164, 200]. In addition, recent experiment showed the feasibility of photoelectron emission microscopy using hard x-ray, a setup named HAXPEEM [191]. The combination of probing depth, spatial resolution and

energy resolution would be a great step forward in the investigation of realistic devices.



# General Conclusion

Screening phenomena at the interface of an electrode and a ferroelectric layer is a rich topic in material science, with important implications for the development of industrial devices. In this thesis, several screening mechanisms have been investigated on  $\text{BaTiO}_3$  and  $\text{BiFeO}_3$ .

Below a critical thickness,  $\text{BiFeO}_3$  thin films on  $(\text{La,Sr})\text{MnO}_3/\text{SrTiO}_3$  adopt a polydomain configuration with 4 nm-wide stripes of opposite polarization. This conclusion comes from the theoretical resolution of paradoxical experimental results on  $\text{BiFeO}_3$  thin films with decreasing thickness. On the one hand, the tetragonality ratio measured by XRD is constant for all thicknesses which is the signature of a non-zero polarization magnitude in the BFO film. On the other hand, the work function difference between oppositely-polarized domains as measured by PEEM drops to zero below a critical thickness of 7 nm. This is the signature of a zero polarization magnitude. To resolve this contradiction, first-principle-based, effective hamiltonian calculations have been conducted and show that a phase with nanostripes of opposite polarization direction is indeed more stable for thicknesses below 7 nm. This phase has a non-zero polarization magnitude which explains the tetragonality ratio. But on the scale of the spatial resolution of the PEEM (about 50 nm, *i.e.* about 10 nanostripes), the averaged polarization magnitude is zero which explains the loss of work function contrast. Therefore, domain re-organization appears as an efficient mechanism to screen the depolarizing field of very thin ferroelectric films.

This is also true of the screening provided by intrinsic free carriers in the ferroelectric slab. For high-enough oxygen vacancy concentration in  $\text{BaTiO}_3$  single crystals, we observe the loss of polarization-induced intensity contrast. The electrons released by oxygen vacancies serve as screening charges and this leads to a thinner dead-layer thickness, or equivalently a smaller screening length. The direct consequence is the loss of work function contrast as measured by PEEM. In addition to an enhanced screening, we find that oxygen vacancies promote the downward over upward polarization.

At the interface between a metallic electrode and a  $\text{BaTiO}_3$  thin film, a binding energy shift in the electronic bands is observed when polarization switches. This shift comes from the switching interface dipole due to the imperfect screening at the electrode/ferroelectric interface. The quantitative estimation of the band shift allows an evaluation of the screening capabilities of a given electrode. Platinum electrodes provides screening via free carriers with high-mobility, even though the interface is not epitaxial. In our case, this leads to

a 0.45 eV binding energy shift. On the one hand, the polarization-induced shift explains well the diode-like behavior of the full Pt/BTO/NSTO heterostructure. On the other hand and contrary to semiconductors material, we observe that the electronic shift is not rigid, namely titanium core-levels shifts more than those of barium. This phenomenon might be due to different dynamical charges at the interface with platinum for Ti and Ba. On the SRO/BTO interface, different mechanisms are responsible for the screening of the polarization. As expected by *ab-initio* calculations from the literature, the ionic relaxation of the SRO interface layer is crucial for the screening of the BTO polarization charges. This is the reason for such a good polarization screening in SRO which is a much worse metal than platinum. Such process is not available for non-epitaxial interface such as Pt/BTO.

This thesis shows the potential of photoemission-based techniques for the investigation of ferroelectric materials. The electron microscopy techniques provide non-contact, full-field, spatially-resolved information on the work function, which can be directly related to polarization magnitude or dead-layer thickness, two key quantities for ferroelectric-based devices. These are unique techniques to *quantitatively* measure such quantity in tunneling thin films. Photoemission spectroscopy with *in-situ* bias gives access to electronic and chemical information of an interface in operating conditions. In the case of ferroelectrics, one can obtain the properties of the interface for opposite polarization switched *in-situ*.

This work will be carried on by using photoemission microscopy and spectroscopy on other ferroelectric materials and heterostructures. Monitoring polarization magnitude in ultra-thin films of  $\text{PbTiO}_3$  would be interesting for the sake of comparison with other techniques found in the literature. An ongoing thesis focuses on a precise understanding of the relationship between oxygen vacancies and ferroelectric properties using a combination of electron microscopy and *ab-initio* calculations. As for photoemission spectroscopy with applied bias, the measurement of dynamical charges close to the interface, if confirmed, would be a significant step forward since no other experimental techniques gives access to these quantities. Of course, photoemission spectroscopy with bias should be applied on other materials beyond the field of ferroelectrics. For instance, the behavior of oxygen vacancies at the  $\text{LaAlO}_3/\text{SrTiO}_3$  interface under bias would be interesting to study with such technique.

# Appendix A

## Electron Emission Microscopy

Some of the most crucial properties of materials systems, *i.e.* properties having exciting fundamental interest or potential industrial applications, are often determined by the surface or the interface between two materials in a layer stack. This is the main point of this thesis which reports the study of ferroelectric surfaces and interfaces. Recently, surface science research is driven by materials such as graphene, topological insulators or multilayers of oxides. The crucial importance of the surface is the cause of the rapid development of surface imaging over the past thirty years, notably with scanning probe microscopy - namely Atomic Force Microscopy and Scanning Tunneling Microscopy - but also with electron microscopy.

In 1933, Brüche showed that a magnetic lens accelerating photo-emitted electrons to high energy can be used to image surfaces [32]. This was the beginning of surface imaging using cathode lenses, also called immersion lenses. Following Brüche's early work, many years of technological improvements in electron lenses and ultra-high vacuum setups were needed to significantly improve spatial resolution and intensity contrasts [20]. A significant rise in material science investigation based on electron microscopy techniques occurred after the work of Telieps and Bauer in the 1980s on the low energy electron microscope [218]. Another significant turning point was the development of dedicated synchrotron radiation sources which provides high brilliance photon flux. It allows photo-electron emission imaging in a reasonable amount of time and x-ray absorption imaging, most notably dichroic absorption imaging applied to magnetic materials [208]. Recent developments give access to time-resolved electron microscopy [231] and energy-resolved electron microscopy as presented in this appendix.

Two surface microscopy techniques based on electrons have been used during this thesis:

- PhotoElectron Emission Microscopy (PEEM) which is based on the photoemission process (see Chapter 1). More specifically, I will present a particular PEEM, the [NanoESCA](http://www.omicron.de/en/products/nanoesca/)<sup>1</sup> from Omicron nanotechnology GmbH, which combines an optic column

---

<sup>1</sup><http://www.omicron.de/en/products/nanoesca-/instrument-concept>

giving spatial resolution and a original energy analyzer stage giving energy resolution while keeping spatial resolution.

- Low Energy Electron Microscopy (LEEM) which is based on a slightly different conceptual framework. I used the [LEEM III<sup>2</sup>](#) from Elmitec GmbH.

PEEM and LEEM are distinct surface imaging techniques though very complementary. The imaging columns are often similar and the spatial resolution are comparable. However, the fundamental process are different: PEEM is based on the photoelectric effect whereas LEEM is based on the interaction between a collimated slow electron beam and the surface. That is why the combination of both techniques provides different information for similar field of view and spatial resolution.

## A.1 PhotoElectron Emission Microscopy

A PhotoElectron Emission Microscope is a photon in - electron out technique, as any photoemission-based experiments. The added value in comparison to photoemission spectroscopy is in the imaging optics which conserve the spatial provenance of the photo-emitted electrons. Imaging optics consist of an immersion lens (objective lens in Figure A.1) which extracts the electrons with a high (12 to 24 kV) electrostatic field. The optic column is often equipped with adjustable contrast apertures of different sizes and stigmators to compensate axial astigmatism. To obtain both spatial and energy resolution, an energy filtering stage has to be added. Several setups exist in the literature [19, 219], but we focus on the nanoESCA shown in Figure A.1, a solution proposed by Omicron nanotechnology.

In this instrument, the energy filtering stage consists in two hemisphere analyzers. The *double* hemisphere geometry is necessary to correct spatial aberration due to the spherical trajectories of the electrons in the analyzer. Indeed, in a spherical electrostatic field, the trajectories of the electrons only coincide after a complete revolution to generate an image without spherical aberrations. The so-called transfer lens couples the first and the second spherical hemispheres to simulate a complete revolution [59, 60]. At the exit of the analyzing stage, projecting lenses magnify the electron image onto the acquisition stage. This last process consists in the succession of multichannel plates to enhance the electron signal, a fluorescent screen and a CCD camera. The instrument has an energy resolution range from 50 meV to 300 meV and a spatial resolution down to 20 nm in ultimate conditions [60, 245].

Figure A.1a shows the schematic of the NanoESCA. The instrument can operate in three modes (see Figure A.1b) depending on the requirements of the experiment:

- (1) is the direct PEEM mode: the PEEM optics collect photo-emitted electrons of any kinetic energy. The signal is therefore mostly due to secondary electrons in that

---

<sup>2</sup><http://www.elmitec-gmbh.com/Leem.php?Bereich=LEEM3>

case. The output of this mode is an PEEM image  $I = f(x, y)$  where  $x, y$  are the spatial coordinates.

- (2) is the micro spectroscopic mode: a specific micron-sized area of the sample can be selected using the field aperture, also called iris aperture, and then probed with classical photoemission spectroscopy. The output of this mode is a photoemission spectrum  $I = f(E_K)$ .
- (3) is the energy-filtered PEEM mode: both energy and spatial provenance can be resolved. The output of this mode is a stack of PEEM images for different kinetic energies  $I = f(E_K, x, y)$ . From this stack, pixel-by-pixel spectra can be extracted and analyzed similarly as in classical photoemission spectroscopy. Furthermore, this mode is ideal for imaging the reciprocal plane of the photo-emitted electron. In that case,  $I = f(E_K, k_x, k_y)$  where  $k_x, k_y$  are the in-plane components of the electron wave vector [135].

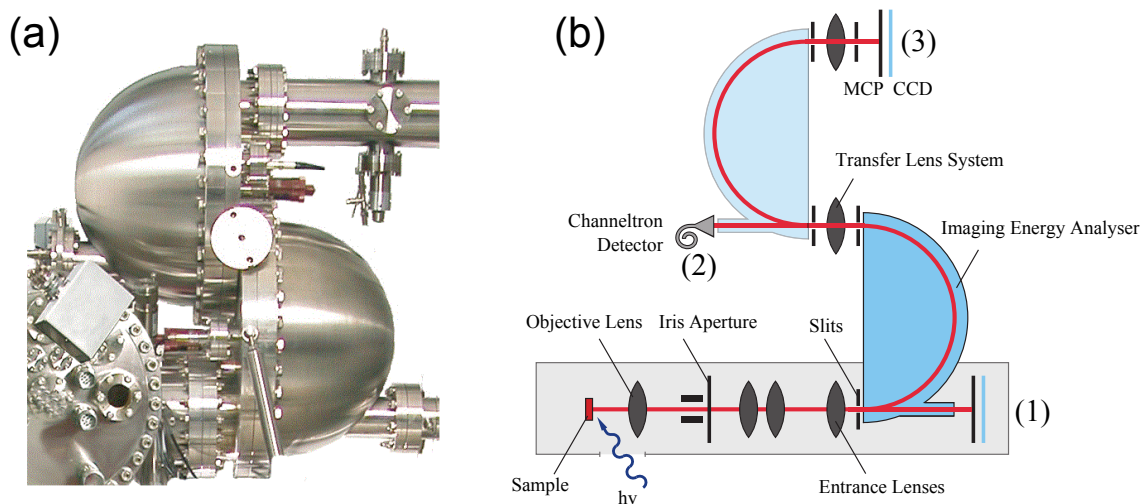


Figure A.1: NanoESCA PEEM photography (a) and schematics (b). It can operate in three modes: (1) direct PEEM, (2) micro-Spectroscopy and (3) energy-filtered PEEM.

The origins of intensity contrast in PEEM are manifold. Firstly, without considering the energy resolution, gradients in surface potential, *i.e.* electrical fields, can significantly deviate photo-emitted electrons causing accumulation (high intensity) or depletion (low intensity) of electrons in some areas of the PEEM image (Figure A.2). These fields can be caused by surface topography, heterogeneous doping in p-n junctions [123], surface charges induced by ferroelectric domains or in-plane fields induced by ferroelectric domain walls. Secondly, the energy resolution permits additional contrasts. Using core levels electrons, the quantitative chemical composition of the sample can be spatially resolved [13]. Using the threshold of photoemission, a map of the work function within the field of view can be extracted and reveals, for instance, the heterogeneous number of layers of epitaxial

graphene (see Appendix B) or the different polarization in a ferroelectric surface (see Chapter 3).

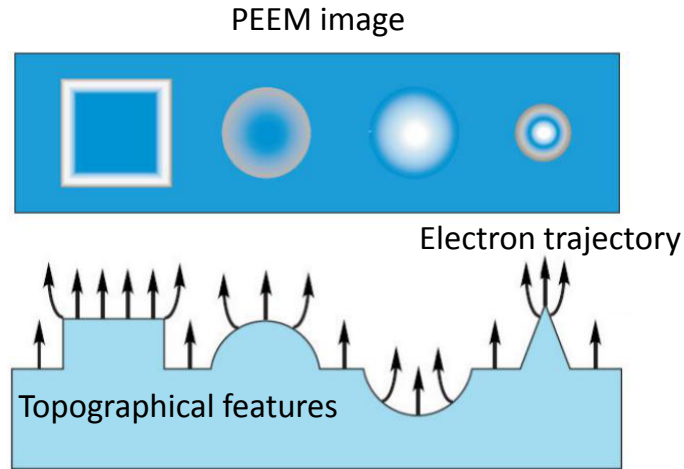


Figure A.2: Topography contrast in PEEM due to local electrostatic fields. Image taken from Ref. [155].

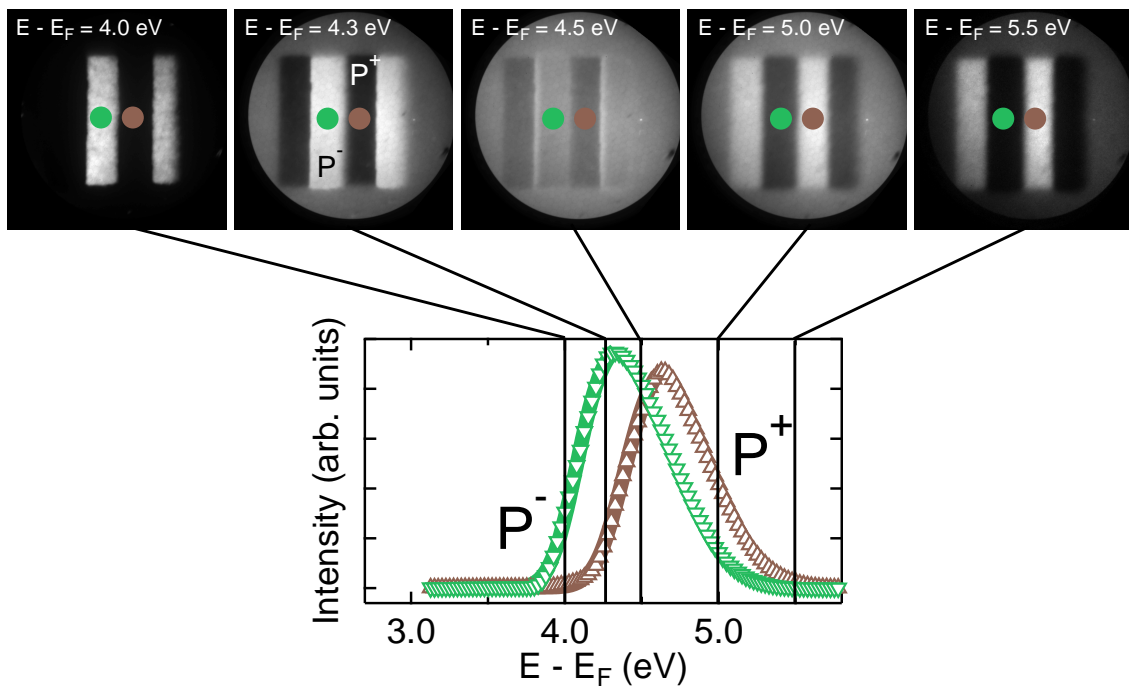


Figure A.3: Typical PEEM image serie on a domain-patterned 70 nm thin  $\text{BiFeO}_3$  film. The photoemission threshold spectrum (triangles) is constructed by taking the mean intensity value from a  $P^+$  (brown) or  $P^-$  (green) region. Then, the spectra can be fitted using an error function (solid lines).

A typical use of PEEM in this thesis is displayed in Figure A.3. The sample is the 70 nm thin  $\text{BiFeO}_3$  film presented in Chapter 3–Section 3.1. Oppositely-polarized domains ( $P^-$  and  $P^+$ ) have been written by PFM. The image serie was acquired over the photoemission threshold region with a mercury lamp excitation ( $h\nu = 4.9$  eV). The lateral

resolution was estimated to be 200 nm and energy resolution 200 meV. Figure A.3 shows 5 images (chosen from a stack of 71 images, from 3.0 to 6.0 eV with a 0.025 eV energy step) to illustrate how the threshold spectrum from each region is obtained. The spectrum can be fitted by an complementary error function (erfc) which gives an accurate value of the inflection point, i.e. the work function  $\Phi_S$  in the case of photoemission threshold [182, 215]. The mapping procedures will be described further in Appendix C. After fitting every spectrum extracted from every pixel of the stack of images by this function, we obtain the work function map of the sample, as shown in Figure A.4.

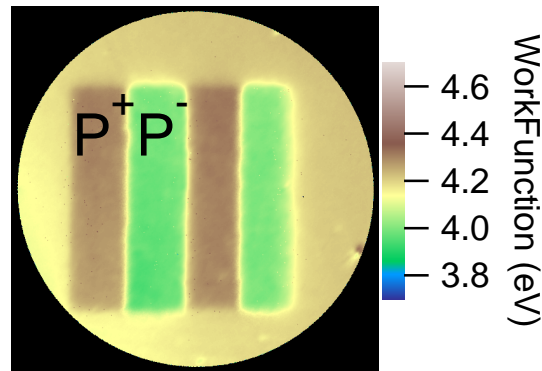


Figure A.4: Work function  $\Phi_S$  map of a domain-patterned 70 nm thin BiFeO<sub>3</sub> film.

Similar procedures can be applied to core-level spectra to obtain chemical maps. Automated procedures for both core-level and work function mapping will be described further in appendix C.

## A.2 Low Energy Electron Microscopy

Contrary to photoemission-based microscopy, LEEM is an electron in - electron out technique. It was developed mainly by E. Bauer [18] and W. Teliëps [218]. It is based on the interaction between an incident beam of low-kinetic energy electrons and a solid-state surface. As in photoemission-based techniques, the use of electrons limits the probing depth to a few nanometers and requires ultra-high vacuum.

Figure A.5 shows the schematic of a typical low-energy electron microscope. It is composed of the illuminating column which focuses a monochromatic beam of electrons - of a few eV kinetic energy - onto the surface. If the incident electron beam has a kinetic energy below the surface potential of the sample, it is merely reflected without further interaction. This regime is often referred as the Mirror Electron Microscopy (MEM) regime. For higher kinetic energy, electrons penetrate the surface and interact strongly with the sample. Some of the incident electrons are back-scattered with a probability which depends on the electronic properties of the sample. The electron intensity versus kinetic energy curve is often referred as the *reflectivity curve* of the sample. For instance in a graphene sample, the incident electrons couple with the conduction band

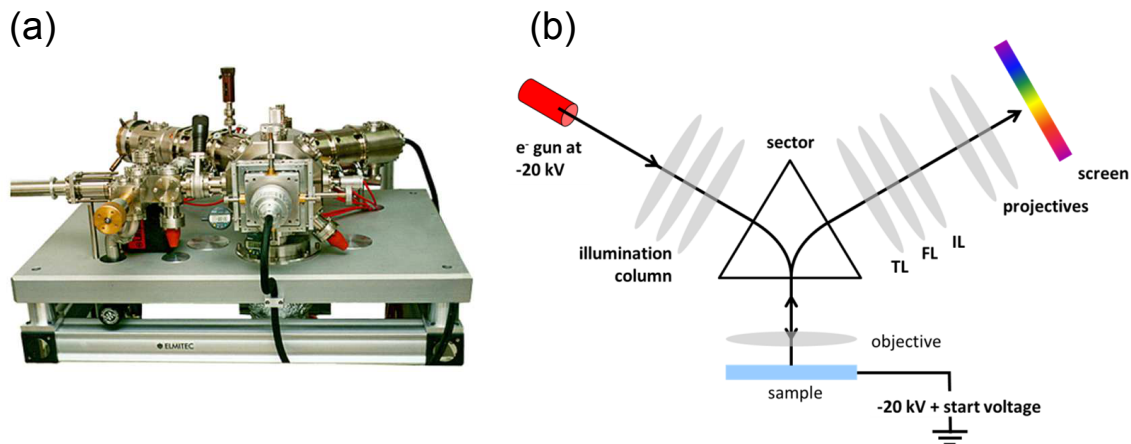


Figure A.5: LEEM III photography (a) and schematics (b). It is composed of the illuminating column which focuses a monochromatic beam of electrons - of a few eV kinetic energy - onto the surface. The reflected and back-scattered electrons are collected by the objective. The most delicate part of a LEEM apparatus is the beam separator (sector) which controls the separation between the illuminating, incident electrons and the imaging, reflected electrons.

states of graphene layers and lead to intensity oscillations in the reflectivity curve. These oscillations are directly related to the number of layers of graphene [88]. The energy transition between the MEM and the LEEM regime can be related to the surface potential of the surface. This feature has been exploited in Chapter 3–Section 3.1.3 on BiFeO<sub>3</sub> thin films. The reflected and back-scattered electrons are collected by the imaging column. As Photoemission microscopes, LEEM allows the imaging of both the real space (LEEM) or reciprocal space (Low-Energy Electron Diffraction, LEED) simultaneously. The most delicate part of a LEEM apparatus is the beam separator which controls the separation between the illuminating, incident electrons and the imaging, reflected electrons.

The energy resolution of such system is limited by the monochromaticity of the incident beam. This beam is generated by an electron gun by thermal emission of a LaB<sub>6</sub> crystal. In practice, the monochromaticity of such electron beams is below the minimal step size of the acquisition system, i.e. 50 meV in this thesis. A typical LEEM image has a field of view of 10 to 50 microns with a spatial resolution of 10 to 20 nanometers, which is better than most PEEMs. Using state-of-the-art aberration-correcting lenses and even smaller field of views, some LEEM end-station can achieve a spatial resolution of 2 nanometers.

Imaging contrast in LEEM can come from many factors. As any electron emission microscopy techniques, it is sensitive to surface electric fields (or equivalently surface potential differences) due for instance to differential doping, surface topography (see the work from Nepijko *et al.* in Refs. [154, 153, 155]) or work function differences. An important feature of LEEM is the possibility to do dark-field imaging. A specific diffraction order (electron momentum) can be selected by a micro-aperture in LEED mode: back in imaging mode, the bright areas are only due to electron with this specific momentum.

It has been widely used in surface science to discriminate areas with different surface reconstruction by selecting LEED spots due to specific crystallographic order [6].

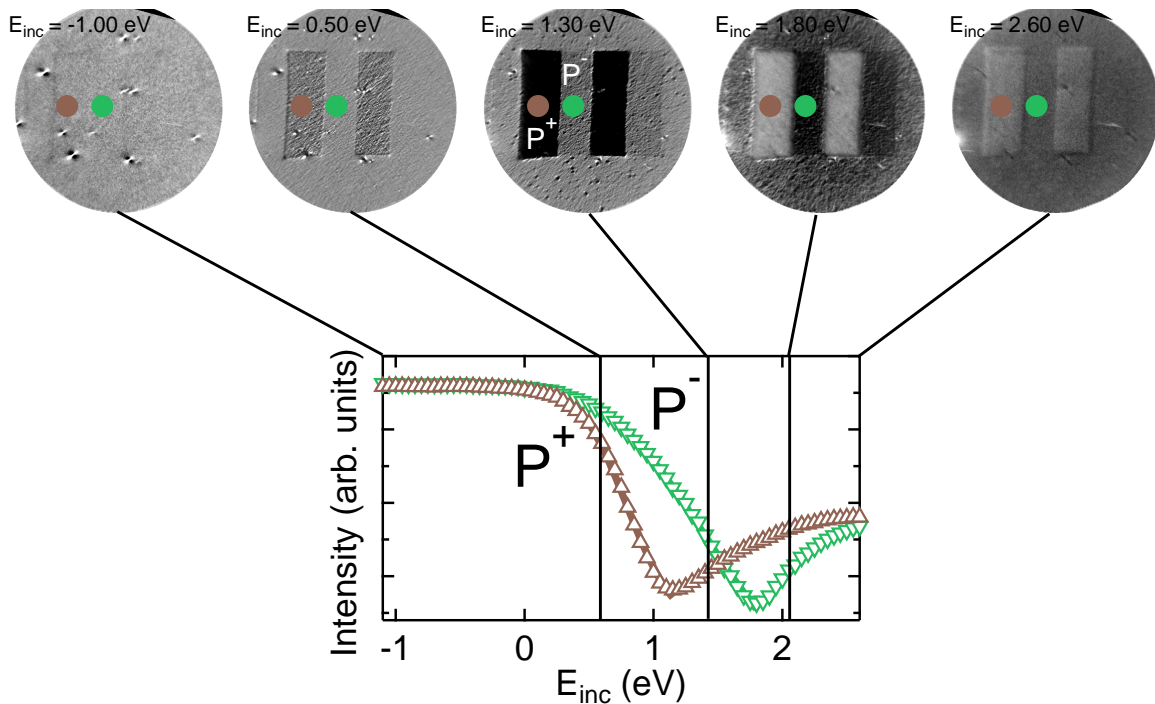


Figure A.6: Typical LEEM image serie on a domain-patterned 70 nm thin  $\text{BiFeO}_3$  film. The reflectivity spectrum (triangles) is constructed by taking the mean intensity value from a  $\text{P}^+$  (brown) or  $\text{P}^-$  (green) region. Then, the spectra can be fitted using an error function (solid lines).

A typical use of LEEM in this thesis is displayed in Figure A.6. The sample is the same as the one presented in the PEEM section. We have measured the electron kinetic energy of the MEM (reflected electrons)–LEEM (backscattered electrons) transition with a spatial resolution of 30 nm. Figure A.6 shows 5 images (chosen from a stack of 91 images, from -1.5 to 3.0 eV with a 0.050 eV energy step) to illustrate how the MEM–LEEM transition from each region is obtained. The spectrum can be fitted by an complementary error function (erfc) which gives an accurate value of the inflection point, i.e. the MEM–LEEM transition point  $E$ . After fitting every spectrum extracted from every pixel of the image stack by this function, we obtain the surface potential map of the sample shown in Figure A.7.

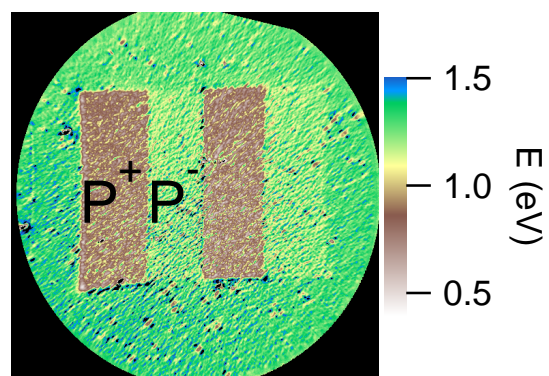


Figure A.7: MEM-LEEM transition  $E$  map of a domain-patterned 70 nm thin  $\text{BiFeO}_3$  film.

# Appendix B

## PEEM investigation of Few-layers Graphene

In addition to the study of ferroelectrics and at the very beginning of this thesis, I used photoemission-based techniques on other materials. Of particular interest is the investigation of epitaxial graphene grown on Silicon Carbide (SiC) substrate using energy-filtered PEEM. In this study, I worked on core-level and photoemission threshold imaging of few layers graphene using PEEM, and developed the mapping procedures described in Appendix B. This work was published in Ref. [135] and has been added to the manuscript after the following introduction.

Graphene is one of the most studied material in solid state physics nowadays<sup>1</sup>. It consists in a two-dimensional honeycomb lattice made of carbon atoms. The properties of graphene has been known since the early theoretical work of P. R. Wallace in 1947 [232]. But research on graphene really peaked after the discovery of a seemingly simple way to isolate layers of graphene from graphite by mechanical exfoliation [159]. This discovery was rewarded by the Nobel Prize six years later<sup>2</sup>. Graphene has exciting electronic properties - charge carriers behave as massless, relativistic particles - suitable for high-performance nano-electronics, mostly because of a very high electron mobility.

Another way to produce graphene is to heat silicon carbide (SiC) at high temperatures (over 1750 K) and under low pressures (below  $10^{-6}$  mbar) to sublimate surface silicon and reduce the remaining carbon atoms at the surface to graphene [22]. Epitaxial layers of graphene grown on SiC have similar electronic properties as exfoliated graphene [23, 67] but are more compatible with the microfabrication processes of the electronic industry [210]. Graphene grown on the C-terminated surface of the SiC substrate - SiC(000 $\bar{1}$ ) - has a particular interest due to a rotational stacking which decouples adjacent graphene sheets [80]. This leads to higher charge carrier mobility and allows potential devices to be less sensitive to thickness variations. However, few-layers graphene (FLG) grown on such substrates show microscopic heterogeneity which might be detri-

---

<sup>1</sup>[http://europa.eu/rapid/press-release\\_IP-13-54\\_en.htm](http://europa.eu/rapid/press-release_IP-13-54_en.htm)

<sup>2</sup>[http://www.nobelprize.org/nobel\\_prizes/physics/laureates/2010/](http://www.nobelprize.org/nobel_prizes/physics/laureates/2010/)

mental to device properties. In spite of massive work on graphene, little is known on the microscopic organization of few-layers graphene on SiC(000 $\bar{1}$ ). Energy-filtered PEEM offers spatially-resolved chemical and electronic information simultaneously which makes it the ideal tool to investigate heterogeneous FLG properties.

In our experiment, the substrate was a 6H conducting SiC(000 $\bar{1}$ ). Graphene was grown by annealing the substrate following a well-know procedure [22, 23] and was cleaned by flash heating before introduction in the ultrahigh vacuum chamber of the PEEM. In this experiment, the PEEM was a NanoESCA and the photon beam was provided by the synchrotron SOLEIL at the branch line of the TEMPO beamline. PEEM images taken at the threshold of photoemission clearly showed the heterogeneity of the sample on the scale of the field of view (53  $\mu\text{m}$ ). A work function map (Figure 5) of the surface reveals five regions of different work functions. It has been shown that each additional layer increases the work function of the FLG because of a smaller charge transfer from the substrate to the surface layer of graphene as thickness increases [66]. Therefore, five different work functions might indicate five different thicknesses. However, the difference in work function of 40 meV between two regions is smaller than expected for this scenario (135 meV according to Ref. [66]). In addition, our LEEM measurements (Figure 3) demonstrates that the sample only shows regions with one, two or three layers of graphene.

To understand this paradox, PEEM images at the C 1s core-level were acquired. Local spectra from the five ROIs show two main components: the lower binding energy component is due to the SiC substrate, the higher to graphene (Figure 8). The signal coming from the buried substrate was used as a probe of FLG thickness. The more graphene layers, the weaker is the signal from the buried SiC. An automatized procedure similar as the one described in Appendix C was written to produce a map of the intensity of the substrate component. Figure 7 correlates the work function to the signal from the substrate for each region. It confirmed that there is no one-to-one correspondence between the work function and the substrate signal, *i.e.* the graphene coverage. The C1s spectra shows additional components which we attributed to the SiC/graphene interface. From the analysis of this additional components as a function of the region, it seems that there is two different interfaces. In the litterature, Scanning Tunneling Microscopy (STM) experiments showed that the upper SiC layer has two possible reconstruction: ( $2 \times 2$ ) and ( $3 \times 3$ ) [89]. This is most likely the cause of the two different SiC/graphene interfaces. So we observed three different possible thicknesses (1,2 or 3 layers as observed by LEEM) and two different graphene/SiC interface environment. This combination leads to five work functions in this particular experiment.

**Microscopic correlation between chemical and electronic states in epitaxial graphene on SiC(000 $\bar{1}$ )**

C. Mathieu

*IRAMIS/SPCSI/LENSIS, F-91191 Gif-sur-Yvette, France and CEA, LETI, MINATEC Campus, F-38054 Grenoble Cedex 09, France*

N. Barrett,\* J. Rault, and Y. Y. Mi

*IRAMIS/SPCSI/LENSIS, F-91191 Gif-sur-Yvette, France*

B. Zhang and W. A. de Heer

*The Georgia Institute of Technology, Atlanta, Georgia 30332-0430, USA*

C. Berger

*The Georgia Institute of Technology, Atlanta, Georgia 30332-0430, USA and CNRS/Institut Néel, BP166, F-38042 Grenoble, France*

E. H. Conrad

*The Georgia Institute of Technology, Atlanta, Georgia 30332-0430, USA*

O. Renault

*CEA, LETI, MINATEC Campus, F-38054 Grenoble Cedex 09, France*

(Received 6 April 2011; revised manuscript received 26 May 2011; published 30 June 2011)

We present energy filtered electron emission spectromicroscopy with spatial and wave-vector resolution on few-layer epitaxial graphene on SiC(000 $\bar{1}$ ) grown by furnace annealing. Low-energy electron microscopy shows that more than 80% of the sample is covered by 2–3 graphene layers. C1s spectromicroscopy provides an independent measurement of the graphene thickness distribution map. The work function, measured by photoelectron emission microscopy (PEEM), varies across the surface from 4.34 to 4.50 eV according to both the graphene thickness and the graphene-SiC interface chemical state. At least two SiC surface chemical states (i.e., two different SiC surface structures) are present at the graphene/SiC interface. Charge transfer occurs at each graphene/SiC interface.  $k$ -space PEEM gives 3D maps of the  $|\bar{k}_\parallel|$   $\pi$ - $\pi^*$  band dispersion in micron-scale regions showing that the Dirac point shifts as a function of graphene thickness. Bragg diffraction of the Dirac cones via the superlattice formed by the commensurately rotated graphene sheets is observed. The experiments underline the importance of lateral and spectroscopic resolution on the scale of future electronic devices in order to precisely characterize the transport properties and band alignments.

DOI: [10.1103/PhysRevB.83.235436](https://doi.org/10.1103/PhysRevB.83.235436)

PACS number(s): 73.22.Pr, 61.48.Gh, 79.60.–i

**I. INTRODUCTION**

With the demonstration of GHz FETs based on epitaxial graphene grown on SiC,<sup>1,2</sup> this material has become the leading candidate for graphene-based electronics. Nonetheless, exploiting the remarkable properties of graphene for carbon based electronics remains an important challenge. The band structure and transport properties of graphene must be either preserved or modified in a reproducible fashion on typical device scales. While a good deal of work has already focused on monolayer graphene grown on the SiC(0001) (Si face),<sup>3</sup> the ability to grow thin graphene films on the SiC(000 $\bar{1}$ ) (C face) has only recently been demonstrated.<sup>4</sup> C-face films offer a particular advantage because of their rotational stacking that effectively decouples adjacent graphene layers.<sup>5,6</sup> This leads to very high mobilities<sup>7,8</sup> and allows devices to be less sensitive to thickness variations. While these systems continue to make progress toward realistic carbon electronics, significant research problems remain. One in particular is the study and control of the graphene-SiC interface.

When graphene is grown on the Si-terminated SiC on SiC(0001) (Si face), the first graphene layer grows on an insulating carbon buffer layer with a  $(6\sqrt{3} \times 6\sqrt{3})R30^\circ$

symmetry.<sup>9</sup> This buffer layer has a graphene structure and can be isolated from the SiC by intercalating hydrogen between the SiC substrate and the buffer layer.<sup>10</sup> However, mobilities in this isolated buffer layer remain low suggesting either some type of prior disorder in the layer before hydrogenation or an effect caused by the hydrogenation itself. Very little is known about the C-terminated SiC(000 $\bar{1}$ ) graphene-SiC interface. However, it is known that the C-face and Si-face interfaces must be very different.<sup>11</sup> X-ray studies show that the atomic density gradient at the interface is different for Si face and C face,<sup>12,13</sup> and core level photoelectron spectroscopy shows clear differences between the two interfaces.<sup>14</sup> Also, unlike the Si face, the C-face interface is known to have two coexisting structures (at least in the early growth phase). Scanning tunneling microscopy (STM) studies have shown that, in UHV growth conditions, poorly ordered  $(2 \times 2)$  and  $(3 \times 3)$  surface reconstructions exist below the first graphene layer.<sup>15</sup> However, these structures may become disordered or simply not exist when growth occurs at higher temperatures. In high-temperature furnace growth, there is no real evidence that the interface has a reconstruction. It is either an ordered  $(1 \times 1)$  or a disordered reconstruction. The most important observation demonstrating that the C-face interface is very different from

the Si face is that C-face graphene has a rotational stacking very different from that of Si-face graphene even when growth temperatures are the same.<sup>5,6,9</sup> This implies that the registry forces, and thus the interfaces, must be different on the two surfaces. Finally the rapid growth of C-face graphene at temperatures lower than those observed on the Si face point to a significant difference in the chemistry of the interface.<sup>9</sup>

In this work we present a detailed study of the C-face graphene-SiC interface. To date, most of the experimental techniques used to study the atomic and electronic structure are area averaged and are therefore not sensitive to variations on the micron scale. Near-field methods such as scanning tunneling microscopy (STM) can reduce the probed area by two orders of magnitude. However STM does not probe the interface itself and still provides very little information on the intervening length scales, which are precisely those of interest in many potential device applications. Recently this intermediate length scale has begun to be explored using low-energy electron microscopy (LEEM). Luxmi *et al.*<sup>16</sup> have studied the morphology of both UHV and argon furnace growth C-face graphene. Their work revealed a great deal of graphene thickness variation in these thick argon grown films.

We focus on the spatial variation of both the electronic structure and chemical bonding of the C-face graphene-SiC interface. The studies were carried out on thin C-face graphene films grown by a controlled Si sublimation technique. In particular, we investigate the chemical homogeneity of the interface, and correlate it with changes in doping, the graphene work function, and graphene's 2D band structure near the Fermi level. We show that the interface is very complicated with local chemical changes that are not all associated with the local graphene thickness. To carry out these studies, we use LEEM, photoemission electron microscopy (PEEM), and x-ray photoemission electron microscopy (X-PEEM). In addition, by using a suitable lens configuration the focal (or diffraction) plane of the PEEM can be imaged to give parallel momentum resolved dispersion curves  $E(k_x, k_y)$ . This technique is known as  $k$ -resolved photoemission electron microscopy ( $k$ -PEEM). Imaging the focal plane in PEEM produces a map for all azimuths simultaneously. Conservation of the component of the electron wave vector parallel to the sample surface automatically transforms this map into one of photoelectron intensity as a function of  $(k_x, k_y)$ , which is a horizontal cut in reciprocal space. Combined with energy analysis, this produces an image in reciprocal space of the local intensity as a function of the wave vector parallel to the surface. For example, the Fermi surface can be acquired in a single-shot experiment.<sup>17</sup>

## II. EXPERIMENT

The substrate used in these studies was a 6H conducting SiC(000 $\bar{1}$ ) from Cree, Inc. Before graphene growth, the sample was first H<sub>2</sub> etched for 30 min at 1400 °C. The sample was then grown in an enclosed graphite RF furnace using the confinement controlled sublimation process, CCS.<sup>4</sup> The growth was done at 1475 °C for 20 min.

Before all measurements, the sample was annealed at 500 °C for 1 minute in UHV to remove surface contamination. The surface cleanliness was checked by Auger electron

spectroscopy and x-ray photoemission (XPS). LEEM was used to quantify the graphene-layer thickness. LEEM experiments were carried out using a commercial Elmitec PEEM/LEEM III with base pressure of  $4 \times 10^{-8}$  Pa. The energy filtered X-PEEM experiments were conducted on the TEMPO beamline of the SOLEIL synchrotron (Saint Aubin, France) using a NanoESCA X-PEEM (Omicron Nanotechnology GmbH).<sup>18,19</sup> A double-pass hemispherical energy analyzer was used to compensate single-analyzer aberrations. This resulted in a PEEM energy resolution of 0.2 eV with a lateral resolution of  $\sim 100$  nm for core level emission. Experiments were conducted in ultrahigh vacuum (UHV) at a pressure of  $6 \times 10^{-9}$  Pa.

The X-PEEM image series was acquired over the photoemission threshold region and the C1s core level ( $h\nu = 654.3$  eV). A  $53 \mu\text{m}$  field of view (FoV) was used with 12 kV extraction voltage. For the real-space PEEM mode (threshold and C1s), a contrast aperture of  $70 \mu\text{m}$  was used; the lateral resolution was estimated to be 100 nm. The analyzer entrance slit was set to 0.5 mm with a 100 eV pass energy to give a resolution of 200 meV. The resolving power of the TEMPO beamline is approximately 5000, giving an overall estimated energy resolution better than 250 meV. Dark images were acquired with the MCP turned off in order to remove camera noise. Flat-field images were acquired to correct for MCP defects. The parabolic non-isochromaticity of the instrument was corrected for all images.<sup>19</sup>

The  $k$ -PEEM results were acquired using the same incident x-ray spot position on the sample as the X-PEEM analysis (beam size  $\sim 100 \mu\text{m} \times 50 \mu\text{m}$  provides uniform illumination). Because of the high extraction voltage between the sample and the lens, the wave vector resolution and the dimensions of the reciprocal-space image are independent of the photon energy for the typical spectral ranges used in these experiments. The lateral spatial resolution in the  $k$ -PEEM mode was purposefully reduced by operating with a full open aperture. This was required to image a sufficient portion of reciprocal space in order to cover a full Brillouin zone. In this setup, the area of interest on the sample surface is chosen by a field aperture situated in an intermediate image plane that was closed down to about  $7 \mu\text{m}$ . A transfer lens then projected the  $1500 \mu\text{m}$  diameter disk of the focal plane via the energy analyzer onto the detector giving a 2D  $k$ -space dimension of about  $\pm 2.5 \text{ \AA}^{-1}$  around the  $\Gamma$  point. The spectrometer resolution was 200 meV, the photon bandwidth 20 meV, and the wave-vector resolution  $\sim 0.05 \text{ \AA}^{-1}$ . The detector response was corrected by the flat field of the detector and camera defects were eliminated using dark images. Operating this way gave a  $\sim 1 \mu\text{m}$  lateral resolution for the band structure imaging.

## III. RESULTS

While Si-face graphene is known to grow oriented  $30^\circ$  relative to the principle SiC(21 $\bar{3}$ 0) direction, multilayer C-face graphene is known to be stacked with sheets within the stack having multiple rotation angles peaked at  $30^\circ$  and  $0^\circ \pm \sim 7^\circ$ . These C-face graphene rotations are due to interleaved rotated graphene sheets with non-Bernal stacking (i.e., non- $60^\circ$  rotations). In thin C-face samples there are only a few rotations. This is demonstrated in the LEED patterns in Fig. 1.

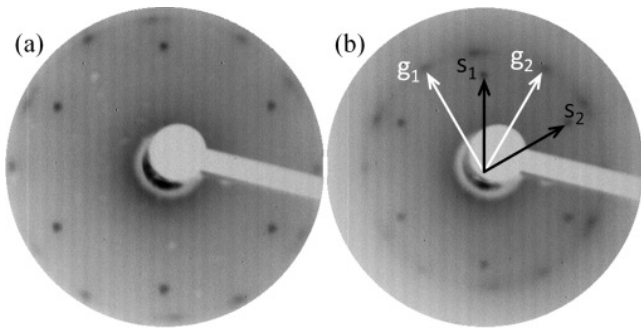


FIG. 1. LEED patterns from a nominally 3-layer C-face graphene sample with primary electron energy of (a) 76 eV and (b) 126 eV.

Because the films are thin, the LEED pattern clearly shows the sixfold SiC substrate spots ( $S_1$  and  $S_2$ ). In addition, the LEED shows a set of graphene spots rotated by  $30^\circ$  with respect to the  $S_2$  ( $g_1$  and  $g_2$ ) and a second set of spots rotated  $\sim 4^\circ$ – $5^\circ$  relative to  $S_2$ . Weaker graphene arcs around  $0^\circ$  are also visible. The SiC substrate LEED pattern is  $1 \times 1$  and no additional diffraction spots that would suggest that a significant reconstruction is visible. However, these LEED images are macroscopic area-averaged results, and are not expected to be sensitive to microscopic variations in the interface structure. More detailed spatial information is obtained using LEEM and X-PEEM as discussed below.

**A. LEEM**

LEEM data were obtained by using the (0,0) specular backscattered electron beam. Figure 2 shows typical bright-field images with a FoV of  $10 \mu\text{m}$  for electron energies ( $E$ ) of 3.0 and 4.8 eV. A full image series was acquired by varying  $E$  from 1.5 to 12.9 eV (using a 50 meV step size). The low-energy onset of the backscattered electron signal depends on the potential just above the surface and thus on the local work function. Clear differences in contrast as a function of  $E$  are observed across the field of view suggesting distinct work functions for different regions of the surface.

In two-dimensional layered systems there are oscillations in the LEEM reflectivity at low electron energies.<sup>20–22</sup> Several groups have used these reflectivity oscillations to determine the number of graphene layers in the epitaxial film. Figure 2(c)

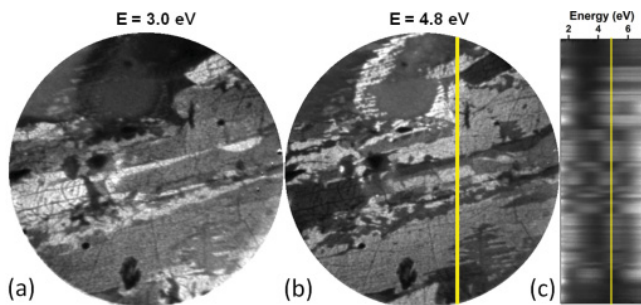


FIG. 2. (Color online) (a)–(c) Typical LEEM images ( $10 \mu\text{m}$  FoV) of the graphene surface as a function of electron energy (a) 3.0 eV and (b) 4.8 eV. (c) Reflectivity spectra extracted along the dotted line in (b) showing clearly the variation in the number of intensity minima and therefore the number of graphene layers.

shows the spectra along the dotted line in Fig. 2(b). We observe oscillations between 1.5 and about 7.5 eV. In graphite there are band gaps below 0 eV and above 7 eV along the  $\Gamma A$  direction. In an ideal multilayer graphene film, the number of minima in the reflectivity between successive Bragg peaks gives directly the number of graphene layers. We have similarly extracted pixel-by-pixel reflectivity curves from the image stack and mapped the LEEM reflectivity across the  $10 \mu\text{m}$  FoV and used the number of minima in each reflectivity curve to produce a thickness map of the C-face graphene film. Figure 3(a) shows the typical reflectivity curves for each distinct contrast region in the FoV. Two slightly different curves without a clear oscillation between 1.5 and 7 eV are observed. They are both attributed to the zero'th layer or C-terminated layer of the SiC substrate. This layer is thought to interact strongly with the SiC substrate through  $sp^3$  bonding. Luxmi *et al.*<sup>16</sup> have shown even flatter reflectivity curves for the zero'th layer (0 ML) for surfaces prepared at higher temperature under an argon back pressure. The thickness map constructed from the intensity minima is shown in Fig. 3(b) using the same color coding. The data show that more than 80% of the surface is covered by 2- or 3-layer graphene.

The reflectivity oscillation can be understood as quantum interference between electrons reflected by different graphene layers.<sup>20</sup> Hibino *et al.*<sup>20</sup> pointed out that although the conduction band is continuous in bulk graphite between 4.3 and

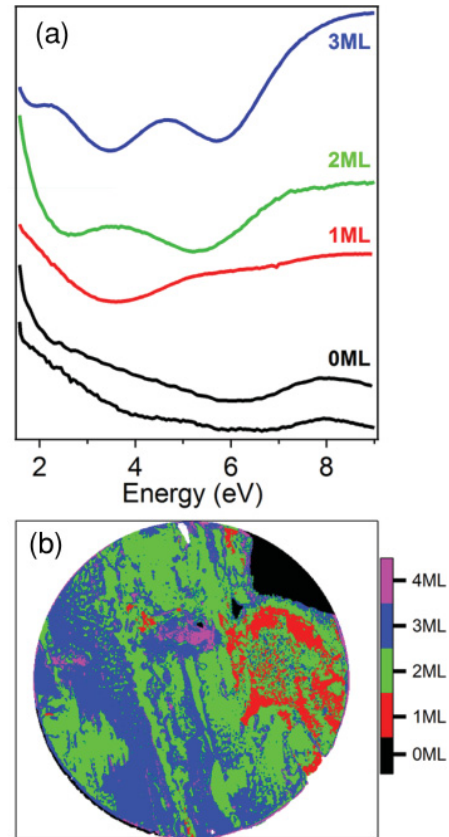


FIG. 3. (Color online) (a) Typical reflectivity curves extracted from the LEEM data set showing 0 to 3 oscillations below 7.5 eV. (b) Graphene thickness map (FoV =  $10 \mu\text{m}$ ) generated by counting the number of minima in the reflectivity curves.

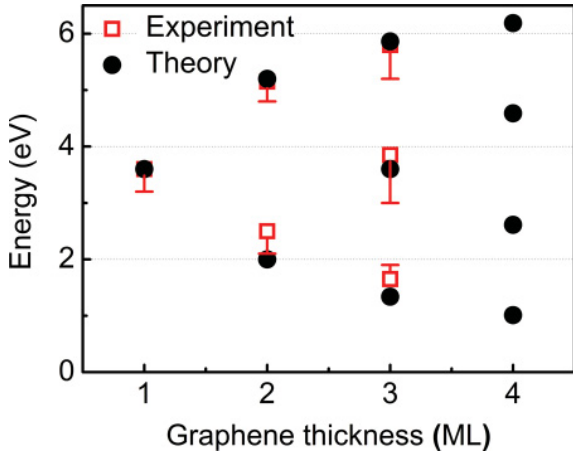


FIG. 4. (Color online) The position (boxes) of dips in reflectivity curves from Fig. 2(c) and Fig. 3(a), compared with theoretical estimation based on tight-binding model ( $\bullet$ ). The error bar on the experimental data indicates the correlations between the spread in the energy of the reflectivity minima.

11 eV along  $\Gamma A$ , few-layer graphene should have discrete states; thus the reflectivity oscillations are correlated with the electron structure of the thin films. The quantized conduction band states enhance the transmission of the incident electrons producing the dips in the reflectivity curves. This is confirmed by the good agreement between the experimental minima positions and the resonant energies predicted by a tight-binding calculation. For an  $m$ -layer thin film the bulk band dispersion has discrete energy states when the wave vector satisfies the quantized condition  $E = \epsilon - 2t \cos K\alpha$ , where  $\epsilon$  is the energy of the band center,  $t$  is the transfer integral, and  $\alpha$  is the interlayer distance. At these values, the dips in the reflectivity are predicted by projecting the wave vector onto the calculated band structure along the  $\Gamma A$  direction, the normal to the graphene layers.

Figure 4 shows the comparison of experimental reflectivity minima with the discrete energy levels predicted by the tight-binding theory. The spread in the experimental energy of the reflectivity minima in different regions of the FoV is indicated as an error bar. The center energy of the tight-binding theory calculation is at 3.6 eV compared to 3 eV used by Hibino for Si-face graphene.<sup>20</sup> Note that the third calculated

minimum (highest energy) in the nominally 3 ML region is at a slightly higher energy whereas the first and second minima are at slightly lower energy than the experimental data. This trend is also seen in the 2 ML minima. The difference may be due to the approximations inherent in the tight-binding calculation.

## B. X-PEEM

While LEEM measurements give information on the structural spatial variation of the graphene thickness, lateral variations in the electronic structure of epitaxial graphene have never been mapped. X-PEEM offers a unique method to begin to understand the role the SiC-graphene interface plays in graphene's electronic structure. In this section we present a submicron chemical and electronic mapping of the graphene-SiC interface.

### 1. Work function

Probing the transition from the mirror reflection of the electrons to the backscattering regime, commonly referred to as mirror electron microscopy to low-energy electron microscopy (MEM-LEEM), one finds that it is highly sensitive to the local variations of the electric potential just above the surface, as small differences in the latter determine large differences in the electron reflectivity. In energy-filtered PEEM, at high photon energies (654.3 eV in these experiments), the photoemitted intensity at threshold is directly related to the work function. An example of a raw image obtained in the threshold region is shown in Fig. 5(a). As  $E - E_F$  is scanned, dark areas become bright and vice versa, giving rise to spatial contrast as a function of photoelectron kinetic energy. This is direct evidence for a distribution of work function values over the sample surface.

After correction for the Schottky effect due to the high extractor field,  $\Delta E = 98$  meV for 12 kV,<sup>23</sup> the photoemission threshold spectra can be used to directly measure the local work function. The threshold spectrum is extracted from each pixel in the FoV (pixel area  $65 \times 65$  nm<sup>2</sup>). The position of the threshold is obtained from a fit using a complementary error function,

$$I(E) = A \operatorname{erfc} \left( \frac{\Phi_{WF} - E}{\sqrt{2}\sigma} \right) + I_{\min}, \quad (1)$$

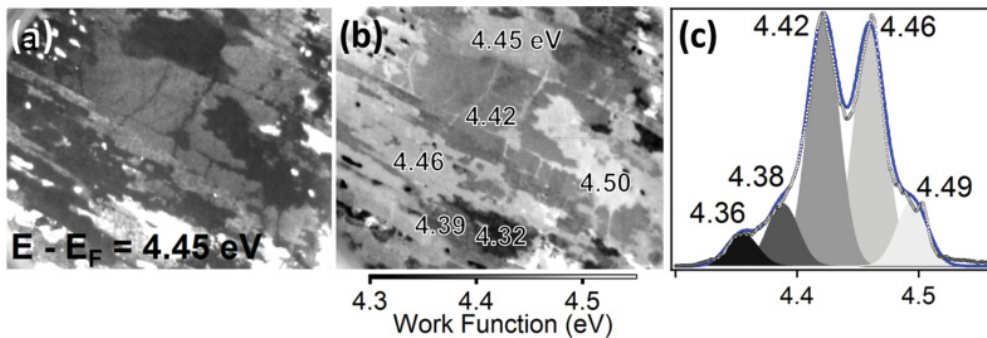


FIG. 5. (Color online) (a) Threshold image at  $E - E_F = 4.45$  eV with a  $53 \mu\text{m}$  field of view showing clear intensity contrast due to work function variation across the surface. (b) Work function map of the FoV obtained from a pixel by pixel analysis of the threshold spectra. (c) Histogram of the work function values in (b) showing five distinct Gaussian distributions, corresponding to five distinct work function values.

where  $\Phi_{WF}$  is the work function and  $\sigma$  the half-width of the rising side of the secondary electron peak (0.1 eV here). We note that because the theoretical shape of the photoemission onset is modeled, this method is a more reliable way of obtaining absolute work function values than simply extrapolating a straight line down to zero intensity. The results of this analysis are presented in the form of a map of the work function within the field of view in Fig. 5(b). A histogram of the work function values across the whole FoV is shown in Fig. 5(c). Five Gaussians, with width  $\pm 25$  meV, are able to describe the work function frequency distribution suggesting that there are only five distinct values of the work function. Actually, as we show when we discuss the X-PEEM results, the peak in the work function distribution centered at 4.46 eV includes two slightly different different work functions ( $\Delta\Phi = 10$  meV). While these two regions of the surface have nearly the same work function they can be distinguished by their very different core level spectra.

The work function distribution spans a range from 4.34 eV to 4.50 eV, a range well below the work function of bulk graphite (4.6 eV); thus our results confirm that no significant part of the surface within the FoV consists of many-layer graphene or graphite. On the contrary, this epitaxial film is indeed nearly uniform few-layer graphene, with local variations in the graphene coverage. However, we cannot necessarily attribute each peak in the work function distribution to a distinct graphene thickness. For example, recent Kelvin force microscopy showed that the work function difference between one- and two-layer graphene is 0.135 eV.<sup>24</sup> The graphene thickness calibration, based on the local C1s X-PEEM spectra presented below, excludes such a difference between regions with one- and two-layer graphene; therefore the observed variations cannot only be due to thickness changes. This is particularly true for regions of the surface with work function values of 4.46–4.49 eV. For these regions the C1s spectra (as discussed in the next section) indicate that the graphene film is in fact very thin.

There are also more substantial changes to the threshold spectra than the work function measurements suggest. To demonstrate this, Fig. 6(a) shows two examples of threshold spectra for regions of the sample with a small work function difference of  $\sim 30$  meV (4.42 and 4.45 eV). These regions will be analyzed in more detail using both core level X-PEEM and the  $k$ -PEEM data in the next sections. There are interesting variations in the structure of the secondary electron (SE) peak up to 4–5 eV above the vacuum level (i.e., above the photoemission threshold). The SE peak structure can be related to the conduction band.<sup>25</sup> Figure 6(b) shows the negative of the second derivative threshold spectra. The data have been smoothed in order to more clearly see the peak structure. The low work function regions in Fig. 5(c) have a single main structure in the SE at  $\sim 6.0$  eV whereas the higher work function regions have a clear double structure at  $\sim 6.0$  eV and  $\sim 7.5$  eV. The structure around 6 eV could be due to the bulk SiC bands observed along  $\Gamma A$ , which extend from 5.6 to above 6 eV.<sup>26</sup> Other conduction bands also disperse along the bulk directions  $ML$  and  $HK$ . In fact, all the high work function spectra show a double-peak structure in the SE whereas the low work function spectra show only one peak. This sort of SE structure has already been observed in threshold X-PEEM

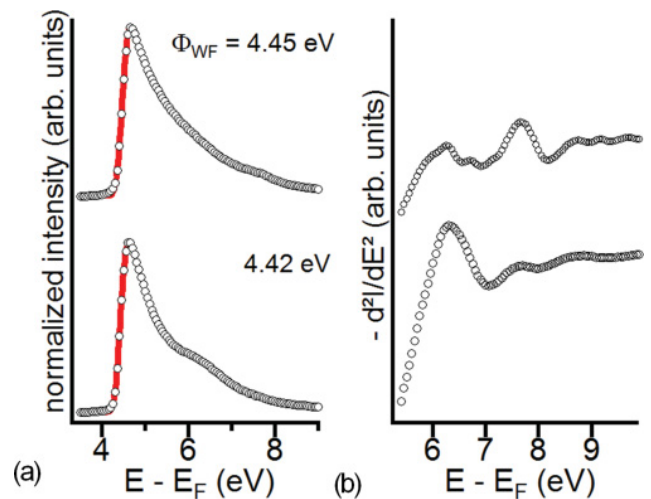


FIG. 6. (Color online) (a) Local threshold spectra extracted from regions in Fig. 5(b) with work functions of 4.42 and 4.45 eV. The best complementary error function fits of the rising edge of the photoemission threshold are indicated by the solid line. (b) Second derivative smoothed threshold spectra from (a) showing peaks corresponding to the empty conduction band structure.

analysis of graphene on SiC(0001).<sup>27</sup> It has been known for a long time that bulk graphite produces an intense secondary electron signal at 7.5 eV above the Fermi level (about 3 eV above the vacuum).<sup>28</sup> For example, the photocurrent carried by the Bloch constituent of the time-reversed LEED wave function is indeed a maximum near 7.5 eV.<sup>29</sup> Thus although the work function difference in Fig. 5(a) is small ( $\sim 30$  meV), we can identify the presence of a band at 7.5 eV, which for thicker samples could develop into the typical structure of graphite.

## 2. C1s core level

A series of energy filtered images have been acquired over the full C1s spectrum in the same FoV as the threshold data, allowing a pixel-by-pixel extraction of the local C1s spectra that can then be directly compared to the work function map. The C1s spectrum has two main components, one assigned to the SiC substrate near 283 eV, and the other to graphene near 285 eV.<sup>14</sup> Figure 7(a) shows a map of the total area of the SiC component. Because thicker graphene regions attenuate the photoelectrons from the SiC more, the map in Fig. 7(a) is a good estimate of the variations in the graphene thickness within the FoV. Comparison of the C1s intensity map with the work function map in Fig 5(b) shows that there is no simple one-to-one correlation between graphene thickness and work function. Instead we will show that much of the contrast variations are a combination of both work function and core level spatial variations, indicating a complex chemical structure in the SiC-graphene interface.

In order to obtain more chemical-spatial detail, local, C1s core level spectra were extracted from each of the regions identified in Fig. 7 and are presented in Fig. 8. The graphene and SiC intensities show significant variations from one region to another, not only in total intensity but also in terms of the fine structure of both the graphene and SiC components. To fit

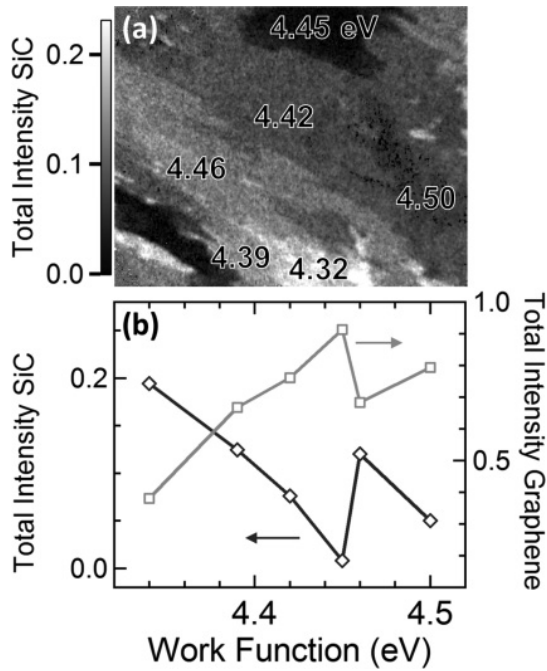


FIG. 7. (a) Intensity map (arbitrary units) of the SiC substrate component of C1s spectrum after background subtraction. The darker regions correspond to lower intensity and therefore thicker graphene; FoV 53  $\mu\text{m}$ . (b) The C1s intensities from graphene (squares) and from SiC (diamonds) as a function of work function.

the spectra, we use five peaks, after subtraction of a Shirley background (a linear background fit was also tested but does not significantly change the results). Three components are necessary to fit the main peak of the spectrum that represents the graphene. For each of these components a Doniach-Sunjic line shape was used with a 0.2 eV Lorentzian width, 0.3 eV Gaussian width, and 0.05 asymmetry factor. A one-component Gaussian line shape (FWHM of 0.5 eV) is used to fit the low binding energy peak ascribed to the SiC substrate. A Gaussian is more suitable for a wide-gap semiconductor. The binding energy of this component can vary by up to 0.5 eV. Finally, a small broad component, which is always present in the C1s spectrum around 285.7 eV, is ascribed to slight surface contamination due to residual gas in the vacuum chamber since the C1s image series were obtained  $1.3 \times 10^5$  s after the cleaning process. This peak was fitted using a Gaussian with a FWHM = 1.1 eV. The contamination component increases slightly for thinner graphene, and is largest in the region with a work function of 4.34 eV. Immediately after cleaning, no such peak was visible. The *k*-PEEM data described below were obtained only  $\sim 10^4$  s after cleaning; thus the residual gas contamination in that case is expected to be negligible. The best fits are also reported in Fig. 8. Each spectrum is correlated with a region of the sample that is specified by its local work function and thickness (determined by the C1s intensities, as described below).

The main graphene component lies between 284.30 and 284.56 eV and is always the dominant contribution to the spectrum, confirming that there is graphene or a graphene-like layer over the whole film. This statement is supported by

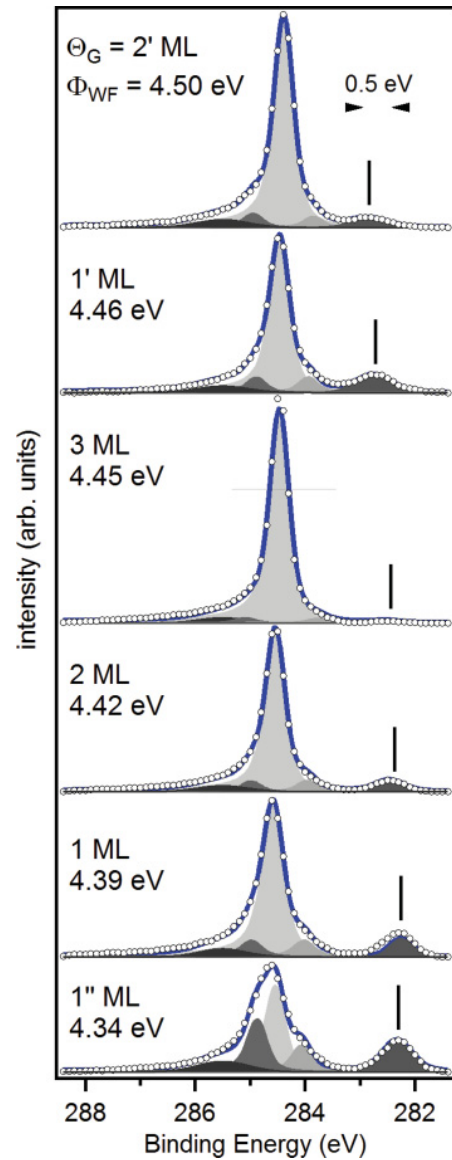


FIG. 8. (Color online) C1s core level spectra extracted from the regions shown in Fig. 7 together with the best 5-peak fits. The vertical lines indicate the position of the peak attributed to the SiC substrate. The main graphene peak is light gray, the contamination peak is in black, and the SiC component is dark gray. The two other graphene peaks, labeled HBE-G and LBE-G, flank the main graphene peak. The thickness (calibration is described in the text) and work function are given for each spectra.

the behavior of the SiC component, at lower binding energy. It is always much smaller than the main graphene component suggesting a nearly continuous graphene coverage. As the graphene intensity increases (i.e., the number of graphene layers increases), the intensity of the SiC decreases. We can estimate the local graphene thickness from the relative SiC and graphene C1s intensity. Using a graphene interlayer spacing of 0.34 and a 1 nm<sup>30</sup> electron mean free path for 654.3 eV photons in graphite, the estimated attenuation of the substrate C1s signal is 22% per graphene layer. Assuming C atom surface densities for graphene ( $3.8 \times 10^{15} \text{ cm}^{-2}$ ) and SiC ( $1.22 \times 10^{15} \text{ cm}^{-2}$ ), the thickness of the graphene within the

TABLE I. C1s BE for the main graphene peak and for the SiC peak together, and the G/SiC core level intensity ratio for different graphene thicknesses and work functions.

Coverage (ML)	$\Phi_{WF}$ (eV)	C1s BE (eV)		Ratio $I_G/I_{SiC}$
		Graphene	Substrate	
3	4.45	284.45	282.52	112.3
2	4.42	284.55	282.46	10.0
2'	4.50	284.30	282.84	15.8
1	4.39	284.56	282.32	5.3
1'	4.46	284.45	282.75	5.7
1''	4.34	284.54	282.32	2.0

FoV is between 1 and 3 ML. This estimate is in agreement with the spread in the number of ML deduced from oscillations in the LEEM backscattered reflectivity curves. The thickness values obtained by this method are given in Fig. 8. The work function, C1s core level binding energies, and graphene thicknesses are summarized in Table I.

It is immediately obvious that there is not a simple one-to-one correspondence between work function and graphene coverage. The same graphene thickness is obtained in regions with significantly different work functions. We can group the six different contrast regions in Figs. 5(b) and 7(a) into three families. The first consists of graphene with 1, 2, or 3 layers. The second, denoted by a prime superscript, has either 1 or 2 ML graphene, while the third, denoted by a double prime, has only 1 ML graphene.

The complexity of the graphene-SiC interface is revealed by a detailed look at the C1s spectra in Fig. 8. There are always two other graphene-like peaks besides the main peak in all regions, a high binding energy (HBE-G) peak around 284.9 eV and a low binding energy (LBE-G) peak at 284.0. The intensity of these two peaks is lowest for 3 ML graphene and highest for the single-layer graphene, whatever the family. We therefore associate these two structures with carbon *below* the graphene layers, either in the C-terminating SiC layer or from some of the graphene at the SiC interface. Note that these HBE- and LBE-G peak intensities are not the same for the three single-layer graphene regions. They are most intense for the 1'' ML region, which also had the strongest SE structure associated with the SiC substrate. The 1 ML and 1'' ML graphene have similar C1s binding energies ( $\Delta BE = 100$  meV). The total work function variation over the three single-layer graphene regions is 120 meV. Similarly, 2 ML graphene has significant differences in its C1s binding energy and in its work function. The main graphene C1s peak BE in the 2' ML graphene is shifted 250 meV lower than the 2 ML graphene. At the same time, the SiC component shifts 380 meV to higher BE in the 2' ML. However, the work function difference between the 2 ML and 2' ML regions is 80 meV. The work function, C1s graphene, and SiC binding energies are plotted together in Fig. 9.

It follows that a uniform charge transfer over the whole graphene/SiC interface cannot be explained by these experimental observations. Charge transfer from the substrate to the graphene should result in a rigid shift of the electronic levels and the work function. However, in regions with the

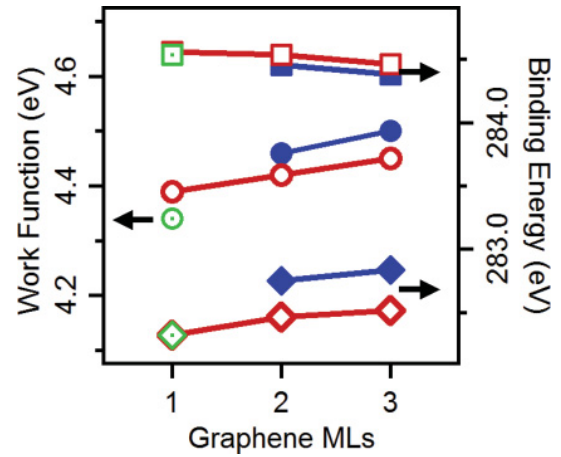


FIG. 9. (Color online) C1s graphene BE (squares), C1s SiC BE (diamonds), and work function (circles), as a function of graphene thickness. The unfilled symbols are for 1, 2, and 3 ML regions; filled symbols are for 1' and 2' ML regions. Open symbols with dots are for the 1'' ML.

same number of graphene layers we observe a spread in the work function. The work function difference between 1 ML and 1'' ML might be ascribed to the slightly higher surface contamination, but this cannot explain the work function and C1s BE difference with the 1' ML region which should have the same surface contamination. The most direct evidence for a nonuniform G/SiC interface is the shift of up to 220 meV in C1s SiC binding energy for different coverages. The trend in the SiC component binding energy emission is shown in Fig. 9. If we assume that the SiC C1s signal is dominated by the first substrate layer, the trend suggests two possible interfaces. Indeed, STM studies have shown that for very thin UHV grown graphene layers there are two different interface reconstructions ( $2 \times 2$  and  $3 \times 3$ ).<sup>15</sup> The BE variation of the C1s components as a function of thickness is also shown in Fig. 9. Different core level binding energies for the same graphene thickness further support the interpretation of a nonuniform G/SiC interface. Comparing the main G and SiC components, we see that as the SiC BE increases (charge transfer) there is a corresponding decrease in the G BE. Thus, the magnitude of the charge transfer depends on the local interface chemistry or structure.

### C. *k*-PEEM results

In addition to the spatially resolved core level data, we are able to create local isointensity surfaces in  $(k_x, k_y, E)$  space. In this way, we can immediately visualize the full band dispersion in all directions parallel to the graphene planes for a selected micron-scale region. The objective is to correlate the chemical and electronic states obtained in X-PEEM with a quantitative analysis of the band structure of the same micron-scale region. Figure 10(a) shows a complete three-dimensional data set of the band dispersion near the Fermi level of the 2 ML region. The image series were taken from 2.9 eV below the Fermi level to 0.3 eV above  $E_F$  in 50 meV steps. The linearly polarized photon beam was incident at  $25^\circ$  with respect to the sample surface, giving a mainly *p*-polarized geometry in an arbitrary

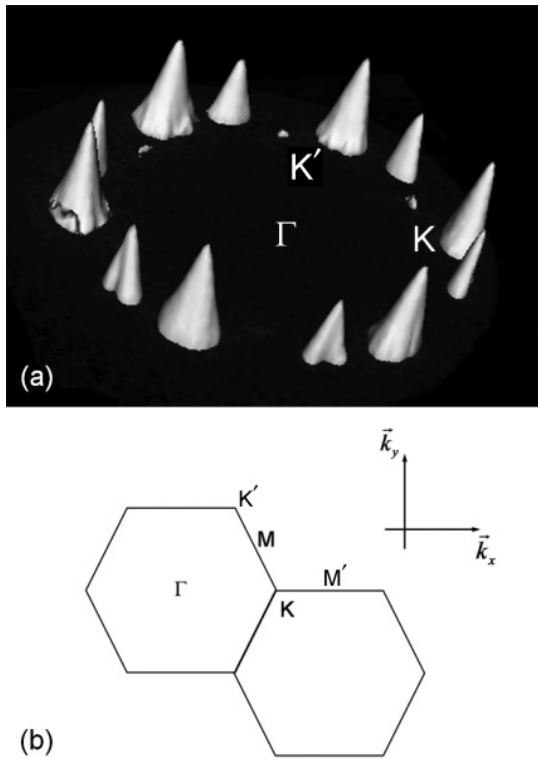


FIG. 10. (a) Experimental  $I(k_x, k_y, E)$  data collected in the 2 ML region of Fig. 7. The principal and secondary Dirac cones at the  $K$  and  $K'$  points of the first Brillouin zone are clearly visible. The secondary cones are rotated by  $21.9^\circ$  with respect to the primary cones. Also evident is the already documented suppression of the photoemission intensity outside the first Brillouin zone due to the pseudospin structure when using  $p$ -polarized light. The tertiary cones are just visible inside the double hexagon defined by the principal and secondary cones. (b) Schematic of the Brillouin zone of graphene showing the two high-symmetry directions parallel and perpendicular to  $\Gamma K M'$  ( $k_x$  and  $k_y$ , respectively) extracted from the  $k$ -PEEM data sets. An open source volume viewer, designed for medical imaging, was used to produce the image (Ref. 31).

azimuth ( $14.5^\circ$  off  $\Gamma K$ ). The acquisition of each image series took 22 minutes and they were repeated eight times in order to improve statistics without introducing camera noise.

Instead of the single set of six Dirac cones usually reported for Si-face films,<sup>32</sup> Fig. 10(a) shows three sets of Dirac cones, which we will call principal, secondary, and tertiary cones. The first two are much more intense than the latter. All three have the typical sixfold symmetry, although the tertiary cones appear inside the primary and secondary cone radius (i.e., at position  $< \Gamma K$ ). Also note the symmetry of the primary and secondary cones. They are not full circles because of the suppression of intensity in the second zone due to matrix element effects (an effect well known in graphene).<sup>32,33</sup> However, the tertiary cones have their symmetry flipped  $180^\circ$ . As we will demonstrate below, these three sets of cones are all due to two commensurately rotated graphene sheets.

The secondary Dirac cones have reciprocal lattice vectors  $*\Gamma K$  rotated by  $21.9^\circ$  with respect to the primary cones. This is very close to the value of  $21.8^\circ$  expected for a particular pair of commensurate rotated graphene sheets.<sup>35</sup> At first

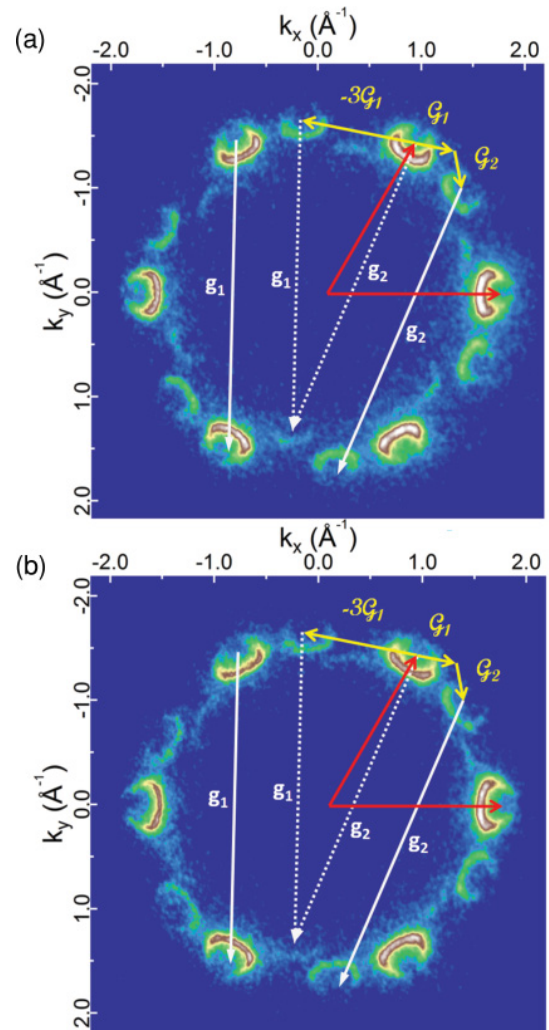


FIG. 11. (Color online) Horizontal slice in the 3D  $k$ -PEEM data set of (a) 2 ML and (b) 3 ML at a binding energy of 1.3 eV. Secondary Dirac cones (graphene reciprocal lattice constant  $g_1$ ) are rotated by  $21.9^\circ$  with respect to the principal cones (graphene reciprocal lattice constant  $g_2$ ). The tertiary cones are obtained by diffraction of either the secondary cone by the principal lattice vector  $g_1$  (dotted line), or by the primary cone by the secondary lattice vector  $g_2$  (dotted line). The tertiary cones are stronger in 2 ML graphene.

sight, one would be tempted to interpret the tertiary cones in terms of replicas, like those observed on the SiC(0001) Si face.<sup>34</sup> However, those replicas are due to registry between the  $(6\sqrt{3} \times 6\sqrt{3})R30^\circ$  reconstructed substrate and the graphene overlayer. On SiC(000 $\bar{1}$ ) the graphene layers are known to form commensurate rotated layers where the average rotation between pairs is  $30^\circ \pm \sim 7^\circ$ .<sup>5</sup> The tertiary cones in Fig. 11 are instead due to a diffraction effect caused by the supercell formed by the commensurate rotations. To understand this, note that the supercell formed by the stacked rotated sheets is defined by reciprocal lattice vectors  $\vec{G}_1$  and  $\vec{G}_2$ . These supercell vectors are, in turn, an integer sum of the primary graphene reciprocal vectors,  $\vec{g}_{1a}$ ,  $\vec{g}_{1b}$ ,  $\vec{g}_{2a}$ , and  $\vec{g}_{2b}$ , from the two layers (i.e.,  $\vec{G}_1 = p\vec{g}_{1a} + q\vec{g}_{1b}$  and  $\vec{G}_2 = p'\vec{g}_{2a} + q'\vec{g}_{2b}$ , where  $p$ ,  $q$ ,  $p'$ , and  $q'$  are integers).<sup>35</sup>

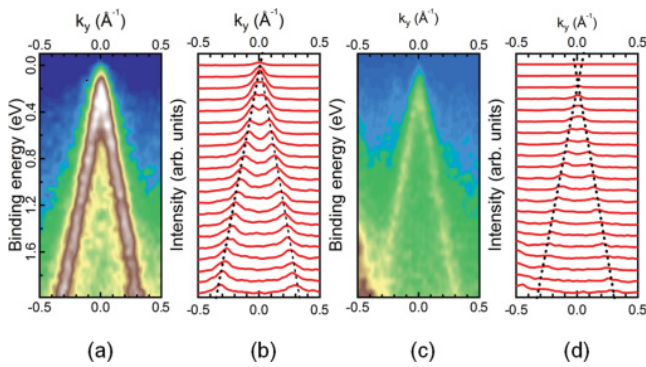


FIG. 12. (Color online) Band dispersion as a function of  $k_y$  around the  $K$  point at the first Brillouin zone boundary observed in the 3ML region for (a) principal and (c) secondary cones. The respective momentum distribution curves over the same energy range are shown in (b) and (d). The peak positions are highlighted by the dotted lines showing the variation in the position of the Dirac point for successive graphene layers.

In Fig. 11, we show two examples where two of the secondary cones are separated by linear sums of lattice vectors  $\vec{G}_1$  and  $\vec{G}_2$ , i.e.,  $-3\vec{G}_1$  and  $-(\vec{G}_1 + \vec{G}_2)$ . Note that  $(\vec{G}_1 + \vec{G}_2) = (\vec{g}_{1a} - \vec{g}_{2a})$ , indicating that the two rotated graphene sheets are indeed a commensurate rotated pair. For the purpose of discussion, we use the notation that  $\vec{g}_1$ 's are the graphene lattice vectors of the primary cones and  $\vec{g}_2$ 's are the graphene lattice vectors of the secondary cones. Using this notation, it is easy to show that the tertiary cones are diffracted replicas of the primary and secondary cones. Figure 11 shows that a tertiary cone is formed by diffracting a primary cone by  $\vec{g}_2$  or a secondary cone by  $\vec{g}_1$ . This diffraction process explains why the tertiary cones are rotated by  $180^\circ$  relative to the primary and secondary cones; they are simply translated Dirac cones from a  $K$  and  $K'$  point of one lattice by the  $\vec{g}$  of the second lattice. Because any tertiary cones can be formed by diffraction of either of the rotated graphene lattices (primary or secondary), the two rotated graphene sheets must be stacked on top of each other with a commensurate rotation. Separated rotated sheets cannot give rise to this type of diffraction.

The  $\pi$  bands of the primary cones cross at a Dirac point of 0.30 eV for the 2 ML film and 0.25 eV for the 3 ML film relative to the Fermi level. Figure 12 shows cuts perpendicular to  $\Gamma KM$  of the primary and secondary cones for 3 ML. The linear dispersion of the  $\pi$  band near the Dirac point is evident. Panels (a) and (c) show the raw experimental data around the  $K$  point of the Dirac cones. Panels (b) and (d) show the corresponding momentum distribution curves (MDCs) extracted from the data. The Fermi level calibration was checked by extracting the local spectra from a small zone around the Dirac cones. This has the advantage of minimizing noise and thus allowing a more precise location of the Fermi level. The dotted lines show that the  $\pi$  bands cross at a Dirac point 50–75 meV closer to the Fermi level for the principal cones. The group velocity of the quasiparticle is  $(1.05 \pm 0.05) \times 10^6 \text{ m s}^{-1}$  in both 2 ML and 3 ML regions.

This confirms that the electron doping is a function of film thickness and is consistent with the results for graphene on

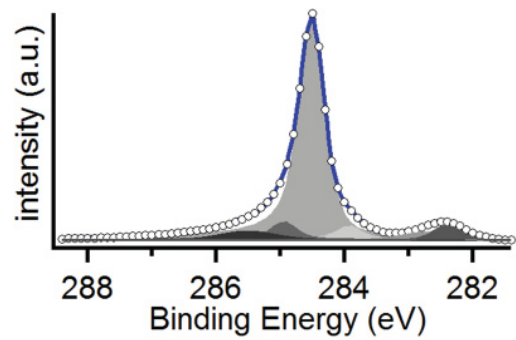


FIG. 13. (Color online) Area averaged C1s core level spectrum. The average is over the  $53 \mu\text{m}$  FoV.

the Si face where the charge transfer induced shift of the band structure is greater for thinner films.<sup>36</sup>

#### IV. CONCLUSION

We have studied spatial variations in and correlations between the work function, chemical states, and electronic states of few-layer graphene grown epitaxially on SiC(000 $\bar{1}$ ). These experiments demonstrate that near uniformly thick graphene films can be prepared using the CCS growth method; in this sample more than 80% of the surface is 2–3 layers thick. More importantly, they also show that while LEEM can be used to give local information on the graphene film's thickness, LEEM contrast variation on C-face graphene films is not simply due to film thickness alone. X-PEEM's spatial resolution has proven to be very useful in illuminating the origin of these contrast variations. The  $0.1 \mu\text{m}$  spatial resolution in the present experiment is much better than that currently obtained in area-averaged high-resolution ARPES with synchrotron radiation. The work function variations in Fig. 5, derived from the X-PEEM, combined with the local C1s spectra in Fig. 8, show an interface chemistry that is more complex than originally suspected.

To demonstrate this, Fig. 13 shows an area-averaged C1s spectrum from the  $53 \mu\text{m}$  FoV. The overall spectrum is broader, and the fine structure visible in the local spectra of Fig. 8 is smeared out in the area-averaged spectrum. Without the spatial resolution, one would have concluded that only one broad substrate peak was present rather than a narrower peak whose energy shift depends on the graphene thickness. Similarly, the area-averaged work function masked the complexity of charge transfer at the graphene-SiC interface.

While the X-PEEM data agree with the general trend observed by others that the work function tends to higher values with thicker graphene films, it shows that the situation is more complicated. For a given thickness, both the local work function and C1s BE vary appreciably. The data suggest that at least two SiC terminations with different local bonding appear to be present at the interface. We note that the long-range order of these different bonding areas is not very high since the micro-LEED never sees any superlattice diffraction spots. For a given graphene-SiC interface, the core level data can be interpreted within the framework of a charge transfer model between the substrate and the graphene that rigidly shifts the

C1s core level. The effect of the charge transfer on binding energy is greater for carbon closer to the interface, i.e., for carbon in thinner graphene films. The correlation between the work function and the core level BE strongly supports this interpretation. On the basis of these results we suggest that there are two distinct interfacial chemical regions.

There are several possible reasons for these two distinct regions. It is known that UHV grown C-face graphene can have a  $2 \times 2$  and  $3 \times 3$  interface phases coexisting.<sup>15</sup> The structures are thought to have very different binding configurations with the graphene. While no reconstructions are observed in LEED on our samples, the high growth temperatures encountered during furnace growth (1550 °C versus 1100 °C) may cause these regions to be very disordered. Nonequilibrium local Si concentrations may also be the cause of the different interface regions. Because Si diffusion (a required step for graphene growth) is difficult through graphene, local defect driven Si outflow may increase or decrease the interfacial Si concentration in different regions of the sample. It is clear that more experimental work needs to be done to resolve this issue, notably imaging of the Si 2*p* core levels. Experiments are now being planned for such studies.

We have also demonstrated that *k*-PEEM gives detailed band structure information from commensurately rotated

graphene sheets. The easy switching between real- and *k*-space imaging modes allows, within the limits of the spatial resolution and field aperture size, correlation between the chemical and electronic states of the surface and graphene-SiC interface. In this study we conclusively show that commensurately rotated graphene pairs exist.

#### ACKNOWLEDGMENTS

C.M. benefited from a grant of the Nanosciences programme of the French Atomic and Alternative Energy Authority. J.R. is funded by a CEA Ph.D. grant Contrat de Formation par la recherche. The work was supported by the French National Research Agency (ANR) through the Recherche Technologique de Base (RTB) program. We acknowledge SOLEIL for provision of synchrotron radiation facilities, and we would like to thank F. Sirotti, the TEMPO beamline staff, D. Martinotti, B. Delomez, and F. Merlet for technical assistance. E.C., W.A.d.H., and C.B. would like to acknowledge support from the W. M. Keck Foundation, the Partner University Fund from the Embassy of France, and the NSF under Grant No. DMR-0820382. E.C. would also like to acknowledge additional support from the NSF under Grant No. DMR-1005880.

\*Correspondence should be addressed to nick.barrett@cea.fr

<sup>1</sup>J. S. Moon, D. Curtis, M. Hu, D. Wong, C. McGuire, P. M. Campbell, G. Jernigan, J. L. Tedesco, B. VanMil, R. Myers-Ward, C. Eddy Jr., and D. K. Gaskill, *IEEE Electron Device Lett.* **30**, 650 (2009).

<sup>2</sup>Yu-Ming Lin, K. A. Jenkins, A. Valdes-Garcia, J. P. Small, D. B. Farmer, and P. Avouris, *Nano Lett.* **9**, 422 (2009).

<sup>3</sup>C. Riedl, C. Coletti, and U. Starke, *J. Phys. D: Appl. Phys.* **43**, 374009 (2010).

<sup>4</sup>W. A. de Heer, C. Berger, M. Ruan, M. Sprinkle, X. Li, Y. Hu, B. Zhang, J. Hankinson, and E. H. Conrad, e-print arXiv:1104.1359 [cond-mat].

<sup>5</sup>M. Sprinkle, D. Siegel, Y. Hu, J. Hicks, A. Tejada, A. Taleb-Ibrahimi, P. Le Fèvre, F. Bertran, S. Vizzini, H. Enriquez, S. Chiang, P. Soukiassian, C. Berger, W. A. de Heer, A. Lanzara, and E. H. Conrad, *Phys. Rev. Lett.* **103**, 226803 (2009).

<sup>6</sup>J. Hass, F. Varchon, J. E. Millan-Otoya, M. Sprinkle, N. Sharma, W. A. de Heer, C. Berger, P. N. First, L. Magaud, and E. H. Conrad, *Phys. Rev. Lett.* **100**, 125504 (2008).

<sup>7</sup>C. Berger, Z. Song, X. Li, X. Wu, N. Brown, C. Naud, D. Mayou, T. Li, J. Hass, A. N. Marchenkov, E. H. Conrad, P. N. First, and W. A. de Heer, *Science* **312**, 1191 (2006).

<sup>8</sup>M. Orlita, C. Faugeras, P. Plochocka, P. Neugebauer, G. Martinez, D. K. Maude, A.-L. Barra, M. Sprinkle, C. Berger, W. A. de Heer, and M. Potemski, *Phys. Rev. Lett.* **101**, 267601 (2008).

<sup>9</sup>J. Hass, W. A. de Heer, and E. H. Conrad, *J. Phys. Condens. Matter* **20**, 323202 (2008).

<sup>10</sup>C. Riedl, C. Coletti, T. Iwasaki, A. A. Zakharov, and U. Starke, *Phys. Rev. Lett.* **103**, 246804 (2009).

<sup>11</sup>U. Starke and C. Riedl, *J. Phys. Condens. Matter* **21**, 134016 (2009).

<sup>12</sup>J. Hass, J. E. Millán-Otoya, P. N. First, and E. H. Conrad, *Phys. Rev. B* **78**, 205424 (2008).

<sup>13</sup>J. Hass, R. Feng, J. E. Millan-Otoya, X. Li, M. Sprinkle, P. N. First, W. A. de Heer, E. H. Conrad, and C. Berger, *Phys. Rev. B* **75**, 214109 (2007).

<sup>14</sup>K. V. Emtsev, F. Speck, Th. Seyller, L. Ley, and J. D. Riley, *Phys. Rev. B* **77**, 155303 (2008).

<sup>15</sup>F. Hiebel, P. Mallet, F. Varchon, L. Magaud, and J.-Y. Veuillein, *Phys. Rev. B* **78**, 153412 (2008).

<sup>16</sup>Luxmi, N. Srivastava, Guowei He, R. M. Feenstra, and P. J. Fisher, *Phys. Rev. B* **82**, 235406 (2010).

<sup>17</sup>B. Krömker, M. Escher, D. Funnemann, D. Hartung, H. Engelhard, and J. Kirschner, *Rev. Sci. Instrum.* **79**, 053702 (2008).

<sup>18</sup>M. Escher, N. Weber, M. Merkel, C. Ziethen, P. Bernhard, G. Schonhense, S. Schmidt, F. Forster, F. Reinert, B. Krömker, and D. Funnemann, *J. Phys. Condens. Matter* **17**, S1329 (2005).

<sup>19</sup>M. Escher, K. Winkler, O. Renault, and N. Barrett, *J. Electron Spectrosc. Relat. Phenom.* **178–179**, 303 (2010).

<sup>20</sup>H. Hibino, H. Kageshima, F. Maeda, M. Nagase, Y. Kobayashi, and H. Yamaguchi, *Phys. Rev. B* **77**, 075413 (2008).

<sup>21</sup>T. Ohta, F. El Gabaly, A. Bostwick, J. L. McChesney, K. V. Emtsev, A. K. Schmid, T. Seyller, K. Horn, and E. Rotenberg, *New J. Phys.* **10**, 023034 (2008).

<sup>22</sup>W. F. Chung, Y. J. Feng, H. C. Poon, C. T. Chan, S. Y. Tong, and M. S. Altman, *Phys. Rev. Lett.* **90**, 216105 (2003).

<sup>23</sup>O. Renault, R. Brochier, A. Roule, P.-H. Haumesser, B. Krömker, and D. Funnemann, *Surf. Interface Anal.* **38**, 375 (2006).

<sup>24</sup>T. Filleter, K. V. Emtsev, Th. Seyller, and R. Bennewitz, *Appl. Phys. Lett.* **93**, 133117 (2008).

- <sup>25</sup>R. Feder and J. B. Pendry, *Solid State Commun.* **26**, 529 (1978).
- <sup>26</sup>C. Persson and U. Lindelfelt, *J. Appl. Phys.* **82**, 5496 (1997).
- <sup>27</sup>H. Hibino, H. Kageshima, M. Kotsugi, F. Maeda, F.-Z. Guo, and Y. Watanabe, *Phys. Rev. B* **79**, 125437 (2009).
- <sup>28</sup>R. F. Willis, B. Feuerbacher, and B. Fitton, *Phys. Rev. B* **4**, 2441 (1971).
- <sup>29</sup>N. Barrett, E. E. Krasovskii, J.-M. Themlin, and V. N. Strocov, *Phys. Rev. B* **71**, 035427 (2005).
- <sup>30</sup>S. Tanuma, C. J. Powell, and D. R. Penn, *Surf. Interface Anal.* **17**, 911 (1991).
- <sup>31</sup>The program may be downloaded at [<http://microview.sourceforge.net/>].
- <sup>32</sup>A. Bostwick, T. Ohta, T. Seyller, K. Horn, and E. Rotenberg, *Nature Phys.* **3**, 36 (2007).
- <sup>33</sup>E. L. Shirley, L. J. Terminello, A. Santoni, and F. J. Himpsel, *Phys. Rev. B* **51**, 13614 (1995).
- <sup>34</sup>K. Nakatsuji, Y. Shibata, R. Niikura, F. Komori, K. Morita, and S. Tanaka, *Phys. Rev. B* **82**, 045428 (2010).
- <sup>35</sup>E. J. Mele, *Phys. Rev. B* **81**, 161405(R) (2010).
- <sup>36</sup>T. Ohta, A. Bostwick, J. L. McChesney, T. Seyller, K. Horn, and E. Rotenberg, *Phys. Rev. Lett.* **98**, 206802 (2007).



# Appendix C

## Automatized Data Analysis

The output of PEEM/LEEM experiments as described in Appendix A is a 3D stack of images which consists in the measured intensity  $I$  as a function of three parameters : the two spatial lateral coordinates  $(x,y)$  and the energy of the emitted (reflected) electrons. From each pixel a spectrum can be extracted. In LEEM, we obtain a reflectivity spectrum which can be used to access the electrostatic potential of a surface (Chapter 3) or the number of layers of few-layers graphene [88]. In energy-filtered PEEM, we obtain a photoemission spectrum which can be due to a core-level or the threshold of photoemission. A typical image acquired with a PEEM/LEEM has  $800 \times 600$  pixels. The corresponding stack has 50 to 100 images depending on the energy range and step. Obviously, data analysis of each individual spectrum is impossible. Two solutions are available. On the one hand, the signal coming from region of interests (ROIs) can be averaged using a image processing software. Then, a reasonable amount of spectra extracted from different ROIs can be individually analyzed. On the other hand, pixel-by-pixel analysis is more potent in terms of statistics but it has to be automatized. Automatized procedures for pixel-by-pixel analysis of PEEM/LEEM data will be presented in this appendix in the particular case of energy-filtered PEEM. It can easily be extended to LEEM data provided minor modifications in the code.

### C.1 Pixel-by-pixel Data Analysis

The main software used for data analysis during this thesis was [Igor Pro](http://www.wavemetrics.com/)<sup>1</sup> by Wavemetrics. This software is widely used in material science due to its excellent programming and processing capabilities. In addition, many user procedures are available on [Igor Exchange](http://www.igorexchange.com/)<sup>2</sup> thanks to a very active community.

The goal of the analysis procedures presented in this appendix is to fit each spectrum extracted from every pixel of a PEEM stack to the relevant lineshape in order to output

---

<sup>1</sup><http://www.wavemetrics.com/>

<sup>2</sup><http://www.igorexchange.com/>

a map of spatially-resolved properties such as binding energy, maximum peak intensity or work function<sup>3</sup>. In this section, the focus is on a specific part of the photoemission spectroscopy spectrum: the photoemission threshold. It is the most intense part of a photoemission spectrum and therefore easily measurable in PEEM experiments with both high spatial ( $\approx 20$  nm) and energy ( $\approx 200$  meV) resolutions. The threshold spectrum can be fitted by the complementary error function which gives an accurate value of the work function  $\Phi_S$  [182, 215]:

$$I(E - E_F) = 1 - \operatorname{erf}\left(\frac{\Phi_S - (E - E_F)}{\sqrt{2}\sigma}\right) \quad (\text{C.1})$$

where  $E_F$  is the common Fermi level of the sample and spectrometer,  $\Phi_S$  is the work function of the area of interest and  $\sigma$  is modeling the instrumental broadening due to the analyzing stage. Knowing this, the procedure is straightforward:

1. Load the data as a 3D *wave* in Igor Pro.
2. Extract a spectrum from the pixel  $(x_n, y_n)$ .
3. Fit the spectrum using the equation (C.1).
4. Return the fitting parameters *i.e.* the work function, the maximum intensity and any other relevant property to fill 2D *waves* (or maps).
5. Repeat steps [2-4] for every pixel.

The result is therefore a map of the useful quantity, often a work function map as shown on Figure A.4. The procedure and a detailed tutorial are available [here](#)<sup>4</sup>. It can easily be extended to other features of the photoemission spectrum. For instance, pixel-by-pixel analysis of core-level images is very interesting to obtain a chemical mapping of a surface. However, contrary to the photoemission threshold, the lineshapes of core-levels spectra can be very different from one element to another. The carbon 1s spectrum of graphene is highly asymmetric due to the metallic nature of graphene: the lineshape is therefore a Dunjac-Sunjic lineshape. On the contrary, bismuth 4f in BiFeO<sub>3</sub> is a convolution of a Gaussian and a Lorentzian shape (Voigt lineshape)<sup>5</sup>. Thus, at the moment, procedures analyzing PEEM images acquired at core-levels are case-by-case and only suitable to a specific experiment. This is the case for the study of C 1s in few-layers graphene presented in Appendix B.

This procedure is readily compatible with MEM-LEEM transition. Indeed, MEM-LEEM transition can also be modeled by a complementary error function from which we extract the inflection point corresponding to the transition from high reflectivity (MEM regime) to low reflectivity (LEEM regime).

<sup>3</sup>See Chapter 3 and Appendix B for the utilization of work function mapping.

<sup>4</sup>[http://iramis-i.cea.fr/Pisp/julien.rault/NanoESCA\\_Igor\\_Procedures.rar](http://iramis-i.cea.fr/Pisp/julien.rault/NanoESCA_Igor_Procedures.rar)

<sup>5</sup>See Chapter 15 of Ref. [34] for a more detailed description of lineshapes in photoemission spectroscopy.

## C.2 Energy Dispersion Correction

Though the mapping procedures for LEEM and PEEM are compatible, data analysis is more convoluted in the case of energy-filtered PEEM. Indeed, by design of hemispherical analyzers, electron kinetic energy slightly spreads along the vertical direction ( $y$  in the following). In microscopy experiments and for a given image taken at the kinetic energy  $E$ , the true kinetic energy of electron detected at the position  $y$  is  $E + \Delta E(y)$  where  $\Delta E(y)$  is given by the following equation [60]:

$$\Delta E(y) = E_p \left( \frac{M_1 \cdot (y - y_0)}{f} \right)^2 \quad (\text{C.2})$$

where  $E_p$  is the pass energy of the analyzers,  $M_1$  is the first lateral magnification of the microscope in the image plane in front of the analyzer and  $y$  is the vertical position with respect to a reference position  $y_0$  where  $\Delta E$  is zero.  $f$  is the focal length of the extractor voltage. We notice that the dispersion is parabolic in  $y$ . For typical parameters ( $M_1 = 50$ ,  $f = 29$  mm,  $E_p = 100$  eV) the energy difference between the center and the edge of an image can be as high as 200 meV for a 50  $\mu\text{m}$  field of view. This phenomenon has to be corrected in every energy-filtered PEEM experiment before the mapping procedures described in the previous section.

The issue of energy dispersion will be described with the case of few-layers graphene presented in Appendix B. Figure C.1a shows a work function map of the sample (field of view of 53  $\mu\text{m}$ , pass energy of 100 eV) without any correction. Figure C.1b displays the work function as a function of  $y$  and clearly shows the parabolic shape of the energy dispersion along the vertical direction and a maximum energy difference of about 250 meV.

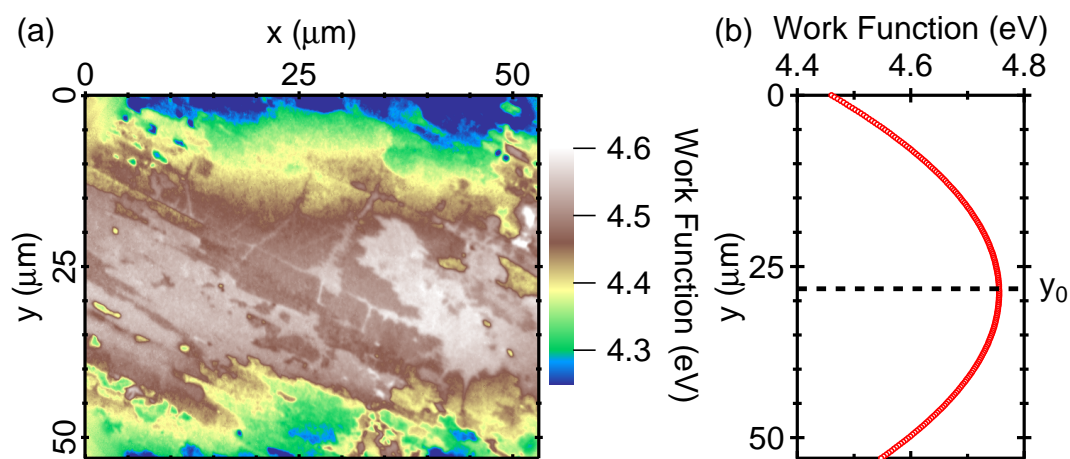


Figure C.1: (a) Work function map of few-layers graphene without any corrections on the data stack and (b) evolution of work function as a function of  $y$ .  $y_0$  is the reference position where there is no energy dispersion.

To obtain the true work function map, the effect of energy dispersion has to be cor-

rected. Two steps are required:

- The first step consists in finding the parabolic relation  $\Delta E = f(y)$ . In theory, equation (C.2) shows that the dispersion is the same for identical pass energy and field of view. Therefore, a set of parabolic relations for various (pass energy, field of view) couples can be obtained with a reference, homogeneous sample and applied on any sample. However, it is often more convenient to be self consistent and use the sample of interest itself as the source of the parabolic relation. To obtain the parabolic relation, the procedure averages every spectrum extracted from the same  $y$  value (integration over all  $x$  values for a given  $y$ ). The resulting spectrum is fitted with equation (C.1) which gives an averaged work function  $\Phi(y)$  for the position  $y$ . This step is repeated over the whole  $y$  range and the procedure returns a parabolic function  $\Phi_S = f(y)$  as shown in Figure C.1b. The reference position  $y_0$  is the central point of the parabola. It is then straightforward to obtain  $\Delta E(y) = \Phi_S(y) - \Phi_S(y_0)$ .
- The second steps consists in applying a kinetic energy shift of  $\Delta E(y)$  to every spectrum extracted from the pixels located at the vertical position  $y$ .

This procedure is available [here](#)<sup>6</sup>. The result of the dispersion correction is shown on Figure C.2.

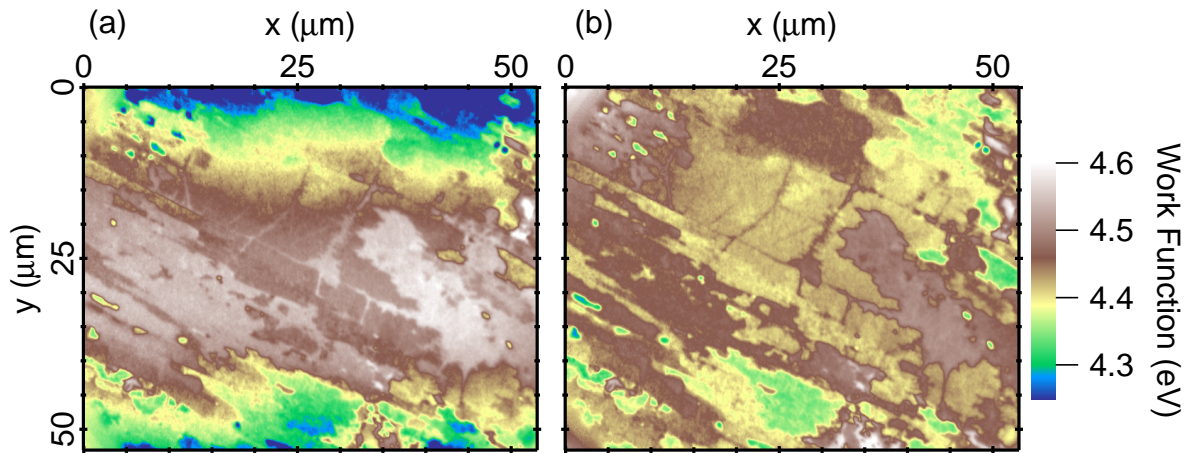


Figure C.2: Work function map of few-layers graphene before (a) and after (b) correction of the energy dispersion.

<sup>6</sup>[http://iramis-i.cea.fr/Pisp/julien.rault/NanoESCA\\_Igor\\_Procedures.rar](http://iramis-i.cea.fr/Pisp/julien.rault/NanoESCA_Igor_Procedures.rar)

# Appendix D

## Landau Theory Applied to BiFeO<sub>3</sub> Ultrathin Films

This appendix describes the Landau development in the case of the BiFeO<sub>3</sub> thin films described in Chapter 3–Section 3.1.

We start from the Ginzburg-Landau Free energy expressed in the form of the expansion with respect to the polarization P:

$$F(P) = \frac{1}{2}\alpha_{\perp} (P_x^2 + P_y^2) + \frac{1}{2}\alpha_z P_z^2 + \frac{1}{4}\beta_1 (P_x^4 + P_y^4) + \frac{1}{4}\beta_2 P_z^4 \quad (\text{D.1})$$
$$+ \frac{1}{2}\beta_3 P_x^2 P_y^2 + \frac{1}{2}\beta_4 (P_x^2 + P_y^2) P_z^2 + \frac{1}{6}\gamma P_z^6 - (E_z + E_d) P_z$$

If  $P_x = P_y = P_{\perp}$  then the equilibrium conditions result in the following equations:

$$\alpha_z P_z + \beta_2 P_z^3 + 2\beta_4 P_z P_{\perp}^2 + \gamma P_z^5 = E_z + E_d \quad (\text{D.2})$$

$$\alpha_{\perp} P_{\perp} + \beta_1 P_{\perp}^3 + \beta_3 P_z^2 P_{\perp} + \beta_4 P_{\perp} P_z^2 = 0 \quad (\text{D.3})$$

Where:

$$E_d = \frac{U\epsilon_0\epsilon_d - P_z d}{\epsilon_0(\epsilon_d h' + \epsilon_b d)} - \frac{U}{h} \quad (\text{D.4})$$

Here,  $h'$  is the width of the polarized region. The total thickness of the film is  $h = h' + d$ , where  $d$  is the dead layer width. We will assume that  $d \ll h$ .  $\epsilon_0$  is the vacuum permittivity.  $\epsilon_d$  is the dielectric constant of the dead layer and  $\epsilon_b$  is the so-called background dielectric constant (which is independent of the film thickness)[31].  $U$  is the voltage between the contacts. Furthermore,  $E_d$  is the depolarizing field [31, 131], and  $E_z = U/h$ .

From (D.3), we have two choices:, whether  $P_{\perp} = 0$  or:

$$\begin{cases} P_{\perp} = 0 \\ P_{\perp}^2 = -\frac{1}{\beta_1 + \beta_3} (\alpha_{\perp} + \beta_4 P_z^2) \end{cases} \quad (\text{D.5})$$

This latter equality reveals that the z-component of the polarization influences the in-plane component, and *vice versa*, the magnitude of the in-plane component of the polarization influences the z-component. Now we substitute Eq. (D.5) into Eq. (D.2) and get:

$$\alpha^P P_z + \beta^P P_z^3 + \gamma P_z^5 = \frac{U \epsilon_d}{\epsilon_d h + \epsilon_b d} \quad (\text{D.6})$$

Where:

$$\begin{aligned} \alpha^P &= \alpha_z + \frac{d}{\epsilon_0 (\epsilon_d h' + \epsilon_b d)} - 2\beta_4 \frac{\alpha_{\perp}}{\beta_1 + \beta_3} \\ &= \alpha^L + \frac{d}{\epsilon_0 (\epsilon_d h' + \epsilon_b d)} \\ &\approx \alpha^L + \frac{d}{\epsilon_0 \epsilon_d h} \\ \beta^P &= \beta_2 - \frac{2\beta_4^2}{\beta_3 + \beta_1} \\ \alpha^L &= \alpha_z - 2\beta_4 \frac{\alpha_{\perp}}{\beta_1 + \beta_3} \end{aligned}$$

Notice that  $\alpha^P$  is modified with respect to  $\alpha_z$ , and can even change sign, because of the depolarizing field and the correction due to the coupling of the in-plane component of polarization with its out-of plane component. Furthermore,  $\beta^P$  is smaller compared to  $\beta_2$  when all  $\beta$ 's are positive. This modification can even result in a negative  $\beta^P$  and therefore change the second-order phase transition to a first-order one. In the case  $U = 0$ , Equation (D.6) has two stable solutions. One is  $P_z = 0$ , while the other is:

$$P_z^2 = \frac{-\beta^P + \sqrt{(\beta^P)^2 - 4\alpha^P \gamma}}{2\gamma} \quad (\text{D.7})$$

One can easily show that such latter solution can be rewritten as:

$$\frac{P_z}{P_{max}} = A \sqrt{B + \sqrt{1 - \frac{h_{eff}}{h}}} \quad (\text{D.8})$$

Where

$$D = \sqrt{(\beta^p)^2 - 4\alpha^L\gamma} \quad (\text{D.9})$$

$$A = \frac{1}{\sqrt{B+1}} \quad (\text{D.10})$$

$$B = \frac{-\beta^p}{D} \quad (\text{D.11})$$

$$h_{eff} = \frac{4d\gamma}{\epsilon_0\epsilon_d D^2} \quad (\text{D.12})$$

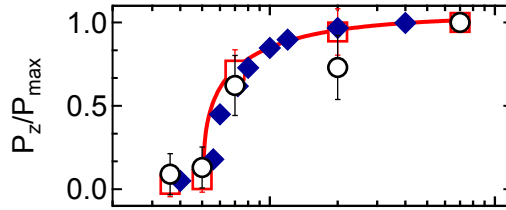


Figure D.1:  $P_z/P_{\max}$  calculated from PEEM (red squares) and MEM-LEEM (black circles). Red curve is fit to PEEM/LEEM data with  $h_{\text{eff}} = 5.6$  nm. Blue diamonds are  $P_z/P_{\max}$  values used for numerical simulations.

Equation (D.8) has been used in Chapter 3–Section 3.1 to fit the data of the Figure D.1. Note that in this fitting, we allowed  $A$  to take an arbitrary value, because  $P_{\max}$  in experiment is not very well defined (one cannot consider very thick films since they become too insulating for Photoemission Microscopy). However, the resulting  $A$  was numerically found to be very close to its ideal value provided in (D.10). Specifically, the ratio between the actual and ideal values for  $A$  was found to be about 1.05.

Note that Equation (D.8) is, of course, valid provided that

$$1 - \frac{h_{eff}}{h} \geq 0$$

$$B + \sqrt{1 - \frac{h_{eff}}{h}} \geq 0$$

These two conditions were met in the fit of the data of Fig. 5b for films thicker than 5.6 nm, since we numerically found that  $h_{eff} = 5.6$  nm and  $B = 0.16$ .

It is also interesting to realize that the solution of Equation (D.7) can adopt a more simple form than Equation (D.8) in some particular cases. For instance, if  $\alpha^p < 0$ ,  $\beta^p > 0$  and  $\gamma = 0$  then:

$$P_z^2 = \frac{-\alpha^p}{\beta^p} = P_{\max}^2 \left(1 - \frac{g_{eff}}{h}\right) \quad (\text{D.13})$$

Where

$$g_{eff} = \frac{d}{\epsilon_0 \epsilon_d \alpha^L}$$

$$P_{max}^2 = -\frac{\alpha^L}{\beta p}$$

Equation (D.13) has the same analytical form than the formula provided by Maksymovych *et al* [131]. However, the physical meaning of the parameters entering Equation (D.13) is different from those given in Ref. [131], because, here, the polarization has three non-zero Cartesian components (rather than a single one).

# Appendix E

## Publications

1. J. E. Rault, G. Agnus, T. Maroutian, V. Pillard, P. Lecoœur, G. Niu, B. Vilquin, M. G. Silly, A. Bendounan, F. Silly, and N. Barrett, *Interface Electronic Structure in a Metal/Ferroelectric Heterostructure under Applied Bias*. [arXiv](#), accepted in Phys. Rev. B (2013)
2. J. E. Rault, W. Ren, S. Prosandeev, S. Lisenkov, D. Sando, S. Fusil, M. Bibes, A. Barthélémy, L. Bellaïche, and N. Barrett, *Thickness-Dependent Polarization of Strained  $\text{BiFeO}_3$  Films with Constant Tetragonality*. [Physical Review Letters](#) 109, 267601 (2012).
3. Y. Mi, G. Geneste, J. E. Rault, C. Mathieu, A. Pancotti, and N. Barrett, *Polarization dependent chemistry of ferroelectric  $\text{BaTiO}_3$  (001) domains*. [Journal of Physics: Condensed Matter](#) 24, 275901 (2012).
4. C. Mathieu, N. Barrett, J. Rault, Y. Y. Mi, B. Zhang, W. A. de Heer, C. Berger, E. H. Conrad, and O. Renault, *Microscopic correlation between chemical and electronic states in epitaxial graphene on  $\text{SiC}(000-1)$* . [Physical Review B](#) 83, 235436 (2011).
5. N. Barrett, J. Rault, I. Krug, B. Vilquin, G. Niu, B. Gautier, D. Albertini, P. Lecoœur, and O. Renault, *Influence of the ferroelectric polarization on the electronic structure of  $\text{BaTiO}_3$  thin films*. [Surface Interface Analysis](#) 42, 1690–1694 (2010)



# Bibliography

- [1] K. Abe, S. Komatsu, N. Yanase, K. Sano, and T. Kawakubo. Asymmetric ferroelectricity and anomalous current conduction in heteroepitaxial BaTiO<sub>3</sub> thin films. *Japanese Journal of Applied Physics*, 36(Part 1, No. 9B):5846–5853, Sept. 1997.
- [2] K. Abe, N. Yanase, and T. Kawakubo. Asymmetric switching of ferroelectric polarization in a heteroepitaxial BaTiO<sub>3</sub> thin film capacitor. *Japanese Journal of Applied Physics*, 39(Part 1, No. 7A):4059–4063, July 2000.
- [3] I. Adawi. Theory of the surface photoelectric effect for one and two photons. *Physical Review*, 134(3A):A788–A798, May 1964.
- [4] D. Albrecht, S. Lisenkov, W. Ren, D. Rahmedov, I. A. Kornev, and L. Bellaiche. Ferromagnetism in multiferroic BiFeO<sub>3</sub> films: A first-principles-based study. *Physical Review B*, 81(14):140401, Apr. 2010.
- [5] E. Almahmoud, I. Kornev, and L. Bellaiche. Dependence of curie temperature on the thickness of an ultrathin ferroelectric film. *Physical Review B*, 81(6):064105, 2010.
- [6] M. Altman and E. Bauer. LEEM/LEED investigation of reconstruction and initial oxidation of the w(001) surface. *Surface Science*, 347(3):265–279, Feb. 1996.
- [7] F. Z. Amir, W. Donner, M. Aspelmeyer, B. Noheda, X. X. Xi, and S. C. Moss. Strain profile and polarization enhancement in Ba<sub>0.5</sub>Sr<sub>0.5</sub>TiO<sub>3</sub> thin films. *Physica Status Solidi (a)*, 209(11):2255–2259, 2012.
- [8] E. Ascher, H. Rieder, H. Schmid, and H. Stössel. Some properties of ferromagneto-electric nickel-iodine boracite Ni<sub>3</sub>B<sub>7</sub>O<sub>13</sub>I. *Journal of Applied Physics*, 37(3):1404–1405, Mar. 1966.
- [9] H. Béa, M. Bibes, A. Barthélémy, K. Bouzehouane, E. Jacquet, A. Khodan, J.-P. Contour, S. Fusil, F. Wyczisk, A. Forget, D. Lebeugle, D. Colson, and M. Viret. Influence of parasitic phases on the properties of BiFeO<sub>3</sub> epitaxial thin films. *Applied Physics Letters*, 87(7):072508, 2005.

- [10] H. Béa, M. Bibes, S. Petit, J. Kreisel, and A. Barthélémy. Structural distortion and magnetism of BiFeO<sub>3</sub> epitaxial thin films: A raman spectroscopy and neutron diffraction study. *Philosophical Magazine Letters*, 87(3-4):165–174, 2007.
- [11] H. Béa, M. Bibes, M. Sirena, G. Herranz, K. Bouzehouane, E. Jacquet, S. Fusil, P. Paruch, M. Dawber, J. P. Contour, and A. Barthélémy. Combining half-metals and multiferroics into epitaxial heterostructures for spintronics. *Applied Physics Letters*, 88(6):062502–062502–3, Feb. 2006.
- [12] H. Béa, S. Fusil, K. Bouzehouane, M. Bibes, M. Sirena, G. Herranz, E. Jacquet, J. P. Contour, and A. Barthélémy. Ferroelectricity down to at least 2 nm in multiferroic BiFeO<sub>3</sub> epitaxial thin films. *Japanese Journal of Applied Physics*, 45(4-7):L187–L189, 2006.
- [13] A. Bailly, O. Renault, N. Barrett, L. F. Zagonel, P. Gentile, N. Pauc, F. Dhalluin, T. Baron, A. Chabli, J. C. Cezar, and N. B. Brookes. Direct quantification of gold along a single si nanowire. *Nano Letters*, 8(11):3709–3714, Nov. 2008.
- [14] J. D. Baniecki, M. Ishii, T. Shioga, K. Kurihara, and S. Miyahara. Surface core-level shifts of strontium observed in photoemission of barium strontium titanate thin films. *Applied Physics Letters*, 89(16):162908–162908–3, Oct. 2006.
- [15] W. Bardyszewski and L. Hedin. A new approach to the theory of photoemission from solids. *Physica Scripta*, 32(4):439, Oct. 1985.
- [16] C. W. Bark, P. Sharma, Y. Wang, S. H. Baek, S. Lee, S. Ryu, C. M. Folkman, T. R. Paudel, A. Kumar, S. V. Kalinin, A. Sokolov, E. Y. Tsymbal, M. S. Rzchowski, A. Gruverman, and C. B. Eom. Switchable induced polarization in LaAlO<sub>3</sub>/SrTiO<sub>3</sub> heterostructures. *Nano Lett.*, 2012.
- [17] N. Barrett, J. Rault, I. Krug, B. Vilquin, G. Niu, B. Gautier, D. Albertini, P. Lecoeur, and O. Renault. Influence of the ferroelectric polarization on the electronic structure of BaTiO<sub>3</sub> thin films. *Surface and Interface Analysis*, 42(12-13):1690–1694, Dec. 2010.
- [18] E. Bauer. Low energy electron microscopy. *Reports on Progress in Physics*, 57(9):895–938, Sept. 1994.
- [19] E. Bauer. Photoelectron spectromicroscopy: present and future. *Journal of Electron Spectroscopy and Related Phenomena*, 114–116:975–987, Mar. 2001.
- [20] E. Bauer. A brief history of PEEM. *Journal of Electron Spectroscopy and Related Phenomena*, 185(10):314–322, Oct. 2012.

- [21] N. Bergeard, M. G. Silly, D. Krizmancic, C. Chauvet, M. Guzzo, J. P. Ricaud, M. Izquierdo, L. Stebel, P. Pittana, R. Sergo, G. Cautero, G. Dufour, F. Rochet, and F. Sirotti. Time-resolved photoelectron spectroscopy using synchrotron radiation time structure. *Journal of Synchrotron Radiation*, 18(2):245–250, Mar. 2011.
- [22] C. Berger, Z. Song, T. Li, X. Li, A. Y. Ogbazghi, R. Feng, Z. Dai, A. N. Marchenkov, E. H. Conrad, P. N. First, and W. A. de Heer. Ultrathin epitaxial graphite: 2D electron gas properties and a route toward graphene-based nanoelectronics. *The Journal of Physical Chemistry B*, 108(52):19912–19916, Dec. 2004.
- [23] C. Berger, Z. Song, X. Li, X. Wu, N. Brown, C. Naud, D. Mayou, T. Li, J. Hass, A. N. Marchenkov, E. H. Conrad, P. N. First, and W. A. d. Heer. Electronic confinement and coherence in patterned epitaxial graphene. *Science*, 312(5777):1191–1196, May 2006.
- [24] A. Berlich, H. Strauss, C. Langheinrich, A. Chassé, and H. Morgner. Surface termination of BaTiO<sub>3</sub>(001) single crystals: A combined electron spectroscopic and theoretical study. *Surface Science*, 605(1-2):158–165, Jan. 2011.
- [25] T. Bertaud, M. Sowinska, D. Walczyk, S. Thiess, A. Gloskovskii, C. Walczyk, and T. Schroeder. In-operando and non-destructive analysis of the resistive switching in the Ti/HfO<sub>2</sub>/TiN-based system by hard x-ray photoelectron spectroscopy. *Applied Physics Letters*, 101(14):143501–143501–5, Oct. 2012.
- [26] M. Bibes. Nanoferronics is a winning combination. *Nature Materials*, 11(5):354–357, 2012.
- [27] D. I. Bilc, F. D. Novaes, J. Íñiguez, P. Ordejón, and P. Ghosez. Electroresistance effect in ferroelectric tunnel junctions with symmetric electrodes. *ACS Nano*, 6(2):1473–1478, Feb. 2012.
- [28] M. Born. Eine thermochemische anwendung der gittertheorie. *Verh Dtsch Physik Ges*, 21:13–24, 1919.
- [29] M. Born and M. Goppert-Mayer. Dynamic lattice theory in crystals. *Handb. Phys.*, 24:623, 1933.
- [30] R. Bouregba, B. Vilquin, G. Le Rhun, G. Poullain, and B. Domenges. Sawyer–Tower hysteresis measurements on micron sized Pb(Zr,Ti)O<sub>3</sub> capacitors. *Review of Scientific Instruments*, 74(10):4429, 2003.
- [31] A. M. Bratkovsky and A. P. Levanyuk. Abrupt appearance of the domain pattern and fatigue of thin ferroelectric films. *Physical Review Letters*, 84(14):3177–3180, Apr. 2000.

- [32] E. Brüche. Elektronenmikroskopische abbildung mit lichtelektrischen elektronen. *Zeitschrift für Physik*, 86(7-8):448–450, July 1933.
- [33] C. J. Brennan. Characterization and modelling of thin-film ferroelectric capacitors using c-v analysis. *Integrated Ferroelectrics*, 2(1-4):73–82, 1992.
- [34] D. Briggs and J. T. Grant. *Surface Analysis by Auger and x-Ray Photoelectron Spectroscopy*. IM Publications LLP, Sept. 2003.
- [35] C. Brundle. Elucidation of surface structure and bonding by photoelectron spectroscopy. *Surface Science*, 48(1):99–136, Mar. 1975.
- [36] M.-Q. Cai, Y.-J. Zhang, Z. Yin, and M.-S. Zhang. First-principles study of structural and electronic properties of BaTiO<sub>3</sub>(001) oxygen-vacancy surfaces. *Physical Review B*, 72(7):075406, Aug. 2005.
- [37] H. B. Callen. Electric breakdown in ionic crystals. *Physical Review*, 76(9):1394–1402, Nov. 1949.
- [38] G. Catalan, H. Béa, S. Fusil, M. Bibes, P. Paruch, A. Barthélémy, and J. F. Scott. Fractal dimension and size scaling of domains in thin films of multiferroic BiFeO<sub>3</sub>. *Physical Review Letters*, 100(2):027602, Jan. 2008.
- [39] G. Catalan and J. F. Scott. Physics and applications of bismuth ferrite. *Advanced Materials*, 21(24):2463–2485, June 2009.
- [40] J. Cazaux. Calculated influence of work function on SE escape probability and secondary electron emission yield. *Applied Surface Science*, 257(3):1002–1009, Nov. 2010.
- [41] H. J. Chang, S. V. Kalinin, A. N. Morozovska, M. Huijben, Y. Chu, P. Yu, R. Ramesh, E. A. Eliseev, G. S. Svechnikov, S. J. Pennycook, and A. Y. Borisevich. Atomically resolved mapping of polarization and electric fields across Ferroelectric/Oxide interfaces by z-contrast imaging. *Advanced Materials*, 23(21):2474–2479, June 2011.
- [42] M. Chelvayohan and C. H. B. Mee. Work function measurements on (110), (100) and (111) surfaces of silver. *Journal of Physics C: Solid State Physics*, 15(10):2305–2312, Apr. 1982.
- [43] F. Chen and A. Klein. Polarization dependence of schottky barrier heights at interfaces of ferroelectrics determined by photoelectron spectroscopy. *Physical Review B*, 86(9):094105, Sept. 2012.

- [44] S. Cherifi, R. Hertel, S. Fusil, H. Béa, K. Bouzehouane, J. Allibe, M. Bibes, and A. Barthélémy. Imaging ferroelectric domains in multiferroics using a low-energy electron microscope in the mirror operation mode. *Physica Status Solidi (RRL) - Rapid Research Letters*, 4(1-2):22–24, Feb. 2010.
- [45] S. Y. Chiam, Z. Q. Liu, J. S. Pan, K. K. Manippady, L. M. Wong, and W. K. Chim. Effects of electric field in band alignment measurements using photoelectron spectroscopy. *Surface and Interface Analysis*, 44(8):1091–1095, 2012.
- [46] N. Choudhury, L. Walizer, S. Lisenkov, and L. Bellaïche. Geometric frustration in compositionally modulated ferroelectrics. *Nature*, 470:513–517, 2011.
- [47] Y. H. Chu, T. Zhao, M. P. Cruz, Q. Zhan, P. L. Yang, L. W. Martin, M. Huijben, C. H. Yang, F. Zavaliche, H. Zheng, and R. Ramesh. Ferroelectric size effects in multiferroic BiFeO<sub>3</sub> thin films. *Applied Physics Letters*, 90(25):252906, 2007.
- [48] P. H. Citrin and G. K. Wertheim. Photoemission from surface-atom core levels, surface densities of states, and metal-atom clusters: A unified picture. *Physical Review B*, 27(6):3176–3200, Mar. 1983.
- [49] W. Cochran. Crystal stability and the theory of ferroelectricity. *Advances in Physics*, 9(36):387–423, 1960.
- [50] R. E. Cohen. Origin of ferroelectricity in perovskite oxides. *Nature*, 358(6382):136–138, 1992.
- [51] D. Céolin, J. Ablett, D. Prieur, T. Moreno, J.-P. Rueff, T. Marchenko, L. Journel, R. Guillemin, B. Pilette, T. Marin, and M. Simon. Hard x-ray photoelectron spectroscopy on the GALAXIES beamline at the SOLEIL synchrotron. *Journal of Electron Spectroscopy and Related Phenomena*, 2013.
- [52] R. Comès, M. Lambert, and A. Guinier. Désordre linéaire dans les cristaux (cas du silicium, du quartz, et des pérovskites ferroélectriques). *Acta Crystallographica Section A*, 26(2):244–254, Mar. 1970.
- [53] R. Courths and S. Hüfner. Photoemission experiments on copper. *Physics Reports*, 112(2):53–171, Oct. 1984.
- [54] A. Damascelli. Probing the electronic structure of complex systems by ARPES. *Physica Scripta*, T109:61, 2004.
- [55] A. Devonshire. Theory of barium titanate .1. *Philosophical Magazine*, 40(309):1040–1063, 1949.
- [56] A. Devonshire. Theory of barium titanate .2. *Philosophical Magazine*, 42(333):1065–1079, 1951.

- [57] A. Devonshire. Theory of ferroelectrics. *Advances in Physics*, 3(10):85–130, 1954.
- [58] A. Einstein. On a heuristic viewpoint concerning the production and transformation of light. *Annalen der Physik*, 17:132–148, 1905.
- [59] M. Escher, N. Weber, M. Merkel, C. Ziethen, P. Bernhard, G. Schönhense, S. Schmidt, F. Forster, F. Reinert, B. Krömker, and D. Funnemann. NanoESCA: a novel energy filter for imaging x-ray photoemission spectroscopy. *Journal of Physics: Condensed Matter*, 17(16):S1329, Apr. 2005.
- [60] M. Escher, K. Winkler, O. Renault, and N. Barrett. Applications of high lateral and energy resolution imaging XPS with a double hemispherical analyser based spectromicroscope. *Journal of Electron Spectroscopy and Related Phenomena*, 178-179:303–316, May 2010.
- [61] D. Estève, T. Maroutian, V. Pillard, and P. Lecoœur. Step velocity tuning of SrRuO<sub>3</sub> step flow growth on SrTiO<sub>3</sub>. *Physical Review B*, 83(19):193401, May 2011.
- [62] C. Fadley, R. Baird, W. Siekhaus, T. Novakov, and S. Bergström. Surface analysis and angular distributions in x-ray photoelectron spectroscopy. *Journal of Electron Spectroscopy and Related Phenomena*, 4(2):93–137, 1974.
- [63] C. S. Fadley. Angle-resolved x-ray photoelectron spectroscopy. *Progress in Surface Science*, 16(3):275–388, 1984.
- [64] S. Farokhipoor and B. Noheda. Conduction through 71° domain walls in BiFeO<sub>3</sub> thin films. *Physical Review Letters*, 107(12):127601, Sept. 2011.
- [65] M. Fechner, S. Ostanin, and I. Mertig. Effect of the surface polarization in polar perovskites studied from first principles. *Physical Review B*, 77(9):094112, Mar. 2008.
- [66] T. Filleter, K. V. Emtsev, T. Seyller, and R. Bennewitz. Local work function measurements of epitaxial graphene. *Applied Physics Letters*, 93(13):133117–133117–3, Oct. 2008.
- [67] P. N. First, W. A. de Heer, T. Seyller, C. Berger, J. A. Stroscio, and J.-S. Moon. Epitaxial graphenes on silicon carbide. *MRS Bulletin*, 35(04):296–305, 2010.
- [68] V. Y. Fominski, O. I. Naoumenko, V. N. Nevolin, A. P. Alekhin, A. M. Markeev, and L. A. Vyukov. Photochemical removal of organic contaminants from silicon surface at room temperature. *Applied Physics Letters*, 68(16):2243, 1996.
- [69] D. D. Fong, A. M. Kolpak, J. A. Eastman, S. K. Streiffer, P. H. Fuoss, G. B. Stephenson, C. Thompson, D. M. Kim, K. J. Choi, C. B. Eom, I. Grinberg, and

- A. M. Rappe. Stabilization of monodomain polarization in ultrathin  $\text{PbTiO}_3$  films. *Physical Review Letters*, 96(12):127601, Mar. 2006.
- [70] V. M. Fridkin. *Photoferroelectrics*, volume 9. Springer-Verlag, New-York, 1979.
- [71] V. Garcia, M. Bibes, L. Bocher, S. Valencia, F. Kronast, A. Crassous, X. Moya, S. Enouz-Vedrenne, A. Gloter, D. Imhoff, C. Deranlot, N. D. Mathur, S. Fusil, K. Bouzheouane, and A. Barthelemy. Ferroelectric control of spin polarization. *Science*, 327(5969):1106–1110, 2010.
- [72] V. Garcia, S. Fusil, K. Bouzheouane, S. Enouz-Vedrenne, N. D. Mathur, A. Barthelemy, and M. Bibes. Giant tunnel electroresistance for non-destructive readout of ferroelectric states. *Nature*, 460(7251):81–84, 2009.
- [73] G. Geneste and B. Dkhil. Adsorption and dissociation of  $\text{H}_2\text{O}$  on in-plane-polarized  $\text{BaTiO}_3(001)$  surfaces and their relation to ferroelectricity. *Physical Review B*, 79(23):235420, 2009.
- [74] G. Gerra, A. K. Tagantsev, and N. Setter. Ferroelectricity in asymmetric metal-ferroelectric-metal heterostructures: A combined first-Principles–Phenomenological approach. *Physical Review Letters*, 98(20):207601, 2007.
- [75] P. Ghosez, E. Cockayne, U. V. Waghmare, and K. M. Rabe. Lattice dynamics of  $\text{BaTiO}_3$ ,  $\text{PbTiO}_3$ , and  $\text{PbZrO}_3$ : a comparative first-principles study. *Physical Review B*, 60(2):836–843, July 1999.
- [76] P. Ghosez, J.-P. Michenaud, and X. Gonze. Dynamical atomic charges: The case of  $\text{ABO}_3$  compounds. *Physical Review B*, 58(10):6224, 1998.
- [77] A. Gruverman, D. Wu, and J. F. Scott. Piezoresponse force microscopy studies of switching behavior of ferroelectric capacitors on a 100-ns time scale. *Physical Review Letters*, 100(9):097601, Mar. 2008.
- [78] M. Guzzo, G. Lani, F. Sottile, P. Romaniello, M. Gatti, J. J. Kas, J. J. Rehr, M. G. Silly, F. Sirotti, and L. Reining. Valence electron photoemission spectrum of semiconductors: Ab initio description of multiple satellites. *Physical Review Letters*, 107(16):166401, Oct. 2011.
- [79] F. Haber. Theory of the heat of reaction. *Verhandl Deut Phys Ges*, 21:750–768, 1919.
- [80] J. Hass, W. A. de Heer, and E. H. Conrad. The growth and morphology of epitaxial multilayer graphene. *Journal of Physics: Condensed Matter*, 20(32):323202, Aug. 2008.

- [81] R. Haumont, J. Kreisel, P. Bouvier, and F. Hippert. Phonon anomalies and the ferroelectric phase transition in multiferroic BiFeO<sub>3</sub>. *Physical Review B*, 73(13), Apr. 2006.
- [82] M. J. Haun, E. Furman, S. J. Jang, H. A. McKinstry, and L. E. Cross. Thermodynamic theory of PbTiO<sub>3</sub>. *Journal of Applied Physics*, 62(8):3331–3338, Oct. 1987.
- [83] L. He and D. Vanderbilt. First-principles study of oxygen-vacancy pinning of domain walls in PbTiO<sub>3</sub>. *Physical Review B*, 68(13):134103, Oct. 2003.
- [84] M. H. Hecht. Role of photocurrent in low-temperature photoemission studies of schottky-barrier formation. *Physical Review B*, 41(11):7918–7921, Apr. 1990.
- [85] L. Hedin and S. Lundqvist. Effects of electron-electron and electron-phonon interactions on the one-electron states of solids. In D. T. Frederick Seitz and H. Ehrenreich, editors, *Solid State Physics*, volume Volume 23, pages 1–181. Academic Press, 1970.
- [86] H. Hertz. Ueber einen einfluss des ultravioletten lichtes auf die electrische entladung. *Annalen der Physik*, 267(8):983–1000, 1887.
- [87] S. Hüfner. *Photoelectron Spectroscopy*. Springer, 3rd revised and enlarged ed. edition, July 2003.
- [88] H. Hibino, H. Kageshima, F. Maeda, M. Nagase, Y. Kobayashi, and H. Yamaguchi. Microscopic thickness determination of thin graphite films formed on SiC from quantized oscillation in reflectivity of low-energy electrons. *Physical Review B*, 77(7):075413, 2008.
- [89] F. Hiebel, P. Mallet, F. Varchon, L. Magaud, and J.-Y. Veullen. Graphene-substrate interaction on 6H-SiC(000 $\bar{1}$ ) : A scanning tunneling microscopy study. *Physical Review B*, 78(15):153412, Oct. 2008.
- [90] M. J. Highland, T. T. Fister, D. D. Fong, P. H. Fuoss, C. Thompson, J. A. Eastman, S. K. Streiffer, and G. B. Stephenson. Equilibrium polarization of ultrathin PbTiO<sub>3</sub> with surface compensation controlled by oxygen partial pressure. *Physical Review Letters*, 107(18):187602, Oct. 2011.
- [91] M. J. Highland, T. T. Fister, M.-I. Richard, D. D. Fong, P. H. Fuoss, C. Thompson, J. A. Eastman, S. K. Streiffer, and G. B. Stephenson. Polarization switching without domain formation at the intrinsic coercive field in ultrathin ferroelectric PbTiO<sub>3</sub>. *Physical Review Letters*, 105(16):167601, Oct. 2010.
- [92] M. Hölzer, M. Fechner, S. Ostanin, and I. Mertig. Ab initio study of magnetoelectricity in Fe/BaTiO<sub>3</sub>: the effects of n-doped perovskite interfaces. *Journal of Physics: Condensed Matter*, 23(45):455902, Nov. 2011.

- [93] K. Horn. Photoemission studies of barrier heights in metal–semiconductor interfaces and heterojunctions. *Applied Surface Science*, 166(1–4):1–11, Oct. 2000.
- [94] K. Horn, M. Moreno, M. Alonso, M. Höricke, R. Hey, J. Sacedón, and K. Ploog. Photoelectron emission from heterojunctions with intralayers: band-offset changes vs. band-bending effects. *Vacuum*, 67(1):115–123, Sept. 2002.
- [95] L. T. Hudson, R. L. Kurtz, S. W. Robey, D. Temple, and R. L. Stockbauer. Photoelectron spectroscopic study of the valence and core-level electronic structure of BaTiO<sub>3</sub>. *Physical Review B*, 47(3):1174–1180, Jan. 1993.
- [96] L. T. Hudson, R. L. Kurtz, S. W. Robey, D. Temple, and R. L. Stockbauer. Surface core-level shifts of barium observed in photoemission of vacuum-fractured BaTiO<sub>3</sub>(100). *Physical Review B*, 47(16):10832–10838, Apr. 1993.
- [97] H. Y. Hwang, Y. Iwasa, M. Kawasaki, B. Keimer, N. Nagaosa, and Y. Tokura. Emergent phenomena at oxide interfaces. *Nat Mater*, 11(2):103–113, 2012.
- [98] I. C. Infante, J. Juraszek, S. Fusil, B. Dupé, P. Gemeiner, O. Diéguez, F. Pailloux, S. Jouen, E. Jacquet, G. Geneste, J. Pcaud, J. Íñiguez, L. Bellaiche, A. Barthélémy, B. Dkhil, and M. Bibes. Multiferroic phase transition near room temperature in BiFeO<sub>3</sub> films. *Physical Review Letters*, 107(23):237601, Nov. 2011.
- [99] I. C. Infante, S. Lisenkov, B. Dupé, M. Bibes, S. Fusil, E. Jacquet, G. Geneste, S. Petit, A. Courtial, J. Juraszek, L. Bellaiche, A. Barthélémy, and B. Dkhil. Bridging multiferroic phase transitions by epitaxial strain in BiFeO<sub>3</sub>. *Physical Review Letters*, 105(5):057601, 2010.
- [100] H. Ishii, T. Nakajima, Y. Takahashi, and T. Furukawa. Ultrafast polarization switching in ferroelectric polymer thin films at extremely high electric fields. *Applied Physics Express*, 4(3):031501, Mar. 2011.
- [101] J. Junquera and P. Ghosez. Critical thickness for ferroelectricity in perovskite ultrathin films. *Nature*, 422(6931):506–509, 2003.
- [102] S. V. Kalinin and D. A. Bonnell. Local potential and polarization screening on ferroelectric surfaces. *Physical Review B*, 63(12):125411, Mar. 2001.
- [103] M. Kawasaki, K. Takahashi, T. Maeda, R. Tsuchiya, M. Shinohara, O. Ishiyama, T. Yonezawa, M. Yoshimoto, and H. Koinuma. Atomic control of the SrTiO<sub>3</sub> crystal surface. *Science*, 266:1540–1542, Dec. 1994.
- [104] S. D. Kevan. Design of a high-resolution angle-resolving electron energy analyzer. *Review of Scientific Instruments*, 54(11):1441–1445, Nov. 1983.

- [105] H. Khassaf, G. A. Ibanescu, I. Pintilie, I. B. Misirlioglu, and L. Pintilie. Potential barrier increase due to gd doping of BiFeO<sub>3</sub> layers in Nb:SrTiO<sub>3</sub>/BiFeO<sub>3</sub>/Pt structures displaying diode-like behavior. *Applied Physics Letters*, 100(25):252903–252903–4, June 2012.
- [106] A. Kholkin, S. Kalinin, A. Roelofs, and A. Gruverman. Review of ferroelectric domain imaging by piezoresponse force microscopy. *Alexei Gruverman Publications*, Jan. 2007.
- [107] D. H. Kim, H. N. Lee, M. D. Biegalski, and H. M. Christen. Effect of epitaxial strain on ferroelectric polarization in multiferroic BiFeO<sub>3</sub> films. *Applied Physics Letters*, 92(1):012911, 2008.
- [108] T. H. Kim, S. H. Baek, S. M. Yang, Y. S. Kim, B. C. Jeon, D. Lee, J.-S. Chung, C. B. Eom, J.-G. Yoon, and T. W. Noh. Polarity-dependent kinetics of ferroelectric switching in epitaxial BiFeO<sub>3</sub>(111) capacitors. *Applied Physics Letters*, 99(1):012905, 2011.
- [109] R. D. King-Smith and D. Vanderbilt. Theory of polarization of crystalline solids. *Physical Review B*, 47(3):1651, Jan. 1993.
- [110] A. M. Kolpak, D. Li, R. Shao, A. M. Rappe, and D. A. Bonnell. Evolution of the structure and thermodynamic stability of the BaTiO<sub>3</sub>(001) surface. *Physical Review Letters*, 101(3):036102, July 2008.
- [111] T. Koopmans. Über die zuordnung von wellenfunktionen und eigenwerten zu den einzelnen elektronen eines atoms. *Physica*, 1(1–6):104–113, 1934.
- [112] L. Kornblum, J. A. Rothschild, Y. Kauffmann, R. Brener, and M. Eizenberg. Band offsets and fermi level pinning at metal/Al<sub>2</sub>O<sub>3</sub> interfaces. *Physical Review B*, 84(15):155317, Oct. 2011.
- [113] I. Kornev, H. Fu, and L. Bellaiche. Ultrathin films of ferroelectric solid solutions under a residual depolarizing field. *Physical Review Letters*, 93(19):196104, Nov. 2004.
- [114] I. A. Kornev, S. Lisenkov, R. Haumont, B. Dkhil, and L. Bellaiche. Finite-temperature properties of multiferroic BiFeO<sub>3</sub>. *Physical Review Letters*, 99(22):227602, Nov. 2007.
- [115] G. Koster, L. Klein, W. Siemons, G. Rijnders, J. S. Dodge, C.-B. Eom, D. H. A. Blank, and M. R. Beasley. Structure, physical properties, and applications of SrRuO<sub>3</sub> thin films. *Reviews of Modern Physics*, 84(1):253–298, Mar. 2012.

- [116] E. A. Kraut, R. W. Grant, J. R. Waldrop, and S. P. Kowalczyk. Precise determination of the valence-band edge in x-ray photoemission spectra: Application to measurement of semiconductor interface potentials. *Physical Review Letters*, 44(24):1620–1623, 1980.
- [117] R. Kretschmer and K. Binder. Surface effects on phase transitions in ferroelectrics and dipolar magnets. *Physical Review B*, 20(3):1065–1076, Aug. 1979.
- [118] B. Krömker, M. Escher, D. Funnemann, D. Hartung, H. Engelhard, and J. Kirschner. Development of a momentum microscope for time resolved band structure imaging. *Review of Scientific Instruments*, 79(5):053702, 2008.
- [119] I. Krug, N. Barrett, A. Petraru, A. Locatelli, T. O. Montes, M. A. Nino, K. Rahmanizadeh, G. Bihlmayer, and C. M. Schneider. Extrinsic screening of ferroelectric domains in  $Pb(Zr_{0.48}Ti_{0.52})O_3$ . *Applied Physics Letters*, 97(22):222903, 2010.
- [120] G. H. Kwei, A. C. Lawson, S. J. L. Billinge, and S. W. Cheong. Structures of the ferroelectric phases of barium titanate. *The Journal of Physical Chemistry*, 97(10):2368–2377, Mar. 1993.
- [121] T. Lü and W. Cao. Generalized continuum theory for ferroelectric thin films. *Physical Review B*, 66(2):024102, 2002.
- [122] B.-K. Lai, I. Ponomareva, I. Kornev, L. Bellaiche, and G. Salamo. Thickness dependency of  $180^\circ$  stripe domains in ferroelectric ultrathin films: A first-principles-based study. *Applied Physics Letters*, 91(15):152909, 2007.
- [123] M. Lavayssière, O. Renault, D. Mariolle, M. Veillerot, J. P. Barnes, J. M. Hartmann, J. Leroy, and N. Barrett. Photoemission induced bias in two-dimensional silicon pn junctions. *Applied Physics Letters*, 99:202107, 2011.
- [124] X. L. Li, B. Chen, H. Y. Jing, H. B. Lu, B. R. Zhao, Z. H. Mai, and Q. J. Jia. Experimental evidence of the "dead layer" at Pt/BaTiO<sub>3</sub> interface. *Applied Physics Letters*, 87(22):222905, 2005.
- [125] C. Lichtensteiger, M. Dawber, N. Stucki, J.-M. Triscone, J. Hoffman, J.-B. Yau, C. H. Ahn, L. Despont, and P. Aebi. Monodomain to polydomain transition in ferroelectric PbTiO<sub>3</sub> thin films with  $La_{0.67}Sr_{0.33}MnO_3$  electrodes. *Applied Physics Letters*, 90(5):052907, 2007.
- [126] C. Lichtensteiger, J.-M. Triscone, J. Junquera, and P. Ghosez. Ferroelectricity and tetragonality in ultrathin PbTiO<sub>3</sub> films. *Physical Review Letters*, 94(4):047603, 2005.

- [127] C. Lin, C. Mitra, and A. A. Demkov. Orbital ordering under reduced symmetry in transition metal perovskites: Oxygen vacancy in SrTiO<sub>3</sub>. *Physical Review B*, 86(16):161102, Oct. 2012.
- [128] S. Lizzit, G. Zampieri, L. Petaccia, R. Larciprete, P. Lacovig, E. D. L. Rienks, G. Bihlmayer, A. Baraldi, and P. Hofmann. Band dispersion in the deep 1s core level of graphene. *Nat Phys*, 6(5):345–349, 2010.
- [129] H. Lu, X. Liu, J. D. Burton, C.-W. Bark, Y. Wang, Y. Zhang, D. J. Kim, A. Stamm, P. Lukashev, D. A. Felker, C. M. Folkman, P. Gao, M. S. Rzechowski, X. Q. Pan, C.-B. Eom, E. Y. Tsymbal, and A. Gruverman. Enhancement of ferroelectric polarization stability by interface engineering. *Advanced Materials*, 24(9):1209–1216, 2012.
- [130] G. D. Mahan. Theory of photoemission in simple metals. *Physical Review B*, 2(11):4334–4350, Dec. 1970.
- [131] P. Maksymovych, M. Huijben, M. Pan, S. Jesse, N. Balke, Y.-H. Chu, H. J. Chang, A. Y. Borisevich, A. P. Baddorf, G. Rijnders, D. H. A. Blank, R. Ramesh, and S. V. Kalinin. Ultrathin limit and dead-layer effects in local polarization switching of BiFeO<sub>3</sub>. *Physical Review B*, 85(1):014119, Jan. 2012.
- [132] P. Maksymovych, J. Seidel, Y. H. Chu, P. Wu, A. P. Baddorf, L.-Q. Chen, S. V. Kalinin, and R. Ramesh. Dynamic conductivity of ferroelectric domain walls in BiFeO<sub>3</sub>. *Nano Letters*, 11(5):1906–1912, 2011.
- [133] X. Martí, P. Ferrer, J. Herrero-Albillos, J. Narvaez, V. Holy, N. Barrett, M. Alexe, and G. Catalan. Skin layer of BiFeO<sub>3</sub> single crystals. *Physical Review Letters*, 106(23):236101, 2011.
- [134] R. M. Martin and K. Kunc. Direct method of calculation of dynamic effective charges: Application to GaAs. *Physical Review B*, 24(4):2081–2088, Aug. 1981.
- [135] C. Mathieu, N. Barrett, J. Rault, Y. Y. Mi, B. Zhang, W. A. de Heer, C. Berger, E. H. Conrad, and O. Renault. Microscopic correlation between chemical and electronic states in epitaxial graphene on SiC(000 $\bar{1}$ ). *Physical Review B*, 83(23):235436, 2011.
- [136] R. McQuaid, L. McGilly, P. Sharma, A. Gruverman, and J. Gregg. Mesoscale flux-closure domain formation in single-crystal BaTiO<sub>3</sub>. *Nat Commun*, 2:404, 2011.
- [137] T. O. Mentęs and A. Locatelli. Angle-resolved x-ray photoemission electron microscopy. *Journal of Electron Spectroscopy and Related Phenomena*, 185(10):323–329, Oct. 2012.

- [138] W. J. Merz. Domain properties in BaTiO<sub>3</sub>. *Physical Review*, 88(2):421–422, Oct. 1952.
- [139] W. J. Merz. Double hysteresis loop of BaTiO<sub>3</sub> at the curie point. *Physical Review*, 91(3):513–517, 1953.
- [140] W. J. Merz. Domain formation and domain wall motions in ferroelectric BaTiO<sub>3</sub> single crystals. *Physical Review*, 95(3):690, 1954.
- [141] B. Meyer and D. Vanderbilt. Ab initio study of BaTiO<sub>3</sub> and PbTiO<sub>3</sub> surfaces in external electric fields. *Physical Review B*, 63(20):205426, 2001.
- [142] B. Meyer and D. Vanderbilt. Ab initio study of ferroelectric domain walls in PbTiO<sub>3</sub>. *Physical Review B*, 65(10):104111, Mar. 2002.
- [143] H. L. Meyerheim, F. Klimenta, A. Ernst, K. Mohseni, S. Ostanin, M. Fechner, S. Parihar, I. V. Maznichenko, I. Mertig, and J. Kirschner. Structural secrets of multiferroic interfaces. *Physical Review Letters*, 106(8):087203, 2011.
- [144] Y. Mi, G. Geneste, J. E. Rault, C. Mathieu, A. Pancotti, and N. Barrett. Polarization dependent chemistry of ferroelectric BaTiO<sub>3</sub>(001) domains. *Journal of Physics: Condensed Matter*, 24(27):275901, July 2012.
- [145] M. Mlynarczyk, K. Szot, A. Petraru, U. Poppe, U. Breuer, R. Waser, and K. Tomala. Surface layer of SrRuO<sub>3</sub> epitaxial thin films under oxidizing and reducing conditions. *Journal of Applied Physics*, 101(2):023701–023701–11, Jan. 2007.
- [146] R. Moos and K. H. Hardtl. Defect chemistry of donor-doped and undoped strontium titanate ceramics between 1000° and 1400°C. *Journal of the American Ceramic Society*, 80(10):2549–2562, Oct. 1997.
- [147] S. M. Mukhopadhyay and T. C. Chen. Surface chemical states of barium titanate: Influence of sample processing. *Journal of Materials Research*, 10(06):1502–1507, 1995.
- [148] D. A. Muller, N. Nakagawa, A. Ohtomo, J. L. Grazul, and H. Y. Hwang. Atomic-scale imaging of nanoengineered oxygen vacancy profiles in SrTiO<sub>3</sub>. *Nature*, 430(7000):657–661, Aug. 2004.
- [149] A. Musleh Alrub and L.-H. Ong. Thickness dependence of switching time and coercive field in ferroelectric thin films. *Journal of Applied Physics*, 109(8):084109, 2011.
- [150] T. Nagata, M. Haemori, Y. Yamashita, H. Yoshikawa, Y. Iwashita, K. Kobayashi, and T. Chikyow. Oxygen migration at Pt/HfO<sub>2</sub>/Pt interface under bias operation. *Applied Physics Letters*, 97(8):082902–082902–3, Aug. 2010.

- [151] T. Nagata, M. Haemori, Y. Yamashita, H. Yoshikawa, Y. Iwashita, K. Kobayashi, and T. Chikyow. Bias application hard x-ray photoelectron spectroscopy study of forming process of Cu/HfO<sub>2</sub>/Pt resistive random access memory structure. *Applied Physics Letters*, 99(22):223517, 2011.
- [152] C. T. Nelson, B. Winchester, Y. Zhang, S.-J. Kim, A. Melville, C. Adamo, C. M. Folkman, S.-H. Baek, C.-B. Eom, D. G. Schlom, L.-Q. Chen, and X. Pan. Spontaneous vortex nanodomain arrays at ferroelectric heterointerfaces. *Nano Letters*, 11(2):828–834, 2011.
- [153] S. A. Nepijko and G. Schönhense. Measurement of potential distribution function on object surface by using an electron microscope in the mirror operation mode. *Journal of Microscopy*, 238(1):90–94, Apr. 2010.
- [154] S. A. Nepijko, N. N. Sedov, O. Schmidt, G. Schönhense, X. Bao, and W. Huang. Imaging of three-dimensional objects in emission electron microscopy. *Journal of Microscopy*, 202(3):480–487, June 2001.
- [155] S. A. Nepijko, N. N. Sedov, and G. Schönhense. Peculiarities of imaging one- and two-dimensional structures using an electron microscope in the mirror operation mode. *Journal of Microscopy*, 203(3):269–276, Sept. 2001.
- [156] M. Núñez and M. Buongiorno Nardelli. Interface phase and tuning of polarization in metal-ferroelectric junctions: A theoretical study. *Applied Physics Letters*, 92(25):252903–252903–3, June 2008.
- [157] G. Niu, B. Gautier, S. Yin, G. Saint-Girons, P. Lecoœur, V. Pillard, G. Hollinger, and B. Vilquin. Molecular beam epitaxy growth of BaTiO<sub>3</sub> thin films and crucial impact of oxygen content conditions on the electrical characteristics. *Thin Solid Films*, 520(14):4595–4599, May 2012.
- [158] C. Nordling, E. Sokolowski, and K. Siegbahn. Precision method for obtaining absolute values of atomic binding energies. *Physical Review*, 105(5):1676–1677, Mar. 1957.
- [159] K. S. Novoselov, A. K. Geim, S. V. Morozov, D. Jiang, Y. Zhang, S. V. Dubonos, I. V. Grigorieva, and A. A. Firsov. Electric field effect in atomically thin carbon films. *Science*, 306(5696):666–669, Oct. 2004.
- [160] M. Nuñez and M. Buongiorno Nardelli. Onset of ferrielectricity and the hidden nature of nanoscale polarization in ferroelectric thin films. *Physical Review Letters*, 101(10):107603, 2008.
- [161] A. Ohtomo and H. Y. Hwang. A high-mobility electron gas at the LaAlO<sub>3</sub>/SrTiO<sub>3</sub> heterointerface. *Nature*, 427(6973):423–426, Jan. 2004.

- [162] G. Onida, L. Reining, and A. Rubio. Electronic excitations: density-functional versus many-body green's-function approaches. *Reviews of Modern Physics*, 74(2):601–659, June 2002.
- [163] X. Q. Pan, V. Gopalan, L. Q. Chen, D. G. Schlom, C. B. Eom, A. Tofterup, K. J. Choi, M. Biegalski, Y. L. Li, A. Sharan, J. Schubert, R. Uecker, P. Reiche, and Y. B. Chen. Enhancement of ferroelectricity in strained BaTiO<sub>3</sub> thin films. *Science*, 306(5698):1005–1009, Nov. 2004.
- [164] G. Panaccione and K. Kobayashi. Hard x-ray photoemission spectroscopy: Variable depth analysis of bulk, surface and interface electronic properties. *Surface Science*, 606(3–4):125–129, Feb. 2012.
- [165] C. Papp, L. Plucinski, J. Minar, J. Braun, H. Ebert, C. M. Schneider, and C. S. Fadley. Band mapping in x-ray photoelectron spectroscopy: An experimental and theoretical study of w(110) with 1.25 keV excitation. *Physical Review B*, 84(4):045433, 2011.
- [166] N. Pauly and S. Tougaard. Surface and core hole effects in x-ray photoelectron spectroscopy. *Surface Science*, 604(13-14):1193–1196, 2010.
- [167] J. Pendry. Theory of photoemission. *Surface Science*, 57(2):679–705, 1976.
- [168] N. A. Pertsev and H. Kohlstedt. Elastic stabilization of a single-domain ferroelectric state in nanoscale capacitors and tunnel junctions. *Physical Review Letters*, 98(25):257603, June 2007.
- [169] L. Pintilie and M. Alexe. Metal-ferroelectric-metal heterostructures with schottky contacts. i. influence of the ferroelectric properties. *Journal of Applied Physics*, 98(12):124103, 2005.
- [170] L. Pintilie, I. Boerasu, M. J. M. Gomes, T. Zhao, R. Ramesh, and M. Alexe. Metal-ferroelectric-metal structures with schottky contacts. II. analysis of the experimental current-voltage and capacitance-voltage characteristics of pb(Zr,Ti)O<sub>3</sub> thin films. *Journal of Applied Physics*, 98(12):124104, 2005.
- [171] L. Pintilie, I. Vrejoiu, D. Hesse, G. LeRhun, and M. Alexe. Ferroelectric polarization-leakage current relation in high quality epitaxial pb(Zr,Ti)O<sub>3</sub> films. *Physical Review B*, 75(10):104103, Mar. 2007.
- [172] F. Polack, M. Silly, C. Chauvet, B. Lagarde, N. Bergeard, M. Izquierdo, O. Chubar, D. Krizmancic, M. Ribbens, J.-P. Duval, C. Basset, S. Kubsky, and F. Sirotti. TEMPO: a new insertion device beamline at SOLEIL for time resolved photoelectron spectroscopy experiments on solids and interfaces. *AIP Conference Proceedings*, 1234(1):185–188, June 2010.

- [173] W. Pompe, X. Gong, Z. Suo, and J. S. Speck. Elastic energy release due to domain formation in the strained epitaxy of ferroelectric and ferroelastic films. *Journal of Applied Physics*, 74(10):6012–6019, Nov. 1993.
- [174] I. Ponomareva, I. I. Naumov, I. Kornev, H. Fu, and L. Bellaiche. Atomistic treatment of depolarizing energy and field in ferroelectric nanostructures. *Physical Review B*, 72(14):140102, Oct. 2005.
- [175] S. Prosandeev, S. Lisenkov, and L. Bellaiche. Kittel law in BiFeO<sub>3</sub> ultrathin films: A first-principles-based study. *Physical Review Letters*, 105(14):147603, 2010.
- [176] K. M. Rabe, C. H. Ahn, and J.-M. Triscone. *Physics of Ferroelectrics - A Modern Perspective*. Number 105 in Topics in Applied Physics. Springer, 2007.
- [177] R. Ramesh and N. A. Spaldin. Multiferroics: progress and prospects in thin films. *Nat Mater*, 6(1):21–29, Jan. 2007.
- [178] F. Rao, M. Kim, A. J. Freeman, S. Tang, and M. Anthony. Structural and electronic properties of transition-metal/BaTiO<sub>3</sub>(001) interfaces. *Physical Review B*, 55(20):13953, 1997.
- [179] A. M. Rappe, G. B. Stephenson, R. V. Wang, D. D. Fong, F. Jiang, M. J. Highland, P. H. Fuoss, C. Thompson, A. M. Kolpak, J. A. Eastman, and S. K. Streiffer. Reversible chemical switching of a ferroelectric film. *Physical Review Letters*, 102(4), Jan. 2009.
- [180] J. E. Rault, G. Agnus, T. Maroutian, V. Pillard, P. Lecoeur, G. Niu, B. Vilquin, M. G. Silly, A. Bendounan, F. Silly, and N. Barrett. Interface electronic structure in a Metal/Ferroelectric heterostructure under applied bias. *arXiv:1302.4603*, Feb. 2013.
- [181] B. Ravel, E. A. Stern, R. I. Vedrinskii, and V. Kraizman. Local structure and the phase transitions of BaTiO<sub>3</sub>. *Ferroelectrics*, 206(1):407–430, Feb. 1998.
- [182] O. Renault, R. Brochier, A. Roule, P.-H. Haumesser, B. Krömker, and D. Funne-  
mann. Work-function imaging of oriented copper grains by photoemission. *Surface and Interface Analysis*, 38(4):375–377, 2006.
- [183] R. Resta. Macroscopic polarization in crystalline dielectrics: the geometric phase approach. *Reviews of Modern Physics*, 66(3):899, 1994.
- [184] N. Sai, A. M. Kolpak, and A. M. Rappe. Ferroelectricity in ultrathin perovskite films. *Physical Review B*, 72(2):020101, 2005.

- [185] A. F. Santander-Syro, O. Copie, T. Kondo, F. Fortuna, S. Pailhès, R. Weht, X. G. Qiu, F. Bertran, A. Nicolaou, A. Taleb-Ibrahimi, P. L. Fèvre, G. Herranz, M. Bibes, N. Reyren, Y. Apertet, P. Lecoeur, A. Barthélémy, and M. J. Rozenberg. Two-dimensional electron gas with universal subbands at the surface of SrTiO<sub>3</sub>. *Nature*, 469(7329):189–193, Jan. 2011.
- [186] C. B. Sawyer and C. H. Tower. Rochelle salt as a dielectric. *Physical Review*, 35(3):269–273, Feb. 1930.
- [187] R. Schafranek, S. Payan, M. Maglione, and A. Klein. Barrier height at (Ba,Sr)TiO<sub>3</sub>/Pt interfaces studied by photoemission. *Physical Review B*, 77(19):195310, May 2008.
- [188] D. G. Schlom, L. Chen, X. Pan, A. Schmehl, and M. A. Zurbuchen. A thin film approach to engineering functionality into oxides. *Journal of the American Ceramic Society*, 91(8):2429–2454, Aug. 2008.
- [189] D. G. Schlom, L.-Q. Chen, C.-B. Eom, K. M. Rabe, S. K. Streiffer, and J.-M. Triscone. Strain tuning of ferroelectric thin films. *Annual Review of Materials Research*, 37(1):589–626, Aug. 2007.
- [190] H. Schmid. Multi-ferroic magnetoelectrics. *Ferroelectrics*, 162(1-4):317–338, 1994. INSPEC:4953100.
- [191] C. Schneider, C. Wiemann, M. Patt, V. Feyer, L. Plucinski, I. Krug, M. Escher, N. Weber, M. Merkel, O. Renault, and N. Barrett. Expanding the view into complex material systems: From micro-ARPES to nanoscale HAXPES. *Journal of Electron Spectroscopy and Related Phenomena*, 185(10):330–339, Oct. 2012.
- [192] J. F. Scott. Applications of modern ferroelectrics. *Science*, 315(5814):954–959, 2007.
- [193] J. F. Scott. Ferroelectrics go bananas. *Journal of Physics: Condensed Matter*, 20(2):021001, Jan. 2008.
- [194] J. F. Scott and C. A. P. d. Araujo. Ferroelectric memories. *Science*, 246(4936):1400–1405, Dec. 1989.
- [195] W. Setyawan and S. Curtarolo. High-throughput electronic band structure calculations: Challenges and tools. *Computational Materials Science*, 49(2):299–312, Aug. 2010.
- [196] R. Shao, M. P. Nikiforov, and D. A. Bonnell. Photoinduced charge dynamics on BaTiO<sub>3</sub>(001) surface characterized by scanning probe microscopy. *Applied Physics Letters*, 89(11):112904–112904–3, Sept. 2006.

- [197] J. Shin, A. Y. Borisevich, V. Meunier, J. Zhou, E. W. Plummer, S. V. Kalinin, and A. P. Baddorf. Oxygen-induced surface reconstruction of SrRuO<sub>3</sub> and its effect on the BaTiO<sub>3</sub> interface. *ACS Nano*, 4(7):4190–4196, 2010.
- [198] J. Shin, V. B. Nascimento, A. Y. Borisevich, E. W. Plummer, S. V. Kalinin, and A. P. Baddorf. Polar distortion in ultrathin BaTiO<sub>3</sub> films studied by in situ LEED i-v. *Physical Review B*, 77(24):245437, 2008.
- [199] D. A. Shirley. High-resolution x-ray photoemission spectrum of the valence bands of gold. *Physical Review B*, 5(12):4709, 1972.
- [200] M. Sing, G. Berner, K. Goß, A. Müller, A. Ruff, A. Wetscherek, S. Thiel, J. Mannhart, S. A. Pauli, C. W. Schneider, P. R. Willmott, M. Gorgoi, F. Schäfers, and R. Claessen. Profiling the interface electron gas of LaAlO<sub>3</sub>/SrTiO<sub>3</sub> heterostructures with hard x-ray photoelectron spectroscopy. *Physical Review Letters*, 102(17):176805, 2009.
- [201] J. C. Slater. Wave functions in a periodic potential. *Physical Review*, 51(10):846–851, May 1937.
- [202] N. A. Spaldin. Fundamental size limits in ferroelectricity. *Science*, 304(5677):1606–1607, June 2004.
- [203] M. Stengel, P. Aguado-Puente, N. A. Spaldin, and J. Junquera. Band alignment at metal/ferroelectric interfaces: Insights and artifacts from first principles. *Physical Review B*, 83(23):235112, 2011.
- [204] M. Stengel, D. Vanderbilt, and N. A. Spaldin. Enhancement of ferroelectricity at metal-oxide interfaces. *Nat Mater*, 8(5):392–397, 2009.
- [205] M. Stengel, D. Vanderbilt, and N. A. Spaldin. First-principles modeling of ferroelectric capacitors via constrained displacement field calculations. *Physical Review B*, 80(22):224110, 2009.
- [206] E. A. Stern. Character of order-disorder and displacive components in barium titanate. *Physical Review Letters*, 93(3):037601, 2004.
- [207] J. Stoch and J. Gablankowska-Kukucz. The effect of carbonate contaminations on the XPS o 1s band structure in metal oxides. *Surface and Interface Analysis*, 17(3):165–167, Mar. 1991.
- [208] J. Stohr, Y. Wu, B. Hermsmeier, M. Samant, G. Harp, S. Koranda, D. Dunham, and B. Tonner. Element-specific magnetic microscopy with circularly polarized x-rays. *Science*, 259(5095):658–661, Jan. 1993. WOS:A1993KJ68800035.

- [209] V. N. Strocov. Intrinsic accuracy in 3-dimensional photoemission band mapping. *Journal of Electron Spectroscopy and Related Phenomena*, 130(1–3):65–78, 2003.
- [210] P. Sutter. Epitaxial graphene: How silicon leaves the scene. *Nature Materials*, 8(3):171–172, Mar. 2009.
- [211] S. Suzer, E. Abelev, and S. L. Bernasek. Impedance-type measurements using XPS. *Applied Surface Science*, 256(5):1296–1298, Dec. 2009.
- [212] S. M. Sze and K. K. Ng. *Physics of Semiconductor Devices*. John Wiley & Sons, Nov. 2006.
- [213] A. K. Tagantsev and G. Gerra. Interface-induced phenomena in polarization response of ferroelectric thin films. *Journal of Applied Physics*, 100(5):051607, 2006.
- [214] A. K. Tagantsev, I. Stolichnov, N. Setter, J. S. Cross, and M. Tsukada. Non-kolmogorov-avrami switching kinetics in ferroelectric thin films. *Physical Review B*, 66(21):214109, 2002.
- [215] K. Takeuchi, A. Suda, and S. Ushioda. Local variation of the work function of cu(111) surface deduced from the low energy photoemission spectra. *Surface Science*, 489(1–3):100–106, Aug. 2001.
- [216] M. Takizawa, K. Maekawa, H. Wadati, T. Yoshida, A. Fujimori, H. Kumigashira, and M. Oshima. Angle-resolved photoemission study of nb-doped SrTiO<sub>3</sub>. *Phys. Rev. B*, 79(11):113103, Mar. 2009.
- [217] S. Tanuma, C. J. Powell, and D. R. Penn. Calculations of electron inelastic mean free paths. v. data for 14 organic compounds over the 50–2000 eV range. *Surface and Interface Analysis*, 21(3):165–176, 1994.
- [218] W. Telieps and E. Bauer. An analytical reflection and emission UHV surface electron microscope. *Ultramicroscopy*, 17(1):57–65, 1985.
- [219] B. Tonner, D. Dunham, T. Droubay, and M. Pauli. A photoemission microscope with a hemispherical capacitor energy filter. *Journal of Electron Spectroscopy and Related Phenomena*, 84(1–3):211–229, Mar. 1997.
- [220] S. D. Traynor, T. D. Hadnagy, and L. Kammerdiner. Capacitor test simulation of retention and imprint characteristics for ferroelectric memory operation. *Integrated Ferroelectrics*, 16(1-4):63–76, 1997.
- [221] R. M. Tromp, J. B. Hannon, A. W. Ellis, W. Wan, A. Berghaus, and O. Schaff. A new aberration-corrected, energy-filtered LEEM/PEEM instrument. i. principles and design. *Ultramicroscopy*, 110(7):852–861, June 2010. PMID: 20395048.

- [222] N. T. Tsou, P. R. Potnis, and J. E. Huber. Classification of laminate domain patterns in ferroelectrics. *Physical Review B*, 83(18):184120, May 2011.
- [223] T. Tybell, C. H. Ahn, and J.-M. Triscone. Ferroelectricity in thin perovskite films. *Applied Physics Letters*, 75(6):856–858, Aug. 1999.
- [224] M. Tyunina, R. Oja, M. Plekh, and R. M. Nieminen. Dielectric properties of  $\text{NaNbO}_3/\text{SrTiO}_3$  interface nanolayer. *Journal of Applied Physics*, 109(1):014103–014103–5, Jan. 2011.
- [225] Y. Umeno, J. M. Albina, B. Meyer, and C. Elsässer. Ab initio calculations of ferroelectric instability in  $\text{PbTiO}_3$  capacitors with symmetric and asymmetric electrode layers. *Physical Review B*, 80(20):205122, Nov. 2009.
- [226] Y. Umeno, B. Meyer, C. Elsässer, and P. Gumbsch. Ab initio study of the critical thickness for ferroelectricity in ultrathin  $\text{Pt}/\text{PbTiO}_3/\text{Pt}$  films. *Physical Review B*, 74(6):060101, 2006.
- [227] J. Valasek. Piezo-electric and allied phenomena in rochelle salt. *Physical Review*, 17(4):475–481, Apr. 1921.
- [228] G. Vanacore, L. Zagonel, and N. Barrett. Surface enhanced covalency and madelung potentials in nb doped  $\text{SrTiO}_3$  (100), (110) and (111) single crystals. *Surface Science*, 604(19-20):1674–1683, Sept. 2010.
- [229] J. P. Velev, C.-G. Duan, K. D. Belashchenko, S. S. Jaswal, and E. Y. Tsymbal. Effect of ferroelectricity on electron transport in  $\text{Pt}/\text{BaTiO}_3/\text{Pt}$  tunnel junctions. *Physical Review Letters*, 98(13):137201, Mar. 2007.
- [230] J. P. Velev, C.-G. Duan, K. D. Belashchenko, S. S. Jaswal, and E. Y. Tsymbal. Effects of ferroelectricity and magnetism on electron and spin transport in  $\text{Fe}/\text{BaTiO}_3/\text{Fe}$  multiferroic tunnel junctions. *Journal of Applied Physics*, 103(7):07A701, 2008.
- [231] J. Vogel, W. Kuch, M. Bonfim, J. Camarero, Y. Pennec, F. Offi, K. Fukumoto, J. Kirschner, A. Fontaine, and S. Pizzini. Time-resolved magnetic domain imaging by x-ray photoemission electron microscopy. *Applied Physics Letters*, 82(14):2299–2301, Apr. 2003.
- [232] P. R. Wallace. The band theory of graphite. *Physical Review*, 71(9):622–634, May 1947.
- [233] J. L. Wang, F. Gaillard, A. Pancotti, B. Gautier, G. Niu, B. Vilquin, V. Pillard, G. L. M. P. Rodrigues, and N. Barrett. Chemistry and atomic distortion at the surface of an epitaxial  $\text{BaTiO}_3$  thin film after dissociative adsorption of water. *The Journal of Physical Chemistry C*, 116(41):21802–21809, Oct. 2012.

- [234] J. L. Wang, B. Vilquin, and N. Barrett. Screening of ferroelectric domains on BaTiO<sub>3</sub>(001) surface by ultraviolet photo-induced charge and dissociative water adsorption. *Applied Physics Letters*, 101(9):092902–092902–3, Aug. 2012.
- [235] Y. Wang, X. Liu, J. D. Burton, S. S. Jaswal, and E. Y. Tsybmal. Ferroelectric instability under screened coulomb interactions. *Physical Review Letters*, 109(24):247601, Dec. 2012.
- [236] R. Waser and M. Aono. Nanoionics-based resistive switching memories. *Nature Materials*, 6(11):833–840, 2007.
- [237] S. H. Wemple. Polarization fluctuations and the optical-absorption edge in BaTiO<sub>3</sub>. *Physical Review B*, 2(7):2679–2689, Oct. 1970.
- [238] S. Wendt, R. Bechstein, S. Porsgaard, E. Lira, J. . Hansen, P. Huo, Z. Li, B. Hammer, and F. Besenbacher. Comment on “Oxygen vacancy origin of the surface band-gap state of TiO<sub>2</sub>(110)”. *Physical Review Letters*, 104(25):259703, June 2010.
- [239] S. Wendt, P. T. Sprunger, E. Lira, G. K. H. Madsen, Z. Li, J. . Hansen, J. Matthiesen, A. Blekinge-Rasmussen, E. Lægsgaard, B. Hammer, and F. Besenbacher. The role of interstitial sites in the ti3d defect state in the band gap of titania. *Science*, 320(5884):1755–1759, June 2008.
- [240] H. H. Wieder. Electrical behavior of barium titanate single crystals at low temperatures. *Physical Review*, 99(4):1161–1165, 1955.
- [241] C.-L. Wu, P.-W. Lee, Y.-C. Chen, L.-Y. Chang, C.-H. Chen, C.-W. Liang, P. Yu, Q. He, R. Ramesh, and Y.-H. Chu. Direct spectroscopic evidence of charge reversal at the  $Pb(Zr_{0.2}Ti_{0.8})O_3/La_{0.7}Sr_{0.3}MnO_3$  heterointerface. *Physical Review B*, 83(2):020103, Jan. 2011.
- [242] S. Y. Yang, Seidel J., B. J., Shafer P., Yang C.-H., R. D., Yu P., Chu Y.-H., S. F., A. W., M. W., and Ramesh R. Above-bandgap voltages from ferroelectric photovoltaic devices. *Nat Nano*, 5(2):143–147, 2010.
- [243] J. Yeh and I. Lindau. Atomic subshell photoionization cross sections and asymmetry parameters:  $1 < z < 103$ . *Atomic Data and Nuclear Data Tables*, 32(1):1–155, Jan. 1985.
- [244] C. M. Yim, C. L. Pang, and G. Thornton. Oxygen vacancy origin of the surface band-gap state of TiO<sub>2</sub>(110). *Physical Review Letters*, 104(3):036806, Jan. 2010.
- [245] L. F. Zagonel, N. Barrett, O. Renault, A. Bailly, M. Baeurer, M. Hoffmann, S.-J. Shih, and D. Cockayne. Orientation-dependent surface composition of in situ annealed strontium titanate. *Surface And Interface Analysis*, 40(13):1709–1712, 2008.

- [246] J. Zak. Berry's phase for energy bands in solids. *Physical Review Letters*, 62(23):2747, 1989.
- [247] T. J. Zhang, R. K. Pan, Z. J. Ma, M. G. Duan, D. F. Wang, and M. He. Large rectifying leakage current in Pt/BaTiO<sub>3</sub>/Nb:SrTiO<sub>3</sub>/Pt structure. *Applied Physics Letters*, 99:182106, 2011.
- [248] W. Zhong, D. Vanderbilt, and K. M. Rabe. Phase transitions in BaTiO<sub>3</sub> from first principles. *Physical Review Letters*, 73(13):1861–1864, 1994.
- [249] W. Zhong, D. Vanderbilt, and K. M. Rabe. First-principles theory of ferroelectric phase transitions for perovskites: The case of BaTiO<sub>3</sub>. *Physical Review B*, 52(9):6301–6312, 1995.
- [250] L. Q. Zhu, N. Barrett, P. Jegou, F. Martin, C. Leroux, E. Martinez, H. Grampeix, O. Renault, and A. Chabli. X-ray photoelectron spectroscopy and ultraviolet photoelectron spectroscopy investigation of al-related dipole at the HfO<sub>2</sub>/Si interface. *Journal of Applied Physics*, 105(2), Jan. 2009.
- [251] S. Zhukov, Y. A. Genenko, O. Hirsch, J. Glaum, T. Granzow, and H. von Seggern. Dynamics of polarization reversal in virgin and fatigued ferroelectric ceramics by inhomogeneous field mechanism. *Physical Review B*, 82(1):014109, 2010.

# Chemical and Electronic Structure of the Metal/Ferroelectric Interface as a Function of Ferroelectric Polarization

## Résumé

Les phénomènes d'écrantage à l'interface entre un matériau ferroélectrique (FE) et une électrode sont d'une grande importance pour la compréhension fondamentale de la ferroélectricité et pour de potentielles applications comme les mémoires FE. Dans cette thèse, l'utilisation de la photoémission des électrons a permis d'étudier plusieurs types d'écrantage sur des pérovskites FE. En premier lieu, la microscopie de photoémission (PEEM) a révélé la transition d'une phase FE monodomaine à une phase en domaines striées dans des couches ultraminces de BiFeO<sub>3</sub>. Le PEEM a aussi permis d'étudier quantitativement l'écrantage des surfaces de BaTiO<sub>3</sub> par les lacunes d'oxygène. Enfin, la spectroscopie de photoémission (XPS) a permis d'étudier l'influence de la polarisation FE sur les propriétés électroniques d'une interface électrode/BaTiO<sub>3</sub> grâce à un dispositif original qui permet de polariser la couche FE *in-situ* pendant l'acquisition des spectres XPS.

Mots-clés : Ferroélectricité, couches minces, BaTiO<sub>3</sub>, BiFeO<sub>3</sub>, Spectroscopie de Photoémission, Microscopie de Photoémission.

## Abstract

Screening phenomena at the interface between a ferroelectric (FE) and an electrode are of great interest both from a fundamental point of view and for potential applications using a FE layer (FeRAM, FE tunnel junctions). In this thesis, we used photoemission-based techniques to study several screening phenomena on FE perovskites. Firstly, PhotoElectron Emission Microscopy (PEEM) experiment revealed a FE monodomain to stripe-domains transition in ultrathin film of BiFeO<sub>3</sub> when reducing film thickness. Still by using PEEM, we carried out a quantitative investigation of oxygen vacancies as internal screening in BaTiO<sub>3</sub> single crystals. Secondly, we used x-ray photoemission spectroscopy (XPS) with *in-situ* applied bias to investigate the electronic properties electrode/BaTiO<sub>3</sub> interfaces and measure the polarization-induced band shifts.

Keywords: Ferroelectricity, Thin films, BaTiO<sub>3</sub>, BiFeO<sub>3</sub>, X-ray Photoemission Spectroscopy, PhotoElectron Emission Microscopy